Structural Elucidation of Gas-Phase Peptide Ions by Tandem Mass Spectrometry and Molecular Dynamics Simulations

Huong Thi Huynh Nguyen

A dissertation

Submitted in partial fulfilment of the

Requirements for the degree of

Doctor of Philosophy

University of Washington

2018

Reading Committee:

František Tureček, Chair

Robert Synovec

Niels Andersen

Program Authorized to Offer Degree:

Department of Chemistry

Abstract

Structural Elucidation of Gas-Phase Peptide Ions by Tandem Mass Spectrometry and Molecular Dynamics Simulations

Huong Thi Huynh Nguyen

Chair of the Supervisory Committee:

Professor František Tureček

Department of Chemistry

The invention of the mass spectrometer has enabled scientists to discover numerous fascinating reactive gas-phase chemical species such as peptide cation radicals. The generation of these radicals can be accomplished via several methods including electron-based methods such as electron transfer dissociation or electron capture dissociation, collision-induced dissociation of transition metal-peptide complexes, photodissociation of iodinated peptide ions, etc. The basic mechanism of electron-based methods relies on the electron transfer from an anion radical donor (fluoranthene) to multiply-charged peptide cations. Electron transfer dissociation (ETD) of peptides results in energetic cation radical species, which oftentimes undergo non-specific N-C_α bond dissociation to form N-terminal c-fragment ions and C-terminal z-fragment ions. ETD has been used widely in the field of proteomics for peptide and protein sequence analysis. One of the advantages that ETD offers is its ability to preserve labile post translational modifications within the biological system of study, which enhances its accuracy for diagnosing abnormalities in proteoforms. The fragmentation mechanism of ETD is considered to be affected tremendously by the conformation of the parent ions; and thus the structures of the generated peptide cation radicals is a fascinating topic of study to many analytical chemists.

There are several methods available for probing the conformational structures of gas-phase ions such as collision-induced dissociation (CID), ion mobility (IM), infrared multiphoton dissociation (IRMPD), and UV-Vis photodissociation (UVPD). CID is a slow-heating process in which the ion of study is excited vibrationally via collisions with neutral gas atoms or molecules in the mass spectrometer. IRMPD is also considered as a slow-heating process where the peptide ion must have a chromophore present to absorb multiple IR photons to cause fragmentation. Due to the nature of CID and IRMPD, cation radicals generated from the ETD method oftentimes suffer radical-induced isomerization, which compromises the integrity of their conformational structures. IM relies on the measurement of conformers' collisional cross sections to distinguish one conformer from the others. However, in some cases, IM cannot provide sufficient selectivity due to very similar collisional cross section measurements between ions. UVPD is the only method that enables investigation of the electronic structure of the ion of interest, although it requires the presence of a chromophore. Herein, we present a new method which combines ETD and UVPD at 355 nm to probe the structures of gas-phase ions. In addition, we have also applied computational methods with different density functionals and basis sets in conjunction with molecular dynamics simulations to gain further insights regarding the structures of ETD-formed peptide cation radicals.

In the first part of this work, which includes Chapters 2-5, the electronic structures of ETD-formed z-fragment ions were studied in detail using tandem mass spectrometry and molecular dynamics simulations. Chapter 2 investigates the photoreactivity of z-fragment ions originating from model peptide sequences AAXAR and AAXK, where X is a residue of interest analyzed by both UV-Vis photodissociation at 355 nm and computational methods. UVPD results in dissociations of backbone CO – NH bonds followed by hydrogen transfer to produce fragment

ions $[y_n]^+$. Chapter 3 details the near UV-photoreactivity of the intact peptide reduced cation radicals from the effect of electrontransfer no dissociation, whereas Chapters 4 and 5 focus on elucidating radical-induced reactions that occur in the system of study using UV action spectroscopy and theoretical modeling.

In a further attempt to investigate the 3D structures of peptide ions in the gas phase, we also explored the chemistry of diazirine as a way to freeze the conformations of the ion before subjecting it to structural analysis. Diazirine has been used widely in numerous studies regarding peptide or protein interactions in both solution and gas phase. Diazirine is known for its photoreactivity in the long-wavelength region of 330-370 nm, which is absent in natural peptide or protein chromophores. The photochemistry of diazirine can be summarized as follows: under the exposure to light at 355 nm, the diazirine is photodissociated to form a highly reactive carbene intermediate, which can form a covalent bond (X-H insertion) with a neighboring atom that has a hydrogen available. The X-H insertion competes with a fast carbene intramolecular isomerization by 1,2-hydrogen shift, which forms a nonreactive olefin. This competitive side reaction can take place within 10^{-7} s, which provides an internal clock for the timescale of the covalent bond formation. The carbene insertion can potentially be located by using collision-induced dissociation in combination with molecular dynamics simulations.

In part II of this work, which includes Chapter 6, the chemistry of diazirines was implemented to study non-covalent interactions of peptide complexes generated in the gas phase. Specifically, we incorporated diazirine-tagged amino acids (photoleucine, L*) into the target peptide of study. The non-covalent complex ion was formed via electrospray ionization before being subjected to UVPD at 355 nm to establish a covalent bond between the two moieties. The covalently-bonded complex ion was then subjected to collision-induced dissociation for structural

analysis. In addition, we also combined UVPD/CID tandem mass spectrometry technique and molecular dynamics simulations to pinpoint the location of carbene insertion.

Table of Content

Acknowledgments

I would like to thank my advisor, Dr. František Tureček for his support and guidance throughout my graduate career. I really appreciate Frank for accepting me into his research group, for teaching me so much about chemistry and mass spectrometry, and for giving me so many opportunities to grow as a scientist. You are such a wonderful mentor and possess an enormous enthusiasm for science that I really admire. I feel very fortunate to be one of your students and I am grateful to study under your supervision.

I would like to also thank my doctoral exam committee for being a part of my journey. I would not be able to accomplish this work without you. I also want to extend my gratitude to the Department of Chemistry at the University of Washington for admitting me to the program and giving me the opportunity to pursue my doctoral studies.

I would like to thank everyone in the Turecek group, past and present, for your invaluable help and friendship, especially Dr. Rob Pepin and Dr. Chris Shaffer for having tremendous patience when answering my questions, and Dr. Mariana Barcenas for reading my draft introduction chapter of my dissertation.

Thank you to all my friends and family for supporting my decision and being there for me. I would not be able to survive graduate school without you.

Finally, I would like to acknowledge the financial support from the National Science Foundation for my graduate studies.

Dedication

This dissertation is dedicated to my parents, Nguyen Van Dung and Huynh Thi Thanh Ha, for your support and patience. I thank you for letting me achieve my dream and believe in my ability to accomplish it. This dissertation is also dedicated to my fiancé, Nicholas Andrew Senger. I would not be able to complete this doctoral degree without your love and support. I appreciate you for sharing your passion in higher education and particularly in chemistry with me.

To my parents:

Con cảm ơn ba mẹ đã cho con được chấp cánh ước mơ để hoành thành bài luận án tiến sĩ này. Con dù lớn vẫn là con của ba mẹ và con mong rằng ba mẹ sẽ vẫn tin tưởng vào sự lựa chọn của con. Con cảm ơn mẹ đã dành một phần quyền làm mẹ của mình để con được tự do theo đuổi ước mơ của mình. Con muốn ba mẹ tự hào và hãnh diện về con. Con thương ba mẹ nhiều lắm! Con của ba mẹ.

Chapter 1: Introduction

1. 1 A Brief Introduction to Mass Spectrometry

Mass spectrometry (MS) is an analytical technique that is based on the generation of gas-phase analyte ions, the separation of these ions, and the detection of them according to their mass-to-charge (m/z) ratio. The instrument that is used in the field of mass spectrometry is called a mass spectrometer, which has three main components: an ion source, a mass analyzer, and an ion detector. Each of these components exists in numerous variants, allowing the mass spectrometer to be customized according to the experimental design.

The diverse applications of mass spectrometry have allowed it to quickly achieve an outstanding position among analytical methods. Example applications of mass spectrometry include biochemical pathway elucidation,[1] food and produce quality control,[2] forensic analysis,[3] high throughput drug discovery,[4] metabolomics,[5] and proteomics.[6] Throughout the past few decades, mass spectrometry has advanced rapidly in terms of sensitivity, limit of detection, accuracy in low-mass determination, and resolution. Mass spectrometry has been coupled to various separation methods to meet the needs of proteomics, metabolomics, and other 'omics' fields such as liquid chromatography-mass spectrometry and gas chromatography-mass spectrometry.

Sir J. J. Thomson and his pioneering exploration into the composition of canal rays opened the doors to the development of the first mass spectrometer.[7] In his "theoretical and experimental investigations on the conduction of electricity by gases", Thomson discovered the existence of the electron using an apparatus for magnetic deflection of cathode rays. In 1906, he received the Nobel Prize in Physics for this discovery. In 1912, the mass-to-charge ratio of several gas ions including O_2, N_2, CO, CO_2, and $COCl_2$ was measured by this apparatus, which was then called a parabola

spectrograph.[7] The drawing of this apparatus made by Sir J. J. Thomson is shown in Figure 1. In this figure, the ion source is the sample chamber with a cathode K and an unlabeled anode that is located to the right. The parallel plate A is a mass analyzer, which applies a magnetostatic field and an electrostatic field to separate ions with differing m/z ratios. The ions are detected by their collisions with a phosphorescent screen S located on the left side. Sir J. J. Thomson is now considered the 'father of mass spectrometry" due to his extraordinary discovery. Thomson's assistant, Francis William Aston, was the first scientist to study isotopes using a mass spectrometer that has an improved resolving power. Aston observed that when a stream of gas were subjected to a gas discharge, positive rays with different masses were produced. Aston concluded that gas ions must have varying atomic masses, a concept now known as isotopes. In 1919, Aston built the first functional mass spectrometer with velocity focusing.[8, 9]

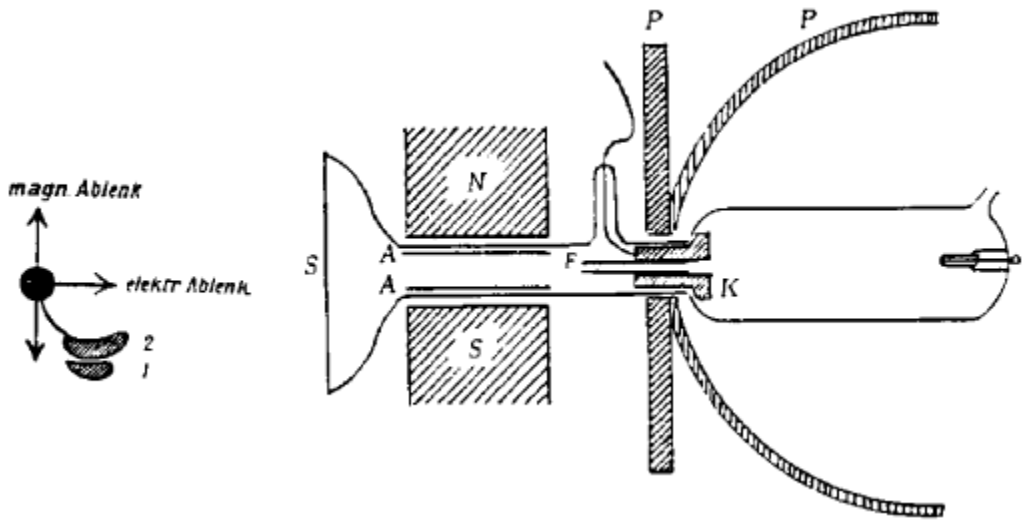

Figure 1. The drawing of the first mass spectrometer by Sir J. J. Thomson and his assistant F. W. Aston. The figure is taken from http://www.scielo.br/img/fbpe/bjp/v29n3/401f7.gif.

Following Sir J.J. Thomson's first studies in 1912, the mass spectrometer has undergone countless cycles of improvement. The combination of mass spectrometry with gas chromatography in 1958 drastically improved/enhanced the study of volatile compounds.[10, 11] In the 1980s, numerous techniques emerged for studying non-volatile compounds using the mass spectrometer.[12] The introduction of electrospray ionization[13, 14] and matrix-assisted laser desorption ionization techniques [15, 16] have opened the doors for analysis of numerous biological molecules with molecular masses exceeding thousands of Dalton such as proteins, glycans, and polynucleotides.

All mass spectrometers must operate at low-pressure conditions in order to reduce the number of collisions that the gas ions undergo before reaching the detector. Collisions with other gas ions or molecules can affect the trajectory of the ions of study and potentially produce unwanted ion-ion or ion-molecule reactions. Controlled collisions however are sometimes useful for determining the composition of molecular ions, such as in peptide or protein sequencing. In order to introduce the gas ions from an atmospheric pressure to a low-pressure region, an efficient pumping system comprising of mechanical pumps and turbo pump is required.

1.1.1 Ion Generation

The first step in mass spectrometry analysis of a compound is generation of the gas-phase ions. A wide variety of ionization techniques are available to produce gas-phase analyte ions, including electron ionization (EI), soft ionization methods such as electrospray ionization (ESI) or surface acoustic wave nebulization (SAWN), and matrix-assisted laser desorption ionization (MALDI). Electron ionization, which is also known as electron impact, is one of the first ionization methods that was developed for mass spectrometry to produce molecular ions.[17, 18] The general scheme of how electron impact works can be depicted as follows:

$$M + e^- \rightarrow M^{\bullet+} + 2e^-$$

Electron impact is considered a hard ionization technique. Under electron ionization conditions, the $M^{\bullet+}$molecular ion normally possesses an excessive amount of internal energy and readily undergoes subsequent fragmentation to form either an odd-electron (cation radical) ion and a neutral molecule or an even-electron ion and a radical.

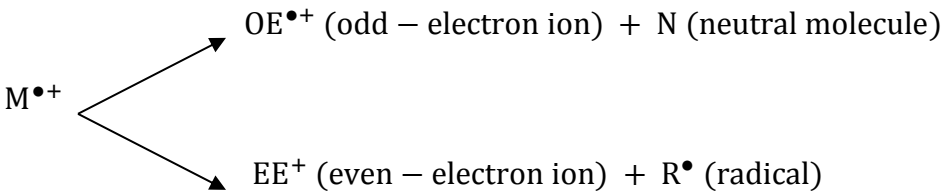

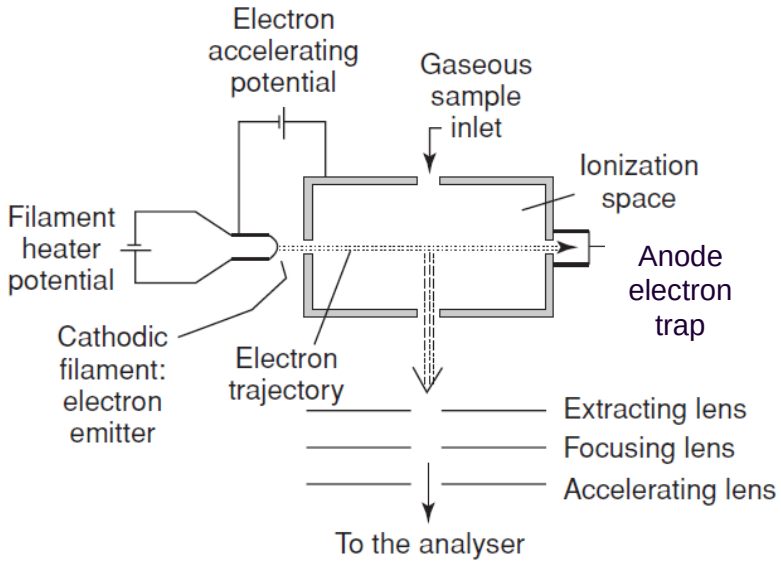

Figure 2. Diagram of an electron ionization source. Picture is adapted from: De Hoffmann, E., & Stroobant, V. (2007). *Mass spectrometry: principles and applications*. John Wiley & Sons.[19]

The structure and energetics of the two types of primary product ions are very different, though each of them can further undergo subsequent fragmentation(s). All fragment ions can be separated by their mass-to-charge ratio (*m/z*) using a mass analyzer to generate a mass spectrum. Since electron impact is a hard ionization technique, the lack of the molecular ion can impede the identification of unknown compounds. To overcome this drawback, a softer ionization method is

needed. In the 1960s, the introduction of chemical ionization made the analysis of fragile volatile compounds possible.[20]

In contrast to electron ionization, chemical ionization (CI) methods generally produce ions with little excess energy; and thus reduce extensive fragmentation of molecular ions. The general mechanism of CI involves collisions between the analyte ion of interest and primary ions generated in the source. Under CI conditions, a wide variety of reactions may take place, however the most common ones are proton transfer, charge transfer, and adduct formation.[17] Chemical ionization techniques that utilize a reaction between the analyte of interest and a reagent gas such as methane have been used widely.[20, 21, 22] If methane is introduced into the ion volume, the primary reaction that will take place is ionization:

$$CH_4 + e^- \rightarrow CH_4^{\bullet +} + 2e^-$$

where the electron is generated by the heated filament. The above reaction holds true since the reagent gas is the excessive reagent while the analyte ion is the limiting reagent. The $CH_4^{\bullet +}$ is a reactive intermediate that can further undergo the following fragmentation reactions:

$$CH_4^{\bullet +} \rightarrow CH_3^+ + H^\bullet$$

$$CH_4^{\bullet +} \rightarrow CH_2^{+\bullet} + H_2$$

It can also collide and react with the other methane molecules available in the ion source in the following manner:

$$CH_4^{\bullet +} + CH_4 \rightarrow CH_5^+ + CH_3^\bullet$$

With an exception to saturated hydrocarbons, the protonated methane molecule CH_5^+ can now undergo an acid-base type of reaction with an analyte ion of interest as follows:

$$M + CH_5^+ \rightarrow MH^+ + CH_4$$

If the analyte ion is a saturated hydrocarbon, it will undergo a hydride abstraction instead:

$$RH + CH_5^+ \rightarrow R^+ + CH_4 + H_2$$

Chemical ionization has also been used to generate anion molecular donors such as fluoranthene, which are widely used in electron transfer dissociation (ETD) processes.[22, 23] Under CI conditions with fluoranthene, nitrogen gas will capture a high-energy electron ejected from the heated filament. The reaction between the nitrogen molecule and the high-kinetic energy electron produces a lower-energy electron, a high-energy electron, and an N_2 cation radical.

$$N_2 + e^-(high\ energy) \rightarrow N_2^{+\bullet} + e^-(high\ energy) + e^-(low\ energy)$$

The low-energy electron collides with the bath gas molecules (N_2) present in the ion source to thermalize. The thermal electron is absorbed to form an excited fluoranthene molecular anion-radical.

$$e^-(low\ energy) + N_2 \rightarrow\ e^-(thermal) + N_2$$

$$C_{16}H_{10} + e^-(thermal) \rightarrow C_{16}H_{10}^{(-\bullet)*}$$

The excited fluoranthene anion-radical collides with the bath gas molecules to produce a stable molecular anion radical that can be used as an electron donor for the electron transfer dissociation process.

Though the CI method avoids the extensive fragmentations of the molecular ion seen with electron ionization, non-volatile compounds still cannot be analyzed by this method. Following the invention of chemical ionization, electrospray ionization was introduced to the world of analytical chemistry by Masamichi Yamashita and John Fenn in 1984.[13] In 2002, Fenn received the Nobel Prize in Chemistry for the development of this technique.[14] Electrospray ionization (ESI) is a technique that is used widely in mass spectrometry to generate gas-phase ions from solution by applying a high voltage to create charged droplets. One of the most significant advantages of using ESI for bioanalytical chemistry is its ability to produce multiply charged ions from

macromolecules. This fact enables the analysis of large molecules such as peptides and proteins by mass spectrometry. These macromolecules typically have a very large mass that is outside the mass range of most mass spectrometers. However, as the charge of these molecules is increased, their molecular masses come within the available mass range, allowing them to undergo further analysis.

ESI is a soft ionization method, in which the ions reach the mass analyzer without breaking chemical bonds. The ions are generated by applying a high electric voltage (~3000V) to the liquid inside a capillary that ends with a sharp tip. Under positive mode, the ions formed usually have an additional proton, but they can also be formed as sodium or potassium adducts. However, if deprotonation is preferred, negative ions would be generated instead during ESI process. The high potential difference between the capillary and the atmospheric inlet of the mass spectrometer leads to the formation of a Taylor cone. The charged droplets are dispersed from the Taylor cone, and attracted down the potential gradient towards the atmospheric inlet before entering the vacuum manifold of the mass spectrometer. The capillary tube can also be heated to increase the speed of solvent evaporation from the charged droplets. A general schematic of ESI is depicted in Figure 3. The mechanism of how the charged droplets are de-solvated and transferred into the gas phase is still not well understood. The two most prominent models used to explain the formation of the charged ions by ESI are the ion evaporation model (IEM)[24, 25] and the charge residue model (CRM).[26]

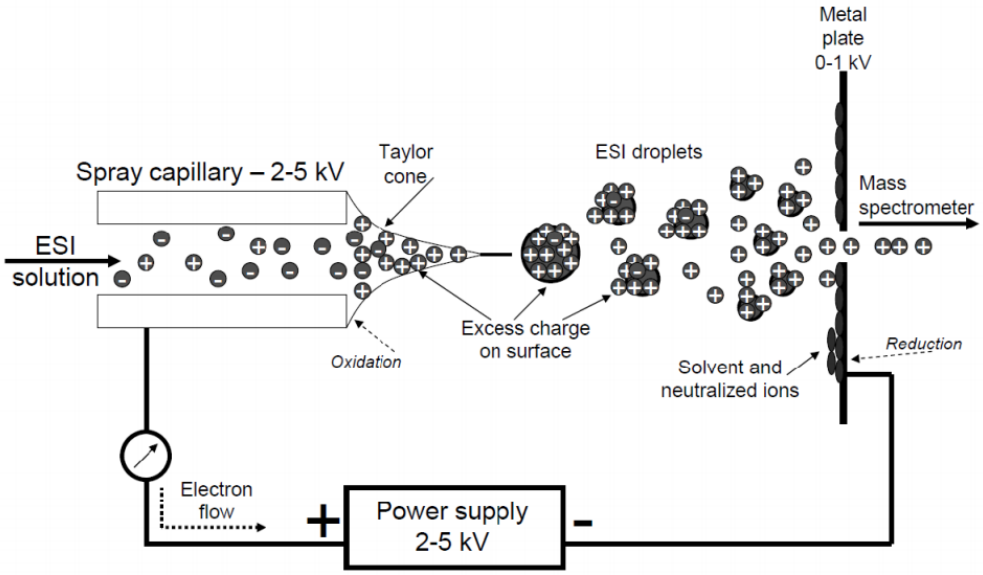

Figure 3. Diagram shows a general process of electrospray ionization. Picture is adapted from https://sea.rice.edu/sites/default/files/ESI_Interpretation_ComputingChargeState.pdf

1.1.2 Mass Analysis

After the generation of the ion, the next step in a mass spectrometry analysis is the mass separation step. Mass analysis can be performed by several types of mass analyzers such as quadrupole mass analyzer, ion traps such as orbitrap mass analyzer, linear ion-trap (LIT) mass analyzer, and time-of-flight mass analyzer. The work report herein mainly uses the LIT in performing mass analysis; thus only this type of mass analyzer will be discussed in detail.

The LIT mass analyzer adapted the basic structure of the Quadrupole Mass Filter (QMS), which has an assembly of four cylindrical rods in a parallel array for ion trapping, ion manipulation, and mass-selective ion ejection. (Figure 4) LIT mass analyzers are sometimes called 2D ion traps due to their elongated geometry. Before the linear ion trap, all ion-trap mass analyzers were of the hyperbolic or circular symmetry, which is also known as Quadrupole Ion Trap (QIT) or 3D ion traps. The principal advantage of a LIT is its capability of trapping more ions (larger ion capacity) than a 3D Quadrupole Ion Trap (QIT). Due to this larger ion capacity, the onset of space

charge repulsion, reduction in mass resolution and reduction in mass accuracy only happen at greater ion loading. The LIT uses a quadrupole field to manipulate ion motion.

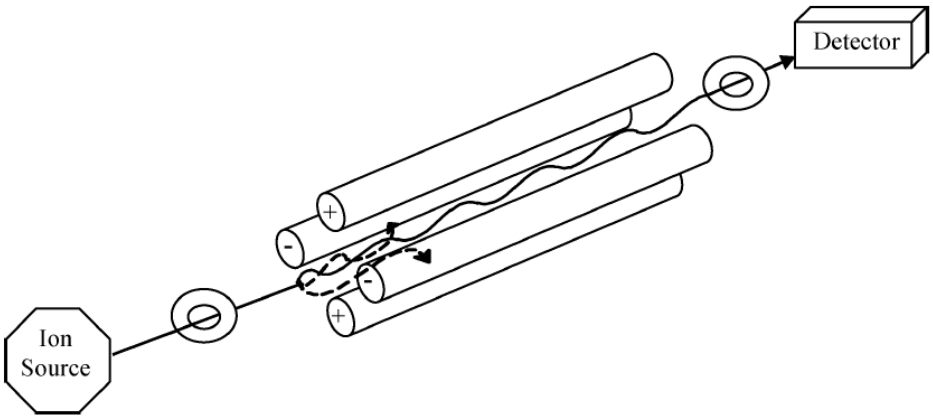

Figure 4. A schematic diagram of a quadrupole mass analyzer. Figure is reproduced from El-Aneed, A., Cohen, A., & Banoub, J. (2009). Mass spectrometry, review of the basics: electrospray, MALDI, and commonly used mass analyzers. *Applied Spectroscopy Reviews*, *44*(3), 210-230.[27]

There are two different versions of LIT that are used frequently: Thermo LIT or LTQ and MDS SCIEX LIT. The former is used throughout this study. In a Thermo LIT, the four parallel rods of a LIT can be segmented into three axial parts with the middle section three times longer than the other two sections. The ions are confined radially by a 2D radio frequency (RF) at the center section for trapping in the xy plane, and axially by applying DC potentials to the three sections for trapping along the z axis.[28, 29] The x electrode in the middle section of the Thermo LIT has a slit which allows for radial ion ejection. As the RF potentials on the xy plane increase, ions of increasing mass become unstable in the radial direction. Mass-selective ion ejection is achieved by radial resonant excitation of the stored ions from this slit of the center section. A cartoon

diagram that demonstrating how DC and RF potentials are applied to ion trapping is shown in Figure 5.

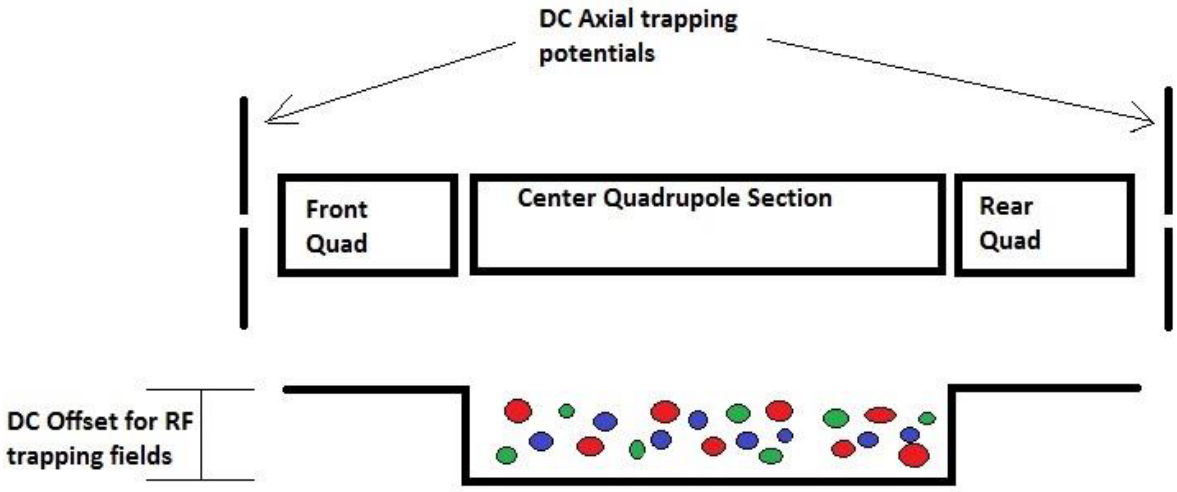

Figure 5. A cartoon diagram shows how the linear ion trap captures ions. The RF and DC potentials are modulated in such a way that the ions are confined radially in the ion trap.

1.1.3 Ion Detection

The last step in generating a mass spectrum is ion detection. After passing through a mass analyzer, ions are detected by a detector which generates a signal proportional to their relative abundance. There are several detectors available commercially to accomplish this step. Most common are the Faraday cup,[13] photographic plates,[9] electron multipliers,[23] and electro-optical ion detectors.[30] The choice of detector is dependent on the instrumental design and the analytical application of interest.

The photographic plate can be considered the first ion detector since it is used in the first mass spectrometer developed by Sir J. J. Thomson.[9] The photographic plate detects ions by as spots generated from the ions hitting the plate after passing through a mass analyzer. The relative abundance of the ions is determined by the darkness of the spot on the plate's surface.

A Faraday cup is a metal cup or a cylinder with a small orifice. The Faraday cup is based on the measurement of charge current that is produced when the ion hits a surface and is neutralized. When an ion hits a surface, it can either donate or gain an electron, which produces a charge current that runs through a resistor. The discharge current is then amplified for detection of ions and determination of their relative abundance. .

Electron multipliers are found in numerous modern mass spectrometers. Electron multipliers use a conversion dynode electrode at a high potential to accelerate ions, which allows them to obtain enhanced detection efficiency. An electron multiplier (EM) can be either a discrete dynode EM or a continuous dynode EM. The discrete dynode electron multiplier is often made of a series of 12-20 dynodes. Electron multiplier uses a process called secondary emission, in which an electron can induce the emission of more electrons through bombarding on a secondary-emissive material, to produce secondary electrons. These secondary electrons are then amplified by a cascade effect to produce a current, which is then detected and converted into relative intensity for each ion.

1.2 A Tutorial to Peptide Radicals and Cation Radicals

The facile formation of gas-phase peptide radicals using mass spectrometry techniques is of great interest due to their unique chemistry and presence in biological systems. Radical species play an important role in several biological activities, such as intracellular elimination of bacteria, and cell signaling. Free radicals are also thought to be involve in the development of several diseases such as Parkinson's disease and Alzheimer's. There are several mass spectrometry techniques that can be used to characterize peptide cation radicals. These methods include:

- Ion mobility (IM),[31] which separates ions based on their mobility with a low applied electric field to obtain collisional cross section (CSS) measurements;

- Collision-induced dissociation (CID),[32] which makes use of an inert gas, such as helium, to induce collisional kinetic energy which is then be converted into internal energy and thereby causing fragmentation when a dissociation threshold energy is reached;
- Infrared multiphoton dissociation (IRMPD),[33] in which multiple photons are absorbed by the molecular ion, resulting in several dissociation channels
- UV-Vis photodissociation,[23] in which the electronic structures of the numerous gas phase ions can be obtained for further characterization.

Each of these methods has limitations. Collision-induced dissociation is a slow-heating process that can trigger hydrogen migration and facilitate the isomerization of the charge-reduced species.[34, 35, 36] Ion mobility does not have a sufficient specificity to provide definite structural information of gas-phase ions that have very similar collisional cross section measurements.[37] Infrared action spectroscopy is another slow-heating process which can facilitate isomerization within the radical, compromising the integrity of the species in question. Moreover, when subjected to infrared multiple photon dissociation, anharmonic vibrational modes can obscure the analysis of the spectra.[38, 39] Recently, the combination of electron transfer dissociation with UV-Vis photodissociation has been used to elucidate the structure of gas-phase peptide cation-radicals.[40] Briefly, the intact charge-reduced peptide cation radical is formed by electron transfer process (ETD) and then stored in the ion trap. The ions then absorb the high-energy UV photons at 355 nm and dissociates into different channels. The absorption at 355 nm selectively excites only the radical chromophores produced by electron transfer. The use of the ETD/UVPD tandem mass spectrometry method is discussed in detail in Chapter 2.

Peptide cation radicals are categorized into two groups: hydrogen-rich, $(M+nH)^{(n-1)+\bullet}$ and hydrogen-deficient radicals, $(M+(n-1)H)^{n+\bullet}$.[41] The generic formations of these radicals is depicted

in Scheme 1. Electron transfer dissociation (ETD) is one of several techniques that can accommodate the formation of both types. In ETD, hydrogen-rich peptide ions can be generated by collisional electron transfer from a molecular anion radical, such as fluoranthene, to a multiply charged peptide, forming intact charge-reduced peptide cation-radicals $(M+nH)^{(n-1)+\bullet}$. Subsequent dissociation of $(M+nH)^{(n-1)+\bullet}$ cation radicals via facile backbone C_α – N cleavage can produce hydrogen-deficient $\mathbf{z_n}^{+\bullet}$ fragment ions (odd-electron ions originating from the C-terminus).[41] Generally, in electron-transfer (ET) reactions, intact charge-reduced ions are very reactive and thus further dissociate within the ion trap before reaching the mass detector. Hence, a full accounting for the ET channel must include both the charged-reduced cation radicals with no subsequent dissociation and the ETD-formed products. The former was previously termed by Mc Luckey *et al* as electron transfer no dissociation (ET-no-D) process.[42] One of the many exceptions to this ET-no-D process is in the case of histidine.[42] The photoreactivity of the intact charge-reduced histidine-containing peptide cation radical produced from this process is discussed in Chapter 3.

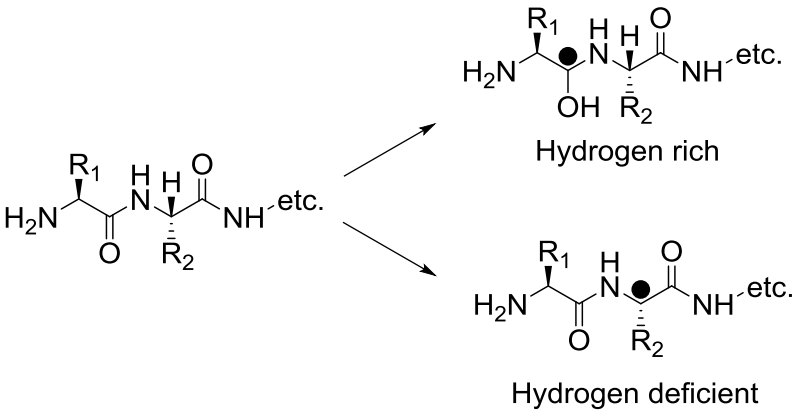

Scheme 1. A generic scheme shows the formation of both hydrogen-rich and hydrogen-deficient peptide cation-radicals. Figure is adapted from: Turecek, F., & Julian, R. R. (2013). Peptide radicals and cation radicals in the gas phase. *Chemical reviews, 113*(8), 6691-6733.[41]

Beyond ETD, other methods are available for generation of hydrogen-rich or hydrogen-deficient peptide-cation radicals. The formation of a hydrogen-rich peptide cation-radical can also be accomplished via electron capture dissociation (ECD) in a Penning trap of a Fourier Transform ion cyclotron resonance (FT-ICR) mass spectrometer.[41] Collision-induced dissociation of a transition metal-peptide complex has been used to generate hydrogen-deficient peptide cation radical as previously reported.[43] This method utilizes the transition metal to strip off an electron from the peptide ligand in the gas phase. Another method used in forming a hydrogen-deficient peptide cation radical is to photodissociate an iodinated tyrosine-containing peptide at the natural peptide chromophore (266 – 280 nm).[44]

1.3 UV-Vis Photodissociation of Gas-Phase Biomolecules

Over more than 30 years, MS has undergone a spectacular development in terms of both its technical specifications and the extent of its application. Recently, the Turecek lab has used the combination of mass spectrometry and UV-Vis photodissociation to study reactive species such as radical cations.[23, 40] While infrared photons correspond to vibrational excitations of a molecule, photodissociation that takes place in the visible and UV range corresponds to electronic excitation of valence electrons, and allow for the study of molecular electronic structure. In the case of single photon absorption, the energy deposit into the system is well-defined. However, when numerous excited electronic states are populated, multiple de-excitation pathways could take place, such as: emission of a photon (fluorescence), internal conversion (IC) from electronic energy to vibrational energy followed by internal vibrational redistribution (IVR) or fragmentation in the electronic excited state. The combination of mass spectrometry with photodissociation has allowed us to investigate potential relaxation pathways.

Due to the higher energy of the UV-Vis region, the absorption of a single photon usually overcomes the dissociation threshold to form multiple primary, and sometimes secondary fragments. Photodissociation can take place through three common routes. In the first route, the UV photon absorption causes a vertical transition from the ground electronic state (S_0) to a highly excited unbound vibrational state in the excited electronic state (S_1), resulting in dissociation. In the second route, the UV photon absorption causes dissociation from the ground electronic state, following an internal conversion from the electronic excited state. An internal conversion is defined as energy conversion from an electronic state to a vibrational state. The third route is dissociation that takes place via dissociative state, which has a shallow potential energy minimum that could cause pre-dissociation. A general schematic shows how these mechanisms work is shown in Figure 5.[45]

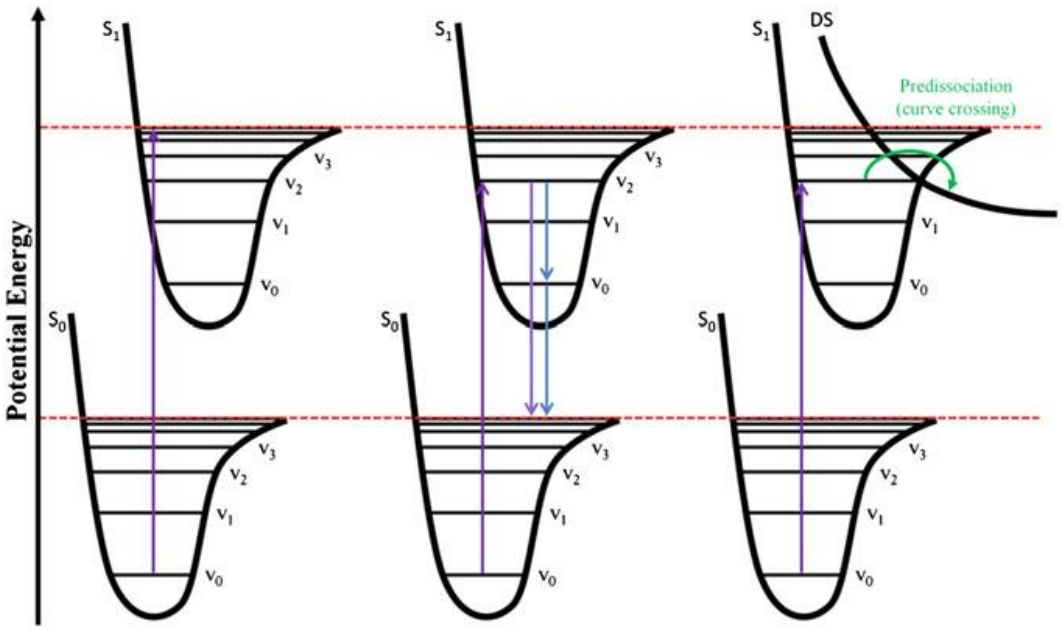

Figure 5. Three potential mechanism of UVPD. Figure is adapted from: Polfer, N. C., & Dugourd, P. (Eds.). (2013). *Laser photodissociation and spectroscopy of mass-separated biomolecular ions* (pp. 13-19). Heidelberg, Germany: Springer.[45]

One disadvantage of UV-Vis photodissociation is its multitude of available vibronic transitions, which cause broad spectral features when obtained at room temperature in conformational studies. In order to avoid this, UV-Vis photodissociation experiments can be conducted at low temperature. To accomplish photodissociation, the analyte ion must contain a suitable chromophore. Depending on the chromophore, different types of photodissociation will take place for differing wavelength regions. There are two different chromophores that absorb at 355 nm wavelength, which will be discussed in detail throughout this work. The first one involves the presence of a diazirine functional group, which is used in photocrosslinking to study peptide or protein interactions in the gas phase. The second type of chromophore is formed via the generation of the *z* cation radical during the electron transfer dissociation process. The utility of these two chromophores will be discussed throughout this work.

1.4 UV Action Spectroscopy

Action spectroscopy is a resonant excitation process in which one or multiple photon(s) are absorbed by the ion of study, and the resulting fragment ions are then detected by the mass spectrometer at differing wavelengths. The term "action" refers to the detection of fragment ions which are formed by photon absorption of the analyte at different energy levels. In an action spectroscopy experiment, the analyte ion is subjected to irradiation at different energy levels generated by a tunable light source at discrete frequency steps. The photon absorption causes photofragments, which are monitored by plotting the fragment ions and the parent ion's relative abundance against the wavelength region. An illustration of the workflow for a typical action spectroscopy experiment is shown in Figure 6.[45]

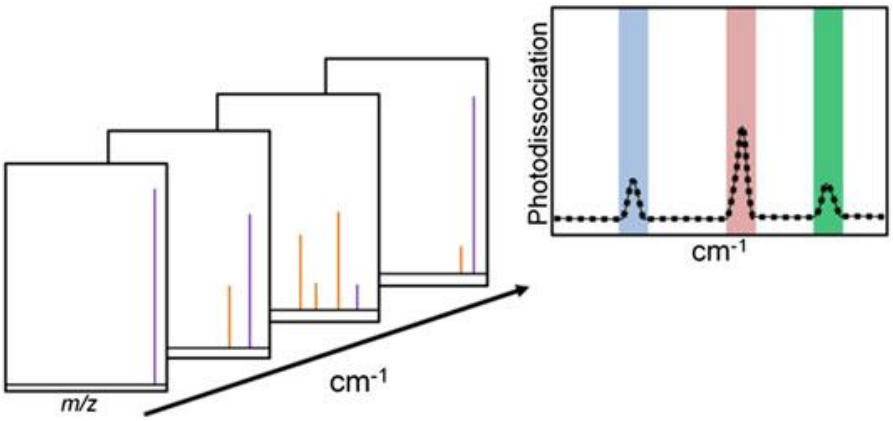

Figure 6. A schematic workflow of an action spectroscopy experiment where the purple line represents the parent ion and the orange lines represent the photo-fragment ions. An action spectroscopy spectrum is conducted by plotting the relative intensities of all ions at different wavelength. Figure is adapted from: Polfer, N. C., & Dugourd, P. (Eds.). (2013). *Laser photodissociation and spectroscopy of mass-separated biomolecular ions* (pp. 13-19). Heidelberg, Germany: Springer.[45]

Over the past few decades, several action spectroscopy methods have been developed for studying the structures and physicochemical properties of biological molecules. These methods include infrared multiphoton dissociation (IRMPD) spectroscopy, ultraviolet (UV) photodissociation action spectroscopy, infrared ultraviolet ion dip spectroscopy, infrared predissociation spectroscopy, and photoelectron spectroscopy. UV photodissociation action spectroscopy has been used to investigate radical-induced isomerization, which often takes place in peptide cation radicals generated in the gas phase. The details of this topic will be demonstrated in Chapter 4 of this work.

1.5 Molecular Dynamics Simulations

Molecular dynamics (MD) is a computer simulation method which adapts Newtonian dynamics to study the motion of atoms of a molecular assembly in terms of their structures and interactions. Molecular dynamics simulation was first developed by Fermi, Pasta, and Ulam in the mid-50s,[46] and later improved by Alder and Wainwright in the late 50s,[47] and Rahman in the 60s.[48]

The first simulation was developed in 1957 to depict elastic collisions between hard spheres.[49] Molecular dynamics is one of the two main families of simulation techniques (MD and Monte Carlo). MD simulations help to connect the microscopic world provided by statistical mechanics to the macroscopic world composing of experimental results. In addition, MD simulations also aid in establishing a relationship between theory and experimental results. We can use simulations to complement or replace conventional experiments that are impossible to carry out within the laboratory environment due to their extreme conditions. Ultimately, simulations are often directly compared with experimental results on a specific topic or material, in which case both a well-developed algorithm and model are required.

Molecular dynamics simulation is a numerical step-by-step solution of a classical Newton equation of motion: F = ma. The computational tools that are used for MD simulations include two primary branches. While quantum mechanics (QM) uses the Schrodinger equations to accurately and extensively predict the behavior of the molecular system within a 10-100 picosecond time scale, classical molecular mechanics (MM) uses the Newton empirical forces for modeling in the range of 10-100 nanoseconds. Beyond those main tools, there are also hybrid techniques that combine QM and MM for simulations. MD simulations are commonly used to (but not limited to) simulate and predict processes such as polypeptide folding, biomolecular association, partitioning between solvents, micelle formation, enzyme catalysis, photochemical reactions, electron transfer reactions, and protein-protein interactions. A model for an MD simulation is defined under 4 main criterias:

- Degrees of freedom, which is defined by the number of atoms in the system
- Force fields between the atoms
- Method for generating the configuration of the atoms

- Boundary conditions or constraints

The work here only uses semi-empirical method MD (PM6-D3H4) in simulating the given systems. Semi-empirical MD uses the semi-empirical force in simulating the N-body system. The goal of semi-empirical force fields (*V(r)*) is to use the empirical potential energy differentiable functions to compute the forces acting on each atom. Even though this type of MD simulation is fast and easy to implement, it does not give information regarding the electronic polarization of the system. In order to resolve that problem, a full QM MD simulation can be done instead on capable computer systems.

Generally, MD simulations are accomplished by solving the Newton equations of motion at constant volume under constant volume and adiabatic conditions; however, such conditions cannot be used if the system of interest is dissipative or non-equilibrated Moreover, an equilibrium system that has long interactions involved cannot avoid slow energy drift. Thus, simulations that perform under constant temperature and/or pressure are preferred.

A molecular dynamics simulation is performed as follows:

1. After extensive conformational search for the system of interest, the most stable configuration which best represents the system is chosen with selected initial atomic coordinates and velocity for all of the atoms. If a conformational search cannot be performed, multiple configurations will need to be run in order to obtain a statistical analysis for the system of study.
2. The forces acting on all atoms are then calculated. For a given pair of atoms, the α-component ($\alpha = x, y, z$) of the force is given by:

$$F_\alpha = -\frac{\partial \phi(r)}{\partial r_\alpha} = -\frac{r_\alpha}{r} \times \frac{\partial \phi(r)}{\partial r}$$

where $\phi(r)$ is the pair potential of the two atoms, $r = \sqrt{r_x^2 + r_y^2 + r_z^2}$ is the distance between the two atoms. Thus, the total force acting on a particular atom i is calculated by considering its interactions with all other atoms j in the system ($i \neq j$).

3. The new positions and velocities of all atoms are determined by integrating the Newton's equations of motion given by:

$$F_i = m_i \times \frac{dv_i}{dt} = m_i \times \frac{d^2 r_i}{dt^2}$$

$$v_i = \frac{dr_i}{dt}$$

where v_i is the velocity of atom i, m_i is its atomic mass, F_i is the total force acting on the atom i, and r_i is its position.

4. Steps 2 and 3 are repeated until the system reaches equilibrium or until a given timeframe is achieved.

The above steps can be simplified by the following shell script format (Figure 7), which is adapted from Frenkel, D., Vlugt, T. J. H., Van der Eerden, J. P. J. M., Dijkstra, M., & Smit, B. (2009). Introduction to Molecular Simulation and Statistical Thermodynamics. *http://homepage. tudelft. nl/v9k6y/imsst/index. html*.[49]

```
program md                          Molecular Dynamics algorithm
call initials                       select initial positions and velocities
t=0.0                               time t = 0
do while (t < tmax)                 for t < tmax
     call force(f,en)               calculate the forces on all particles
     call integrate(f,en)           integrate equations of motion
     t=t+deltat                     update the time
     call sample                    sample the time averages
enddo
end
```

Figure 7. Psuedo code represents the steps in a molecular dynamics simulation. Code is adapted from Frenkel, D., Vlugt, T. J. H., Van der Eerden, J. P. J. M., Dijkstra, M., & Smit, B. (2009). Introduction to Molecular Simulation and Statistical Thermodynamics. *http://homepage. tudelft. nl/v9k6y/imsst/index. html*.[49]

In step 1, the MD is initiated by choosing an initial configuration of N numbers of atoms that is contained in a fixed volume V. The chosen initial configuration thus determines the initial atomic coordinates $\alpha(x, y, z)$ and the initial atomic velocities. The positions of the atoms are chosen such that each weighted Boltzmann value associated to each atom is non-zero. The atoms are positioned in a random manner or in a lattice fashion. The velocity of each atom is assigned randomly in the interval [-1, 1] for each $x, y,$ or z coordinate or by using the Maxwell-Boltzmann velocity distribution such that the following conditions are satisfied:

- The total momentum of all atoms must be added to zero
- The mean kinetic energy of the system ($E_{kinetic}$) must be scaled to match the desired temperature

$$E_{kinetic} = \sum_{i=1}^{N} \frac{mv_i^2}{2} = \frac{3Nk_BT}{2}$$

where $v_i^2 = v_{x,i}^2 + v_{y,i}^2 + v_{z,i}^2$, N is the number of atoms in the system, T is the desired temperature, k_B is the Boltzmann constant.

In step 2, the force acting on each atom is calculated using the pairwise additive interaction method, which considers the interaction between atom i and the other atoms j present in the system of interest. If the system has N atoms in total, there are $N(N-1)/2$ pairs of atoms that must be accounted for. The whole process of calculating the force acting the atoms can be summarized by the following shell script in Figure 8.

```
subroutine init                  Initialization of MD program
sumv=0
sumv2=0
do i=1,npart
     x(i)=latticepos(i)          place the particle on a lattice position
     v(i)=2×(ranf()-0.5)         give random velocity
     sumv=sumv+v(i)              total momentum
     sumv2=sumv2+v(i)**2         kinetic energy
enddo
sumv=sumv/npart
sumv2=sumv2/npart
fs=sqrt(3*temp/sumv2)            we assume a three-dimensional system
do i=1,npart                     scale velocities to desired temperature
     v(i)=(v(i)-sumv)*fs         set total momentum to zero
enddo
end return
     end
```

Figure 8. Psuedo code represents the force calculation in a molecular dynamics simulation. Code is adapted from http://homepage.tudelft.nl/v9k6y/imsst/book-15-6-2009.pdf [49]

In order to find the positions and velocities for all of the atoms in the system of interest, the Newton's equations of motion will need to be integrated. There are several algorithms available to accomplish this step such as the Verlet algorithm,[50] the Euler algorithm,[49] the Berendsen

thermostat algorithm[51] and the Leap Frog algorithm.[49] Only the Berendsen thermostat algorithm will be discussed briefly since it is used in this work. Choosing a good algorithm is important to minimize the amount of computational time, memory capacity, and artifacts developed during the simulation. In addition, the algorithm should be able to accurately estimate the positions and velocities for large timesteps since this will reduce the number of evaluation cycles. Moreover, the algorithm should satisfy the conservation of momentum (total momentum is zero), and the mean kinetic energy should match the desired temperature. Most importantly, the algorithm needs to be time-reversible. While the Verlet and the Leap Frog algorithms are time-reversible, the Euler method is not and thus it suffers slow energy (temperature) drift during the simulation.[49]

In the Berendsen thermostat algorithm, the system is weakly coupled to a heat bath that has a fixed reference temperature.[51] The kinetic energy of the system is then monitored by the thermostat to suppress the temperature fluctuation. The coupling between the system of interest and an external heat bath with a fixed temperature can be accomplished by inserting stochastic and friction terms into the Newton's equations of motions as follows:[51]

$$F_i - m_i\gamma_i v_i + R(t) = m_i \frac{dv_i}{dt}$$

where $R(t)$ is the Gaussian stochastic term and γ_i is the damping constant that determines the strength of the coupling. The above equation is also known as the Langevin's equation. When employing the Berendsen thermostat algorithm, it should be noted that the produced trajectory of the system is not consistent with a canonical ensemble. The deviation from a canonical system is worse for smaller systems; however, with large systems on the order of hundreds of atoms, the properties obtained using this algorithm are roughly accurate. In this work, all systems of interest have at least 100 atoms or more, and thus the use of the Berendsen algorithm is justified. In this algorithm, the slow drift in temperature is corrected by the using the following equation: $dT/dt =$

$(T_O - T)/\tau$, where τ is the timeframe that the simulation runs for.[51] All the MD simulations in this work are ran by using Berendson thermostat algorithm, at semi-empirical (PM6-D3H4) level, with constant temperature of 310 K condition.

Much of the work in this dissertation focuses on investigating the conformational structures and photoreactivity of numerous systems including intact charge-reduced peptide cation-radicals, $z_n^{+\bullet}$ cation radicals formed from electron transfer dissociation process, and dimer complexes generated in the gas phase using tandem mass spectrometry techniques, in combination with molecular dynamics simulations. The entire dissertation can be separated into two parts. Part I includes chapters 2 – 5, which detail the experimental and computational work on probing the conformational structures of peptide cation radicals. Briefly, chapter 2 discusses the photoreactivity of the $z_n^{+\bullet}$ cation radicals generated from the electron transfer dissociation of lysine-c-terminal and arginine-c-terminal tryptic peptides. Chapter 3 details the photoreactivity study of the intact charge-reduced histidine-containing peptide cation radicals formed from the electron transfer no dissociation (ET-no-D) process. Chapter 4 focuses on the UV action spectroscopy of cation radicals generated from phenylalanine- and tryptophan-containing pentapeptides. Chapter 5 explains the radical-induced isomerization in the $z_n^{+\bullet}$ cation radicals of the threonine-containing peptide AATAR. Part II includes chapter 6 which focuses on the interaction of complexes formed in the gas phase using the chemistry of the diazirine functional group, tandem mass spectrometry techniques, and molecular dynamics simulations. Chapter 6 discusses the interaction between proline- and phenylalanine- containing peptides and modelled photolabelled peptides.

1.5 References

1. Finehout, E. J., & Lee, K. H. (2004). An introduction to mass spectrometry applications in biological research. *Biochemistry and molecular biology education*, *32*(2), 93-100.
2. Krishnamurthy, T., Rajamani, U., & Ross, P. L. (1996). Detection of pathogenic and non-pathogenic bacteria by matrix-assisted laser desorption/ionization time-of-flight mass spectrometry. *Rapid Communications in Mass Spectrometry*, *10*(8), 883-888. Fiehn, O. (2002).
3. Metabolomics—the link between genotypes and phenotypes. In *Functional Genomics* (pp. 155-171). Springer Netherlands.
4. Wood, M., Laloup, M., Samyn, N., Fernandez, M. D. M. R., de Bruijn, E. A., Maes, R. A., & De Boeck, G. (2006). Recent applications of liquid chromatography–mass spectrometry in forensic science. *Journal of Chromatography A*, *1130*(1), 3-15.
5. Kostiainen, R., Kotiaho, T., Kuuranne, T., & Auriola, S. (2003). Liquid chromatography/atmospheric pressure ionization–mass spectrometry in drug metabolism studies. *Journal of Mass Spectrometry*, *38*(4), 357-372.
6. Yates, J. R., Ruse, C. I., & Nakorchevsky, A. (2009). Proteomics by mass spectrometry: approaches, advances, and applications. *Annual review of biomedical engineering*, *11*, 49-79.
7. Thomson, J. J. (1921). *Rays of positive electricity and their application to chemical analyses* (Vol. 1). Longmans, Green and Company.
8. Aston, F. W. (1919). LXXIV. A positive ray spectrograph. *The London, Edinburgh, and Dublin Philosophical Magazine and Journal of Science*, *38*(228), 707-714.
9. Aston, F. W. (1942). *Mass spectra and isotopes* (p. 167). London: Edward Arnold.
10. McLafferty, F. W. (1957). Mass spectrometry in chemical research and production. *Applied*

Spectroscopy, *11*(4), 148-156.

11. Gohlke, R. S. (1959). Time-of-flight mass spectrometry and gas-liquid partition chromatography. *Analytical Chemistry*, *31*(4), 535-541.
12. Blakley, C. R., Carmody, J. J., & Vestal, M. L. (1980). A new soft ionization technique for mass spectrometry of complex molecules. *Journal of the American Chemical Society*, *102*(18), 5931-5933.
13. Whitehouse, C. M., Dreyer, R. N., Yamashita, M., & Fenn, J. B. (1989). Electrospray ionization for mass-spectrometry of large biomolecules. *Science*, *246*(4926), 64-71.
14. Yamashita, M., & Fenn, J. B. (1984). Electrospray ion source. Another variation on the free-jet theme. *The Journal of Physical Chemistry*, *88*(20), 4451-4459.
15. Tanaka, K., Waki, H., Ido, Y., Akita, S., Yoshida, Y., Yoshida, T., & Matsuo, T. (1988). Protein and polymer analyses up to m/z 100 000 by laser ionization time-of-flight mass spectrometry. *Rapid communications in mass spectrometry*, *2*(8), 151-153.
16. Karas, M., Bachmann, D., Bahr, U. E., & Hillenkamp, F. (1987). Matrix-assisted ultraviolet laser desorption of non-volatile compounds. *International journal of mass spectrometry and ion processes*, *78*, 53-68.
17. Bleakney, W. (1929). A new method of positive ray analysis and its application to the measurement of ionization potentials in mercury vapor. *Physical Review*, *34*(1), 157.
18. Nier, A. O. (1947). Electron impact mass spectrometry. *Rev Sci Instrum*, *18*, 415.
19. De Hoffmann, E., & Stroobant, V. (2007). *Mass spectrometry: principles and applications*. John Wiley & Sons.
20. Munson, M. S., & Field, F. H. (1966). Chemical ionization mass spectrometry. I. General introduction. *Journal of the American Chemical Society*, *88*(12), 2621-2630.

21. Chassagne, D., Crouzet, J., Baumes, R. L., Lepoutre, J. P., & Bayonove, C. L. (1995). Determination of trifluoroacetylated glycosides by gas chromatography coupled to methane negative chemical ionization mass spectrometry. *Journal of Chromatography A*, *694*(2), 441-451
22. Choi, N. R., Kim, Y. P., Ji, W. H., Hwang, G. S., & Ahn, Y. G. (2016). Identification and quantification of seven volatile n-nitrosamines in cosmetics using gas chromatography/chemical ionization–mass spectrometry coupled with head space-solid phase microextraction. *Talanta*, *148*, 69-74.
23. Nguyen, H. T., Shaffer, C. J., & Tureček, F. (2015). Probing peptide cation–radicals by near-uv photodissociation in the gas phase. structure elucidation of histidine radical chromophores formed by electron transfer reduction. *The Journal of Physical Chemistry B*, *119*(10), 3948-3961.
24. Iribarne, J. V., & Thomson, B. A. (1976). On the evaporation of small ions from charged droplets. *The Journal of Chemical Physics*, *64*(6), 2287-2294.
25. Nguyen, S., & Fenn, J. B. (2007). Gas-phase ions of solute species from charged droplets of solutions. *Proceedings of the National Academy of Sciences*, *104*(4), 1111-1117.
26. Dole, M., Mack, L. L., Hines, R. L., Mobley, R. C., Ferguson, L. D., & Alice, M. D. (1968). Molecular beams of macroions. *The Journal of Chemical Physics*, *49*(5), 2240-2249.
27. El-Aneed, A., Cohen, A., & Banoub, J. (2009). Mass spectrometry, review of the basics: electrospray, MALDI, and commonly used mass analyzers. *Applied Spectroscopy Reviews*, *44*(3), 210-230.
28. March, R. E., & Todd, J. F. (2005). *Quadrupole ion trap mass spectrometry* (Vol. 165). John Wiley & Sons.

29. Schwartz, J. C., Senko, M. W., & Syka, J. E. (2002). A two-dimensional quadrupole ion trap mass spectrometer. *Journal of the American Society for Mass Spectrometry*, *13*(6), 659-669.
30. Posthumus, M. A., Kistemaker, P. G., Meuzelaar, H. L. C., & Ten Noever de Brauw, M. C. (1978). Laser desorption-mass spectrometry of polar nonvolatile bio-organic molecules. *Analytical Chemistry*, *50*(7), 985-991.
31. Kanu, A. B., Dwivedi, P., Tam, M., Matz, L., & Hill, H. H. (2008). Ion mobility–mass spectrometry. *Journal of Mass Spectrometry*, *43*(1), 1-22.
32. Wells, J. M., & McLuckey, S. A. (2005). Collision-induced dissociation (CID) of peptides and proteins. *Methods in enzymology*, *402*, 148-185.
33. Little, D. P., Speir, J. P., Senko, M. W., O'Connor, P. B., & McLafferty, F. W. (1994). Infrared multiphoton dissociation of large multiply charged ions for biomolecule sequencing. *Analytical Chemistry*, *66*(18), 2809-2815.
34. Chung, T. W., & Tureček, F. (2011). Proper and improper aminoketyl radicals in electron-based peptide dissociations. *International Journal of Mass Spectrometry*, *301*(1), 55-61.
35. Chu, I. K., Zhao, J., Xu, M., Siu, S. O., Hopkinson, A. C., & Siu, K. M. (2008). Are the radical centers in peptide radical cations mobile? The generation, tautomerism, and dissociation of isomeric α-carbon-centered triglycine radical cations in the gas phase. *Journal of the American Chemical Society*, *130*(25), 7862-7872.
36. Chung, T. W., & Tureček, F. (2010). Backbone and side-chain specific dissociations of z ions from non-tryptic peptides. *Journal of the American Society for Mass Spectrometry*, *21*(8), 1279-1295.
37. Moss, C. L., Chamot-Rooke, J., Nicol, E., Brown, J., Campuzano, I., Richardson, K., ... & Turecek, F. (2012). Assigning structures to gas-phase peptide cations and cation-radicals. An

infrared multiphoton dissociation, ion mobility, electron transfer, and computational study of a histidine peptide ion. *The Journal of Physical Chemistry B*, *116*(10), 3445-3456.

38. Turecek, F., Moss, C. L., Pikalov, I., Pepin, R., Gulyuz, K., Polfer, N. C., ... & Richardson, K. (2013). Gas-phase structures of phosphopeptide ions: a difficult case. *International Journal of Mass Spectrometry*, *354*, 249-256.
39. Leavitt, C. M., DeBlase, A. F., Johnson, C. J., van Stipdonk, M., McCoy, A. B., & Johnson, M. A. (2013). Hiding in plain sight: unmasking the diffuse spectral signatures of the protonated N-terminus in isolated dipeptides cooled in a cryogenic ion trap. *The Journal of Physical Chemistry Letters*, *4*(20), 3450-3457.
40. Nguyen, H. T., & Tureček, F. (2017). Near-UV Photodissociation of Tryptic Peptide Cation Radicals. Scope and Effects of Amino Acid Residues and Radical Sites. *Journal of The American Society for Mass Spectrometry*, 1-12.
41. Turecek, F., & Julian, R. R. (2013). Peptide radicals and cation radicals in the gas phase. *Chemical reviews*, *113*(8), 6691-6733.
42. Xia, Y., Gunawardena, H. P., Erickson, D. E., & McLuckey, S. A. (2007). Effects of cation charge-site identity and position on electron-transfer dissociation of polypeptide cations. *Journal of the American Chemical Society*, *129*(40), 12232-12243.
43. Chu, I. K., Rodriquez, C. F., Lau, T. C., Hopkinson, A. C., & Siu, K. M. (2000). Molecular radical cations of oligopeptides. *The Journal of Physical Chemistry B*, *104*(15), 3393-3397.
44. Cheng, P. Y., Zhong, D., & Zewail, A. H. (1995). Kinetic-energy, femtosecond resolved reaction dynamics. Modes of dissociation (in iodobenzene) from time-velocity correlations. *Chemical physics letters*, *237*(5-6), 399-405.
45. Polfer, N. C., & Dugourd, P. (Eds.). (2013). *Laser photodissociation and spectroscopy of*

mass-separated biomolecular ions (pp. 13-19). Heidelberg, Germany: Springer.

46. Fermi, E., Pasta, J., Ulam, S., & Tsingou, M. (1955). Los Alamos Report No. *LA-1940*, 978.
47. Alder, B. J., & Wainwright, T. E. (1959). Studies in molecular dynamics. I. General method. *The Journal of Chemical Physics*, *31*(2), 459-466.
48. Rahman, A. (1964). Correlations in the motion of atoms in liquid argon. *Physical Review*, *136*(2A), A405.
49. Frenkel, D., Vlugt, T. J. H., Van der Eerden, J. P. J. M., Dijkstra, M., & Smit, B. (2009). Introduction to Molecular Simulation and Statistical Thermodynamics. *http://homepage. tudelft. nl/v9k6y/imsst/index. html*.
50. Verlet, L. (1967). Computer" experiments" on classical fluids. I. Thermodynamical properties of Lennard-Jones molecules. *Physical review*, *159*(1), 98.
51. Berendsen, H. J., Postma, J. V., van Gunsteren, W. F., DiNola, A. R. H. J., & Haak, J. R. (1984). Molecular dynamics with coupling to an external bath. *The Journal of chemical physics*, *81*(8), 3684-3690.

Chapter 2: Near-UV Photodissociation of Tryptic Peptide Cation Radicals. Scope and Effects of Amino Acid Residues and Radical Sites

Reproduced with permission from Nguyen, H. T., & Tureček, F. (2017). *Journal of The American Society for Mass Spectrometry*, 1-12.

Abstract: Peptide cation-radical fragment ions of the z-type, [$^{\bullet}$AXAR^{+}], [$^{\bullet}$AXAK^{+}], and [$^{\bullet}$XAR^{+}] where X = A, C, D, E, F, G, H, K, L, M, N, P, Y, and W, were generated by electron transfer dissociation of peptide dications and investigated by MS^3-near-ultraviolet photodissociation (UVPD) at 355 nm. Laser-pulse dependence measurements indicated that the ion populations were homogeneous for most X residues except phenylalanine. UVPD resulted in dissociations of backbone CO─NH bonds that were accompanied by hydrogen atom transfer, producing fragment ions of the $[y_n]^+$ type. Compared with collision-induced dissociation, UVPD yielded less side-chain dissociations even for residues that are sensitive to radical-induced side-chain bond cleavages. The backbone dissociations are triggered by transitions to second (*B*) excited electronic states in the peptide ion R-CH$^{\bullet}$-CONH- chromophores that are resonant with the 355-nm photon energy. Electron promotion increases the polarity of the *B* excited states, R-CH^{+}-C$^{\bullet}$(O^{-})NH-, and steers the reaction to proceed by transfer of protons from proximate acidic C_α and amide nitrogen positions.

2. 1 Introduction

Photodissociation is one of the tools for accomplishing dissociations of gas-phase ions[1-4] that more recently has been widely applied to biomolecular ions.[5-13] Photodissociation in the far UV (157 nm[14,15]) and middle UV (193 nm[16]) regions of the spectrum has been used to dissociate peptide ions. Recently, photodissociation has been combined with another ion activation method, electron transfer dissociation (ETD)[17] to drive non-selective dissociations of primary peptide fragment ions produced by ETD, thus increasing the number of fragment ions to be potentially used in peptide sequencing.[18] Near-UV photodissociation at 355 nm of ETD peptide fragment ions of the z-type has been shown to be a selective tool for determining the ion structure by targeting the radical chromophores generated by electron transfer.[19] Infrared multiphoton dissociation of ETD-produced peptide fragment ions has also been implemented to provide useful information of the structure and conformation of c-[20] and z-type[21] ions. Whereas UV photoexcitation (UVPD) at 193 nm results in non-specific dissociation of many bonds in ETD fragment ions, UVPD at 355 nm has been shown to trigger backbone and side-chain bond cleavage that were specific for amino acid residues in the peptide ion.[22-26] When combined with action spectroscopy,[9] UV-VIS photodissociation provides information on mass-resolved photodissociation channels pertinent to different excited electronic states of the ion.[27,28]

UVPD differs from the more traditional collision-induced dissociation (CID) in a few important aspects. UV photon absorption is a vertical process that generates a resonant excited electronic state and thus delivers a well-defined excitation energy. In contrast, low-energy CID as employed in ion traps operates in the slow-heating regime of multiple collisions occurring on a millisecond time scale [29] and resulting in vibrational excitation of the ion ground electronic state. The electronic excited state generated by UV photon absorption can decay by a vibronic transition

to a highly vibrationally excited ground electronic state to trigger dissociations that are of similar nature as those produced by CID. Since the laser pulses used in UVPD are typically a few nanoseconds wide, vibronic decay after the absorption of the first photon can be followed by absorption of more photons from the same laser pulse that compete with dissociation. Alternatively, dissociation can proceed on the potential energy surface of the pertinent excited electronic state. To distinguish these processes, it is of interest to compare UVPD and CID of a series of peptide ions and point out dissociations that are orthogonal to these ion activation modes. A recent study of tyrosine-containing peptide cation-radicals indeed reported essential differences in dissociations triggered by UV absorption and collisional activation.[26]

Here, we report a comparative UVPD study of a series of peptide fragment ions of the z-type. These ions are generated by ETD of a tryptic peptide library AAXAB, where X is a natural amino acid residue (X = A, C, D, E, F, G, H, K, L, M, N, P, R, W) and B is Arg (R) or Lys (K). CID of a related series of AAXAR ions have been analyzed previously and are used here as a reference for matching X residues. [30,31] We selected to study UVPD of the following types of z-ions. The first type is $[^{\bullet}AXAB^{+}]$, or $[z_4 + H]^{+\bullet}$, ions (for nomenclature see ref [32]), that have the C_{α}-radical defect at the deaminated *N*-terminal Ala residue and contain a common chromophore for all combinations of X and B. Second, ETD fragment ions by loss of ammonia from peptides of the Lys-C-terminated (AAXAK) series were studied. These correspond to $[^{\bullet}AAXAK^{+}]$, or $[z_5 + H]^{+\bullet}$, ions according to previous studies of ion structure that established that the ammonia molecule selectively originates from the peptide *N*-terminus.[33,34] Analogous fragment ions by ETD loss of ammonia from the Arg-C-terminated (AAXAR) series were not considered because they are likely to be mixtures of isomers formed by ammonia elimination from the *N*-terminus and the Arg side chain.[19,34] Third, $[^{\bullet}XAR^{+}]$, or $[z_3 + H]^{+\bullet}$ ions that have the C_{α}-radical defect at the

variable X residue were studied for the Arg C-terminated peptides. Photoinduced and collision-induced dissociation pathways of these ion series are analyzed and related to the nature of the X and B residues as well as the excitation mode.

2. 2 Experimental

2. 2. 1 Materials and Methods

Synthetic peptides were purchased from NEOPeptide Laboratories (Cambridge, MA, USA) or CHI Scientific (Maynard, MA, USA) and their identity and purity was checked by mass spectrometry. Mass spectra were measured on an LTQ-XL-ETD linear ion trap (LIT) tandem mass spectrometer (ThermoElectron Fisher, San Jose, CA, USA) that has been modified to allow photodissociation studies.[19].Doubly charged peptide ions were generated by electrospray of solutions in 50:50:0.5 methanol-water-acetic acid and mass-selected in the LIT. The $[z_n + H]^{+\bullet}$ fragment ions of interest were formed by electron transfer dissociation using fluoranthene anion radicals as reagent. The $[z_n + H]^{+\bullet}$ ions were mass-selected and exposed to a train of typically 1-10 laser pulses to generate ETD-UVPD-MS^3 spectra. The laser beam at 355 nm was produced from an EKSPLA NL 301 HT Nd–YAG laser (Altos Photonics, Bozeman, MT, USA) providing the third harmonics line at 355 nm, as described previously.[19] The photodissociation yields were measured as a function of the laser power for the $[z_4 + H]^{+\bullet}$ (*m/z* 487) ion from AAWAR and showed approximately linear increase in the range of 3.3-9 mJ/pulse, indicating single photon absorption.

2. 2. 2 Computational Methods

Standard ab initio and density functional theory (DFT) calculations were performed with the Gaussian 09 suite of programs[59] to obtain ion structures, harmonic frequencies, and energies. Geometries were optimized with the hybrid functional ωB97X-D[60] and the 6-31+G(d,p) basis set.

All calculations of open shell species were carried out with the spin-unrestricted formalism. Excited-state energies and oscillator strength were calculated with time-dependent DFT (TD-DFT)[61] using ωB97X-D and the 6-31+G(d,p) and 6-311++G(2d,p) basis sets. This combination of TD-DFT and basis sets has been previously benchmarked for excited-state calculations of peptide radical groups.[62]

2. 2. 3 Note on Nomenclature

Hydrogen transfers accompanying dissociations of peptide cation radicals produce fragment ions that differ in the number hydrogen atoms. This feature and the ion charge and electron parity are conveniently expressed by the all-inclusive nomenclature described recently that uses the hydrogen count in neutral peptide fragments as reference.[32] The conversion to the common Roepstorff-Fohlman-Biemann nomenclature[35,36] is as follows for the fragment ions described here: $[z_n + H]^{+\bullet} = z_n$, $[z_n]^+ = z_n - 1 = w_n$, $[x_m + H]^{+\bullet} = x_m$, $[y_i + 2H]^+ = y_i$, $[y_i]^+ = y_i - 2 = v_n$.

2. 3 Results

The ions of interest were generated by ETD of doubly charged peptide ions, as illustrated with AACAR (*m/z* 246, Figure 1a). The ETD-produced $[z_4 + H]^{+\bullet}$ and $[z_3 + H]^{+\bullet}$ ions at *m/z* 404 and 333, respectively, were selected by mass and exposed to laser pulses at 355 nm. Note that the $[z_3 + H]^{+\bullet}$ ion from ETD undergoes spontaneous loss of SH radical to *m/z* 300 that decreases the primary fragment ion intensity. [34, 37] The single-pulse UVPD-MS^3 spectrum of the $[z_4 + H]^{+\bullet}$ ion (Figure 1b) shows a dominant backbone dissociation of the Cys-Ala amide bond, forming the $[y_2]^+$ fragment ion at *m/z* 244. This dissociation requires a hydrogen atom migration to the departing neutral fragment, as studied previously.[19, 23] In contrast, CID of the $[z_4 + H]^{+\bullet}$ ion results in

dominant Cys side-chain dissociations[30,31] whereas backbone cleavages are competitively suppressed.

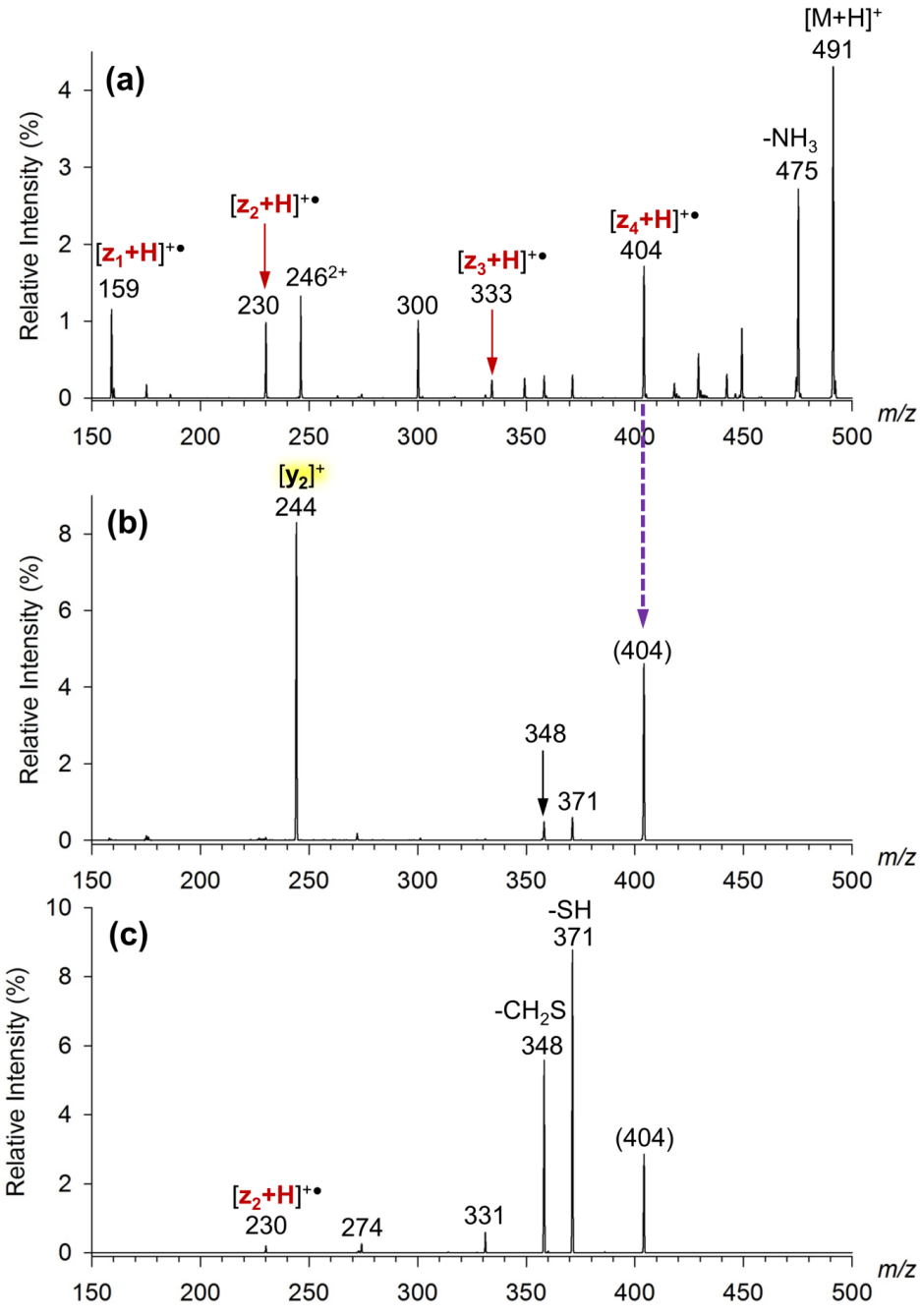

UV

Figure 1. (a) ETD-MS^2 mass spectrum (fluoranthene, 200 ms ion-ion reaction time) of (AACAK + 2H)$^{2+}$ (*m/z* 246); (b) UVPD-MS^3 mass spectrum (single pulse at 355 nm) of the $[z_4 + H]^{+\bullet}$ *m/z* 404 ion from ETD. (c) CID-MS^3 mass spectrum of the $[z_4 + H]^{+\bullet}$ *m/z* 404 ion from ETD.

The UVPD and CID spectra of all the $[z_4 + H]^{+\bullet}$ ions from AAXAR are summarized in Table 1. The UVPD relative intensities were normalized to the sum of the fragment ions in the MS^3 spectra. To highlight the differences in the UVPD and CID spectra, we denote as *significantly specific* the MS^3 fragment ions that show a ten-fold difference in relative intensity in either spectrum. The fragment ions that are more than ten-fold more abundant upon UVPD are shown in bold characters, those more than ten-fold more abundant upon CID are given as italics in Table 1. Fragment ions appearing in both types of spectra, albeit at different relative intensities are shown as normal characters. The Table 1 data indicate three types of photodissociation reactions of the Arg-C-terminated $[z_4 + H]^{+\bullet}$ ions : (1) Amide CO-NH bond cleavages leading to $[y_n]^+$ ions, (2) N─C_α bond cleavages leading to $[z_2+H]^{+\bullet}$ ions,[30,31] and (3) residue specific side-chain dissociations. Peptide ions with residues lacking reactive side chains (G, A, P) gave dominant $[y_3]^+$ photofragment ions, resulting from cleavage of the CO-NH bond next to the *N*-terminal radical carrying residue and involving a hydrogen transfer onto the departing C_3H_5O radical (Scheme 1).

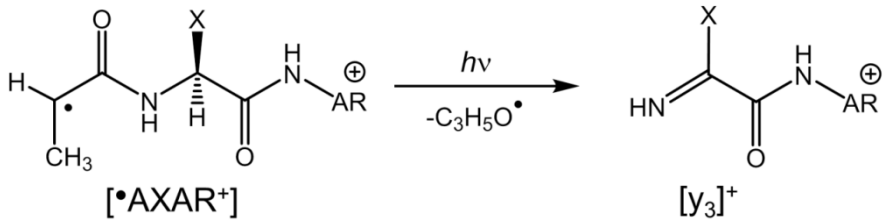

Scheme 1. Formation of $[y_3]^+$ fragment ions.

Residues that are potentially susceptible to radical-induced side-chain dissociations showed mixed results. [37-39] With $[z_4 + H]^{+\bullet}$ ions containing Asp, Asn, Glu, Leu, Arg, and Met, side-chain dissociations were abundant, although they did not outcompete backbone CO-NH

cleavages forming the $[y_3]^+$ and $[y_2]^+$ ions. Remarkably, the photodissociative SH loss from the Cys side-chain was only minor (Figure 1b) whereas it was predominant in the CID spectrum. Likewise, the internal Lys residue did not undergo extensive radical side-chain dissociations,[37] the main side-chain loss of $C_2H_8N_3$ occurring from the C-terminal Arg residue. An interesting comparison can be made for $[z_4 + H]^{+\bullet}$ ions containing residues that are known to favor cascade N─C_α bond cleavages leading to $[z_2 + H]^{+\bullet}$ ions (Asp, Asn, Phe, His, and Trp).[30,31] Among these, Asp, Asn and His gave abundant $[z_2 + H]^{+\bullet}$ photofragments that competed with the formation of the $[y_n]^+$ ions. In contrast, Phe and Trp produced dominant $[y_2]^+$ photofragments that were virtually absent in the CID spectra.

The photodissociations of the Lys-C-terminated $[z_4 + H]^{+\bullet}$ ions are compiled in Table 2. The backbone CO-NH bond and side-chain dissociations follow a similar trend as observed for the analogous Arg-C-terminated ions. The combined relative intensities of the $[y_3]^+$ and $[y_2]^+$ UVPD fragment ions from $[^\bullet AXAR^+]$ and $[^\bullet AXAK^+]$ are summarized in Figure 2. A novel feature with the $[^\bullet AXAK^+]$ series is the more pronounced photodissociative loss of water from Ala, Phe, and His-containing ions that was not observed for the Arg-C-terminated ions. Another distinctive feature is the enhanced elimination of ammonia from the $[y_3]^+$ ions from the His and Arg-containing ions. It should be noted that the diagnostic $[z_2 + H]^{+\bullet}$ ions in this series (*m/z* 202) overlap with a background peak of photoionized fluoranthene and thus their relative intensities could not be quantified.

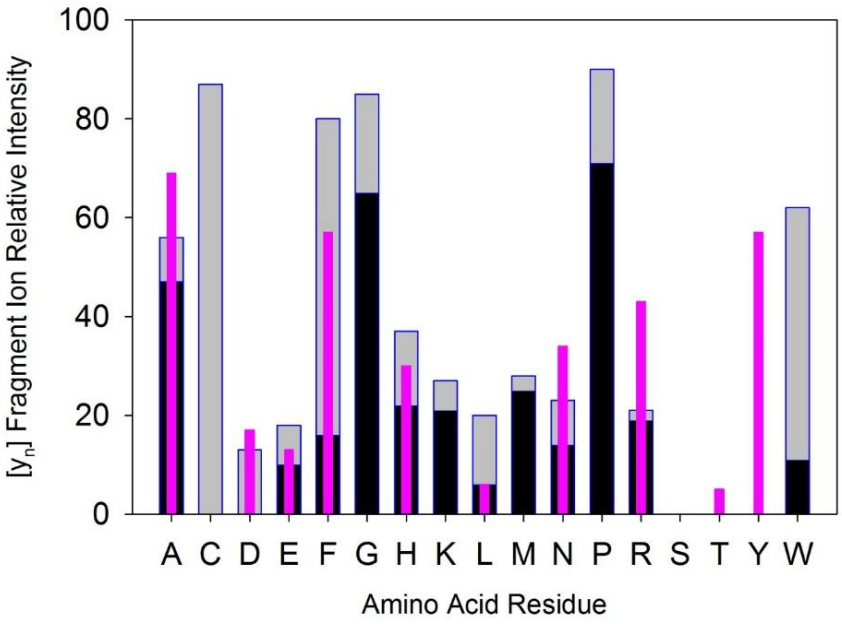

Figure 2. UVPD relative intensities of $[y_3]^+$ and $[y_2]^+$ fragment ions. Black bars: $[y_2]^+$ relative intensities from $[^{\bullet}AXAR^+]$; gray bars: $[y_3]^+$ relative intensities from $[^{\bullet}AXAR^+]$; magenta bars: combined $[y_3]^+$ and $[y_2]^+$ relative intensities from $[^{\bullet}AXAK^+]$.

Table 1. Intensities and Assignments from UVPD of $[z_4 + H]^{+\bullet}$ Fragment Ions from AAXAR.

	Backbone Cleavages			Side-Chain Dissociations		
Residue (ion *m/z*)	*m/z*	assignment[a]	rel. intensity (%)[b,c]	*m/z*	assignment	rel. intensity (%)
A (372)	315	$[y_3]^+$	47	*354*	$-H_2O$	*<1*
	244	$[y_2]^+$	9	*328*	$-CO_2$	*<1*
	271	$[x_2]^{+\bullet}$	-	*327*	$-CO_2H$	*<1*
	230	$[z_2 + H]^{+\bullet}$	*5*	298	$-C_2H_8N_3$	3
	175	$[y_1 + 2H]^+$	25			
	159	$[z_1 + H]^{+\bullet}$	11			
C (404)	272	$[x_2 + H]^{+\bullet}$	2	*371*	-SH	*6*
	244	$[y_2]^+$	**87**	*358*	$-SCH_2$	*5*
D (416)	272	$[x_2 + H]^{+\bullet}$	5	372	$-CO_2$	26
	246	$[y_2 + 2H]^+$	2	*371*	-COOH	*7*
	244	$[y_2]^+$	**13**	**315**	$-C_4H_{11}N_3$	**11**
	230	$[z_2 + H]^{+\bullet}$	35			
E (430)	**373**	$[y_3]^+$	**10**	429	-H	9
	358	$[z_3 + H]^{+\bullet}$	12	371	$-C_2H_3O_2$	57
	244	$[y_2]^+$	**8**	301	$-(C_2H_3O_2 + C_3H_5NO)$	2
	230	$[z_2 + H]^{+\bullet}$	4			
F (448)	**391**	$[y_3]^+$	**16**	*404*	$-CO_2$	*<1*
	272	$[x_2 + H]^{+\bullet}$	4			
	244	$[y_2]^+$	**64**			

	230	$[z_2 + H]^{+\bullet}$	16			
G (358)	**301**	$[y_3]^+$	**65**	*340*	$-H_2O$	*<1*
	246	$[y_2 + 2H]^+$	7	*314*	$-CO_2$	*6*
	244	$[y_2]^+$	**20**			
	230	$[z_2 + H]^{+\bullet}$	**2**			
H (438)	**381**	$[y_3]^+$	**22**	**301**	$[z_3 + H]^{+\bullet} - C_3H_3N_2$	**4**
	366	$[z_3 + H]^{+\bullet}$	2			
	272	$[x_2 + H]^{+\bullet}$	12			
	244	$[y_2]^+$	**15**			
	230	$[z_2 + H]^{+\bullet}$	44			
K (429)	**372**	$[y_3]^+$	**21**	413	$-NH_2$	4
	358	$[z_3 + H]^{+\bullet}$	15	*411*	$-H_2O$	*<1*
	272	$[x_2 + H]^{+\bullet}$	2	386	$-C_2H_5N$	5
	244	$[y_2]^+$	**6**	**355**	$-C_2H_8N_3$	**30**
	230	$[z_2 + H]^{+\bullet}$	4	**301**	$[z_3 + H]^{+\bullet} - C_3H_7N$	**4**
				286	$[z_3 + H]^{+\bullet} - C_4H_{10}N$	**9**
L (414)	**357**	$[y_3]^+$	6	371	$-C_3H_7$	38
	244	$[y_2]^+$	**14**	358	$-C_4H_8$	35
	230	$[z_2 + H]^{+\bullet}$	5	**301**	$[z_3 + H]^{+\bullet} - C_3H_6$	**2**
M (432)	**375**	$[y_3]^+$	25	417	$-CH_3$	0.7
	244	$[y_2]^+$	**3**	385	$-SCH_3$	10
	175	$[y_1 + 2H]^+$	3	371	$-CH_2SCH_3$	51
				358	$-C_3H_6S$	7
N (415)	**358**	$[y_3]^+$	**14**	371	$-CONH_2$	43
	272	$[x_2 + H]^{+\bullet}$	6	315	$-C_4H_{10}N_3$	2
	244	$[y_2]^+$	**9**			

	230	$[z_2 + H]^{+\bullet}$	26			
P (398)	341	$[y_3]^+$	71	*354*	$-CO_2$	*<1*
	272	$[x_2]^+$	1	**300**	$-C_5H_8NO$	**10**
	244	$[y_2]^+$	19			
R (457)	**400**	$[y_3]^+$	**19**	439	$-H_2O$	<1
	244	$[y_2]^+$	2	413	$-CO_2$	<1
	230	$[z_2 + H]^{+\bullet}$	8	**385**	$-C_2H_6N_3$	**13**
				383	$-C_2H_8N_3$	**8**
				371	$-C_3H_8N_3$	42
				358	$-C_4H_9N_3$	8
W (487)	430	$[y_3]^+$	11	443	$-CO_2$	<1
	272	$[x_2 + H]^{+\bullet}$	6	415	$-C_2H_6N_3$	4
	244	$[y_2]^+$	**51**	*358*	$-C_9H_7N$	1
	230	$[z_2 + H]^{+\bullet}$	1	**301**	$[z_3 + H]^{+\bullet} - C_8H_5N$	**2**
	175	$[y_1 + 2H]^+$	4			
	159	$[z_1 + H]^{+\bullet}$	4			

---

[a]The all-inclusive fragment ion nomenclature is used [32]. Conversion to the Roepstorff-Fohlman-Biemann system [35,36] is as follows: $[y_n]^+ = (\boldsymbol{y_n} - 2H)^+$; $[y_n + 2H]^+ = \boldsymbol{y_n}$; $[z_n + H]^{+\bullet} = \boldsymbol{z_n}$; $[x_n + H]^{+\bullet} = \boldsymbol{x_n}$. [b]CID fragment ions whose relative intensities exceed ten fold those from UVPD are given as italics. [c]UVPD fragment ions whose relative intensities exceed ten fold those from CID are given as bold characters.

Table 2. Intensities and Assignments from UVPD of $[z_4 + H]^{+\bullet}$ Fragment Ions from AAXAK.

	Backbone Cleavages			Side-Chain Dissociations		
Residue (ion m/z)	*m/z*	assignment[a]	rel. intensity (%)[b,c]	*m/z*	assignment	rel. intensity (%)
A (344)	287	$[y_3]^+$	33	326	$-H_2O$	30
	217	$[y_2 + H]^{+\bullet}$		*285*	$-C_3H_9N$	
	216	$[y_2]^+$	**36**	*273*	$-C_4H_{11}N$	
D (388)	**287**	$[y_3]^+ - CO_2$	**6**	*370*	$-H_2O$	
	270	$287 - NH_3$	**4**	344	$-CO_2$	45
	245	$[x_2 + H]^{+\bullet}$	8	326	$-(CO_2 + H_2O)$	6
	218	$[y_2 + 2H]^+$	14			
	217	$[y_2 + H]^{+\bullet}$				
	216	$[y_2]^+$	17			
E (402)	345	$[y_3]^+$	6	*384*	$-H_2O$	*<1*
	330	$[z_3]^+$	21	343	$-C_2H_3O_2$	61
	218	$[y_2 + 2H]^+$	5			
	217	$[y_2 + H]^{+\bullet}$				
	216	$[y_2]^+$	**7**			
F (420)	363	$[y_3]^+$	35	402	$-H_2O$	12
	349	$[z_3 + H]^{+\bullet}$	4			
	346		7			
	293		5			
	245	$[x_2 + H]^{+\bullet}$	12			
	216	$[y_2]^+$	22			

	202[d]	$[z_2 + H]^{+\bullet}$				
G (330)	216	$[y_2]^+$		312	$-H_2O$	
				279		
H (410)	353	$[y_3]^+$	19	392	$-H_2O$	23
	336	$[y_3]^+ - NH_3$	**24**	352	$-C_3H_8N$	9
	218	$[y_2 + 2H]^+$	14			
	216	$[y_2]^+$	11			
	202[d]	$[z_2 + H]^{+\bullet}$				
L (386)	218	$[y_2 + 2H]^+$	10	*368*	$-H_2O$	
	216	$[y_2]^+$	6	343	$-C_3H_7$	34
	202[d]	$[z_2 + H]^{+\bullet}$		330	$-C_4H_8$	42
				270		8
N (387)	330	$[y_3]^+$	17	369	$-H_2O$	5
	245	$[x_2 + H]^{+\bullet}$	6	343	$-CONH_2$	33
	218	$[y_2 + 2H]^+$	15	270		7
	216	$[y_2]^+$	17			
	202[d]	$[z_2 + H]^{+\bullet}$				
R (429)	**372**	$[y_3]^+$	**19**	**428**	$-H$	**29**
	355	$[y_3]^+ - NH_3$	**6**	*411*	$-H_2O$	<1
	218	$[y_2 + 2H]^+$	20	*385*	$-CO_2$	<1
	216	$[y_2]^+$	24	*342*	$-C_3H_9N_3$	<1
				371	$-CH_4N_3$	9
S (360)	218	$[y_2 + 2H]^+$	6	342	$-H_2O$	37
				330	$-CH_2O$	6
				287	$-C_4H_{11}N$	51
T (374)	218	$[y_2 + 2H]^+$	8	356	$-H_2O$	51

	216	$[y_2]^+$	5	330	$-C_2H_4O$		7
				302	$-C_4H_{11}N$		8
				301	$-C_4H_{11}N$		16
					256 301 - COOH		5
Y (436)	**379**	$[y_3]^+$	**22**	418	$-H_2O$	8	
	245	$[x_2 + H]^{+\bullet}$		330	$-C_7H_6O$	4	
	218	$[y_2 + 2H]^+$	30				
	216	$[y_2]^+$	35				
	202[d]	$[z_2 + H]^{+\bullet}$					

[a]The all-inclusive fragment ion nomenclature is used [32]. Conversion to the Roepstorff-Fohlman-Biemann system [35,36] is as follows: $[y_n]^+ = (\boldsymbol{y_n} - 2H)^+$; $[y_n + 2H]^+ = \boldsymbol{y_n}$; $[z_n + H]^{+\bullet} = \boldsymbol{z_n}$; $[x_n + H]^{+\bullet} = \boldsymbol{x_n}$. [b]CID fragment ions whose relative intensities exceed ten fold those from UVPD are given as italics. [c]UVPD fragment ions whose relative intensities exceed ten fold those from CID are given as bold characters.

Moving the radical site one Ala residue away, as in $[z_5 + H]^{+\bullet}$ Lys-C-terminated ions, resulted in homologous shifts and enhancement of the $[y_n]^+$ photofragment ions. For most $[z_5 + H]^{+\bullet}$, UVPD produced diagnostic $[y_4]^+$, $[y_3]^+$, and $[y_2]^+$ fragment ions, enhancing sequence readout. Conversely, radical-induced side-chain eliminations, such as loss of CO_2 from Asp, $CONH_2$ from Asn, $C_2H_3O_2$ from Glu, C_4H_8 from Leu, and H_2O from Ser and Thr, were less prominent than for the $[z_4 + H]^{+\bullet}$ ions. Another common feature was that the $[y_n]^+$ ions underwent further loss of ammonia (Table 3). A distinctively different UVPD spectrum was produced from the Arg-containing $[z_5 + H]^{+\bullet}$ ion, $[^{\bullet}AARAK^+]$, that showed the formation of $[z_3]^+$ ions (w_3 according to the Biemann nomenclature) and their secondary dissociation products by loss of ammonia (Table 3). These differences are probably related to the mechanism of NH_3 loss from $[AARAK + 2H]^{+\bullet}$ that can involve the *N*-terminus as well as the Arg side chain, producing isomeric ions. Nevertheless, the UVPD and CID spectra of this ion were quite distinct, indicating different dissociations proceeding from the ground and excited electronic state.

Table 3. Intensities and Assignments in UVPD of $[z_5 + H]^{+\bullet}$ Fragment Ions from AAXAK.

	Backbone Cleavages			Side-Chain Dissociations		
Residue (ion *m/z*)	*m/z*	assignment[a]	rel. intensity (%)[b,c]	*m/z*	assignment	rel. intensity (%)
A (415)	358	$[y_4]^+$	20			
	341	$[z_4 - H]^+$	**4**			
	287	$[y_3]^+$	28			
	270	$[z_3 - H]^+$	16			
	218	$[y_2 + 2H]^+$	**10**			
	216	$[y_2]^+$	**22**			
D (459)	**402**	$[y_4]^+$	**22**	*441*	$-H_2O$	<0.1
	385	$[z_4 - H]^+$	**4**	**431**	-CO	**2**
	314	$[z_3 - H]^+$	6	415	$-CO_2$	15
	270	$287 - NH_3$	5	*400*	$-C_3H_9N$	*<1*
	218	$[y_2 + 2H]^+$	**12**	*388*	$-C_4H_{10}N$	*<1*
	216	$[y_2]^+$	**25**	**287**	$[y_3 - CO_2]^+$	**7**
E (473)	**416**	$[y_4]^+$	**30**	455	$-H_2O$	<1
	401	$[z_4 - H]^+$	*3*	414	$-C_2H_3O_2$	15
	399	$[y_4 - NH_3]^+$	**7**			
	345	$[y_3]^+$	**4**			
	328	$[y_3 - NH_3]^+$	4			
	272	$[w_3]^+$	4			
	257		9			
	218	$[y_2 + 2H]^+$	10			
	217	$[y_2 + H]^{+\bullet}$				

	216	$[y_2]^+$	**17**			
F (491)	434	$[y_4]^+$	18	*473*	$-H_2O$	
	417		4	**463**	-CO	**3**
	363	$[y_3]^+$	31	*432*	$-C_3H_9N$	
	346	$[y_3 - NH_3]^+$	7	*420*	$-C_4H_9N$	
	275		10			
	218	$[y_2 + 2H]^+$	10			
	216	$[y_2]^+$	15			
H (481)	424	$[y_4]^+$	18	*463*	$-H_2O$	
	407	$[y_4 - NH_3]^+$	**12**	423	$-C_3H_8N$	7
	353	$[y_3]^+$	6	410	$-C_4H_{11}N$	4
	336	$[y_3 - NH_3]^+$	**24**			
	318		2			
	309		5			
	264		2			
	246					
	238		7			
	237		13			
	202[d]					
L (457)	**400**	$[y_4]^+$	**34**	*439*	$-H_2O$	<1
	383	$[y_4 - NH_3]^+$	**6**	414	$-C_3H_7$	9
	339		2	401	$-C_4H_8$	20
	329	$[y_3]^+$	**8**	386	$-C_4H_9N$	<1
	312	$[y_3 - NH_3]^+$	5			
	272		4			
	218	$[y_2 + 2H]^+$	**4**			
	216	$[y_2]^+$	**9**			
N (458)	**401**	$[y_4]^+$	**17**	*440*	$-H_2O$	*1*

	387	$[y_4 - NH_3]^+$	**3**	**430**	-CO	**4**
	384		4	414	$-CONH_2$	13
	330	$[y_3]^+$	**24**			
	313	$[y_3 - NH_3]^+$	6			
	287		5			
	270		4			
	218	$[y_2 + 2H]^+$	**5**			
	216	$[y_2]^+$	**8**			
	202[d]	$[z_2 + H]^{+\bullet}$				
R (500)	372	$[y_3]^+$	1	**499**	-H	**25**
	357	$[z_3]^+$	**25**	*482*	$-H_2O$	*<1*
	340	$[z_3 - NH_3]^+$	**16**	*456*		*<1*
	323	$[z_3 - 2NH_3]^+$	**4**	429	$-C_4H_9N$	17
	313		**7**	413	$-C_3H_9N_3$	<1
	270		1			
	256		2			
S (431)	**374**	$[y_4]^+$	**35**	*413*	$-H_2O$	*3*
	357	$[y_4 - NH_3]^+$	**14**	*401*	$-CH_2O$	
	339	$[357 - H_2O]^+$	2	*360*	$-C_4H_{11}N$	
	313		4			
	303	$[y_3]^+$	**4**			
	288	$[z_3]^+$	<1			
	287	$[z_3 - H]^{+\bullet}$	3			
	268		6			
	218	$[y_2 + 2H]^+$	7			
	216	$[y_2]^+$	**21**			
T (445)	388	$[y_4]^+$	34	*427*	$-H_2O$	*3*
	371	$[y_4 - NH_3]^+$	13	*401*	$-C_2H_4O$	
	353	$[371 - H_2O]^+$	2	374	$-C_4H_{11}N$	2
	327		6			

	302	$[z_3]^+$	2			
	301	$[z_3 - H]^{+\bullet}$	2			
	229		10			
	218	$[y_2 + 2H]^+$	5			
	216	$[y_2]^+$	14			
Y (507)	450	$[y_4]^+$	19	*489*	$-H_2O$	
	433	$[y_4 - NH_3]^+$	4	479	-CO	3
	379	$[y_3]^+$	**26**	*436*	$-C_4H_{11}N$	
	362	$[y_3 - NH_3]^+$	8	401	$-C_7H_6O$	19
	336		3			
	291		10			
	218	$[y_2 + 2H]^+$	7			
	216	$[y_2]^+$	17			
	202[d]	$[z_2 + H]^{+\bullet}$				

The all-inclusive fragment ion nomenclature is used [32]. Conversion to the Roepstorff-Fohlman-Biemann system [35,36] is as follows: $[y_n]^+ = (\boldsymbol{y_n} - 2H)^+$; $[y_n + 2H]^+ = \boldsymbol{y_n}$; $[z_n + H]^{+\bullet} = \boldsymbol{z_n}$; $[x_n + H]^{+\bullet} = \boldsymbol{x_n}$. [b]CID fragment ions whose relative intensities exceed ten fold those from UVPD are given as italics. [c]UVPD fragment ions whose relative intensities exceed ten fold those from CID are given as bold characters. [d]Overlapped with photodesorbed fluoranthene ions

2. 3. 1 Pulse Dependence

Further information about the nature of the ETD fragment ions can be obtained from pulse-dependent UVPD measurements.[25] The first pulse induces dissociation of light-absorbing ions at the selected wavelength. The product ions that are closed-shell species, such the $[y_n]^+$ ions, do not absorb light at 355 nm and are inactive upon irradiation with subsequent laser pulses. The relative intensities of these ions increase with the number of laser pulses. Cation-radical product ions, for example the $[z_2 + H]^{+\bullet}$ ions, absorb light at 355 nm and are photolyzed upon subsequent exposure to laser pulses. The relative intensities of these ions grow to a maximum and then decrease. This is illustrated with pulse-dependent UVPD relative ion intensities of the $[z_2 + H]^{+\bullet}$ and $[y_3]^+$ fragment ions from $[^{\bullet}AHAR^+]$ (Figure 3). Fitting the $[^{\bullet}AHAR^+]$ ion relative intensity with a single exponential function, $I(n) = I_0e^{-0.3669n}$, where I_0 is the initial normalized ion intensity and $I(n)$ is the normalized intensity after n laser pulses, gives the broken-line curve in Figure 3 with a root-mean square deviation, rmsd = 2.7%. However, a substantially tighter fit (rmsd = 1.2%) can be obtained by fitting in a two-parameter formula, $I(n)= I_0(0.94e^{-0.3669n} +0.06)$, that includes a 6% fraction of non-photodegradable residual ions, as shown by the solid blue line curve in Figure 3.

In general terms, ion photodepletion upon laser irradiation can follow an exponential decay law (eq 1) where I_0 is the initial molar fraction of the photoactive species, $I(n)$ is the normalized intensity after n laser pulses, and $\alpha > 0$ is the photodissociation efficiency per pulse

$$I(n) = I_0e^{-n\alpha} \qquad (1)$$

that depends on the photon flux (Φ) and the wavelength-dependent ion absorption cross section (σ), $\sigma = \Phi\alpha$. Eq 1 applies when the ion population is homogeneous and every photon absorption is dissociative on the time scale of the experiment, which is often justified by the low activation energies for radical dissociations[23, 25, 31, 40, 41] and the substantial excitation energy delivered by the

photon (3.49 eV or 337 kJ mol^{-1} at 355 nm). The Table 4 data indicate that $[z_4 + H]^{+\bullet}$ ions from most peptide sequences follow a single exponential decay law. However, if the ion population initially contains a molar fraction $x_0(M_2)$ of an isomer M_2 that does not absorb at 355 nm, the photodepletion process follows eq 2, where $I(n)$ converges to $I_0 x_0(M_2)$.

$$\frac{I(n)}{I_0} = x_0(M_1)e^{-n\alpha} + x_0(M_2) \qquad (2)$$

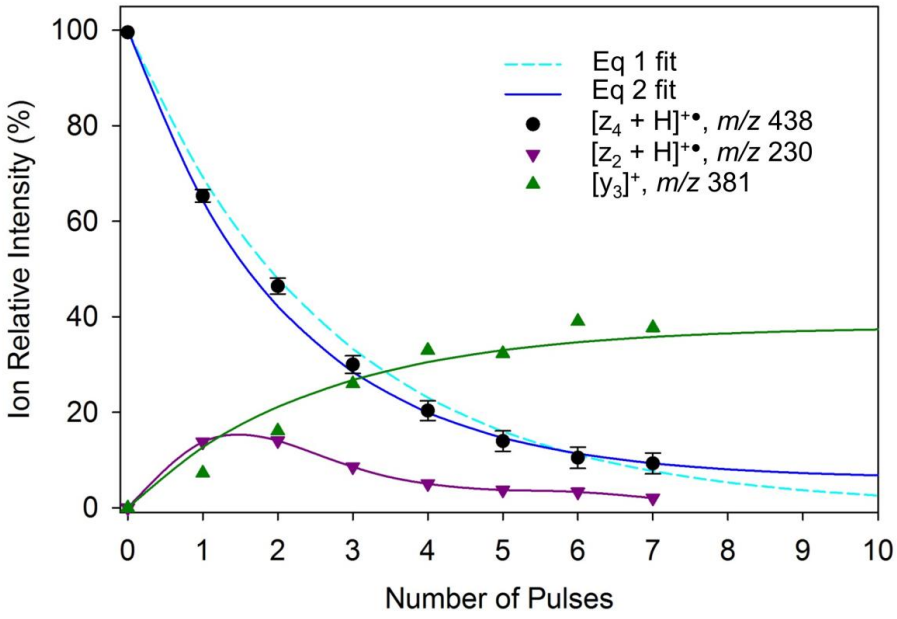

Figure 3. Laser pulse dependence of selected photofragment ion intensities from [$^{\bullet}$AHAR^{+}] (*m/z* 438).

Table 4. Photodissociation efficiencies of $^{\bullet}AXAR^{+}$ $[z_4 + H]^{+\bullet}$ Ions at 355 nm.

Residue X	α_{eff}[a]	$x_0(M_2)$[a]	rmsd (%)
P	0.226	0	0.7
R	0.292	0	4.2
G	0.302	0	10.9
H	0.478	0.06	1.2
K	0.548	0	8.8
C	0.567	0	10.9
N	0.686	0	2.6
D	0.689	0	6.6
E	0.710	0	6.1
A	0.702	0	10.9
F	0.721	0.20	2.5
L	0.742	0	1.8
W	0.895	0	5.9
M	0.978	0	1.2

[a]From least square fits to equation 2.

An even more general scenario has been considered previously for photodissociation of peptide cation-radicals, whereby the photoactive ions (M_1) of an initial molar fraction equal to $x_0(M_1)$ competitively dissociate with efficiency α and isomerize with efficiency β to a new isomer (M_3) which then photodissociates with efficiency γ (Eq 3).[22] For $\beta = 0$ (no photoisomerization), Eq 3 reduces to Eq 2.

$$\frac{I(n)}{I_0} = \frac{x_0(M_1)}{\alpha+\beta-\gamma}\left[(\alpha-\gamma)e^{-(\alpha+\beta)n} + \beta e^{-\gamma n}\right] + x_0(M_2) \qquad (3)$$

The data in Table 1 indicate that most peptide ions do not contain photostable isomers either initially present or produced by photoisomerization. Analysis of eq 3 for several

combinations of the α, β, and γ parameters indicates that increasing β and decreasing γ relative to α results in a slower photodepletion. However, eq 3 curves where $x_0(M_2) = 0$ can be fitted with single exponential decay functions with rmsd < 4% showing an apparent lower photodissociation efficiency $\alpha_{eff} < \alpha$. Thus, it is difficult to distinguish from the pulse dependence alone whether the ion undergoes only photodissociation or the dissociation is accompanied by the formation of another photoactive isomer. Distinction has been made for [$^{\bullet}$AFAR^{+}] ions using single-pulse action spectroscopy that clearly indicated the presence of two $[z_4 + H]^{+\bullet}$ ion isomers produced by ETD.[27] It should be noted that the data reported in ref [27] were obtained at a lower laser power (0.8-2.1 mJ/pulse) than the present 355 nm data, which accounts for the different α_{eff}.

1.4.2 $[z_4 + H]^{+\bullet}$ Ions

The Table 4 data rank the photodissociation efficiencies of the $[z_4 + H]^{+\bullet}$ ions. The light-absorbing chromophore at 355 nm in all these ions is the Ala C$_{\square}$ radical.[25] The electron transitions leading to the second (*B*) doublet excited state (ΔE_{exc} = 3.509 eV, 353 nm, oscillator strength *f* = 0.024) are shown for [$^{\bullet}$AAAR^{+}] (Figure 4). These transitions lead to absorption at 355 nm and photodissociation; note, however, that the absorption maximum is likely to be red-shifted by vibronic broadening at ambient temperature.[42] The first (*A*) doublet excited state is dark (ΔE_{exc} = 3.19 eV, 388 nm, *f* = 0.0001). The *B* state excitations involve transitions to the semioccupied π_z molecular orbital (MO100) starting from the underlying doubly occupied π_z (MO99 and MO95) and π_{xy} (MO97) orbitals. All the involved MOs are delocalized over the *N*-terminal $CH_3CH^{\bullet}CONH$ group with very little involvement of the more remote amide, carboxyl, or guanidine π-electron systems. This suggests that similar types of excitations can be expected for all [$^{\bullet}$AXAR^{+}] ions with saturated side chains (G, K, L, P) lacking π or lone pair electrons and possibly also for Arg. In spite of this common trait, the [$^{\bullet}$AXAR^{+}] (X = G, K, L, P, R) ions show

different photodissociation efficiencies, $\alpha_{eff}(P) < \alpha_{eff}(R) < \alpha_{eff}(G) < \alpha_{eff}(K) < \alpha_{eff}(A) < \alpha_{eff}(L)$. These large differences cannot be attributed to variations of the laser power which was calibrated to be within ±10%. Changes in the position of the pertinent ion absorption band would affect the absorbance at 355 nm. These can be caused by different conformations of the [$^{\bullet}$AXAR^{+}] ions depending on the X residue. However, time-dependent DFT calculations of several ion conformers indicated only minor effects of ion conformation on the 355 nm absorption band position.[27] The high photodissociation efficiency of [$^{\bullet}$ALAR^{+}] can be associated with the facile dissociation by loss of the Leu side chain (Table 1). With the other residues in this group, photo-induced hydrogen migrations among the C_{α} positions[23] can deplete the initial *N*-terminal chromophore and affect absorption at 355 nm. Residues possessing π-electron systems (H, N, D, F, W) or lone pairs (C, M) may undergo electron transitions involving these orbitals; a detailed description of these

interactions would require a substantial effort in analyzing the pertinent ion conformers and their electronic excitations.

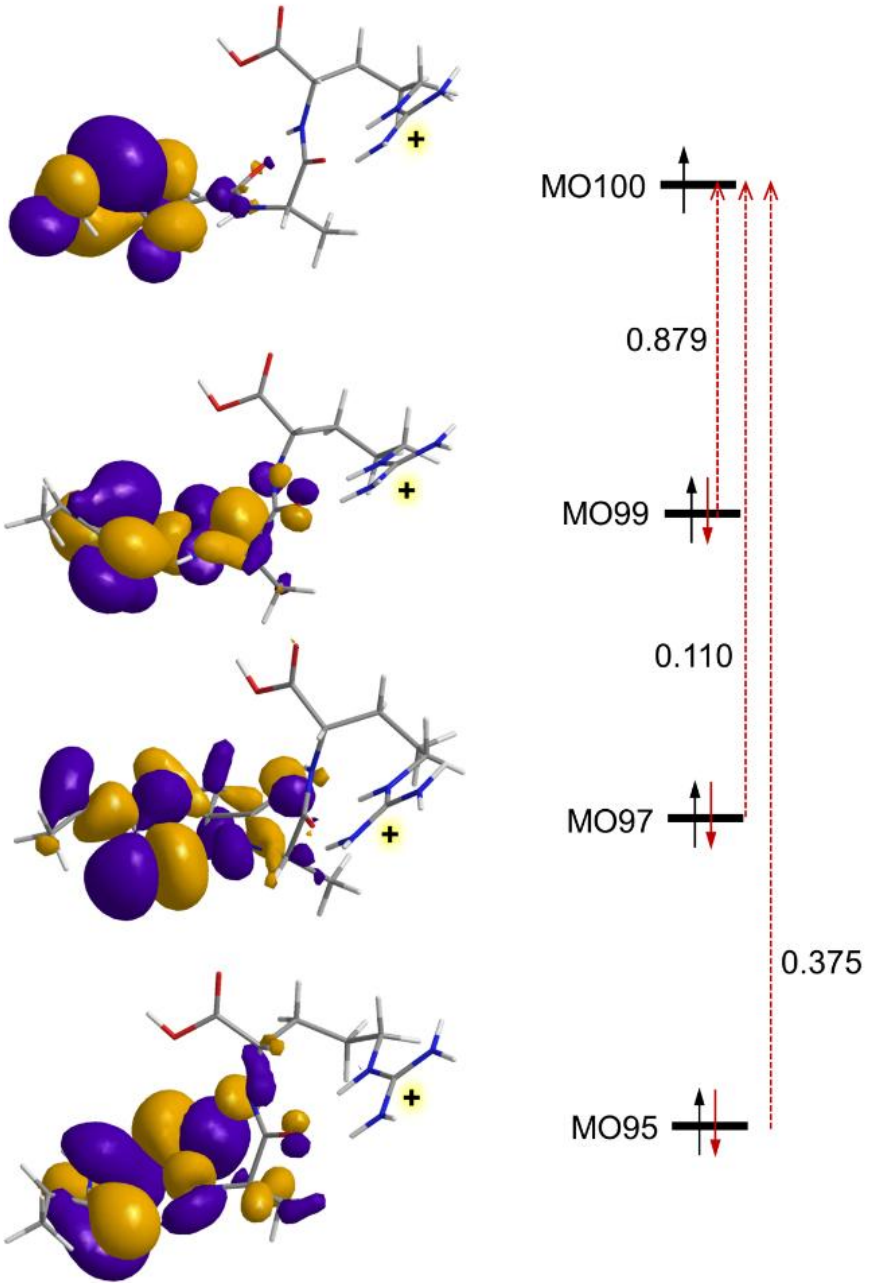

Figure 4. Molecular orbitals involved in electronic excitation to the *B* state of [$^{\bullet}$AAAR^{+}] (ΔE_{exc} = 3.51 eV, 353 nm, f = 0.024). From ωB97X-D/6-311++G(2d,p) time-dependent DFT calculations. The calculated transition vector amplitudes from the inner beta molecular orbitals (MO95, MO97, and MO99) to the SOMO (MO100) are shown next to the red arrows.

2.3.3 $[z_3 + H]^{+\bullet}$ Ions

These cation-radical ETD fragment ions have the radical sites at the C_α position of the variable X residue. This greatly affects the ion dissociations, as summarized in Table 5. UVPD of the $[z_3 + H]^{+\bullet}$ ions gives both sequence $[y_2]^+$ fragment ions and products of side-chain cleavages. $[^\bullet LAR^+]$ is the only sequence that dissociates entirely by side chain loss. UVPD of the $[z_3 + H]^{+\bullet}$ with aromatic residues (Phe and Trp) also produces $[x_2]^+$ fragment ions in addition to $[y_2]^+$ ions. The photodissociation efficiencies (α_{eff}) of the $[z_3 + H]^{+\bullet}$ ions follow a different order than those for $[z_4 + H]^{+\bullet}$. Notably, $[^\bullet FAR^+]$ and $[^\bullet DAR^+]$ show large populations of photostable ion isomers, and mixtures are also indicated for $[^\bullet AAR^+]$ and $[^\bullet WAR^+]$. In contrast to UVPD, CID of the $[z_3 + H]^{+\bullet}$ chiefly results in CO_2 loss or side-chain dissociations, yielding only minor sequence fragment ions (data is not shown). The aromatic residues (Phe, Trp) are exceptional in that they produce $[z_2 + H]^{+\bullet}$ sequence fragment ions upon CID, in similarity with CID of higher homologous $[z_n + H]^{+\bullet}$ ions[30,31].

Table 5. Photodissociation at 355 nm of $[z_3 + H]^{+\bullet}$ Ions from AAXAR Peptides.

Residue X	α_{eff}[a]	$x_0(M_2)$[a]	rmsd (%)	Major fragment ions
H	0.308	0	6.1	-H, $[y_2]^+$
M	0.343	0	6.4	$-CH_3$, $-C_2H_5S$, $[y_2]^+$
K	0.357	0	0	-H, $-C_3H_6N$, $[y_2]^+$
D	0.374	0.412	5.0	$[y_2]^+$, $[z_2 + H]^{+\bullet}$
N	0.452	0	5.3	$-CH_2CONH_2$, $[y_2]^+$
W	0.463	0.024	13.6	$[y_2]^+$, $[x_2]^+$
G	0.510	0	16.4	$[y_2]^+$
F	0.533	0.394	4.4	$[y_2]^+$, $[x_2]^+$
R	0.614	0	1.3	-H, $-C_3H_8N_3$, $[y_2]^+$
E	0.682	0	2.2	$-C_2H_3O_2$, $[y_2]^+$
A	0.741	0.093	21.7	$[y_2]^+$
L	1.161	0	2.9	$-C_3H_7$

[a]From least square fits to equation 2.

2. 4 Discussion

The main feature distinguishing the UVPD and CID spectra of the $[z_n + H]^{+\bullet}$ ions is the facile photodissociative CO-NH bond cleavages forming $[y_{n-1}]^+$ fragment ions. By stoichiometry, this dissociation must involve a hydrogen atom migration onto the neutral fragments, and this raises the question of why the CO-NH bond cleavage is promoted relative to the other dissociations that also involve hydrogen migrations. UVPD and CID differ in the mode of ion excitation. Absorption of a UV photon leads to a sudden formation of an excited electronic state of the ion, and the deposited energy can be used to drive dissociation or dissipated by collisions with the bath gas. Hence, one may posit that photodissociation should be fast and thus reactions with loose transition states should be preferred. However, previous analysis of potential energy surfaces for $[z_4 + H]^{+\bullet}$ ions from AASAR,[23] AAAAR,[25] AAHAR, AAWAR,[31] AAHAL,[41] and several other peptide cation-radicals[43-53] suggested that the backbone and side-chain dissociations were of similar type, involving radical-induced hydrogen atom migrations through five- and six membered transition

states of very similar energies. [23,31,41] Hence, energy arguments alone are insufficient to explain the preferred formation of $[y_3]^+$ and $[y_2]^+$ fragment ions in UVPD. We now argue that these dissociations proceed from the *B* excited electronic state generated by 355-nm photon absorption. A prerequisite step in the hydrogen migrations occurring in the ground electronic state is amide trans → cis rotation that is necessary to allow the C_α radical to approach the hydrogen atoms to be transferred. This step can be avoided in the excited electronic state. Electronic excitation results in electron density flow from C_α to the adjacent C=O group (Scheme 2). The excitation increases the basicity of the amide oxygen that can abstract the labile proton from the C_α position at the adjacent X residue or from the next amide group. The optimized structure of [•AAAR$^+$] (1, Scheme 2)[25] indicates a close proximity of the reactive amide oxygen to the C_α and amide protons. The hydrogen transfer can be formulated as proton-coupled electron transfer,[54,55] reconstituting the electron density distribution in the intermediates and creating reactive radical sites at the C_α and amide nitrogen (Scheme 2). This polar mechanism, involving enolimine intermediates, can account for the preferred transfer of acidic hydrogen atoms, steering the reaction to radical-induced CO-NH bond dissociations. Note that this is fundamentally different from the standard "mobile proton" model of peptide ion dissociations[56-58] where the C_α-H and amide N-H are not engaged in dissociations proceeding in the ground electronic state. The calculated energy balance for the Scheme 2 reactions, when based on ωB97X-D/6-311++G(2d,p) and zero-point energies, indicates that a transition from the *B* excited state of [•AAAR$^+$] to the C_α enol isomer 2 is 264 kJ mol^{-1} exothermic. Furthermore, the excitation energy is sufficient to drive the C(OH)-NH bond dissociation in 2 where it requires 177 kJ mol^{-1} (251 kJ mol^{-1} relative to 1). At the same time, the enolimine mechanism is unlikely to operate in the ground electronic state of the ion because intermediates 2 and 3 are high-energy isomers of the more conventional amides.[31] The ground-

state reactions, as observed in CID, then can be formulated by conventional radical chemistry involving C_α and side-chain hydrogen migrations combined with amide trans-cis isomerizations.[23,25,31,41]

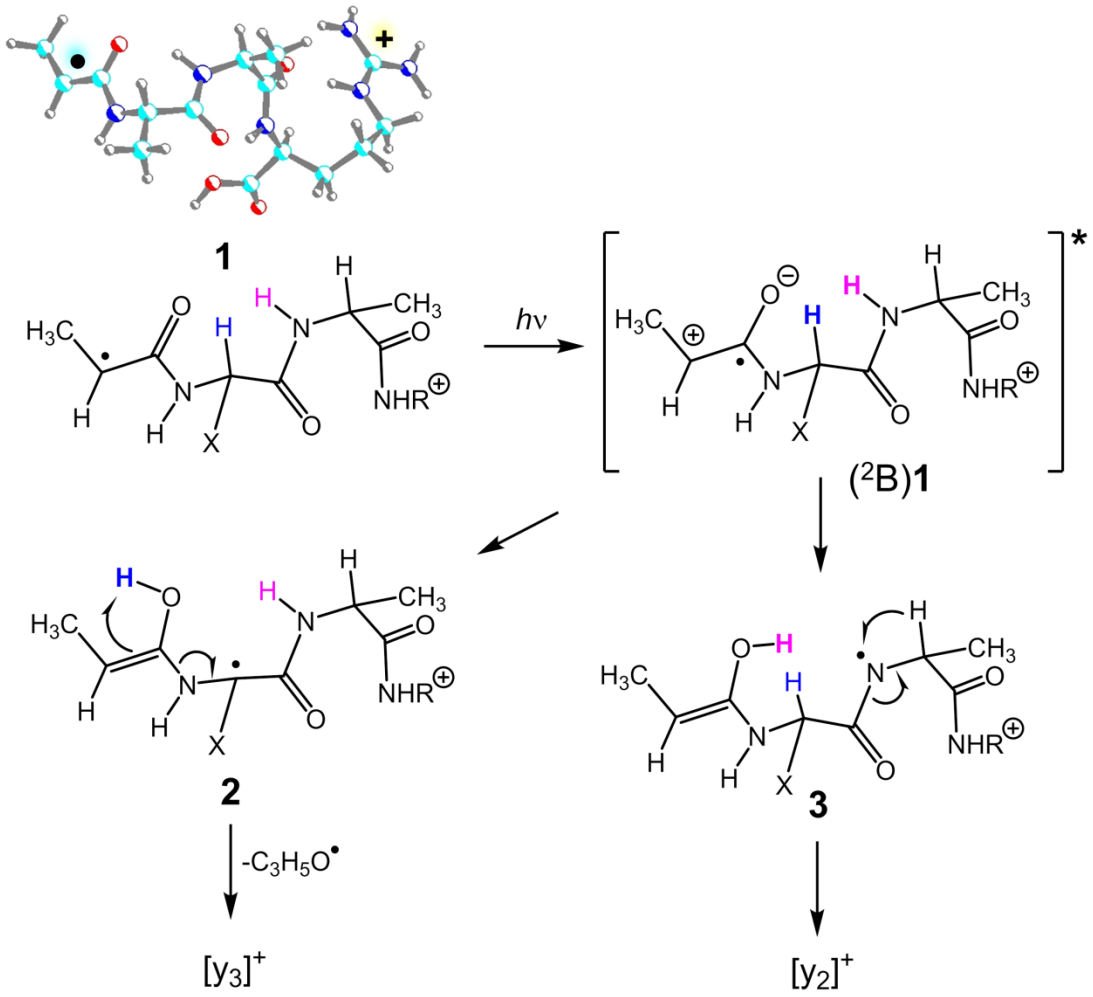

Scheme 2. Proposed mechanism for the formation of $[y_3]^+$ and $[y_2]^+$ fragment ions.

2. 5 Conclusions

Cation-radical $[z_n + H]^{+\bullet}$ fragment ions produced by electron transfer dissociation of tryptic peptides undergo efficient and residue-specific photodissociations at 355 nm. The common feature of this near-UV photodissociation is radical-induced backbone CO─NH bond cleavages accompanied by hydrogen transfer and forming $[y_n]^+$ sequence fragment ions. The photodissociation is associated with Cα radical amide chromophores that undergo electron transitions to second (*B*) excited states to drive proton transfer and backbone cleavages.

2. 6 References

1. Dunbar, R.C.: Photodissociation of the methyl chloride (CH_3Cl^+) and nitrous oxide (N_2O^+) cations. J. Am. Chem. Soc. 93, 4354-4358 (1971)
2. Casassa, M.P., Bomse, D.S., Beauchamp, J.L., Janda, K.C.: Infrared photochemistry of ethylene clusters. J. Chem. Phys. 72, 6805-6806 (1980)
3. Carlin, T. J., Freiser, B.S.: Multiphoton ionization in Fourier transform mass spectrometry. Anal. Chem. 55, 955-958 (1983)
4. Bensimon, M., Rapin, J., Gaumann, T.: Comparison of infrared photodissociation in a Fourier transform mass spectrometer with metastable ion decay in a double-focusing mass spectrometer. Int. J. Mass Spectrom. Ion Proc. 72, 125-135 (1986)
5. Eyler. J.R.: Infrared multiple photon dissociation spectroscopy of ions in Penning traps. Mass Spectrom. Rev. 28, 448–467 (2009)
6. Polfer, N.C.: Infrared multiple photon dissociation spectroscopy of trapped ions. Chem. Soc. Rev. 40, 2211–2221 (2011)

7. Brodbelt, J.S., Wilson, J.J.: Infrared multiphoton dissociation in quadrupole ion traps. Mass Spectrom. Rev. 28, 390–424 (2009).
8. Dunbar, R.C.: Spectroscopy of metal-ion complexes with peptide-related ligands. Top. Curr. Chem. 364, 183-223 (2015)
9. Antoine, R., Dugourd, P.: Visible and ultraviolet spectroscopy of gas phase protein ions. Phys. Chem. Chem. Phys. 13, 16494–16509 (2011)
10. Antoine, R., Dugourd, P.: UV-visible activation of biomolecular ions. Lect. Notes Chem. 83, 93–116 (2013)
11. Byskov, C.S., Jensen, F., Jorgensen, T.J.D., Nielsen, S.B.: On the photostability of peptides after selective photoexcitation of the backbone: prompt versus slow dissociation. Phys. Chem. Chem. Phys. 16, 15831–15838 (2014)
12. Hendricks, N.G., Lareau, N.M., Stow, S.M., McLean, J.A., Julian, R.R.: Bond-specific dissociation following excitation energy transfer for distance constraint determination in the gas phase. J. Am. Chem. Soc. 136, 13363-13370 (2014)
13. Lai, C.-K., Ng, D.C.M., Pang, H.F., Le Blanc, J.C.Y., Hager, J,W., Fang, D.-C., Cheung, A. S.-C., Chu I.K.: Laser-induced dissociation of singly protonated peptides at 193 and 266 nm within a hybrid linear ion trap mass spectrometer. Rapid Commun. Mass Spectrom. 27, 1119-1127 (2013)
14. Zhang, L., Reilly, J.P.: Peptide de novo sequencing using 157 nm photodissociation in a tandem time-of-flight mass spectrometer. Anal. Chem. 82, 898–908 (2010)
15. Reilly, J.P.: Ultraviolet photofragmentation of biomolecular ions. Mass Spectrom. Rev. 28, 425–447 (2009)

16. Brodbelt, J.S.: Photodissociation mass spectrometry: new tools for characterization of biological molecules. Chem. Soc. Rev. 43, 2757–2783 (2014)
17. Syka, J.E.P., Coon, J.J., Schroeder, M.J., Shabanowitz, J., Hunt, D.F.: Peptide and protein sequence analysis by electron transfer dissociation mass spectrometry. Proc. Natl. Acad. Sci. U. S. A. 101, 9528–9533 (2004)
18. Cannon, J.R., Holden, D.D., Brodbelt, J.S.: Hybridizing ultraviolet photodissociation with electron transfer dissociation for intact protein characterization. Anal. Chem. 86, 10970–10977 (2014)
19. Shaffer, C.J., Marek, A.. Pepin, R., Slováková, K., Tureček, F.: Combining UV photodissociation with electron transfer for peptide structure analysis. J. Mass. Spectrom. 50, 470-475 (2015)
20. Shaffer, C.J., Martens, J., Marek, A., Oomens, J., Tureček, F.: Photoleucine survives backbone cleavage by electron transfer dissociation. A near-UV photodissociation and infrared multiphoton dissociation action spectroscopy study. J. Am. Soc. Mass Spectrom. 27, 1176-1185 (2016)
21. Martens, J., Grzetic, J., Berden, G., Oomens, J.: Structural identification of electron transfer dissociation products in mass spectrometry using infrared ion spectroscopy. Nat. Commun. 7, 11754 (2016)
22. Nguyen, H.T.H., Shaffer, C.J.; Tureček, F.: Probing peptide cation-radicals by near-UV photodissociation in the gas phase. Structure elucidation of histidine radical chromophores formed by electron transfer reduction. J. Phys. Chem. B 119, 3948-3961 (2015)

23. Nguyen, H.T.H., Shaffer, C.J., Ledvina, A., Coon, J.J., Tureček, F.: Serine effects on collision-induced dissociation and photodissociation of peptide cation radicals of the $z^{+\bullet}$ type. Int. J. Mass Spectrom. 378, 20-30 (2015)
24. Shaffer, C.J., Marek, A., Nguyen, H.T.H., Tureček, F.: Combining near-UV photodissociation with electron transfer. Reduction of the diazirine ring in a photomethionine-labeled peptide ion. J. Am. Soc. Mass Spectrom. 26, 1367-1381 (2015)
25. Shaffer, C.J., Slováková, K., Tureček, F.: Near-UV photodissociation of phosphopeptide cation-radicals. Int. J. Mass Spectrom. 390, 71-80 (2015)
26. Viglino, E., Lai, C.K., Mu, X., Chu, I.K., Tureček, F.: Ground and excited-electronic-state dissociations of hydrogen-rich and hydrogen-deficient tyrosine peptide cation radicals. J. Am. Soc. Mass Spectrom. 27, 1454-1467 (2016)
27. Nguyen, H.T.H., Shaffer, C.J., Pepin, R., Tureček, F.: UV action spectroscopy of gas-phase peptide radicals. J. Phys. Chem. Lett. 6, 4722-4727 (2015)
28. Viglino. E., Shaffer, C.J., Tureček, F.: UV-VIS action spectroscopy and structures of tyrosine peptide cation radicals in the gas phase. Angew. Chem. Int. Ed. 55, 7469-7473 (2016)
29. McLuckey, S.A., Goeringer, D.E.: Slow heating methods in tandem mass spectrometry. J. Mass Spectrom. 32 ,461– 474 (1997)
30. Chung, T.W., Hui, R., Ledvina, A.R., Coon, J.J., Tureček, F.: Cascade dissociations of peptide cation- radicals. Part 1. Scope and effects of amino acid residues in penta-, nona- and decapeptides. J. Am. Soc. Mass Spectrom. 23, 1336-1350 (2012)

31. Ledvina, A.R., Chung, T.W., Hui, R., Coon, J.J., Tureček, F.: Cascade dissociations of peptide cation radicals. Part 2. Infrared multiphoton dissociation and mechanistic studies of z ions from pentapeptides. J. Am. Soc. Mass Spectrom. 23, 1351-1363 (2012).
32. Chu, I.K., Siu, C.-K., Lau, J.K.-C., Tang, W.K., Mu, X., Lai, C.K., Guo, X., Wang, X., Li, N., Yao, Z., Xia, Y., Kong, X., Oh, H.-B., Ryzhov, V., Tureček, F., Hopkinson, A.C., Siu, K.W.M.: Proposed nomenclature for peptide ion fragmentation. Int. J. Mass Spectrom. 390, 24-27 (2015)
33. Holm, A.I.S., Hvelplund, P., Kadhane, U., Larsen, M.K., Liu, B., Nielsen, S.B., Panja, S., Pedersen, J.M., Skrydstrup, T., Stochkel, K., Williams, E.R., E. S. Worm, E.S.: On the mechanism of electron-capture-induced dissociation of peptide dications from 15 N-labeling and crown- ether complexation. J. Phys. Chem. A 111, 9641–9643 (2007)
34. Tureček, F., Julian, R.R.: Peptide radicals and cation-radicals in the gas phase. Chem. Rev. 113, 6691-6733 (2013)
35. Roepstorff, P., Fohlman, J.: Proposal for a common nomenclature for sequence ions in mass spectra of peptides. Biomed. Mass Spectrom. 11, 601 (1984)
36. Biemann, K.: Nomenclature for peptide fragment ions (positive ions). Meth. Enzymol. 193, 886–887 (1990)
37. Fung, Y.M.E., Chan, T.-W.D.: Experimental and theoretical investigations of the loss of amino acid side chains in electron capture dissociation. J. Am. Soc. Mass Spectrom. 16, 1523-1535 (2005)
38. Cooper, H.J., Hudgins, R.R., Hakansson, K., Marshall, A.G.: Secondary fragmentation of linear peptides in electron capture dissociation. Int. J. Mass Spectrom. 228, 723-728 (2003)

39. Vaisar, T., Gatlin, C. L., Rao, R. D., Seymour, J. L., Tureček, F.: Sequence information, distinction and quantitation of C-terminal leucine and isoleucine in ternary complexes of tripeptides with Cu(II) and 2,2'-bipyridine. J. Mass Spectrom. 36, 306-316 (2001)
40. Pepin, R., Tureček, F.: Kinetic ion thermometers for electron transfer dissociation. J. Phys. Chem. B, 119, 2818-2826 (2015)
41. Chung, T.W., Tureček, F.: Backbone and side-chain specific dissociations of *z* ions from non-tryptic peptides. J. Am. Soc. Mass Spectrom. 21, 1279-1295 (2010)
42. Barbatti, M., Aquino, A,J.A., Lischka, H.: The UV absorption of nucleobases: semi-classical ab initio spectra simulations. Phys. Chem. Chem. Phys. 12, 4959-4967 (2010)
43. Osburn, S., Berden, G., Oomens, J., O'Hair, R.A.J., Ryzhov, V.: Structure and reactivity of the N-acetyl-cysteine radical cation and anion: does radical migration occur? J. Am. Soc. Mass Spectrom. 22, 1794-1803 (2011)
44. Hao, Q., Song, T., Ng, D.C.M., Quan, Q., Siu, C.K., Chu, I.K.: Arginine-facilitated isomerization: radical-induced dissociation of aliphatic radical cationic glycylarginyl(iso) leucine tripeptides. J. Phys. Chem. B 116, 7627-7634 (2012)
45. Zhao, J., Song, T., Xu,M., Quan, Q., Siu, K.W.M., Hopkinson, A.C., Chu, I.K.: Intramolecular hydrogen atom migration along the backbone of cationic and neutral radical tripeptides and subsequent radical-induced dissociations. Phys. Chem. Chem. Phys. 14, 8723–8731 (2012)
46. Osburn, S., Berden, G., Oomens, J., O'Hair, R.A.J., Ryzhov, V.: S-to-αC radical migration in the radical cations of Gly-Cys and Cys-Gly. J. Am. Soc.Mass Spectrom. 23, 1019-1023 (2012)

47. Laskin, J., Kong, R.P.W., Song, T., Chu, I.K.: Effect of the basic residue on the energetics and dynamics of dissociation of phosphopeptides. Int. J. Mass Spectrom. 330-332, 295-301 (2012)

48. Zhang, X., Julian, R.R.: Exploring radical migration pathways in peptides with positional isomers, deuterium labeling, and molecular dynamics simulations. J. Am. Soc. Mass Spectrom. 24, 524–533 (2013)

49. Osburn, S., Berden, G., Oomens, J., Gulyuz, K., Polfer, N.C., O'Hair, R.A.J., Ryzhov, V.: Structure and reactivity of the glutathione radical cation: radical rearrangement from the cysteine sulfur to the glutamic acid α-carbon atom. ChemPlusChem 78, 970-978 (2013)

50. Lai, C.-K., Mu, X., Hao, Q., Hopkinson, A.C., Chu, I.K.: Formation, isomerization, and dissociation of ε- and α-carbon-centered tyrosylglycylglycine radical cations. Phys. Chem. Chem. Phys. 16, 24235-24243 (2014)

51. Xu, M., Tang, W.-K., Mu, X., Ling, Y., Siu, C.-K., Chu, I.K.: α-Radical-induced CO2 loss from the aspartic acid side chain of the collisionally induced tripeptide aspartylglycylarginine radical cation. Int. J. Mass Spectrom. 390, 56-62 (2015)

52. Lesslie, M., Osburn, S., van Stipdonk, M.J.; Ryzhov, V.: Gas-phase tyrosine-to-cysteine radical migration in model systems. Eur. J. Mass Spectrom. 21, 589-597 (2015)

53. Osburn, S., Chan, B., Ryzhov, V., Radom, L., O'Hair, R.A.J.: Role of hydrogen bonding on the reactivity of thiyl radicals: A mass spectrometric and computational study using the distonic radical ion approach. J. Phys. Chem. A 120, 8184-8189 (2016)

54. Mayer, J.M.: Proton-coupled electron transfer: A reaction chemist's view. Ann. Rev. Phys. Chem. 55, 363-390 (2004)

55. Warren, J.J.; Tronic, T.A.; Mayer, J.M.: Thermochemistry of proton-coupled electron transfer reagents and its implications. Chem. Rev. 110, 6961-7001 (2010)

56. Cox, K.A., Gaskell, S.J., Morris, M., Whiting, A.: Role of the site of protonation in the low-energy decompositions of gas-phase peptide ions. J. Am. Soc. Mass Spectrom. 7, 522–531 (1996)

57. Jones, J.L, Dongre, A.R, Somogyi, A., Wysocki, V.H.: Sequence dependence of peptide fragmentation efficiency curves determined by electrospray ionization/surface-induced dissociation mass spectrometry. J. Am. Chem. Soc. 116, 8368–8369 (1994).

58. Paizs, B., Suhai, S.: Fragmentation pathways of protonated peptides. Mass Spectrom. Rev. 24, 508-548 (2005)

59. Frisch, M.J., Trucks, G.W., Schlegel, H.B.;, Scuseria, G.E., Robb, M.A., Cheeseman, J.R., Scalmani, G., Barone, V., Mennucci, B., Petersson, G.A., Nakatsuji, H., Caricato, M., Li, X., Hratchian, H.P., Izmaylov, A.F., Bloino, J., Zheng, G., Sonnenberg, J.L., Hada, M., Ehara, M., Toyota, K., Fukuda, R., Hasegawa, J., Ishida, M., Nakajima, T., Honda, Y., Kitao, O., Nakai, H., Vreven, T., Montgomery, J.A., Jr., Peralta, J.E., Ogliaro, F., Bearpark, M., Heyd, J.J., Brothers, E., Kudin, K.N., Staroverov, V.N., Kobayashi, R., Normand, J., Raghavachari, K., Rendell, A., Burant, J. C., Iyengar, S.S., Tomasi, J., Cossi, M., Rega, N., Millam, J.M., Klene, M., Knox, J.E., Cross, J.B., Bakken, V., Adamo, C., Jaramillo, J., Gomperts, R., Stratmann, R.E., Yazyev, O., Austin, A.J., Cammi, R., Pomelli, C., Ochterski, J.W., Martin, R.L., Morokuma, K., Zakrzewski, V. G., Voth, G.A., Salvador, P., Dannenberg, J.J., Dapprich, S., Daniels, A.D., Farkas, O., Foresman, J. B., Ortiz, J. V., Cioslowski, J., Fox, D.J.: Gaussian 09, Revision A.02, Gaussian, Inc., Wallingford CT, 2009

60. Chai, J.D., Head-Gordon, M.: Long-range corrected hybrid density functionals with damped atom-atom dispersion corrections. *Phys. Chem. Chem.Phys.* 10, 6615–6620 (2008)

61. Furche, F., Ahlrichs, A.: Adiabatic time-dependent density functional methods for excited state properties. *J. Chem. Phys.* 117, 7433–7447 (2002)

62. Turecek, F.: Benchmarking electronic excitation energies and transitions in peptide radicals. *J. Phys. Chem. A* 119, 10101-10111 (2015)

Chapter 3: Probing Peptide Cation-Radicals by Near-UV Photodissociation in the Gas Phase. Structure Elucidation of Histidine Radical Chromophores Formed by Electron Transfer Reduction

Reproduced with permission from Nguyen, H. T., Shaffer, C. J., & Tureček, F. (2015). *The Journal of Physical Chemistry B*, *119*(10), 3948-3961.

Abstract: Electron transfer reduction of gas-phase ions generated from histidine-containing peptides forms stable cation-radicals that absorb light at 355 nm, as studied for AAHAR, AAHAK, DSHAK, FHEK, HHGYK, and HHSHR. Laser photodissociation of mass-selected cation-radicals chiefly resulted in loss of H atoms, contrasting dissociations induced by slow collisional heating. The 355-nm absorption was due to new chromophores created by electron transfer and radical rearrangements in the cation-radicals. The chromophores were identified by time-dependent density functional theory calculations as 2*H*,3*H*-imidazoline and 2*H*-dihydrophenol radicals, formed by hydrogen atom transfer to the histidine and tyrosine side chain groups, respectively. These radicals undergo facile C−H bond dissociations upon photon absorption. In contrast, dissociations of histidine peptide cation-radicals containing the 1*H*,3*H*-imidazoline ring prefer loss of 4-methylimidazole via a multistep reaction pathway. The isomeric cation-radicals can be distinguished by a combination of collision-induced dissociation and near-UV photodissociation. The TD-DFT excitation energies in model imidazoline radicals were benchmarked on EOM-CCSD energies, and a satisfactory agreement was found for the M06-2X and ωB97XD functionals. The combination of electron transfer, photodissociation, collisional activation, and theory is presented as a powerful tool for studying structures and electronic properties of peptide cation-radicals in the gas phase.

3. 1 Introduction

Histidine is one of the most reactive amino acid residues that plays an important role in a number of hydrolytic enzymes and is also involved in regulatory processes associated with protein phosphorylation.[1,2] The histidine imidazole ring acts as a Brønsted acid-base conjugate relaying proton transfer from acidic residues to other polar residues and substrates in enzyme reaction centers. Another salient property of histidine is its propensity for transition metal coordination which is utilized in His-tags containing a chain of multiple histidine residues that are attached to proteins to bind the conjugates on to immobilized metal affinity columns.[3,4] In contrast to these acid-base and metal coordinating properties, redox reactions involving histidine residues have been studied only scarcely and, indeed, very little is known about the chemical properties of histidine radicals and cation-radicals. Previous solution studies of histidine radicals used pulse radiolysis in combination with electron spin resonance,[5] UV-VIS spectroscopy,[6] and various electrochemical redox methods.[7-9]

The redox chemistry of peptide ions containing protonated histidine residues has gained importance with the discovery of the so-called histidine effect[10] on dissociations of gas-phase ions. McLuckey and coworkers first reported a peculiar and specific effect, called ET-no-D, of histidine residues on electron transfer dissociation (ETD) of several peptide ions.[11] ETD is a mass spectrometric method which is based on an ion-ion reaction of a multiply charged analyte cation, e.g., a peptide ion, with a molecular electron donor such as an aromatic anion radical.[12] The reaction results in exothermic electron transfer that reduces the stable peptide dication and converts it into a reactive cation-radical that undergoes spontaneous dissociations through several channels.[12] The main interest in ETD of peptide ions has been focused on backbone dissociations that have been shown to provide information on the peptide ion amino acid sequence which is of

great practical utility in protein analysis.[13] In contrast to this general trend of extensive backbone dissociations, ET-no-D produced apparently intact peptide cation-radicals, also called charge-reduced ions, from histidine-containing peptides,[11] and the effect was shown to be amplified by the number of His residues in the peptide ion.[14]

In light of the high exothermicity of anion-dication electron transfer (> 4 eV)[15] and the reactivity of peptide cation-radicals that require only low activation energies for dissociation (<0.6 eV)[16], the histidine effect was puzzling to explain. Studies of model histidine-containing tri- and pentapeptides indicated that a fraction of charge-reduced species rearranged to new radical structures.[17-19] These were detected by charge-reversal spectroscopy in fast (50 keV kinetic energy) ion beams[20,21] where a peptide monocation was subjected to two consecutive collisions with thermal cesium atoms, and the resulting stable anions were analyzed by mass and detected after a few microseconds (Scheme 1). The microsecond lifetimes of such peptide anion-radicals were interpreted by the formation of isomeric histidine radicals that stabilized the incoming ionizing electron better than the relative precursor structures.

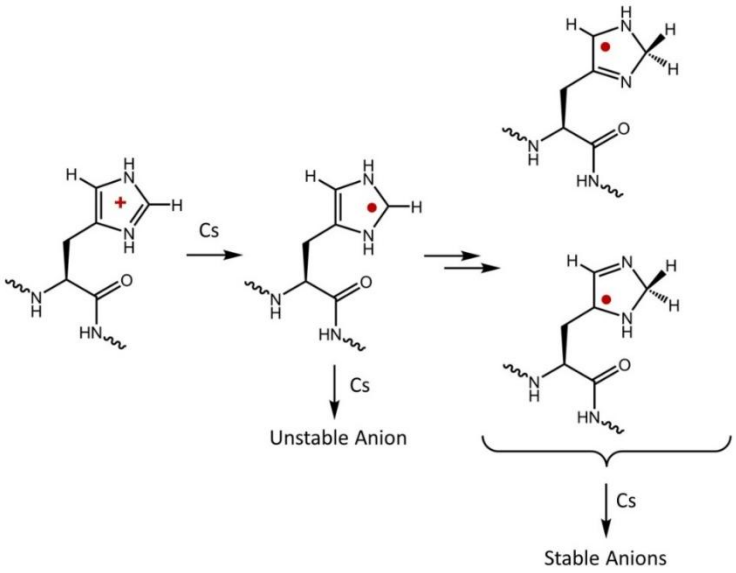

Scheme 1

Whereas the ion beam experiments, in combination with detailed electron structure analysis of the ground doublet electronic states,[10] provided a wealth of information on the histidine effect, they were limited to femtosecond electron transfers to peptide monocations. In contrast, most ETD measurements are performed with di- or polycations that are stored in quadrupole ion traps and allowed to interact with molecular anion-radicals, such as those of fluoranthene or azulene, on the time scale of tens to hundreds of milliseconds. Hence, the energetics and time scales for the histidine effect in ET-no-D are very different, and the structures of peptide cation-radicals formed and isolated in ion traps need to be established.

Current methods for determination of gas-phase ion structures comprise tandem mass spectrometry with collisional activation, ion mobility, and infrared action spectroscopy. Unfortunately, these methods are either inadequate or inaccessible to address peptide cation-radical structures. First, collision-induced dissociation under slow heating conditions pertinent to ion traps[22,23] triggers hydrogen atom migrations, driving radical isomerizations and obliterating the structure integrity of the species under study.[16,24,25] Second, ion mobility measurements of cation-radicals often do not have sufficient selectivity to provide definite structure information. For example, ion mobility of histidine ions $(AAHAL + H)^+$ and $(AAHAL + 2H)^{+\bullet}$ gave indistinguishable collision cross sections for these electronically different species.[26] Third, neither free-electron lasers used for infrared multiphoton dissociation[27-29] nor IR lasers using for single photon dissociation in ion traps[30,31] are currently equipped with ETD capabilities. The single reported IRMPD study of an electron-produced peptide fragment ion dealt with a regular even-electron ***c***-type ion, not a cation-radical.[32] Furthermore, IRMPD of peptide ions containing strong hydrogen bonds suffers from serious anharmonicity effects that make the spectra difficult to interpret.[33-35]

We now report a new method to probe peptide cation-radical structures that utilizes the storage capabilities of ion traps to perform near-UV laser photodissociation at 355 nm (UVPD) of ions produced by electron transfer. In contrast to UV photodissociation at wavelengths below 240 nm,[36-39] near-UVPD at 355 nm selectively excites chromophores produced by electron transfer, whereas those of peptide amide groups, aromatic rings and other standard peptide chromophores are transparent. In contrast to IRMPD, hydrogen bonding of charged groups (Arg, Lys) is likely to have only a minor effect on absorption at 355 nm of radical chromophores. We complement the experimental UVPD mass spectra and multi-stage tandem mass spectrometry (MS^n) measurements with electron structure calculations of ground and excited states to identify intermediates, transition states, and excited states of the peptide cation radicals under study.

3. 2 Experimental Section

3. 2. 1 Materials

All peptides were synthesized on Wang resin (Bachem Americas, Torrance, CA, USA) using the Fmoc technology according to literature procedures.[40] Histidine containing peptides DSHAK, FHEK, HHGYK, and HHSHR were also produced by enzymatic digestion of the small salivary protein histatin 5 (Aroz Technologies, Cincinati, OH, USA) using immobilized trypsin (Catalog No. V9013, Promega Corp., Madison, WI, USA), as described previously.[41] The precursor peptide ion identity was checked by accurate mass measurements on a LTQ-Orbitrap instrument at a 60,000 resolving power.

3. 2. 2 Methods

Electron transfer dissociation (ETD) mass spectra were measured on a modified LTQ-XL ETD linear ion trap (LIT) mass spectrometer (ThermoElectron Fisher, San Jose, CA, USA) which was equipped with an auxiliary chemical ionization (CI) source for the production of fluoranthene

anion-radicals. Peptide solutions (5-10 μM) in 50/50/1 methanol/water/acetic acid were electrosprayed at 2.2-2.3 kV from a pulled fused silica capillary into an open microspray ion source described previously.[41] Doubly charged ions were selected according to their *m/z*, stored in the LIT, and then allowed to react with fluoranthene anions injected into the LIT. The ion-ion reaction times were typically varied between 100 and 300 ms. MS^n experiments were carried out by isolating the fragment ions and exposing them to resonant collisional excitation or photoexcitation.

3. 2. 3 Photodissociation

To accomplish photodissociation of trapped ions in the LIT, the LTQ-XL ETD mass spectrometer was modified as reported previously.[42,43] Briefly, the chemical ionization (CI) source for the anion production was modified by drilling a 1-mm diameter hole into the insert block to provide a line of sight path to the LIT. The backside vacuum gate to the CI source was replaced by an aluminum plate carrying a quartz window. The irradiating light beam was produced by an EKSPLA NL 301 HT (Altos Photonics, Bozeman, MT, USA) Nd-YAG laser operating at 20 Hz frequency with a 3-6 ns pulse width. The laser is equipped with a third harmonics frequency generator producing a single 355 nm wavelength at 120 mJ/pulse peak power. The typical laser power used in the photodissociation experiments was 15-20 mJ/pulse. The laser beam of a 6-mm diameter is aligned by mirrors and focused by a telescopic lens to pass the small aperture drilled in the CI source. The laser beam diameter in the LIT is estimated at 3-4 mm to ensure overlap with the trapped ions. Both the laser system and the LTQ-XL are set on an optical table for optimum alignment. The laser was interfaced to the LTQ by LabView software (National Instruments, Austin, TX, USA) that receives a signal from a TTL pulse on pin14 of the J1 connector on the LTQ console. Laser pulses are triggered internally by the EKSPLA system, but power is controlled for each pulse by commands from the LabView software. The typical

experimental set up consists of selecting the ion to be photodissociated and storing it in the LIT for a chosen time period. For example, 400-ms storage time can accommodate up to 7 laser pulses spaced by 50 ms. This allows one to vary the number of pulses and determine the photodissociation kinetics. Longer storage times of >3 s, allowing >60 laser pulses are readily realized. We note that the ions are stored at the ion trap temperature (310 K), and their absorption bands are likely to be broadened to 20-40 nm by vibronic transitions involving numerous vibrational and rotational states.[37,38] Hence, a match between the laser excitation line and the absorption maximum is not necessary for photodissociation.

3. 2. 4 Computations

All electron structure calculations were carried out with the Gaussian 09 suite of programs.[44] Ion geometries were obtained by gradient optimizations with density functional theory (DFT) calculations using the B3LYP[45] and M06-2X[46] hybrid functionals and the 6-31+G(d,p) basis set. Stationary points were characterized by harmonic frequency analysis to have the appropriate number of imaginary frequencies (0 for local energy minima, 1 for first-order saddle points). Single-point energies were calculated with B3LYP, M062X, and ωB97XD[47,48] DFT methods and perturbational Møller-Plesset theory[49] (MP2, frozen core) truncated at second order, all in the spin unrestricted formalism and using the 6-311++G(2d,p) basis set. Contributions of higher spin states in the MP2 calculations were corrected by the standard spin annihilation procedures.[50,51] Excited state analysis was performed by time-dependent DFT[52] using the M06-2X, LC-BLYP,[53] and ωB97XD functionals with the 6-311++G(2d,p) basis set. The TD-DFT excitation energies were benchmarked on EOM-CCSD/6-311++G(2d,p) calculations[54-56] of 4-methylimidazole radicals that have chromophores analogous to those in the peptide cation-radicals. Exhaustive conformational analysis of $(HHGYK + 2H)^{2+}$ ions was performed by a

multistep ConformSearch routine,[57,58] and the ion relative energies were established by DFT calculations with B3LYP, M06-2X and ωB97XD and the 6-311++G(2d,p) basis set. Rice-Ramsperger-Kassel-Markus calculations[59] of unimolecular rate constants were performed as reported previously.[60]

3. 3 Results and Discussion

3. 3. 1 Photodissociation of (AAHAR + 2H)$^{+\bullet}$

Electron transfer to doubly charged (AAHAR + 2H)$^{2+}$ ion (*m/z* 263.17) yielded the charge-reduced cation-radical, (AAHAR + 2H)$^{+\bullet}$, at *m/z* 526.33, which was the most abundant charge-reduced ion amounting to ca. 30% of ETD-produced ions.[8] The relative abundance of the (AAHAR + 2H)$^{+\bullet}$ ions did not depend on the ion-ion interaction time in the 100-300 ms interval, indicating that the ion was stable under the ion-trap conditions. The *m/z* 526 ion was selected by mass and exposed to a train of laser pulses. Figure 1a shows the UVPD mass spectrum after 1 laser pulse. The main dissociation was loss of an H atom (*m/z* 525) which was accompanied by minor elimination of $C_4H_6N_2$ (82 Da) from the histidine side chain,[61] forming the *m/z* 444 fragment ion. Upon increasing the number of pulses, (AAHAR + 2H)$^{+\bullet}$ underwent an essentially single-channel photodissociation by H atom loss. Figure 1a inset shows that the combined relative intensities of *m/z* 526 and 525 ions stayed nearly constant at >95%. The *m/z* 526 ion intensity showed an approximately exponential decay resulting in the conversion of a 72% fraction of the initial ion population and leaving a 27% fraction of non-dissociating ions after >6 laser pulses. This behavior can be described by assuming a mixture of isomeric precursor ions as shown in eq. (1)

$$I_0 = x_0(M_1) + x_0(M_2) \qquad (1)$$

where $x_0(M_1)$ is the initial molar fraction of the photodissociative ion isomer M_1 and $x_0(M_2)$ is the total initial molar fraction of non-absorbing stable ion isomers. Photodissociation of M_1 can be

described by Scheme 2 where α is the photodissociation rate constant of M_1, β is the photoisomerization rate constant of M_1 forming isomer M_3, and γ is the rate constant for photodissociation of M_3. When γ = 0, Scheme 2 describes competitive photodissociation and photobleaching of M_1.

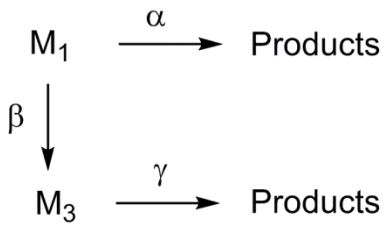

Scheme 2

The molar fractions of the species in Scheme 2 can be expressed by eq. 2-3 that are integrated and combined with eq 1 to give eq 4:

$$\frac{\Delta M_1}{\Delta n} = -(\alpha + \beta)M_1 \qquad (2)$$

$$\frac{\Delta M_3}{\Delta n} = \beta M_1 - \gamma M_3 \qquad (3)$$

$$I(n) = \frac{x_0(M_1)}{\alpha + \beta - \gamma}\left[(\alpha - \gamma)e^{-(\alpha+\beta)n} + \beta e^{-\gamma n}\right] + x_0(M_2) \qquad (4)$$

where $I(n)$ is the intensity of the precursor ions after n laser pulses. Assuming no photoisomerization (β = 0) in $(AAHAR + 2H)^{+\bullet}$ radicals, the best fit to eq 4 was obtained for $x_0(M_1) = 0.721$ and α = 0.742. This is depicted by the blue curve in Figure 1a inset which gave a 2.6% root-mean square deviation (rmsd) from the experimental data. The photodissociation decay rate α can be expressed as a product of the photon density, light beam path length through the ion cloud, and the cation-radical absorption cross section. The first two parameters were kept constant in all photodissociation measurements whereas the cross section depended on the chromophore. Assuming only photoisomerization as the source of the non-dissociating ion fraction of (AAHAR

+ 2H)$^{+\bullet}$, $x_0(M_1) = 1$, $\beta > 0$, one obtains the best fit for $\alpha = 0.535$ and $\beta = 0.207$, which is depicted by the purple curve in Figure 1 inset, and characterized by a 2.7% rmsd. The closeness of these fits did not allow us to distinguish between the two kinetic models, and so further information was sought from investigations of ion reactivity. The non-dissociating fraction of the *m/z* 526 ions was identified as being largely due to ^{13}C isotopologues of the adjacent *m/z* 525 ion in the ETD mass spectrum.

The UVPD mass spectrum in Figure 1a differed from the reference collision-induced dissociation (CID) mass spectrum of the ETD-produced (AAHAR + 2H)$^{+\bullet}$ ions (Figure 1b); this CID illustrates fragmentations induced by slow heating[22,23] under multiple collision conditions. In addition to a major loss of an H atom, CID results in a more prominent loss of the His side-chain $C_4H_6N_2$ group (*m/z* 444), and competitive eliminations of ammonia (*m/z* 509), $HN=C^{\bullet}\text{-}NH_2$ (*m/z* 483) and guanidine (*m/z* 467) from the arginine side chain. These are typical radical dissociations of arginine-containing peptide cation-radicals.[15] Noteworthy is the complete absence of backbone fragments of the ***c*** and ***z*** type which are dominant in ETD of these peptide ions.[10] The fragment identification was aided by determining their elemental compositions from high-resolution measurements (data is not shown). Note that the CID spectrum in Figure 1b was obtained with near-threshold settings of the normalized collision energy (NCE = 11) and at a long excitation time (400 ms), which was commensurable with the UVPD time scale. The different CID conditions may explain the different relative intensities of the fragment ions when compared to more energetic excitation at 30 ms.[14]

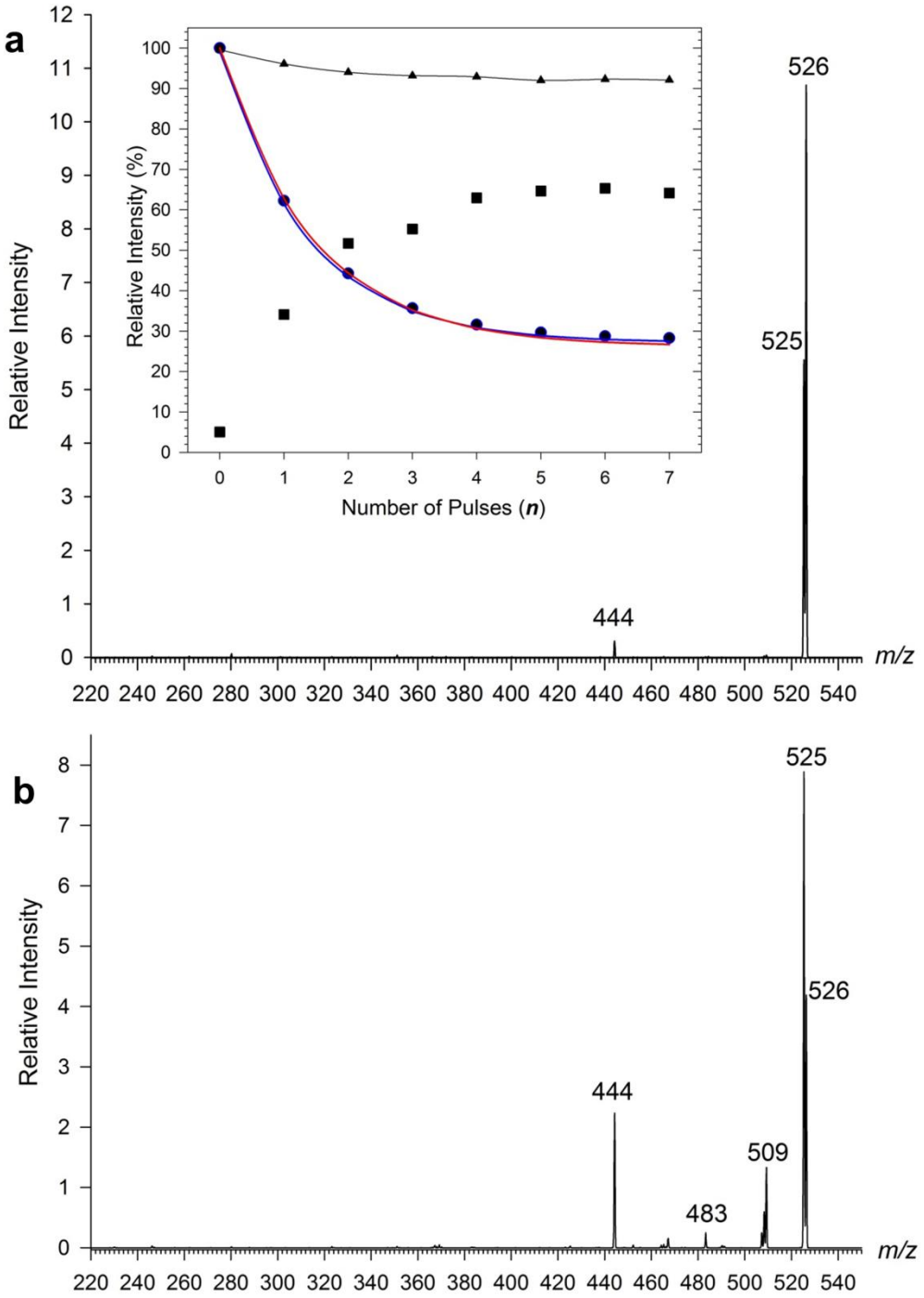

Figure 1. (a) UVPD-MS^3 spectrum of the ETD-formed (AAHAR + 2H)$^{+\bullet}$ cation-radical at *m/z* 526 after one laser pulse. Inset shows the ion relative intensities as a function of the number of laser pulses. The blue and red lines depict the fitting functions according to eq 4. (b) CID-MS^3 spectrum of the *m/z* 526 ion.

The major products of $(AAHAR + 2H)^{+\bullet}$ dissociation were further characterized by MS^4 CID and UVPD spectra. The *m/z* 525 ion by loss of H is an even-electron ion that is transparent at 355 nm. Its CID-MS^4 spectrumwas identical with that of reference *m/z* 525 $(AAHAR + H)^+$ ions generated by electrospray of the peptide or ETD of the doubly charged ion. (Figure S1, Supporting Information of ref [67]) The *m/z* 444 ion by loss of $C_4H_6N_2$ was mass-selected and probed by UVPD and CID-MS^4 spectra. The UVPD spectra (Figure 2a,b) showed that this fragment ion absorbed at 355 nm and photodissociated in an essentially single-channel reaction, forming a dominant photofragment ion at *m/z* 301. This ion was photostable, as evidenced by its retention upon increasing the number of laser pulses (Figure 2b). In contrast, CID of the *m/z* 444 ion produced a number of products (Figure 2c), but virtually no *m/z* 301 fragment ions. When comparing the UVPD and CID spectra, it becomes evident that UVPD accurately locates the original position of the radical center by avoiding radical isomerizations by hydrogen atom migrations.

The UVPD formation of the *m/z* 301 ion is readily explained by a backbone fragmentation of the amide bond adjacent to the radical center created by $C_4H_6N_2$ loss from the His residue. This corresponds to a glycine α-radical, denoted by G($^\bullet$), which dissociates forming a $\boldsymbol{y_3}$ – 2H fragment ion (Scheme 3). The major dissociations upon CID, forming the $\boldsymbol{y_4}$ (*m/z* 374) and $\boldsymbol{y_4}$ – 2H (*m/z* 372) fragment ions require α-hydrogen migrations to move the radical site from the (α-G$^\bullet$) position to the (α-A$^\bullet$) residues toward the peptide N-terminus (Scheme 3).

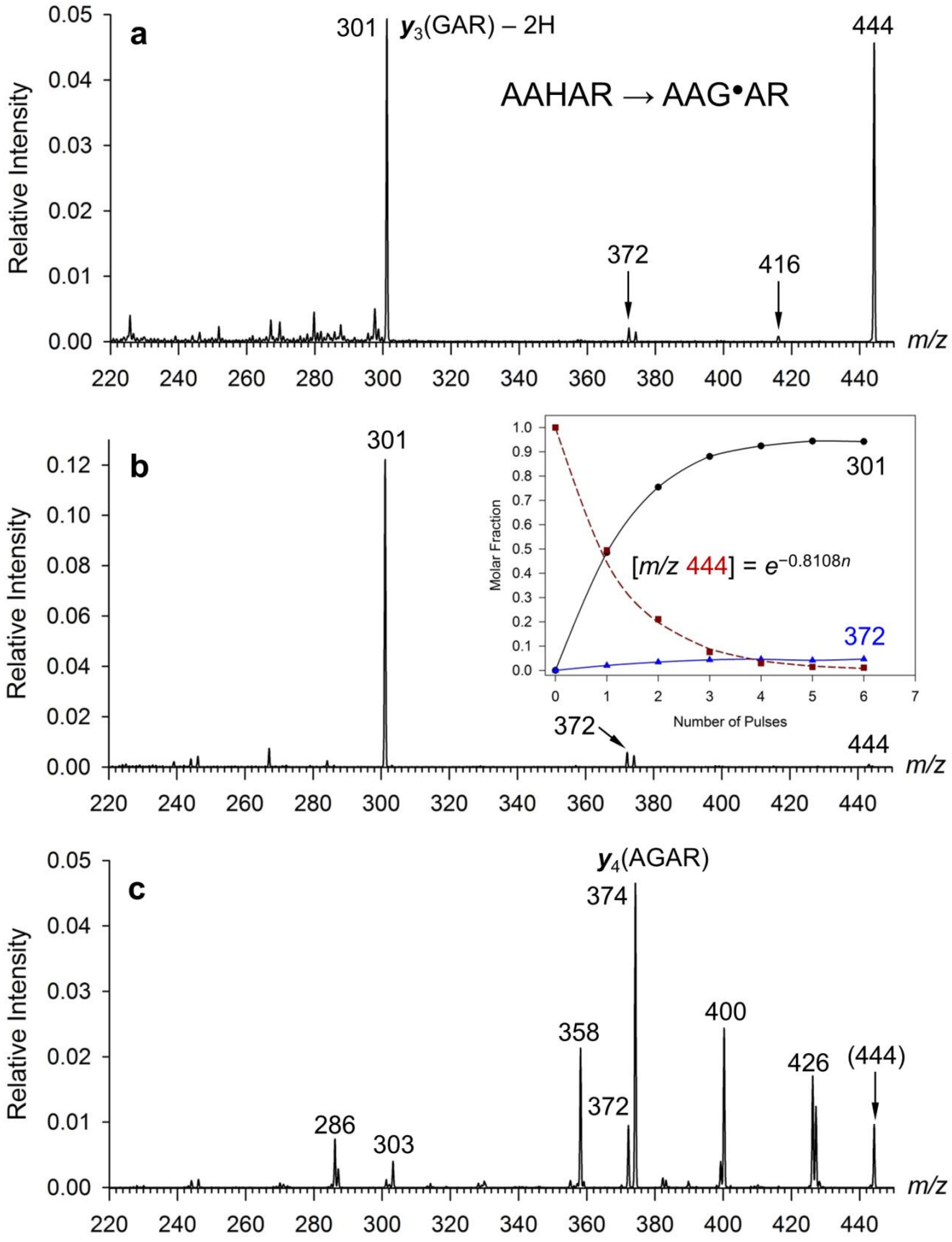

Figure 2. UVPD-MS^4 spectra of the m/z 444 ion after (a) 1 and (b) 6 laser pulses. Inset shows the exponential photodepletion curve. (c) CID-MS^4 spectrum of the *m/z* 444 ion.

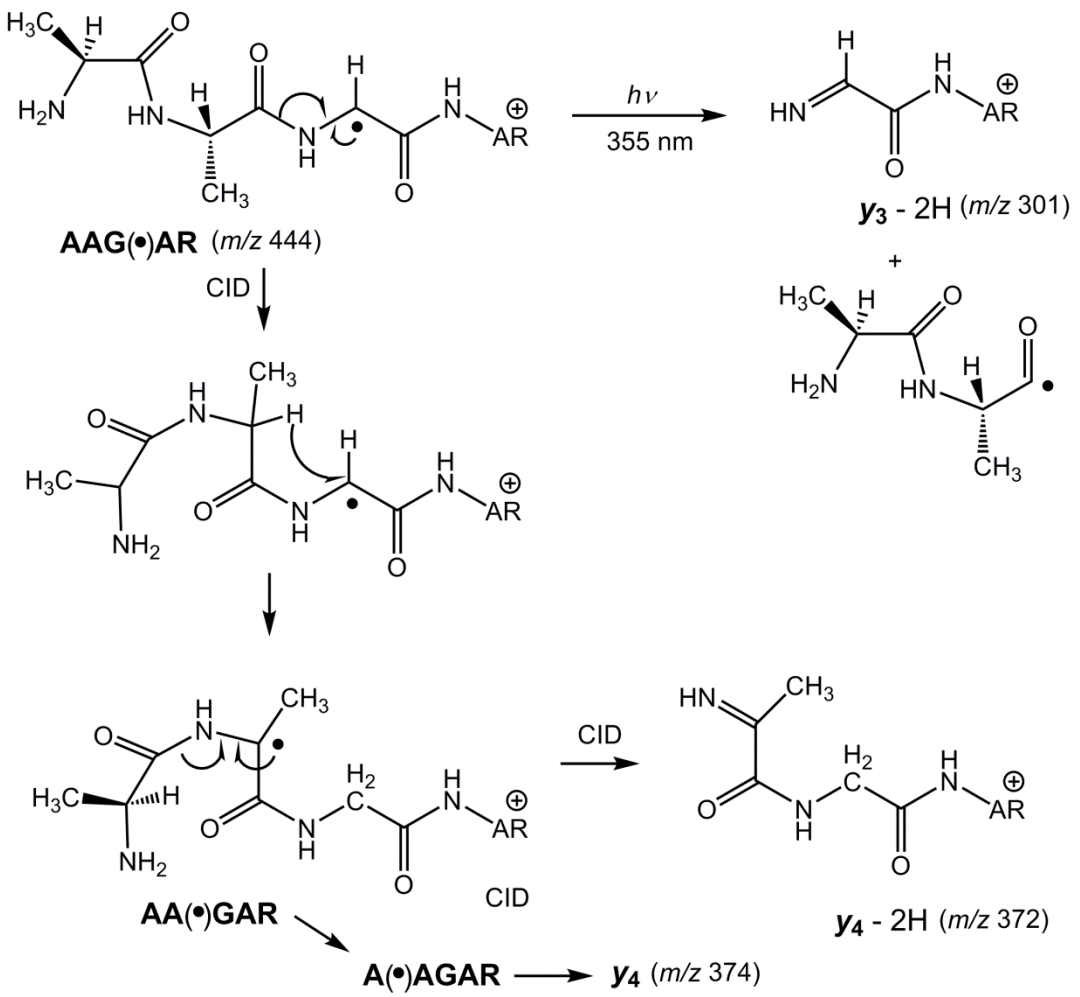

Scheme 3

3. 3. 2 Photodissociation of (AAHAK + 2H)$^{+\bullet}$

To investigate the effect of the peptide ion charge carrier, we obtained ETD-UVPD and ETD-CID mass spectra of (AAHAK + 2H)$^{2+}$ ions in which the *C*-terminal arginine residue was replaced by lysine. Electron transfer dissociation produced abundant charge reduced (AAHAK + 2H)$^{+\bullet}$ cation-radicals at *m/z* 498 along with the $\boldsymbol{c_3}$, $\boldsymbol{c_4}$, $\boldsymbol{z_3}$, and $\boldsymbol{z_4}$ backbone fragment ions (Figure S2, Supporting Information of ref [67]). UVPD of mass-selected (AAHAK + 2H)$^{+\bullet}$ resulted in a dominant loss of a hydrogen atom and a minor loss of $C_4H_6N_2$ from the His residue (*m/z* 416,

Figure S3, ref [67]) . The $(AAHAK + 2H)^{+\bullet}$ ion signal was depleted by ≥95% after 7 laser pulses (Figure S3, inset, Supporting Information of ref [67]), indicating that most of the charge-reduced $(AAHAK + 2H)^{+\bullet}$ ions contained a chromophore absorbing at 355 nm to drive photodissociation. Loss of hydrogen was also the major collision-induced dissociation of $(AAHAK + 2H)^{+\bullet}$ where it was accompanied by the *m/z* 479 and *m/z* 416 ions due to loss of $(H_2O + H)$ and $C_4H_6N_2$, respectively (Figure S4 of ref [67]). The UVPD-MS^3 spectra of $(AAHAR + 2H)^{+\bullet}$ and $(AAHAK + 2H)^{+\bullet}$ showed nearly identical dissociations of the photoactive ions, indicating they contained structurally similar chromophores. The higher photodissociation conversion of $(AAHAK + 2H)^{+\bullet}$ may indicate a greater population of photoactive ions produced by ETD from its precursor dication in combination with a higher photoabsorption cross section at 355 nm.

3. 3. 3 Photodissociation of Peptide Cation-Radicals from Histatin 5

To further illustrate the histidine effect in ETD, we investigated UVPD and CID of non-dissociating cation-radicals produced by electron-transfer charge reduction of doubly charged ions from DSHAK, FHEK, HHGYK, and HHSHR peptides.[14] These peptides are components of the small histidine-rich salivary protein histatin 5, DSHAKRHHGYKRKFHEKHHSHRGY. ETD of their doubly charged ions proceeds at high efficiency (81-99%) and produces abundant charge-reduced cation-radicals.[14]

The UVPD spectra of peptide cation-radicals containing a single histidine residue, $(DSHAK + 2H)^{+\bullet}$ and $(FHEK + 2H)^{+\bullet}$, resembled the corresponding CID-MS^3 spectra. UVPD spectrum of $(DSHAK + 2H)^{+\bullet}$ after a single laser shot that caused 28% depletion of the precursor ion and resulted in a major loss of an H atom. (Figure S5 of ref [67]) Minor dissociations by loss of CO_2 (*m/z* 514), $C_4H_6N_2$ (*m/z* 476) and backbone cleavages leading to $\boldsymbol{y_4}$, $\boldsymbol{b_4}$, and $\boldsymbol{b_3}$ fragment

ions were also observed upon UVPD. Upon increasing the number of pulses (Figure S5, inset, Supporting Information of ref [67]), the primary cation-radical fragment ions (*m/z* 514 and 476) underwent further photodissociation. The photodepletion curve (inset in Figure S5, ref [67]) showed conversion approaching 90%, whereby the majority of products was due to loss of H. The residual 10% of non-dissociating ions can be due to a non-absorbing isomer of $(DSHAK + 2H)^{+\bullet}$ or an isotope contamination. The photodepletion curve can be fitted with eq 4 where $x_0(M_1) = 0.899$, $\alpha = 0.973$, and $\beta = 0$. The CID spectrum of $(DSHAK + 2H)^{+\bullet}$ (Figure S6, Supporting Information of ref [67]) showed a prominent loss of H, although the other dissociations competed more efficiently than in UVPD. The UVPD and CID spectra of $(FHEK + 2H)^{+\bullet}$ also showed similarities (Figure S7, S8 of ref [67]). The photodepletion curve of $(FHEK + 2H)^{+\bullet}$ (Figure S7, inset, Supporting Information of ref [67]) showed a major product due to loss of H and converged to ca. 20% of residual, non-dissociating cation-radicals. The best fit to eq 4 was obtained for $x_0(M_1) = 0.818$, $\alpha = 0.75$ and $\beta = 0$.

The fragment ions formed by loss of $C_4H_6N_2$ from $(DSHAK + 2H)^{+\bullet}$ and $(FHEK + 2H)^{+\bullet}$ were further characterized by UVPD and CID MS^4 spectra. As with $(AAHAR + 2H)^{+\bullet}$, UVPD resulted in backbone cleavage next to the newly formed G($^\bullet$) radical center, forming the respective $y_3 - 2H$ fragment ions, whereas CID resulted in extensive hydrogen migrations as illustrated by multiple backbone fragments in the spectra (Figures S9 and S10 of ref [67]).

A dramatically different behavior was observed for UVPD and CID of cation-radicals containing two or three histidine residues, as in $(HHGYK + 2H)^{+\bullet}$ and $(HHSHR + 2H)^{+\bullet}$, respectively. UVPD of $(HHGYK + 2H)^{+\bullet}$ resulted in a major loss of H which was accompanied by a minor loss of $C_4H_6N_2$ and backbone dissociations (Figure 3a). The photodepletion curve converged to ca. 20% of residual $(HHGYK + 2H)^{+\bullet}$ (Figure 3a, inset). Photodepletion of

$(HHGYK + 2H)^{+\bullet}$ can be expressed by eq 4, where the best fit was obtained for $x_0(M_1) = 0.79$, $\alpha = 0.852$, and $\beta = 0$, which gave a 3.7% rmsd. In contrast to UVPD, the CID spectrum showed nearly no loss of H and the main fragment ions were due to losses of NH_3, H_2O combined with H, and $C_4H_6N_2$ (Figure 3b). Note that the fragment ions in the Figure 3b CID spectrum were essentially pure ^{12}C isotopologues which excluded contamination of the $(HHGYK + 2H)^{+\bullet}$ precursor ion with the ^{13}C isotopologue of $(HHGYK + H)^+$.

UVPD of $(HHSHR + 2H)^{+\bullet}$ showed a major loss of H which was accompanied by a minor loss of $C_4H_6N_2$ (Figure S11 of ref [67]). The resulting *m/z* 592 fragment ion underwent further photodissociation by loss of H, forming an ion at *m/z* 591. In sharp contrast, the CID spectrum was dominated by the *m/z* 592 fragment ion due to loss of $C_4H_6N_2$ (Figure S12 of ref [67]). The photodepletion curve (Figure S11, inset, Supporting Information of ref [67]) showed a nearly complete (>90%) photodissociation of $(HHSHR + 2H)^{+\bullet}$ with the vast majority of dissociation proceeding by loss of H. The experimental data can be tightly fitted by eq.4 with $x_0(M_1) = 0.931$, $\alpha = 0.817$, and $\beta = 0$, giving rmsd = 0.4%.

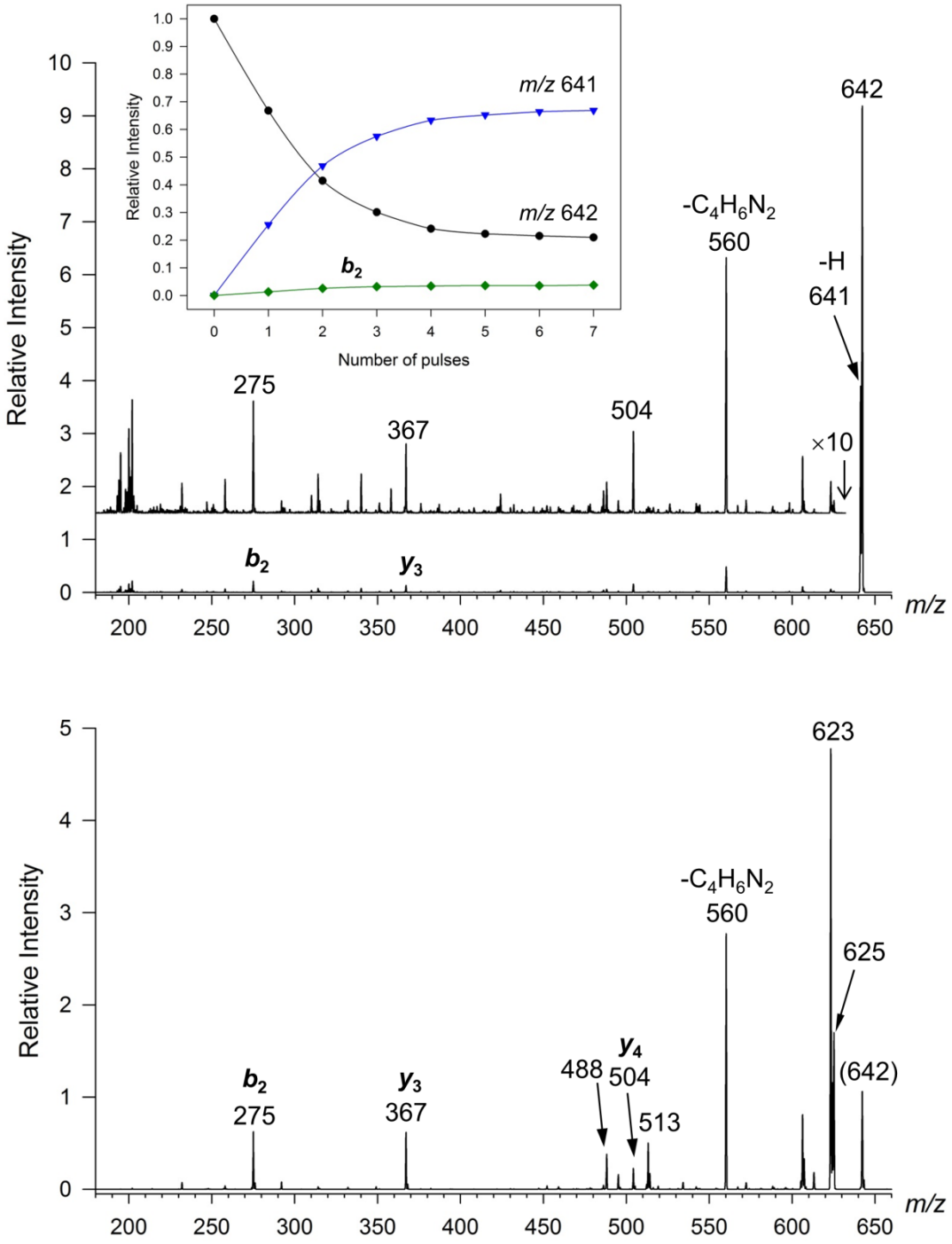

Figure 3. Top: Single-laser shot UVPD-MS^3 spectrum of $(HHGYK + 2H)^{+\bullet}$. Inset shows the relative intensities of major ions in the UVPD spectra of $(HHGYK + 2H)^{+\bullet}$ as a function of the number of laser pulses. Bottom: CID-MS^3 mass spectrum of $(HHGYK + 2H)^{+\bullet}$.

3. 3. 4 Structures, Energies, and Electronic Excitation of AAHAR Cation Radicals

The CID and UVPD spectra of charge-reduced peptide cation-radicals containing a single histidine residue showed competing dissociations by loss of H and $C_4H_6N_2$. We used the optimized structures of lowest free-energy $(AAHAR + 2H)^{2+}$ ions[10] to generate the pertinent cation-radicals and assess their relative and dissociation energies with the goal of explaining the experimental branching ratios for these two major dissociations. The energies were calculated at several levels of theory as summarized in Table 1. The energies discussed in text refer to averaged B3LYP and PMP2 data.[62] Electron transfer to the lowest free-energy conformer of $(AAHAR + 2H)^{2+}$ ($\mathbf{1}^{2+}$) is associated with an adiabatic recombination energy of RE_{ad} = 4.97 eV,[10] forming histidine cation-radical $\mathbf{1}^{+\bullet}$ (Scheme 4), which contains an imidazoline ring of the [1*H*,3*H*] type.

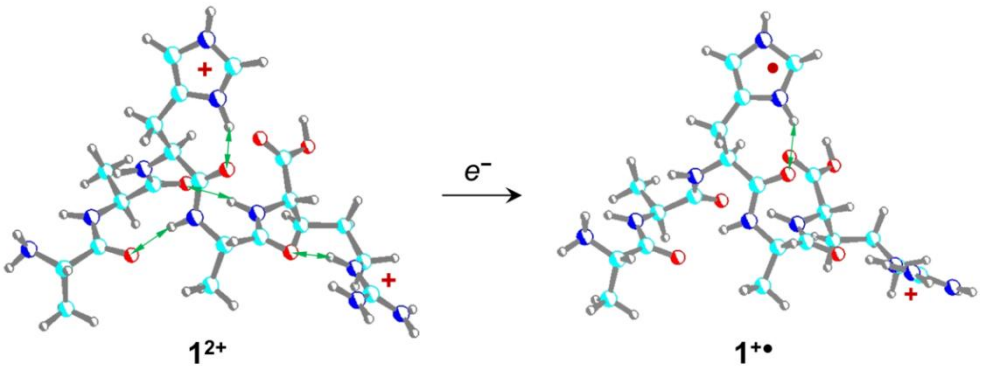

Scheme 4

Radical $\mathbf{1}^{+\bullet}$, which is a local potential energy minimum on the ground doublet electronic state potential energy surface, can undergo an exothermic rearrangement to form an isomer ($\mathbf{3}^{+\bullet}$) which has an imidazoline radical group of the [2*H*,3*H*] type (Scheme 5, *cf*. also Figure 7). This rearrangement is facilitated by protonation of the imidazoline radical in $\mathbf{1}^{+\bullet}$ that requires a participation by a Brønsted acid, e.g., the COOH group.[19] However, proton donor groups are

remote from the reduced imidazole ring in structure $\mathbf{1}^{+\bullet}$**,** and so the rearrangement requires peptide cation-radical refolding with an associated activation energy for the side-chain and backbone rotations. The $\mathbf{1}^{+\bullet} \rightarrow \mathbf{3}^{+\bullet}$ rearrangement can proceed via intermediate $\mathbf{2}^{+\bullet}$ which was found as a shallow local energy minimum according to gradient optimization with B3LYP, but collapsed to $\mathbf{3}^{+\bullet}$ upon optimization with M06-2X. Another tautomer ($\mathbf{4}^{+\bullet}$) of the [3*H*,5*H*] type was found to be comparably stable as $\mathbf{3}^{+\bullet}$ (Table 1). Radicals $\mathbf{3}^{+\bullet}$ and $\mathbf{4}^{+\bullet}$ are prone to a loss of an H atom from the imidazoline methylene groups. The loss of H from the C-2 position was calculated to proceed via **TS1** (116 kJ mol^{-1} relative to $\mathbf{3}^{+\bullet}$), forming ion $\mathbf{5}^{+}$ which represents the *m/z* 525 fragment ion. The dissociation energy was 90 kJ mol^{-1} relative to $\mathbf{3}^{+\bullet}$ but only 7 kJ mol^{-1} relative to $\mathbf{1}^{+\bullet}$, indicating that the $\mathbf{1}^{+\bullet} \rightarrow \mathbf{3}^{+\bullet} \rightarrow \mathbf{5}^{+}$ + H dissociation

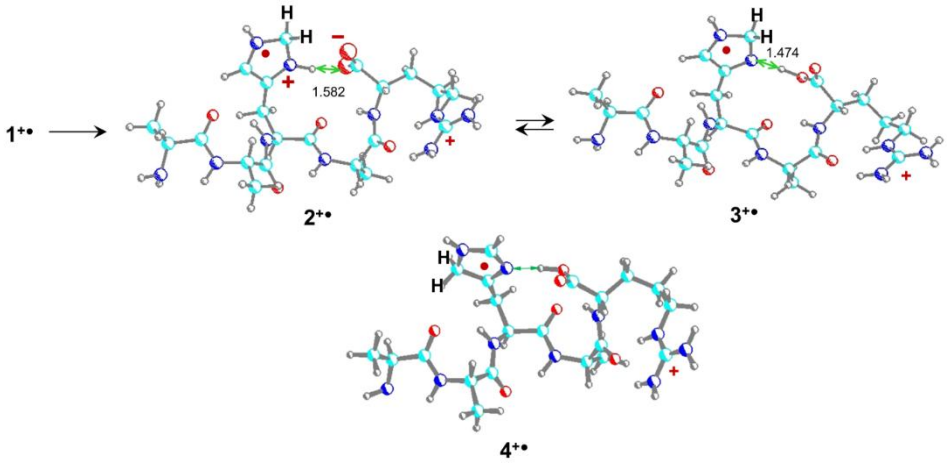

Scheme 5

pathway was energetically favorable. In contrast, the competing C_α–C_β bond cleavage of the histidine side chain in $\mathbf{3}^{+\bullet}$, potentially leading to the loss of $C_4H_6N_2$, required a substantially higher energy in **TS2** (193 kJ mol^{-1} relative to $\mathbf{3}^{+\bullet}$), forming a high-energy ion-molecule complex ($\mathbf{6}^{+\bullet}$, Scheme 6). Based on the calculated TS energies for this isomer it appeared unlikely that the loss of $C_4H_6N_2$ through this pathway could effectively compete with the loss of H-2 from $\mathbf{3}^{+\bullet}$ at near-threshold vibrational excitations pertinent to CID.

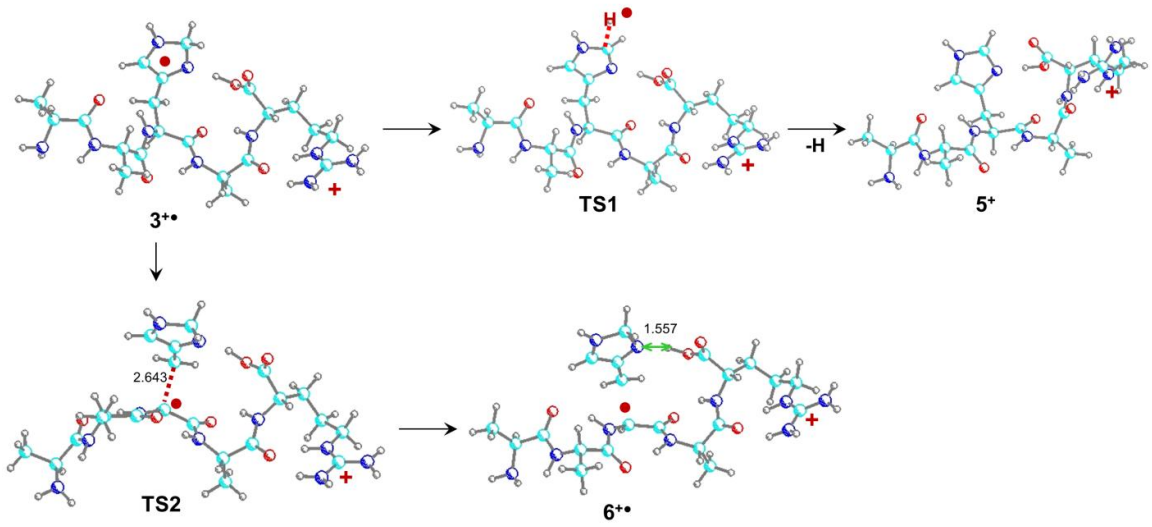

Scheme 6

Table 1. Relative Energies of (AAHAR + 2H)$^{+\bullet}$ Cation-Radicals.

	Relative Energy[a,b]				
species/reaction	B3LYP[c]	PMP2[c]	B3-PMP2[d]	M06-2X[e]	ωB97XD[c]
1^{2+} → **1**$^{+\bullet}$	−495	−463	−479	−489	−485
1$^{+\bullet}$ → **2**$^{+\bullet}$	−89	−82	−86	−78	−93
1$^{+\bullet}$ → **3**$^{+\bullet}$	−91	−76	−83	−79	−92
1$^{+\bullet}$ → **4**$^{+\bullet}$	−83	−72	−78	−74	−85
3$^{+\bullet}$ → **TS1**	132	101	116	130	144
3$^{+\bullet}$ → **5**$^{+}$ + H$^{\bullet}$	115	66	90	103	114
3$^{+\bullet}$ → **TS2**	166	218	192	221	217
3$^{+\bullet}$ → **6**$^{+\bullet}$	141	-[f]	-	196	188
3$^{+\bullet}$ → **7**$^{+\bullet}$ + **8**	104	179	141	170	170
1$^{+\bullet}$ → **9**$^{+\bullet}$	−157	−104	−130	−106	−110
1$^{+\bullet}$ → **7**$^{+\bullet}$ + **10**	−87	−19	−53	−17	−29
1$^{+\bullet}$ → **TS3**	53	54	54	62	74
1$^{+\bullet}$ → **11**$^{+\bullet}$	13	42	28	-[g]	44
1$^{+\bullet}$ → **12**$^{+\bullet}$	2	-[f]	-	−13	9
1$^{+\bullet}$ → **TS4**	38	53	45	48	55
1$^{+\bullet}$ → **TS5**	77	69	73	84	91

[a]In units of kJ mol^{-1}. [b]Including B3LYP/6-31+G(d,p) zero-point vibrational energies and referring to 0 K. [c]From single-point energy calculations with the 6-311++G(2d,p) basis set on B3LYP/6-31+G(d,p) optimized geometries. [d]Averaged B3LYP and PMP2 single point energies. [e]From single-point energy calculations with the 6-311++G(2d,p) basis set on M06-2X/6-31+G(d,p) optimized geometries. [f]MP2 calculations failed. [g]Upon gradient optimization spontaneously rearranged to **12**$^{+\bullet}$.

The relative energies of complex $\mathbf{6}^{+\bullet}$, the pertinent **TS2** for its formation, and the product $\mathbf{7}^{+\bullet}$ threshold energy are affected by the stability of the neutral $C_4H_6N_2$ moiety, which is a 4-methylene-(2*H*)imidazoline (**8**). The complex energy was lowered by >200 kJ mol^{-1} when **8** was replaced by its substantially more stable 4-methylimidazole tautomer (**10**) in isomeric complex $\mathbf{9}^{+\bullet}$ (Scheme 7) which was at a potential energy of −130 kJ mol^{-1} relative to $\mathbf{1}^{+\bullet}$. This energy lowering could presumably also affect the TS for the formation of complex $\mathbf{9}^{+\bullet}$ and make the dissociation competitive with the loss of C-2-H.

A pathway to complex $\mathbf{9}^{+\bullet}$ was found starting from $\mathbf{1}^{+\bullet}$ (Scheme 7). Cleavage of the histidine C_α−C_β bond in $\mathbf{1}^{+\bullet}$ can proceed through **TS3** (54 kJ mol^{-1} relative to $\mathbf{1}^{+\bullet}$) that involves a concomitant proton transfer from the imidazoline group onto the proximate His amide. This rearrangement forms an ion-molecule complex ($\mathbf{11}^{+\bullet}$) with the incipient $C_4H_5N_2$ radical which is at 28 kJ mol^{-1} relative to $\mathbf{1}^{+\bullet}$. In the next step, the $C_4H_5N_2$ radical reorients in another complex ($\mathbf{12}^{+\bullet}$), which allows it to recover the amide OH hydrogen atom by transferring it to the methylene group, thus forming the methyl group of 4-methylimidazole in complex $\mathbf{9}^{+\bullet}$. The TS for the H-atom transfer (**TS4**) was 45 kJ mol^{-1} relative to $\mathbf{1}^{+\bullet}$ and the isomerization was >150 kJ mol^{-1} exothermic.

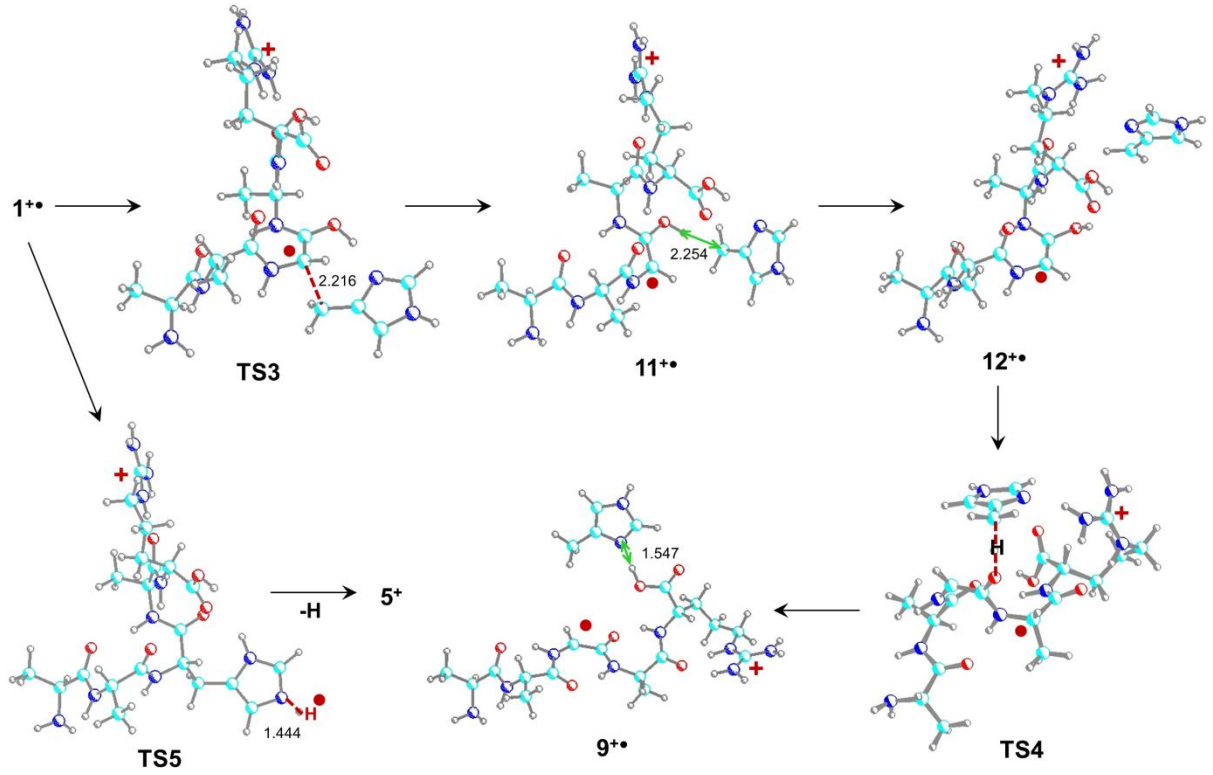

Scheme 7

The pertinent energies of the TS involved in this pathway compare favorably with the TS for direct loss of H from **1**$^{+\bullet}$ (**TS5**, 73 kJ mol^{-1}). This was further corroborated by RRKM analysis of the dissociation kinetics for the competitive pathways **1**$^{+\bullet}$ → **TS3** → **11**$^{+\bullet}$ → **12**$^{+\bullet}$ → **TS4** → **9**$^{+\bullet}$ and **1**$^{+\bullet}$ → **TS5** → **5**$^{+}$ + H$^{\bullet}$. The **1**$^{+\bullet}$ → **TS3** → **11**$^{+\bullet}$ → **12**$^{+\bullet}$ steps were treated as reversible reactions, whereas the highly exothermic isomerization **12**$^{+\bullet}$ → **TS4** → **9**$^{+\bullet}$ was deemed irreversible, proceeding to 4-methylimidazole loss from **9**$^{+\bullet}$. The RRKM rate constants were calculated for the ωB97XD/6-311++G(2d,p) TS energies that represented a complete set in Table 1. Loss of H from **1**$^{+\bullet}$ (**TS5**) was found to have the smallest rate constant (k_1) over a broad range of internal energies (Figure S13, ref [67]). The reversible C_α–C_β bond cleavage (**TS3**) showed a crossover of the rate constants for the forward (k_2) and reverse (k_{-2}) reactions at ca. 200 kJ mol^{-1}.

The irreversible isomerization step, **TS4**, (k_3) was >2 orders of magnitude faster than the reverse $C_\alpha-C_\beta$ bond formation, indicating that when formed, $\mathbf{11}^{+\bullet}$ and $\mathbf{12}^{+\bullet}$ must proceed to form $\mathbf{9}^{+\bullet}$. Solving the system of competitive and consecutive reactions for the loss of H and isomerizations forming complex $9^{+\bullet}$ gave the energy-dependent breakdown diagrams and branching ratios (Figure 4a,b). The breakdown diagrams (Figure 4a) indicated a substantial kinetic shift for 50% dissociation of $\mathbf{1}^{+\bullet}$, which required 174 kJ mol^{-1} internal energy on the longest 100 ms time scale and more so at shorter times. The energy-dependent branching ratios for the loss of H ($k_{N—H}$) and formation of $9^{+\bullet}$ ($k_{C—C}$) are plotted as log functions in Figure 4b. The ratios show a dominant formation of $9^{+\bullet}$, with the loss of H converging to 2.5% at the highest internal energies in $\mathbf{1}^{+\bullet}$ regardless of the dissociation time scale. Hence, the dissociations of $1^{+\bullet}$ greatly prefer the loss of $C_4H_6N_2$ from the histidine residue.

The analysis of the reactivity of $\mathbf{1}^{+\bullet}$ and $\mathbf{3}^{+\bullet}$ allowed us to interpret the UVPD and CID data in a coherent manner. Electron transfer to $\mathbf{1}^{2+}$ is presumed to produce two populations of $(AAHAR + 2H)^{+\bullet}$ cation radicals. One population comprises highly reactive species, presumably produced by electron attachment to amide π^* states,[15,63,64] that rapidly dissociate by backbone N−C□ bond cleavages. The other population comprises species in which the electron entered the histidine imidazolium π-electron system forming cation-radicals $\mathbf{1}^{+\bullet}$ which are local energy minima. These can competitively isomerize to $\mathbf{3}^{+\bullet}$ or $\mathbf{4}^{+\bullet}$, or be stabilized by collisional cooling with the ambient helium gas. Vibrational excitation by CID non-selectively affects $\mathbf{1}^{+\bullet}$, $\mathbf{3}^{+\bullet}$ and $\mathbf{4}^{+\bullet}$, resulting in predominant loss of $C_4H_6N_2$ from $\mathbf{1}^{+\bullet}$, and H atoms from $\mathbf{3}^{+\bullet}$ and $\mathbf{4}^{+\bullet}$. Simultaneously, collisional activation can drive the exothermic isomerization of $1^{+\bullet}$ to $\mathbf{3}^{+\bullet}$ or $\mathbf{4}^{+\bullet}$ which will then undergo loss of H. The experimental CID branching ratio for the H and $C_4H_6N_2$ loss channels showed only a weak dependence on the normalized collision energy (NCE), which

changed from 79:21 to 84:15 at NCE = 9 to NCE =12, respectively. This indicated that the loss of $C_4H_6N_2$ from $\mathbf{1}^{+\bullet}$ was kinetically competitive with isomerization to $\mathbf{3}^{+\bullet}$ or $\mathbf{4}^{+\bullet}$. It also indicated that $\mathbf{3}^{+\bullet}$ or $\mathbf{4}^{+\bullet}$ were the dominant species in the population of non-dissociating $(AAHAR + 2H)^{+\bullet}$ cation radicals produced by electron transfer.

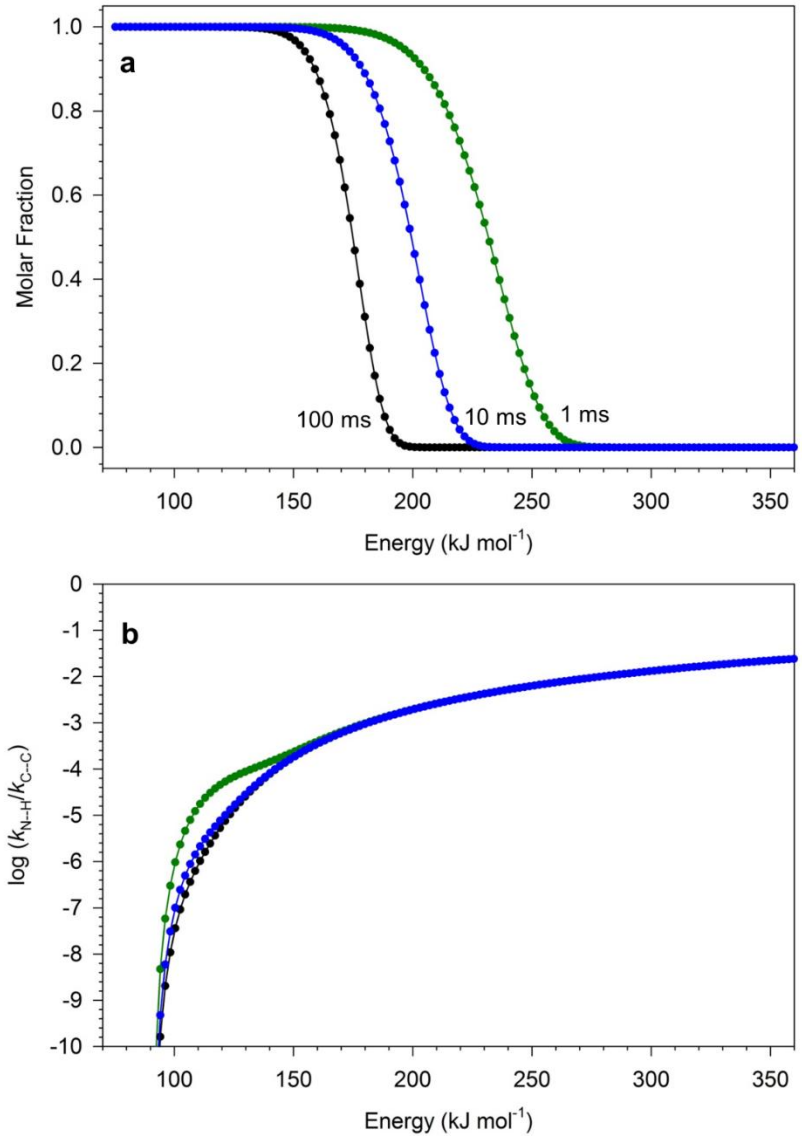

Figure 4. (a) Breakdown diagrams for competitive dissociations of $\mathbf{1}^{+\bullet}$ by loss of H and 4-methylimidazole. The curves indicate the time scales for dissociation. (b) log ratio of dissociation rates for loss of H and 4-methylimidazole from $\mathbf{1}^{+\bullet}$. The rate constants were obtained by RRKM calculations on the ωB97XD/6-311++G(2d,p) potential energy surface.

This interpretation was also consistent with the photodissociation spectra. The calculated absorption spectra of $\mathbf{1}^{+\bullet}$, $\mathbf{3}^{+\bullet}$ and $\mathbf{4}^{+\bullet}$ were substantially different in the critical region around 355 nm (Figure 5). Isomer $\mathbf{1}^{+\bullet}$ was calculated to have several weak absorption bands in the visible region and at 332 nm (Figure 5a). These were all due to various π-π* transitions in the imidazoline radical. Isomer $\mathbf{3}^{+\bullet}$ showed a strong absorption band at 340 nm (Figure 5b) whereas $\mathbf{4}^{+\bullet}$ had only a weak band at 349 nm (Figure 5c). Hence, irradiation with the 355 nm laser line was most likely to photoexcite radical $\mathbf{3}^{+\bullet}$ and cause its dissociation by loss of the imidazoline H atom. Weak absorption by $\mathbf{4}^{+\bullet}$ would have the same effect; these two isomers provide quite different absorption spectra that should render them distinguishable by UV action spectroscopy. The very minor loss of $C_4H_6N_2$ that was observed upon photodissociation can be ascribed to weak absorption by residual isomer $\mathbf{1}^{+\bullet}$ or ion-molecule complexes $\mathbf{9}^{+\bullet}$ and $\mathbf{12}^{+\bullet}$ formed therefrom. At any rate, the UVPD spectra of the long-lived $(AAHAR + 2H)^{+\bullet}$ cation-radicals strongly indicated that $\mathbf{1}^{+\bullet}$ isomerized to another isomer.

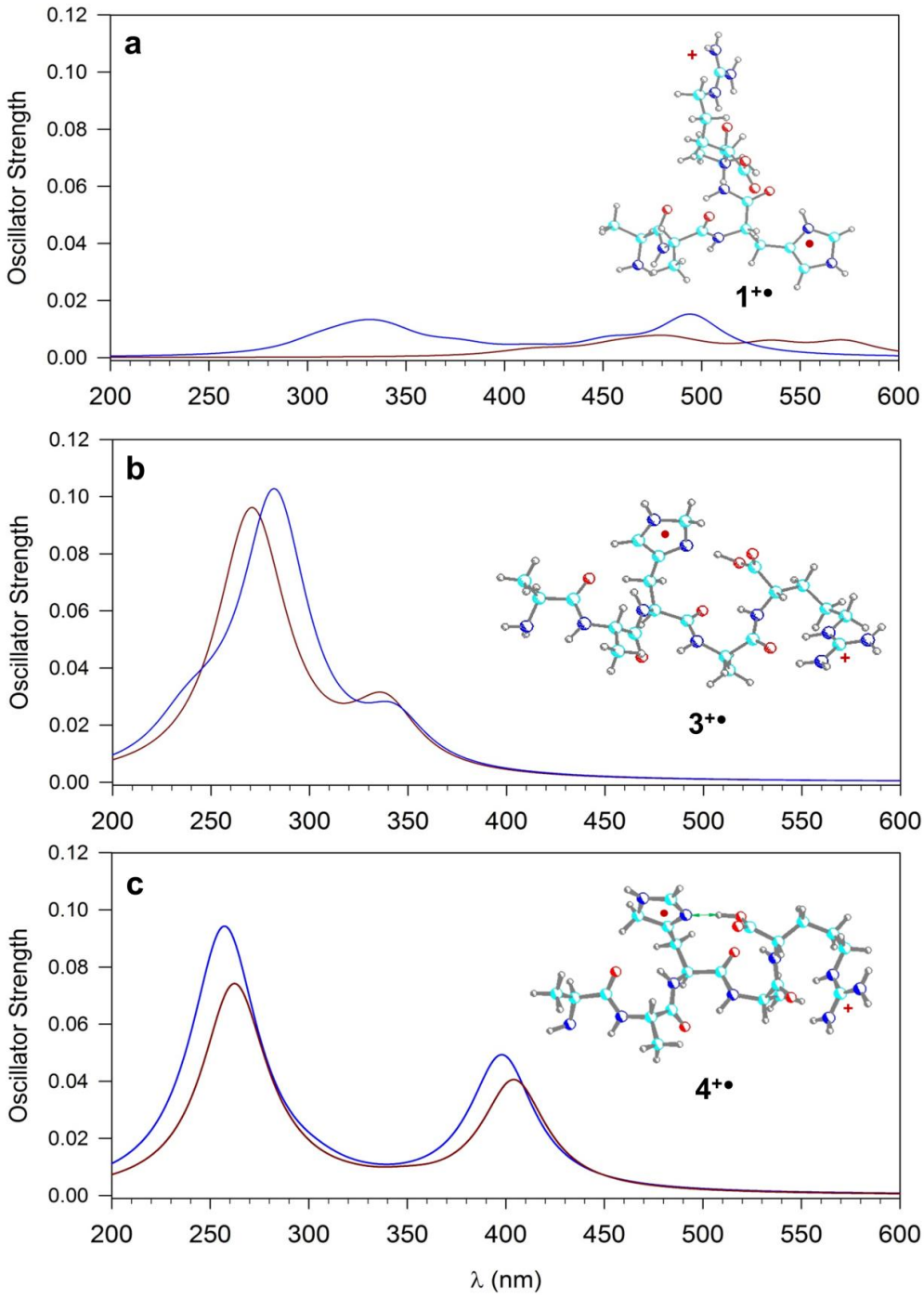

Figure 5. Calculated UV absorption spectra of (a) $\mathbf{1}^{+\bullet}$, (b) $\mathbf{3}^{+\bullet}$, and (c) $\mathbf{4}^{+\bullet}$. The blue curves are from ωB97XD/6-311++G(2d,p) calculations, the brown curves are from M06-2X/6-311++G(2d,p) calculations. The absorption bands were artificially broadened by Lorenztian functions to 20 nm fwhm.

3. 3. 5 Structures, Energies and Electronic Excitations of HHGYK Cation Radicals

The combination of four basic groups and the carboxyl in HHGYK can give rise to six canonical and four zwitterionic tautomers for the doubly-charged ion, each with a large conformational space. A complete analysis of this system would be a daunting task that was not attempted. Exhaustive conformational analysis of gas-phase $(HHGYK + 2H)^{2+}$ ion tautomers protonated on the Arg and both His residues produced as the lowest free-energy isomers zwitterionic structures **h1**-**h3** (Figure 6, Table 2). The related canonical tautomer (**h4**) was only slightly less stable than the zwitterions, leaving open the possibility for other low-energy canonical tautomers and conformers. The two lowest free-energy conformers (**h2** and **h3**) showed hydrogen bonds between the Lys ε-NH_3 group and the π-aromatic system of the Tyr residue. Interestingly, this arrangement in which the COO anion was internally solvated by a single charged His group was energetically more favorable than that in **h1** where the COO anion was solvated by both His and Lys cations.

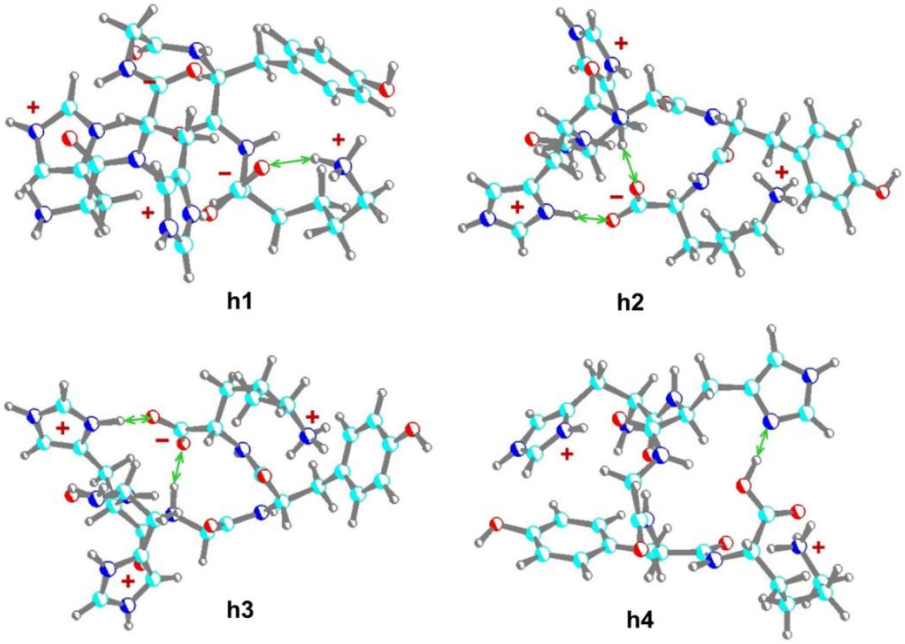

Figure 6. M06-2X/6-31+G(d,p) optimized structures of $(HHGYK + 2H)^{2+}$ ions. The atom color-coding is as follows: Turquoise = C, blue = N, gray = H.

Table 2. Relative Energies of $(HHGYK + 2H)^{2+}$ Ions.

	Relative Energy[a,b]		
Ion	B3LYP[c]	MP2[c]	M06-2X[d]
h1	0	0	0 (0.0)[e]
h2	−13	0.6	3.9 (−6.6)[e]
h3	−10	5.9	6.2 (−3.9)[e]
h4	−4.4	21	12 (0.6)[e]

[a]In units of kJ mol^{-1}. [b]Including B3LYP/6-31+G(d,p) zero-point vibrational energies and referring to 0 K. [c]From single-point energy calculations with the 6-311++G(2d,p) basis set on B3LYP/6-31+G(d,p) optimized geometries. [d]From single-point energy calculations with the 6-311++G(2d,p) basis set on M06-2X/6-31+G(d,p) optimized geometries. [e]Free enthalpies at 298 K.

Electron transfer reduction of **h1**-**h4** resulted in two kinds of cation-radicals, depending on the precursor dication conformation. Reduction of the protonated His ring in the canonical dication (**h4**) led to a histidine radical of the [1*H*,3*H*] type (**hr4**) that was a higher-energy structure (Scheme 7). Reduction of zwitterionic dications (**h2** and **h3**) which have the Lys-Tyr π-hydrogen bonding motif was accompanied by hydrogen atom migration from the Lys ammonium to the Tyr ring along with proton migration from the His ring to the COO group, forming stable radicals (**hr2**)(Scheme 7).

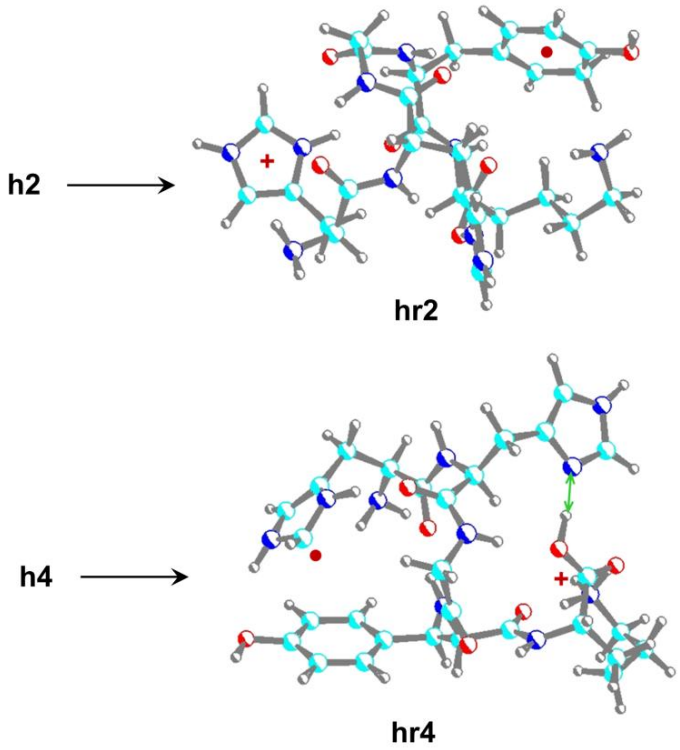

Scheme 7

To assess the propensity for 355-nm photodissociation of these cation radicals, we calculated their absorption spectra that indicated strong bands at 350 nm for radicals of the **hr2** type (Figure S15b of ref [67]). In contrast, the histidine radical **hr4** showed only weak absorption in the region near the laser excitation line (Figure S15a of ref [67]). Because of the radical position, dissociation of the **hr2** radical is unlikely to result in loss of $C_4H_8N_2$, which is consistent with its near absence in the UVPD spectra. Of possible **hr2** dissociations, cleavage of the benzylic C−C bond leading to loss of C_7H_8O followed a pathway on a steep potential energy surface (Figure S16) that exceeded the threshold for loss of a methylene hydrogen atom. The latter dissociation had a transition state at 106-119 kJ mol^{-1} relative to **hr2** when calculated by different DFT calculations. Dissociation of the O−H bond in **hr2** was substantially more endothermic than the C−H bond

dissociation (Figure S16 of ref [67]), which is consistent with the lower energy for the phenol product from the latter as opposed to a cyclohexadienone from the former. Hence, dissociation of **hr2** is expected to proceed by H atom loss, as observed in the UVPD spectrum. In contrast, the dissociations observed in CID cannot be assigned to **hr2** and must originate from another isomer. Histidine radicals of the **hr4** type can account for the abundant loss of $C_4H_6N_2$, as discussed for the analogous dissociation of $\mathbf{1}^{+\bullet}$. The complexity and near energy degeneracy of the HHGYK ion tautomer system did not allow us to identify all relevant cation-radicals to explain the rest of the CID spectra in detail.

3. 3. 6 Benchmarking Excitation Energies of Histidine Radical Chromophores.

The experimental data indicated several effects governing the behavior of charge-reduced peptide cation-radicals upon collisional excitation and electronic excitation by photon absorption at 355 nm. A common feature of all these histidine containing cation-radicals was that they contained one or more chromophores with resonant vibronic transitions overlapping with the laser excitation line. It should be noted that the charge-reduced ions were stored in the ion trap at ambient temperature, and thus their absorption bands were likely to be 30-40 nm (0.3-0.4 eV) broad due to unresolved vibrational and rotational states.[65] Hence, a perfect match of the laser line wavelength with the absorption maximum was not necessary for photodissociation. Peptide amide and side-chain groups, as well as the neutral and protonated imidazole ring of the histidine residue are transparent at 355 nm. Hence, the observed absorption must be due to a chromophore in the charge-reduced peptide ion that was created by electron transfer. At the same time, the stability of these charge-reduced peptide ions is largely due to the presence of the histidine residue,[11] indicating that the new chromophore may be due to a reduced histidine imidazole ring. To assess

electronic excitation in histidine radicals, we first calculated electronic transitions in model imidazole radicals shown in Figure 7.

Structure [1*H*,3*H*] represents a radical formed by H atom addition to the N-1 position in 4-methylimidazole or by reduction of the protonated molecule.[66] The other structures in Figure 7 represent different tautomers of H atom addition to 4-methylimidazole. The formal position of the unpaired electron conforms with valence bond structures; in fact, the odd electron is delocalized over the ring π-orbital system. Structures [1*H*,3*H*] through [1*H*,2*H*] served two purposes, one was to investigate their excited electronic states, and the other was to benchmark the excitation energies calculated by TD-DFT methods against high-level equation-of-motion coupled cluster calculations, EOM-CCSD. Well-performing TD-DFT methods were then selected to treat excitations in peptide cation-radicals for which the high level methods were not applicable. The calculated excitation energies and oscillator strengths are summarized in Table 3.

Table 3. Excitation energies and oscillator strengths in 4-methylimidazole radicals.

Species[b]	Excitation energy[a] (oscillator strength)				
	EOM-CCSD		LC-BLYP	ωB97XD	M06-2X
	6-31+G(d,p)	6-311++G(2d,p)	6-311++G(2d,p)		
[1*H*,3*H*]	2.51 (0.007)	2.35 (0.003)	2.96 (0.008)	2.62 (0.004)	2.28 (0.001)
	2.87 (0.001))	2.81 (0.0002)	3.10 (0.003)	2.85 (0.009)	2.62 (0.0007)
	3.10 (0.012)	3.05 (0.011)	3.58 (0.0003)	3.11 (0.001)	2.89 (0.011)
	3.37 (0.002)	3.19 (0.001)	3.98 (0.0002)	3.40 (0.0007)	2.98 (0.0004)
	3.77 (0.019)	3.55 (0.004)		3.74 (0.006)	3.38 0.003)
	3.99 (0.007)	3.82 (0.001)		4.07 (0.0008)	3.49 (0.001)
					3.79 (0.009)
[3*H*,5*H*]	3.33 (0.003)	3.15 (0.004)	3.64 (0.007)	3.39 (0.009)	3.14 (0.002)
	3.81 (0.017)	3.72 (0.017)	3.83 (0.002)	3.46 (0.009)	3.50 (0.014)
	4.30 (0.004)	3.97 (0.004)	4.66 (0.007)	4.15 (0.003)	3.85 (0.0005)
[1*H*,5*H*]	3.28 (0.004)	3.09 (0.004)	3.45 (0.0.62)	3.30 (0.01)	2.80 (0.003)
	3.46 (0.039)	3.39 (0.041)	3.66 (0.006)	3.38 (0.047)	3.28 (0.042)
	4.00 (0.003)	3.72 (0.004)	4.33 (0.004)	3.89 (0.004)	3.39 (0.001)
	4.32 (0.001)	4.13 (0.001)		4.26 (0.001)	3.74 (0.001)
[2*H*,3*H*]	3.37 (0.001)	3.25 (0.001)	3.82 (0.017)	3.54 (0.006)	3.12 (0.001)
	3.67 (0.014)	3.64 (0.016)	3.91 (0.004)	3.70 (0.01)	3.53 (0.001)
	3.88 (0.003)	3.88 (0.003)	3.98 (0.002)	3.75 (0.004)	3.60 (0.024)
	4.42 (0.002)	4.42 (0.002)	4.66 (0.091)	4.39 (0.006)	3.86 (0.001)
					4.07 (0.006)
[1*H*,2*H*]	3.44 (0.004)	3.33 (0.004)	3.87 (0.002)	3.64 (0.003)	3.17 (0.002)
	3.73 (0.003)	3.70 (0.003)	3.99 (0.002)	3.69 (0.003)	3.62 (0.001)
	3.93 (0.003)	3.89 (0.003)	4.00 (0.003)	3.78 (0.004)	3.72 (0.01)
	4.32 (0.004)	4.13 (0.005)	4.68 (0.100)	4.38 (0.002)	3.91 (0.002)

[a]In units of eV. [b]Refer to Figure 8 for imidazole radical structures.

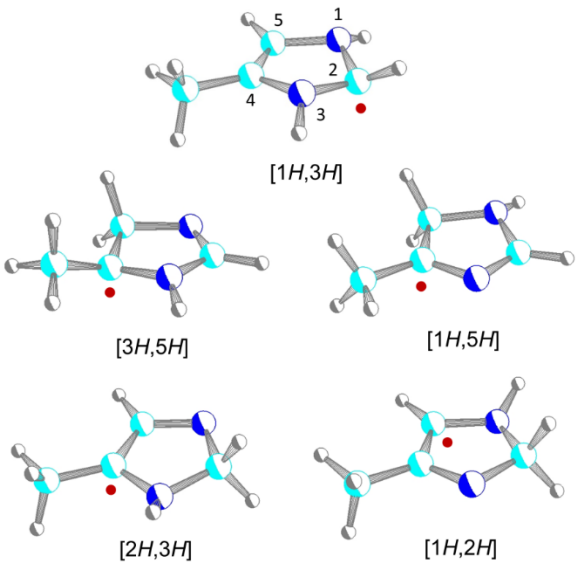

Figure 7. M06-2X/6-31+G(d,p) optimized structures of model 4-methylimidazole radicals.

The EOM-CCSD calculated excitation energies and oscillator strengths indicated that the [1*H*,3*H*] and [1*H*,2*H*] radical tautomers can be expected to be very weak absorbers at 355 nm (3.49 eV). A better match was obtained for [3*H*,5*H*], [1*H*,5*H*], and [2*H*,3*H*], which all had strong transitions within 0.2 eV of the laser photon energy. Interestingly, the solution UV spectrum of reduced histidine showed a strong band at 350 nm that was assigned to a [1*H*,3*H*] radical.[6] Our calculations indicate that the species detected upon pulse radiolysis may have rearranged to the more stable [3*H*,5*H*] or [2*H*,3*H*] radical. Out of the TD-DFT methods, LC-BLYP systematically overestimated the excitation energies, and provided the worst match with the EOM-CCSD-calculated oscillator strengths. M06-2X performed better when compared with the benchmark values; it underestimated the excitation energies by 0.04-0.22 eV and provided good match with the benchmark oscillator strength values. Comparable performance was found for ωB97XD excitation energies; however, ωB97XD somewhat underestimated the oscillator strengths for the critical transitions near 355 nm.

3. 4 Conclusions

Combination of collisional activation, near-UV photodissociation, and theory allowed us to investigate the composition and reactivity of cation-radicals produced by electron transfer to several histidine-containing peptides. Electron attachment creates new chromophores in the reduced histidine ring that can undergo rearrangements, forming intermediates that show different reactivity and absorption at 355 nm. The differences in light absorption were interpreted by time-dependent density functional theory calculations of excited states and oscillator strengths. The presence of multiple histidine residues in the peptide ions leads not only to an increased population of charge-reduced cation-radicals, but also to profound differences between dissociations induced by collisional activation and photon absorption.

3. 5 References

(1) Besant, P. G.; Attwood, P. V. Histidine phosphorylation in histones and in other mammalian proteins. *Meth. Enzymol.* **2010**, *471* (Two-Component Signaling Systems, Part C), 403-426.

(2) Besant, P. G.; Attwood, P. V. Detection and analysis of protein histidine phosphorylation. *Mol. Cell. Biochem.* **2009**, *329*(1&2), 93-106.

(3) Bornhorst, J. A.; Falke, J. J. Purification of proteins using polyhistidine affinity tags. *Meth. Enzymol.* **2000**, *326* (Applications of Chimeric Genes and Hybrid Proteins, Pt. A), 245-254.

(4) Watly, J.; Simonovsky, E.; Wieczorek, R.; Barbosa, N.; Miller, Y.; Kozlowski, H. Insight into the Coordination and the Binding Sites of Cu2+ by the Histidyl-6-Tag using Experimental and Computational Tools. *Inorg. Chem.* **2014**, *53*, 6675-6683.

(5) Samuni, A.; Neta, P. Electron Spin Resoance Study of the Reaction of Hydroxyl Radicals with Pyrrole, Imidazole, and Related Compounds. *J. Phys. Chem.* **1973**, *77*, 1629-1635.

(6) Rao, P. S.; Simic, M.; Hayon, E. Pulse Radiolysis Study of Imidazole and Histidine in Water. *J. Phys. Chem.* **1975**, *79*, 1260-1263.

(7) Dorcak, V.; Ostatna, V.; Palecek, E. Electrochemical reduction and oxidation signals of angiotensin peptides. Role of individual amino acid residues. *Electrochem. Commun.* **2013**, *31*, 80-83.

(8) Enache, T. A.; Oliveira-Brett, A. M. Peptide methionine sulfoxide reductase A (MsrA): Direct electrochemical oxidation on carbon electrodes. *Bioelectrochemistry* **2013**, *89*, 11-18.

(9) Beltra, A. P.; Bonete, P.; Gonzalez-Garcia, J.; Garcia-Garcia, V.; Montiel, V. Electrochemical synthesis of L-histidinol using solvated electrons. *J. Electrochem. Soc.* **2005**, *152*, D65-D68.

(10) Tureček, F.; Chung, T. W.; Moss, C. L.; Wyer, J. A.; Ehlerding, A.; Holm, A. I. S.; Zettergren, H.; Nielsen, S. B.; Hvelplund, P.; Chamot-Rooke, J.; Bythell, B.; Paizs, B. The Histidine Effect. Electron Transfer and Capture Cause Different Dissociations and Rearrangements of Histidine Peptide Cation-Radicals. *J. Am. Chem. Soc.* **2010**, *132*, 10728-10740.

(11) Xia, Y.; Gunawardena, H. P.; Erickson, D. E.; McLuckey, S. A. Effects of Cation Charge- Site Identity and Position on Electron-Transfer Dissociation of Polypeptide Cations. *J. Am. Chem. Soc.* **2007**, *129*, 12232-12243.

(12) Syka, J. E. P.; Coon, J. J.; Schroeder, M. J.; Shabanowitz, J.; Hunt, D. F. Peptide and protein sequence analysis by electron transfer dissociation mass spectrometry. *Proc. Natl. Acad. Sci. U. S. A.* **2004**, *101*, 9528-9533.

(13) Coon, J. J.; Ueberheide, B.; Syka, J. E. P.; Dryhurst, D. D.; Ausio, J.; Shabanowitz, J.; Hunt, D. F. Protein identification using sequential ion/ion reactions and tandem mass spectrometry. *Proc. Natl. Acad. Sci. U. S. A.* **2005**, *102*, 9463-9468.

(14) Chung, T. W.; Tureček, F. Amplified histidine effect in electron-transfer dissociation of histidine-rich peptides from histatin 5. *Int. J. Mass Spectrom.* **2011**, *306*, 99-107.

(15) Tureček, F.; Julian, R. R. Peptide Radicals and Cation-Radicals in the Gas Phase. *Chem. Rev.* **2013**, *113*, 6691-6733.

(16) Chung, T. W.; Tureček, F. Proper and Improper Aminoketyl Radicals in Electron-Based Peptide Dissociations. *Int. J. Mass Spectrom.* **2011**, *301*, 55-61.

(17) Tureček, F.; Jones, J. W.; Towle, T.; Panja, S.; Nielsen, S. B.; Hvelplund, P.; Paizs, B. Hidden Histidine Rearrangements upon Electron Transfer to Gas-Phase Peptide Ions. Experimental Evidence and Theoretical Analysis. *J. Am. Chem. Soc.* **2008**, *130*, 14584-14596.

(18) Tureček, F.; Yao, C.; Fung, Y. M. E.; Hayakawa, S.; Hashimoto, M.; Matsubara, H. Histidine-Containing Radicals in the Gas Phase. *J. Phys. Chem. B* **2009**, *113*, 7347-7366.

(19) Tureček, F.; Panja, S.; Wyer, J. A.; Ehlerding, A.; Zettergen, H.; Nielsen, S. B.; Hvelplund, P.; Bythell, B.; Paizs, B. Carboxyl-Catalyzed Prototropic Rearrangements in Histidine Peptide Radicals upon Electron Transfer. Effects of Peptide Sequence and Conformation. *J. Am. Chem. Soc.* **2009**, *131*, 16472-16487.

(20) Larsson, M. O.; Hvelplund, P.; Larsen, M. C.; Shen, H.; Cederquist, H.; Schmidt, H. T. Electron Capture and Energy Loss in _100 keV Collisions of Atomic and Molecular Ions on C60. *Int. J. Mass Spectrom.* **1998,** *177*, 51–62.

(21) Hvelplund, P.; Liu, B.; Nielsen, S. B.; Panja, S.; Poully, J.-C.; Stochkel, K. Electron capture induced dissociation of peptide ions: identification of neutral fragments from secondary collisions with cesium vapor. *Int. J. Mass Spectrom.* **2007**, *263*, 66-70.

(22) McLuckey, S. A.; Goeringer, D. E. Slow heating methods in tandem mass spectrometry. *J. Mass Spectrom.* **1997**, *32*, 461-474.

(23) Goeringer, D. E.; Asano, K. G.; McLuckey, S. A. Ion internal temperature and ion trap collisional activation: Protonated leucine enkephalin. *Int. J. Mass Spectrom.* **1999**, *182/183*, 275-288.

(24) Chu, I. K.; Zhao, J.; Xu, M.; Siu, S. O.; Hopkinson, A. C.; Siu, K. W. M. Are the radical centers in peptide radical cations mobile? The generation, tautomerism, and dissociation of isomeric α-carbon-centered triglycine radical cations in the gas phase. *J. Am. Chem. Soc.* **2008**, *130*, 7862-7872.

(25) Chung, T. W.; Tureček, F. Backbone and Side-Chain Specific Dissociations of ***z*** Ions from Non-Tryptic Peptides. *J. Am. Soc. Mass Spectrom.* **2010**, *21*, 1279-1295.

(26) Moss, C. L.; Chamot-Rooke, J.; Brown, J.; Campuzano, I.; Richardson, K.; Williams, J.; Bush, M.; Bythell, B.; Paizs, B.; Tureček, F. Assigning Structures to Gas-Phase Peptide Cations and Cation-Radicals. An Infrared Multiphoton Dissociation, Ion Mobility, Electron Transfer and Computational Study of a Histidine Peptide Ion. *J. Phys Chem. B.* **2012**, *116*, 3445-3456.

(27) Valle, J. J., Eyler, J. R., Oomens, J., Moore, D. T., van der Meer, A. F. G., von Helden, G., Meijer, G., Hendrickson, C. L., Marshall, A. G., Blakney, G. T. Free Electron Laser-Fourier Transform Ion Cyclotron Resonance Mass Spectrometry Facility for Obtaining Infrared Multiphoton Dissociation Spectra of Gaseous Ions. *Rev. Sci. Instrum.* **2005**, *76*, 023103.

(28) Eyler, J. R. Infrared Multiple Photon Dissociation Spectroscopy of Ions in Penning Traps. *Mass Spectrom. Rev.* **2009**, *28*, 448-467.

(29) Lemaire, J.; Boissel, P.; Heninger, M.; Mestdagh, H.; Mauclaire, G.; Le Caer, S.; Ortega, J.-M.; Maitre, P. Infrared spectroscopy of trapped ions. *Spectra Analyse* **2003**, *32*, 28-31.

(30) Brodbelt, J. S.; Wilson, J. J. Infrared Multiphoton Dissociation in Quadrupole Ion Traps.

Mass Spectrom. Rev. **2009**, *28*, 390-424.

(31) Polfer, N. C. Infrared Multiple Photon Dissociation Spectroscopy of Trapped Ions. *Chem. Soc. Rev.* **2011**, *40*, 2211-2221.

(32) Frison, G.; Bull, A.; van der Rest, G.; Tureček, F.; Besson, T.; Lemaire, J.; Maître, P.; Chamot-Rooke, J. Structure of ECD fragments from charge-tagged peptides probed by tunable IRMPD. *J. Am. Chem. Soc.* **2008**, *130*, 14916-14917.

(33) Tureček, F.; Moss, C. L.; Pikalov, I.; Pepin, R.; Golyuz, K.; Polfer, N. C.; Bush, M. F.; Brown, J.; Richardson, K. "Gas-Phase Structures of Phosphopeptide Ions: A Difficult Case." *Int. J. Mass Spectrom.* **2013**, *354-355*, 249-256.

(34) Leavitt, C. M.; DeBalse, A. F.; van Stipdonk, M.; McCoy, A. B.; Johnson, M. A. Hiding in plain sight: Unmasking the diffuse spectral signatures of the protonated N-terminus in simple peptides. *J. Phys. Chem. Lett.* **2013**, *4*, 3450–3457.

(35) Hernandez, O.; Pulay, P.; Maitre, P.; Paizs, B. Zundel-Type H-Bonding in Biomolecular Ions. *J. Am. Soc. Mass Spectrom.* **2014**, *25*, 1511-1514.

(36) Reilly, J. P. Ultraviolet Photofragmentation of Biomolecular Ions. *Mass Spectrom. Rev.* **2009**, *28*, 425-447.

(37) Kelly, O.; Calvert, C, R.; Greenwood, J. B.; Zettergren, H.; Nielsen, S. B.; Wyer, J. A. Effects of Charge Location on the Absorptions and Lifetimes of Protonated Tyrosine Peptides in Vacuo. *J. Phys. Chem. A* **2012**, *116*, 1701-1709.

(38) Byskov, C. S.; Jensen, F.; Joergensen, T. J. D.; Nielsen, S. B. On the photostability of peptides after selective photoexcitation of the backbone: prompt versus slow dissociation. *Phys. Chem. Chem. Phys.* **2014**, *16*, 15831-15838.

(39) Lai, C. K.; Ng, D. C. M.; Pang, H. F.; Blanc J. C. Y. L.; Hager, J. W.; Fang, D. C; Cheung, A. S-C.; and Chu, I. K. Laser-induced dissociation of singly protonated peptides at 193 and 266 nm within a hybrid linear ion trap mass spectrometer, *Rapid Commun. Mass Spectrom.* **2013**, *27*, 1119-1127.

(40) Janz, J. M.; Ren, Y.; Looby, R.; Kazmi, M. A.; Sachdev, P.; Grunbeck, A.; Haggis, L.; Chinnapen, D.; Lin, A. Y.; Seibert, C.; McMurry, T.; Carlson, K. E.; Muir, T. W.; Hunt, S.; Sakmar, T. P. Direct interaction between an allosteric agonist pepducin and the chemokine receptor CXCR4. *J. Am. Chem. Soc.* **2011**, *133*, 15878–15881.

(41) Marek, A.; Pepin, R.; Peng, B.; Laszlo, K. J.; Bush, M. F.; Tureček, F. Electron Transfer Dissociation of Photolabeled Peptides. Backbone Cleavages Compete with Diazirine Ring Rearrangements. *J. Am. Soc. Mass Spectrom.* **2013**, *24*, 1641-1653.

(42) Shaffer, C. J.; Marek, A.; Pepin, R.; Slováková, K.; Tureček, F. Combining UV Photodissociation with Electron Transfer for Peptide Structure Analysis. *J. Mass. Spectrom.* in **2015**, *50*, DOI 10.1002/jms.3551.

(43) Nguyen, H. T. H.; Shaffer, C. J.; Ledvina, A.; Coon, J. J.; Tureček, F. Serine Effects on Collision-Induced Dissociation and Photodissociation of Peptide Cation Radicals of the $\boldsymbol{z}^{+\bullet}$ Type. *Int. J. Mass Spectrom.* **2014**, in press (http://dx.doi.org/10.1016/j.ijms.2014.06.028).

(44) Frisch, M. J. et al. Gaussian 09, Revision A.02; Gaussian, Inc.:Wallingford, CT, 2009.

(45) Becke, A. D. A New Mixing of Hartree-Fock and Local Density-Functional Theories. *J. Chem. Phys.* **1993**, *98*, 1372−1377.

(46) Zhao, Y.; Truhlar, D. G. The M06 Suite of Density Functionals for Main Group Thermochemistry, Thermochemical Kinetics, Noncovalent Interactions, Excited States, and Transition Elements: Two New Functionals and Systematic Testing of Four M06-Class

Functionals and 12 Other Functionals. *Theor. Chem. Acc.* **2008**, *120*, 215−241.

(47) Chai, J. D.; Head-Gordon, M. Systematic optimization of long-range corrected hybrid density functionals. *J. Chem. Phys.* **2008**, *128*, 084106/1-084106/15.

(48) Chai, J. D.; Head-Gordon, M. Long-range corrected hybrid density functionals with damped atom-atom dispersion corrections. *Phys. Chem. Chem. Phys.* **2008**, *10*, 6615-6620.

(49) Møller, C.; Plesset, M. S. A note on an approximation treatment for many-electron systems. *Phys. Rev.* **1934**, *46*, 618-622.

(50) Schlegel, H. B. Potential energy curves using unrestricted Moller-Plesset perturbation theory with spin annihilation. *J. Chem. Phys.* **1986**, *84*, 4530.

(51) Mayer, I. Spin-projected UHF method. IV. Comparison of potential curves given by different one-electron methods. *Adv. Quantum Chem.* **1980**, *12*, 189.

(52) Furche, F.; Ahlrichs, A. Adiabatic time-dependent density functional methods for excited state properties. *J. Chem. Phys.* **2002**, *117*, 7433-7447.

(53) Iikura, H.; Tsuneda, T.; Yanai, T.; Hirao, K.: A long-range correction scheme for generalized-gradient-approximation exchange functionals. *J. Chem. Phys.* **2001**, *115*, 3540-3544.

(54) Koch, H.; Jørgensen, P. Coupled Cluster Response Functions. *J. Chem. Phys.* **1990**, *93*, 3333-3344.

(55) Comeau, D. C.; Bartlett, R. J. The equation-of-motion coupled-cluster method. Applications to open- and closed-shell reference states. *Chem. Phys. Lett.* **1993**, *207*, 414-423.

(56) Sonk J. A.; Schlegel, H. B. TD-CI simulation of the electronic optical response of molecules in intense fields II: comparison of DFT functionals and EOM-CCSD. *J. Phys. Chem. A* **2011**, *115*, 11832-11840.

(57) Moss, C. L.; Chung, T. W.; Wyer, J. A.; Nielsen, S. B.; Hvelplund, P.; Tureček, F. Dipole-guided electron capture causes abnormal dissociations of phosphorylated pentapeptides. *J. Am. Soc. Mass Spectrom.* **2011**, *22*, 731-751.

(58) Moss, C. L.; Chamot-Rooke, J.; Brown, J.; Campuzano, I.; Richardson, K.; Williams, J.; Bush, M.; Bythell, B.; Paizs, B.; Tureček, F. Assigning Structures to Gas-Phase Peptide Cations and Cation-Radicals. An Infrared Multiphoton Dissociation, Ion Mobility, Electron Transfer and Computational Study of a Histidine Peptide Ion. *J. Phys. Chem. B.* **2012**, *116*, 3445-3456.

(59) Gilbert, R.G., Smith, S.C.: Theory of Unimolecular and Recombination Reactions, Blackwell Scientific Publications: Oxford 1990; pp. 52-132.

(60) Frank, A.J., Sadílek, M., Ferrier, J.G., Tureček, F.: Sulfur oxoacids and radicals in the gas phase. A variable-time neutralization-photoexcitation-reionization mass spectrometric and ab initio/RRKM study. *J. Am. Chem. Soc.* **1997**, *119*, 12343-12353.

(61) Fung, Y. M. Eva; Chan, T.-W. Dominic. Experimental and Theoretical Investigations of the Loss of Amino Acid Side Chains in Electron Capture Dissociation of Model Peptides. *J. Am. Soc. Mass Spectrom.* **2005**, *16*, 1523-1535.

(62) Tureček, F. Proton Affinity of Dimethyl Sulfoxide and Relative Stabilities of C_2H_6OS Molecules and $C_2H_7OS^+$ Ions. A Comparative G2(MP2) ab Initio and Density Functional Theory Study. *J. Phys. Chem. A*, **1998**, *102*, 4703-4713.

(63) Sobczyk, M.; Anusiewicz, I.; Berdys-Kochanska, J.; Sawicka, A.; Skurski, P.; Simons, J. Coulomb-Assisted Dissociative Electron Attachment: Application to a Model Peptide. *J. Phys. Chem. A* **2005**, *109*, 250-258.

(64) Syrstad, E. A.; Tureček, F. Toward a General Mechanism of Electron-Capture Dissociation. *J. Am. Soc. Mass Spectrom.* **2005**, *16*, 208-224.

(65) Barbatti, M.; Aquino, A. J. A.; Lischka, H. The UV Absorption of Nucleobases: Semi-Classical Ab Initio Spectra Simulations. *Phys. Chem. Chem. Phys.* **2010**, *12*, 4959-4967.

(66) Nguyen, V. Q.; Tureček, F. Protonation Sites in Gaseous Pyrrole and Imidazole and the Stabilities of Their Radicals. *J. Mass Spectrom.* **1996**, *31*, 1173-1184.

(67) Nguyen, H. T., Shaffer, C. J., & Tureček, F. Probing peptide cation–radicals by near-uv photodissociation in the gas phase. structure elucidation of histidine radical chromophores formed by electron transfer reduction. *The Journal of Physical Chemistry B*. **2015**, *119*(10), 3948-3961.

Chapter 4: UV Action Spectroscopy of Gas-Phase Peptide Radicals

Reproduced with permission from Nguyen, H. T., Shaffer, C. J., Pepin, R., & Tureček, F. (2015). *The Journal of Physical Chemistry Letters*, *6*(23), 4722-4727.

Abstract: UV photodissociation action spectroscopy (UVPD) is reported to provide a new sensitive tool for the detection of radical sites in gas-phase peptide ions. UVPD of peptide cation radicals of the ***z***-type generated by electron transfer dissociation points to the presence of multiple structures formed as a result of spontaneous isomerizations by hydrogen atom migration. *N*-terminal C_α-radicals are identified as the dominant components, but the content of isomers differing in the radical defect position depends on the nature of the aromatic residue with phenylalanine being more prone to isomerization than tryptophan.

4.1 Introduction

Radical-containing peptide and protein ions of various protonation types have recently become available thanks to multiple advances in experimental gas-phase ion chemistry.[1] Such gas-phase systems deal with isolated molecules or structures and are complementary to condensed-phase investigations of radical intermediates in enzyme catalysis[2] and radical-induced protein damage.[3] Novel and electronically unusual species such as hydrogen-rich peptide cation radicals can be produced as transient intermediates by electron transfer to multiply charged peptide ions.[4] Hydrogen-deficient peptide cation radicals can be generated by photodissociation[5] or collision-induced dissociation[6,7] of suitably tagged peptide ions. Further hydrogen deficiency can be achieved by yet another method where gas-phase peptide cation-radicals are generated utilizing intramolecular electron transfer to a ligated transition metal ion.[8,9] Stoichiometrically, hydrogen-

deficient peptide cation radicals formally correspond to peptide molecules missing an electron.[1] Importantly, some of these types of gas-phase peptide cation radicals are more accurately described as distonic ions[10,11], in which the charge and radical reside at distant, that is, non-vicinal and non-geminal, sites in the molecule.

A classical example of distonic peptide cation radicals are $\boldsymbol{z}^{+\bullet}$ fragment ions being formed by N−C_α bond cleavage of peptide ions upon electron attachment (Scheme 1).[12] $\boldsymbol{z}^{+\bullet}$-Ions are typically represented as *N*-terminal deaminated peptide C_α radicals carrying the charging proton at a remote basic residue, which is often lysine or arginine. Although various $\boldsymbol{z}^{+\bullet}$ ions have been the subject of mechanistic studies dealing with dissociation energetics and kinetics,[13] their structures remain uncertain. The uncertainty follows from facile hydrogen migrations in peptide radicals that can be induced by thermal collisional activation,[13,14] so that standard product analysis by collision-induced dissociation (CID) cannot be used as a reliable structure probe. Therefore, new structure-specific methods are needed to elucidate the structure of these fascinating radical intermediates.

Peptide cation-radicals of both hydrogen-rich and hydrogen-deficient types have recently been shown to carry radical-associated chromophore groups absorbing light in the near UV region,[15] where the closed-shell peptide groups are transparent and do not interfere with analysis.[16-18] Irradiation at 355 nm has been shown to induce specific photodissociations which has allowed us to assign the radical site positions in peptide cation-radicals.[15] We now extend the near-UV photodissociation (UVPD) of peptide cation radicals to full action spectroscopy in the 210-400 nm region whereby multiple photodissociation channels are monitored as a function of the laser wavelength. The new experimental method is demonstrated with the structure analysis of $\boldsymbol{z}_4^{+\bullet}$ ions generated *in situ* by electron transfer dissociation (ETD) of doubly protonated AAWAR and

AAFAR peptide ions. The ground electronic state chemistry of these $z_4^{+\bullet}$ ions, as probed by CID, consists of a single dominant channel (60%) involving transfer of a benzyl hydrogen atom followed by radical-induced backbone cleavage of the adjacent C_α-CO bond (Scheme 1).[13] The UV action spectroscopy experiments are complemented by time-dependent density functional theory (TD-DFT) calculations of excited electronic states of several cation-radicals of interest.

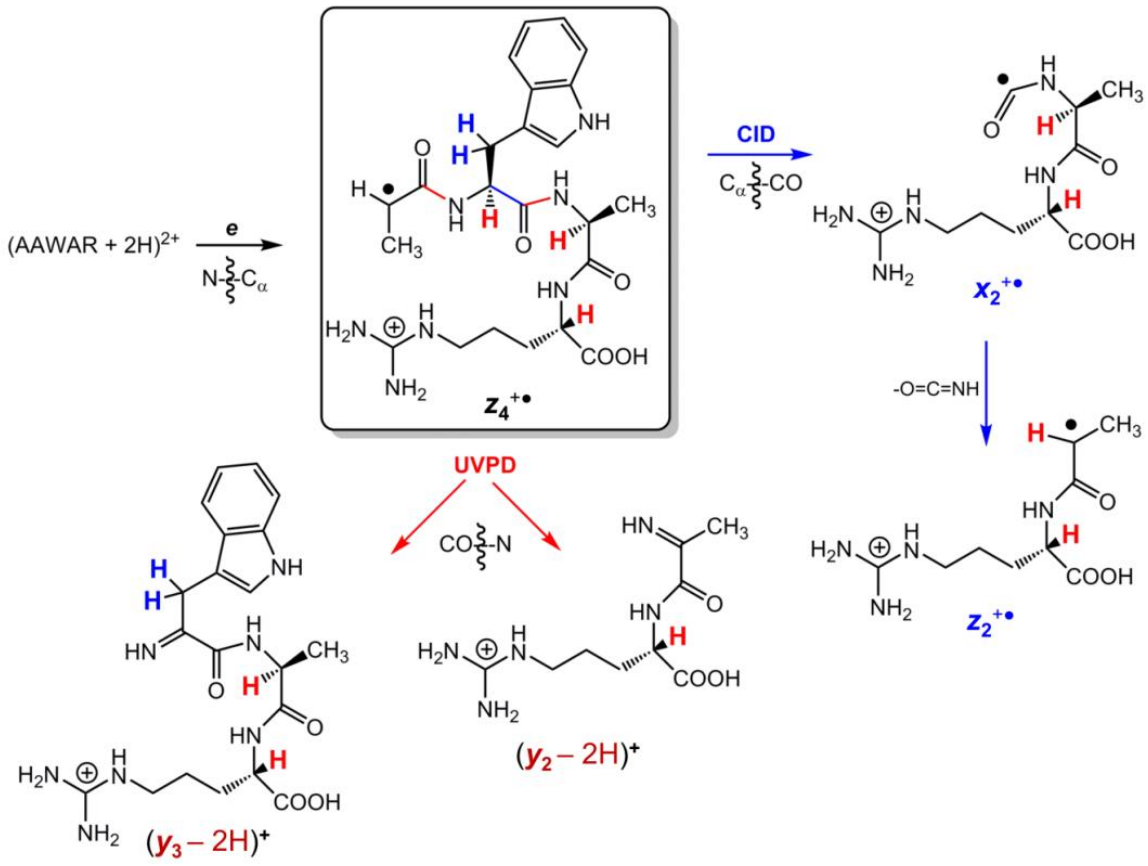

Scheme 1. Principal dissociations of z_4($^\bullet$AWAR$^+$) ions involving α and β hydrogen atom migrations induced by collisional activation (blue coded) and UV photodissociation (red coded).

4.2 Experimental Section

4. 2. 1. Materials

All peptides were synthesized on Wang resin (Bachem Americas, Torrance, CA, USA) using commercially available Fmoc peptides (Life Technologies, Rockford, IL, USA) according to previously described procedures.[19, 20] Ion formation by electrospray ionization and electron transfer dissociation to produce z ions was carried out under standard conditions, as reported previously.[21]

4. 2. 2 Ion Formation

The $\boldsymbol{z_4}^{+\bullet}$ ions were generated by a standard procedure whereby precursor [peptide + 2H]$^{2+}$ dications (peptide = AAWAR or AAFAR) were produced by electrospray ionization, stored in the linear ion trap (LIT) and dissociated by electron transfer in an ion-ion reaction with the fluoranthene anion. The $\boldsymbol{z_4}$ ions formed were selected by mass, stored in the LIT, and irradiated by 3 ns laser pulses at wavelengths that were varied from 210 through 400 nm. Photofragment ions were monitored at *m/z* values >220.

4.2. 3 Photodissociation Experiments

To accomplish photodissociation of trapped ions in the LIT, the LTQ-XL ETD mass spectrometer was modified as reported previously.[22, 23] The irradiating light beam was produced by an Nd-YAG EKSPLA NL301G laser (Altos Photonics, Bozeman, MT, USA) operating at 20 Hz frequency with a 3-6 ns pulse width. Photons exiting the pump laser are fed into a PG142C unit (Altos Photonics, Bozeman, MT, USA which integrates a third harmonic generator and optical parametric oscillator coupled with an optional second harmonic generator (SH) to provide wavelength tuning between 210-409 nm at a pulse peak power ranging between 0.79-2.06 mJ. These powers are measured at each wavelength using an EnergyMax-USB J-10MB energy sensor

(Coherent Inc., Santa Clara, CA, USA) to which the relative laser pulse power is later calibrated as the wavelength is changed. The laser beam is aligned by mirrors and focused by a telescopic lens to pass the small aperture drilled in the auxiliary chemical ionization source used to produce electron donor reagent ions. The laser beam diameter in the LIT is estimated at 3-4 mm to ensure overlap with the trapped ions. The beam position does change by about 3 mrad in switching between the SSH/FSH region (210-354 nm) and the ESH region (355-409 nm) which requires the realignment of mirrors. This realignment does inevitably change the cross section of the ion cloud exposed to irradiation, and different ratios of dissociation are observed in comparing the regions at normalized power and pulse frequency. Thus the ESH region (355-409 nm) of Figures 1a and 4a has been scaled (4x) to compensate for this change. The typical experimental set up consists of selecting the ion to be photodissociated and storing it in the LIT for a chosen time period. For example, 400-ms storage time can accommodate up to 7 laser pulses spaced by 50 ms. This allows one to vary the number of pulses which are also normalized as the number of pulses used is varied depending on the degree of dissociation, such that the ratio of fragmentation products to parent ion does not become 'saturated'.

4. 2. 6 Computations

Standard ab initio and density functional theory calculations were performed with the Gaussian 09 suite of programs.[23] All structures were obtained by gradient optimization using the B3LYP[24] and M06-2X[25] hybrid functionals with the 6-31+G(d,p) basis set and confirmed as local energy minima by harmonic frequency calculations which gave all real frequencies. All calculations of open-shell species were performed for doublet spin states within the spin-unrestricted formalism. Vertical excitation energies for the doublet spin states were obtained by time-dependent DFT calculations[26] using the B3LYP, M06-2X, LC-BLYP[27] and ωB97X-D[28]

functionals and the 6-311++G(2d,p) basis set in a spin unrestricted formalism. Typically 20-25 excited states were generated by TD-DFT calculations and those with spin-expectation values <1.5 were considered. Single-point energies were obtained by calculations that used the above DFT methods and Moller-Plesset perturbational treatment[29] (MP2, frozen core) with the 6-311++G(2d,p) basis set.

4. 3 Results and Discussion

4. 3. 1 UV Action Spectra.

Photodissociation of $\boldsymbol{z_4}(^{\bullet}\text{AWAR}^{+})$ (*m/z* 487) was monitored for several product ion channels. The overall action spectrum, constructed from the sum of normalized fragment ion intensities, shows three major bands at 220, 264, and 358 nm (Figure 1a). The wavelength and mass-resolved relative intensities of two most abundant photofragment ions, $[\boldsymbol{y_2} - 2\text{H}]^{+}$ (*m/z* 244) and $[\boldsymbol{z_4} - \text{H}]^{+}$ (*m/z* 486) are plotted in Figure 2a,b. The latter of these dominated in the <240 nm wavelength region whereas the $[\boldsymbol{y_2} - 2\text{H}]^{+}$ ion was prominent at 358 nm. In addition to the main absorption maxima, the action spectra show shoulders at 320 and 280 nm which are also apparent in the mass-resolved channels (Figure 2a and b).

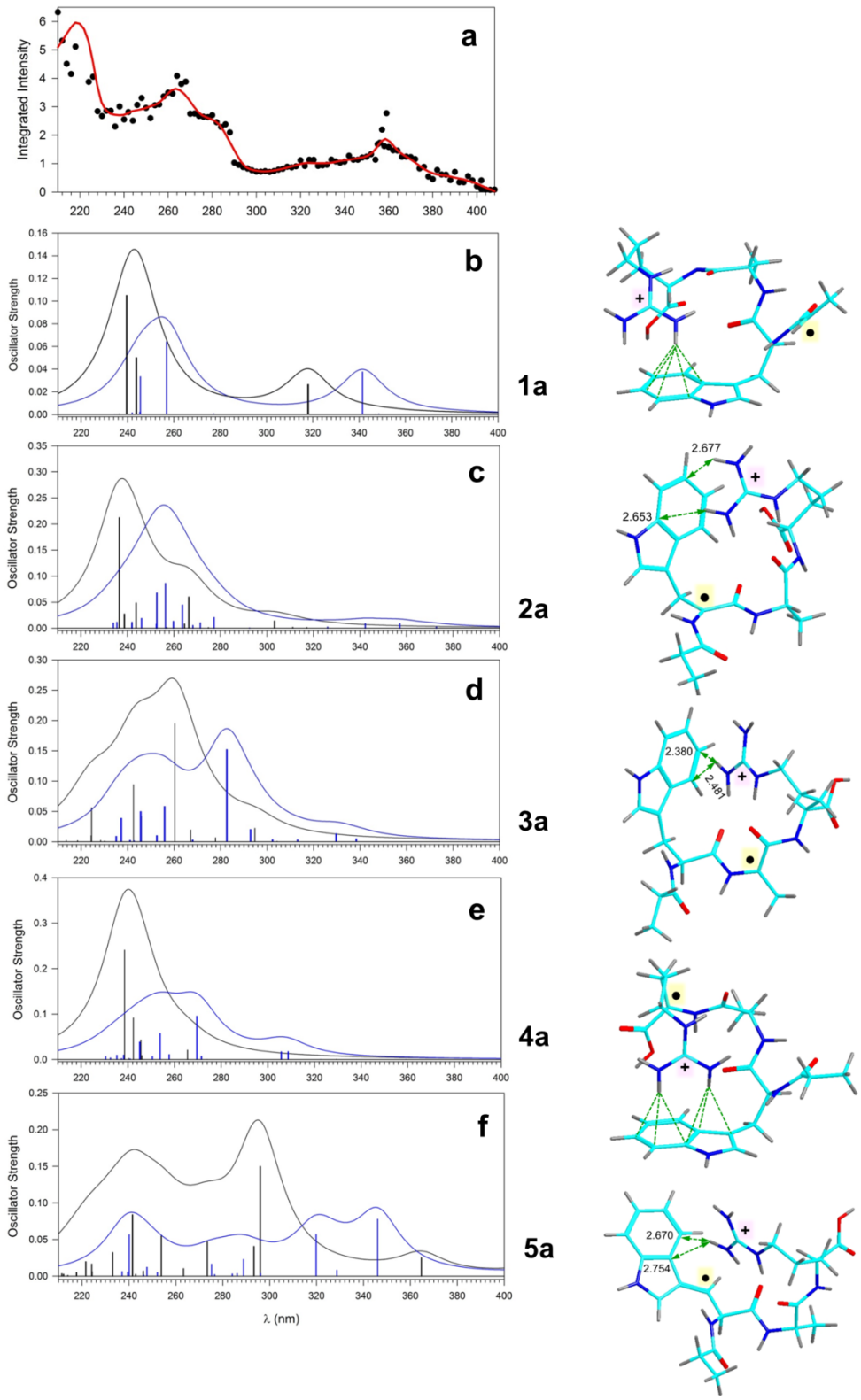

Figure 1. (a) UV action spectrum of z_4(AWAR) cation-radicals. (b-f) TD-DFT calculated absorption spectra of **1a**-**5a**. black lines: LC-BLYP; blue lines: M06-2X.

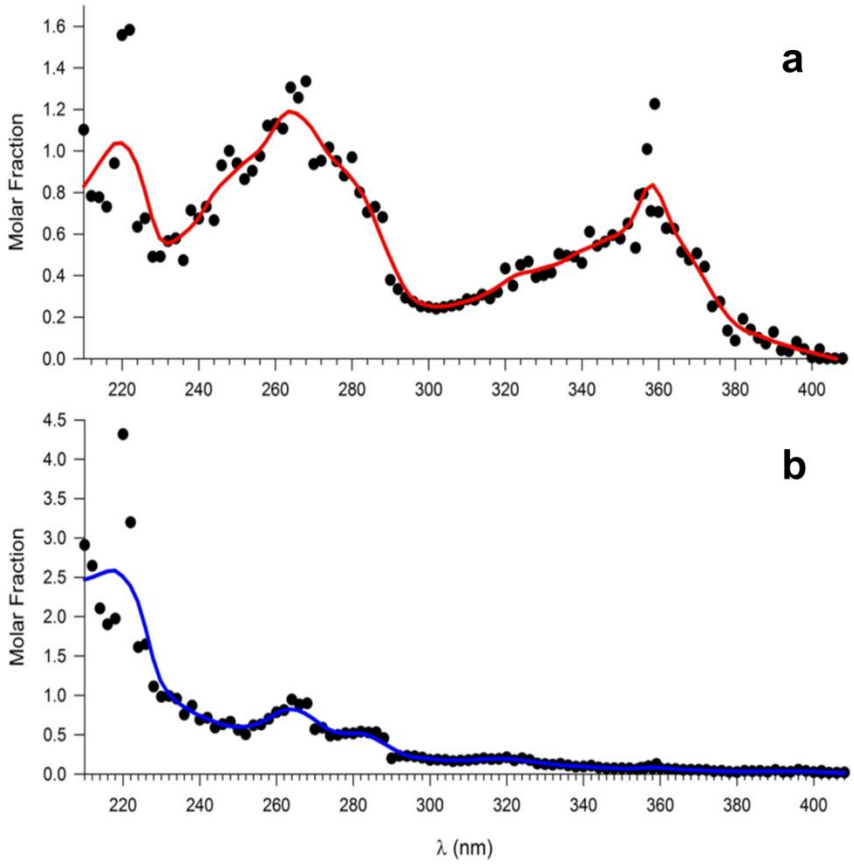

Figure 2. Mass-resolved UV action spectra of $\boldsymbol{z}_4(^{\bullet}\mathrm{AWAR}^+)$ ions. (a) $[\boldsymbol{y}_2 - 2\mathrm{H}]^+$ (*m/z* 244) and (b) $[\boldsymbol{z}_4 - \mathrm{H}]^+$ (*m/z* 486) channels.

4. 3. 2 Pulse-dependent experiments

The population homogeneity of the photoactive species was probed by pulse-dependent measurements at the two absorption maxima of 264 and 358 nm. The $\boldsymbol{z}_4(^{\bullet}\mathrm{AWAR}^+)$ ion intensity was completely depleted at 264 nm and followed a single exponential decay with the number of laser pulses (n) (Figure 3a). A least squares fit, $I(n)/I_0 = e^{-0.248n}$, gave a root-mean square deviation (rmsd) of 0.021. In contrast, photodissociation at 358 nm only partially depleted and retained a non-negligible 11% of non-photoactive residual ions according to the fit $I(n)/I_0 = 0.891e^{-0.0535n} + 0.109$ (rmsd = 0.024, Figure 3b). This clearly indicated that the $\boldsymbol{z}_4(^{\bullet}\mathrm{AWAR}^+)$ ion population contained more than one species whereby all components absorbed light at 264 nm to undergo

complete photodepletion, whereas a 11% fraction of minor component(s) were isomeric ions that did not absorb at 358 nm.

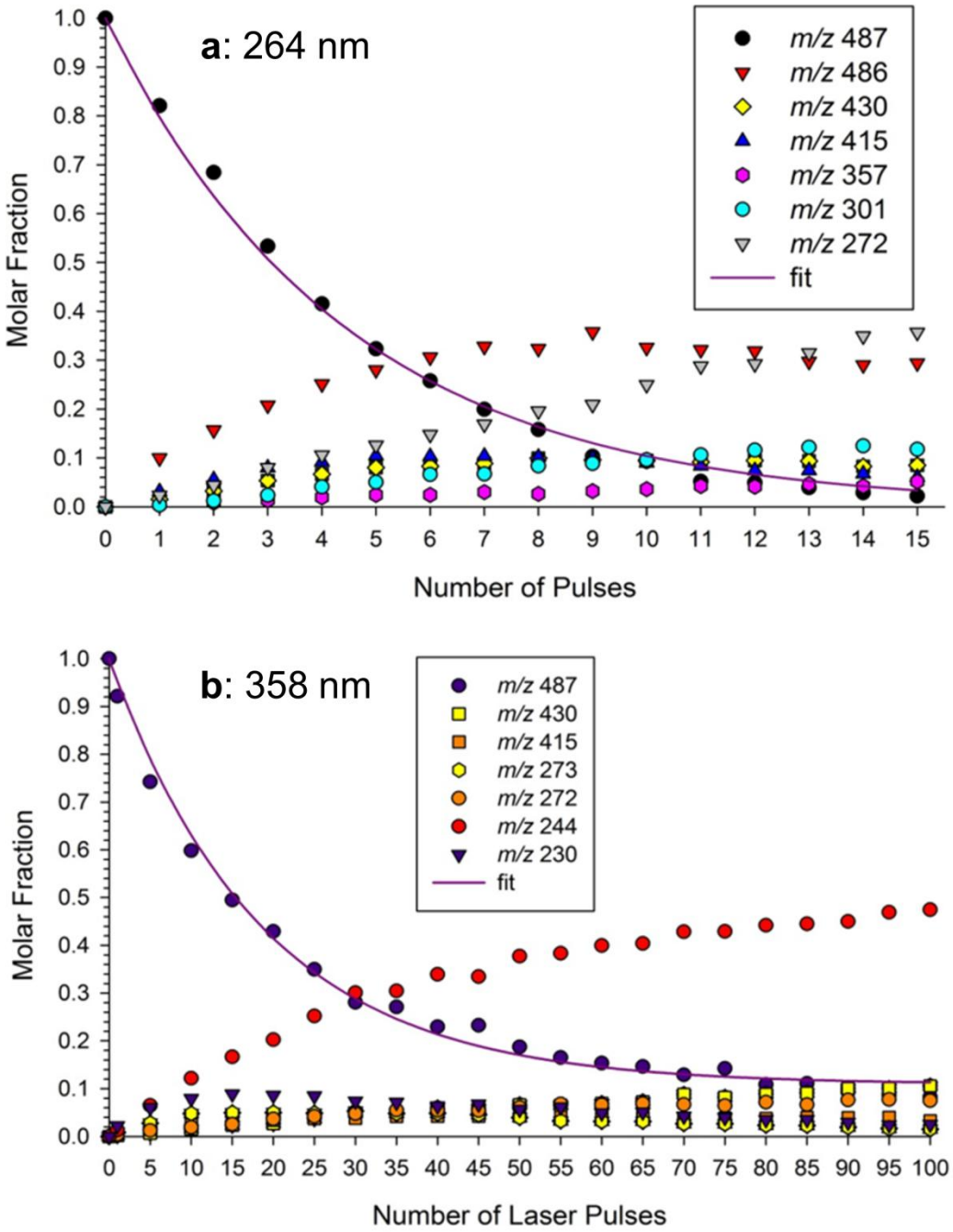

Figure 3. Pulse dependence of $z_4(^{\bullet}AWAR^+)$ ion intensities at (a) 264 nm and (b) 358 nm. Ion assignment is as follows: $z_4(^{\bullet}AWAR^+)$ *m/z* 487, $[z_4 - H]^+$ *m/z* 486, $[y_3 - 2H]^+$ *m/z* 430, $x_2^{+\bullet}$ *m/z* 273, $[x_2 - H]^+$ *m/z* 272, $[y_2 - 2H]^+$ *m/z* 244, , $z_2^{+\bullet}$ *m/z* 230,

4. 3. 3 Photodissociation

Photodissociation of $\boldsymbol{z_4}(^{\bullet}\mathrm{AFAR}^+)$(*m/z* 448) gave the action spectrum showing four distinct bands at 240, 275, 316, and 351 nm with a long-wavelength tail extending to 380 nm (Figure 4a). Most of the photofragment ion current was carried by $[\boldsymbol{y_3} - 2\mathrm{H}]^+$ (*m/z* 391), $[\boldsymbol{y_2} - 2\mathrm{H}]^+$ (*m/z* 244) and $[\boldsymbol{x_2} - \mathrm{H}]^+$ (*m/z* 272) which are all even-electron ions that lack radical chromophores. The population homogeneity of the $\boldsymbol{z_4}(^{\bullet}\mathrm{AFAR}^+)$ ions was probed by pulse dependent measurements at 275, 316, and 351 nm. The 275 nm photodepletion curve (Figure 5) showed an exponential decay, indicating complete dissociation of all ion species at this wavelength. However, the photodepletion curves measured at 316 nm and 351 nm were multimodal. The 351 nm curve was fitted with a composite function $I(n)/I_0 = 0.627e^{-0.0493n} + 0.373$ (rmsd = 0.027, Figure 6), indicating the presence of 37% of ion isomers not-absorbing light at 351 nm. The 316 nm photodepletion curve also indicated ca. 40% of non-absorbing species, although the descending part of the curve did not give a tight fit for a single exponential decay (Figure 7).

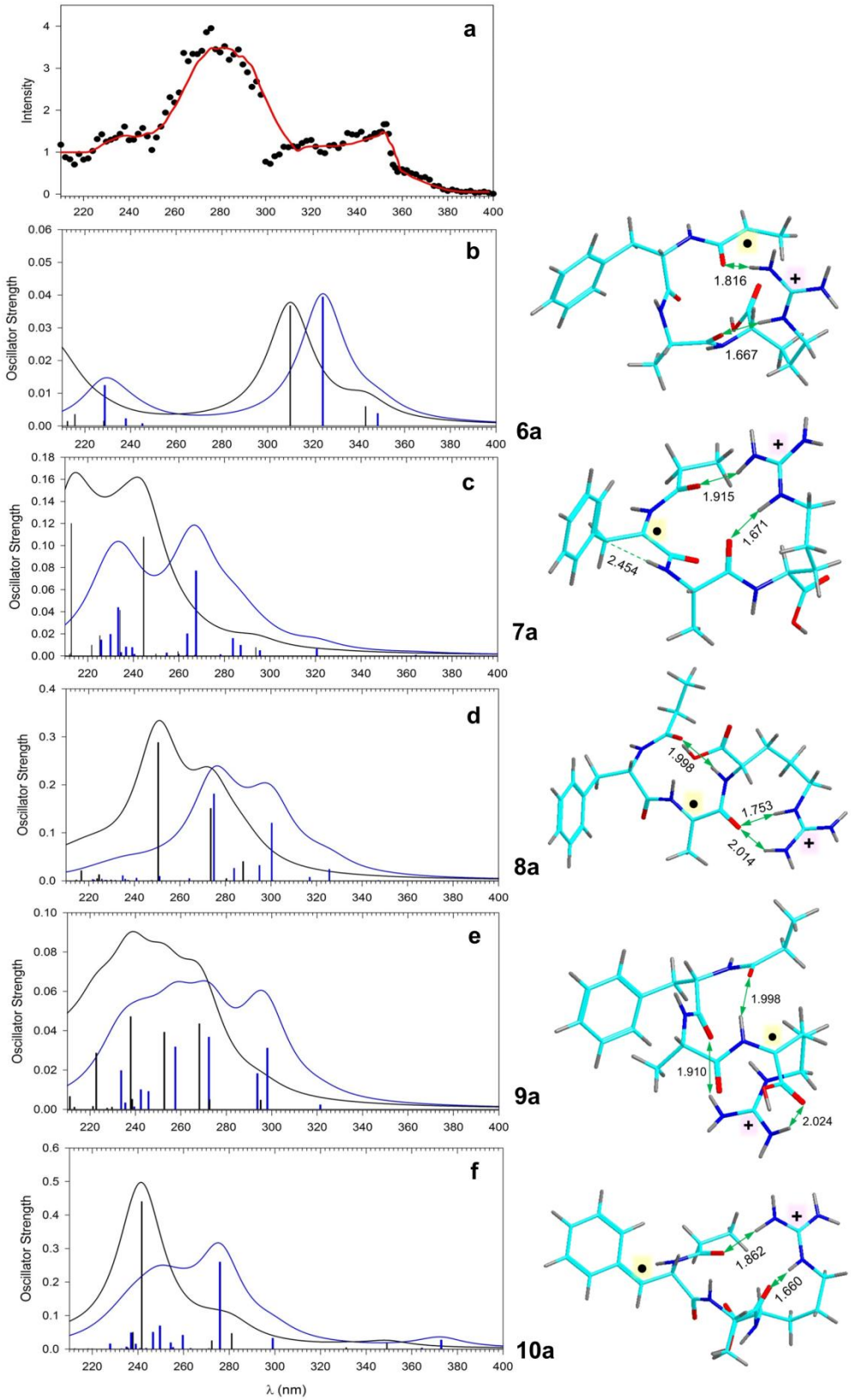

Figure 4. (a) UV action spectrum of z_4(AFAR) cation-radicals. (b-f) TD-DFT calculated absorption spectra of **6a**-**10a**. black lines: LC-BLYP; blue lines: M06-2X.

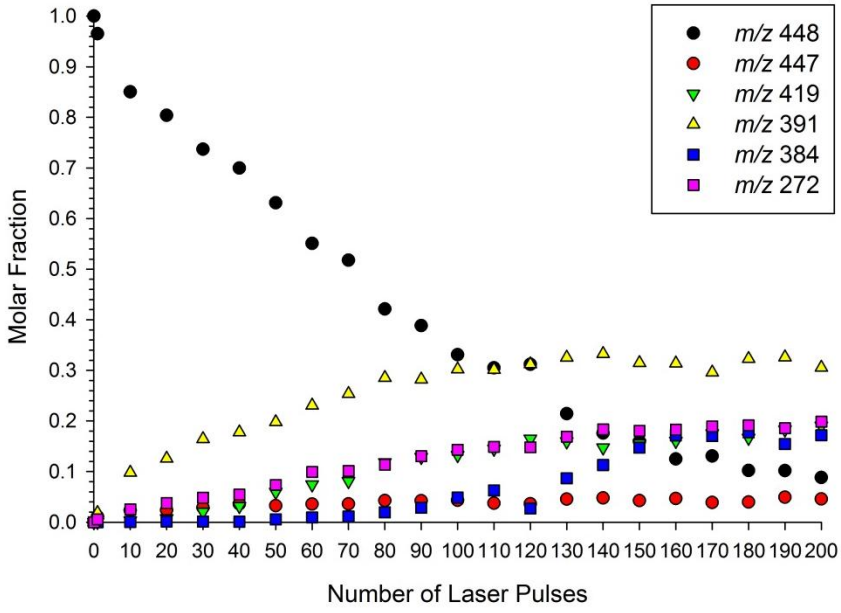

Figure 5. Pulse dependence of the $\boldsymbol{z}_4(^{\bullet}\mathrm{AFAR}^+)$ and photofragment ion intensities at 275 nm. Black circles: $\boldsymbol{z}_4(^{\bullet}\mathrm{AFAR}^+)$ (*m/z* 448); red circles: $[\boldsymbol{z}_4 - \mathrm{H}]^+$ (*m/z* 447); green triangles: $[\boldsymbol{z}_4 - 29]^+$ (*m/z* 419); yellow triangles: $[\boldsymbol{y}_3 - 2\mathrm{H}]^+$ (*m/z* 391); blue squares: unassigned (*m/z* 384); pink squares: $[\boldsymbol{x}_2 - \mathrm{H}]^+$ (*m/z* 272).

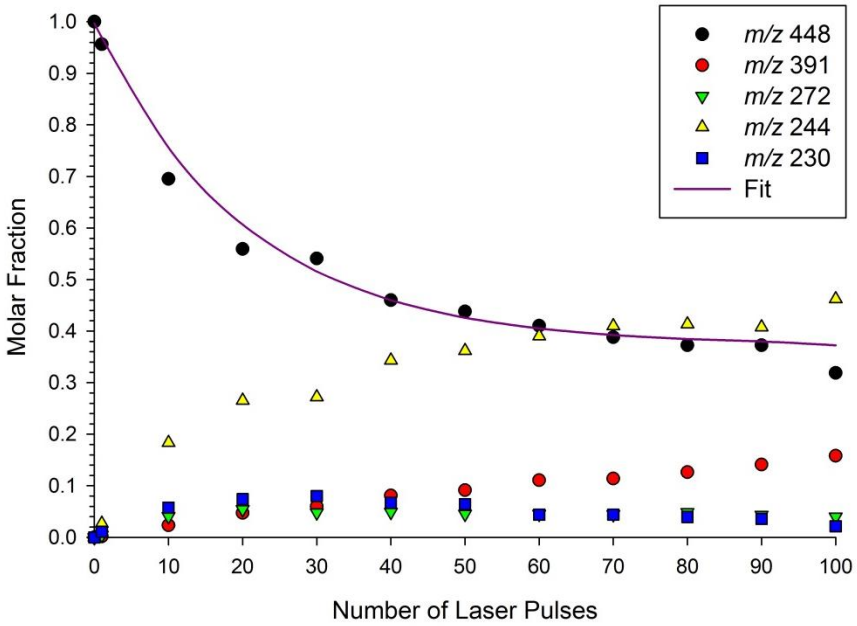

Figure 6. Pulse dependence of the $\boldsymbol{z}_4(^{\bullet}\mathrm{AFAR}^+)$ and photofragment ion intensities at 351 nm. Black circles: $\boldsymbol{z}_4(^{\bullet}\mathrm{AFAR}^+)$ (*m/z* 448); red circles: $[\boldsymbol{y}_3 - 2\mathrm{H}]^+$ (*m/z* 391); green triangles: $[\boldsymbol{x}_2 - \mathrm{H}]^+$ (*m/z* 272); yellow triangles: $[\boldsymbol{y}_2 - 2\mathrm{H}]^+$ (*m/z* 244); blue squares: $\boldsymbol{z}_2^{+\bullet}$ (*m/z* 230). The fit curve for *m/z* 448 is $I(n)/I_0 = 0.627e^{-0.0493n} + 0.373$.

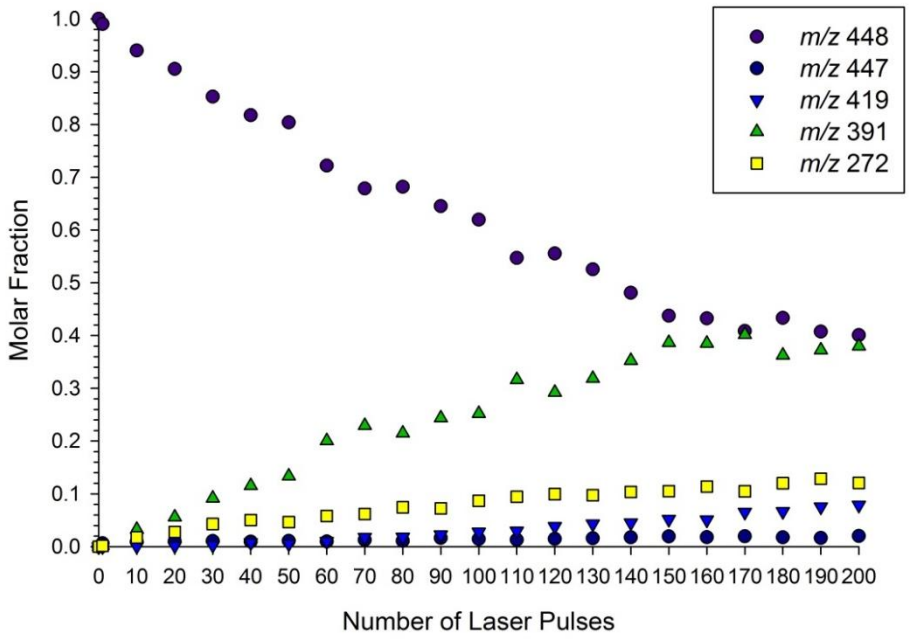

Figure 7. Pulse dependence of the z_4($^{\bullet}$AFAR^{+}) and photofragment ion intensities at 316 nm. The symbol assignments are as in Figures S1 and S2.

4. 3. 4 TD-DFT Analysis of AWAR Radical Isomers

To interpret the UV action spectroscopy data, we carried out extensive TD-DFT calculations of excited-state energies and oscillator strengths of z_4 ($^{\bullet}$AWAR^{+}) and z_4 ($^{\bullet}$AFAR^{+}) isomers differing in the position of the radical defect. The TD-DFT methods used here were previously benchmarked on high-level equation-of-motion coupled cluster excited-state calculations that identified the M06-2X[30], LC-BLYP[31], and wB97X-D[32] hybrid functionals as giving the closest fits of excitation energies for chromophores pertinent to peptide radicals.[33]

The z_4($^{\bullet}$AWAR^{+}) radicals were considered as five valence-bond isomers (**1**-**5**) differing in the position of the radical defect, each in multiple conformations. The lowest-energy conformers for each radical type are shown in Figure 1, the others are in Figure 8. Ions **1a**-**1d** are conformers having the radical defect at C_α of the truncated *N*-terminal Ala-2 residue (numbering as in the original AAWAR peptide). Conformers **2a**, **2b**, **3a**, **3b**, and **4a**, **4b** have the radical defect at C_α of

the Trp-3, Ala-4, and Arg-5 residues, respectively. The calculated relative energies (Table 1) showed that moving the radical defect from C_α-Ala-2 down the peptide chain gradually decreased the ion potential energy, making the Arg-5 C_α radical **4a** the most stable isomer. The relative energies of the Trp C_β radical isomers (**5a**, **5b**) range from slightly lower (B3LYP, LC-BLYP) to slightly higher (M06-2X, ROMP2) compared to **1a**. An interesting feature of ions **1a**-**5a** is that they develop π-hydrogen bonds between the charged Arg^+ group and the Trp aromatic ring that stabilize the low-energy conformations. This salient structure feature, also observed in proteins,[34-36] is much less represented in low-energy $(AAWAR + 2H)^{2+}$ ions (Figure 9, Table 2) where the Arg^+ group prefers hydrogen bonding to amide carbonyls.

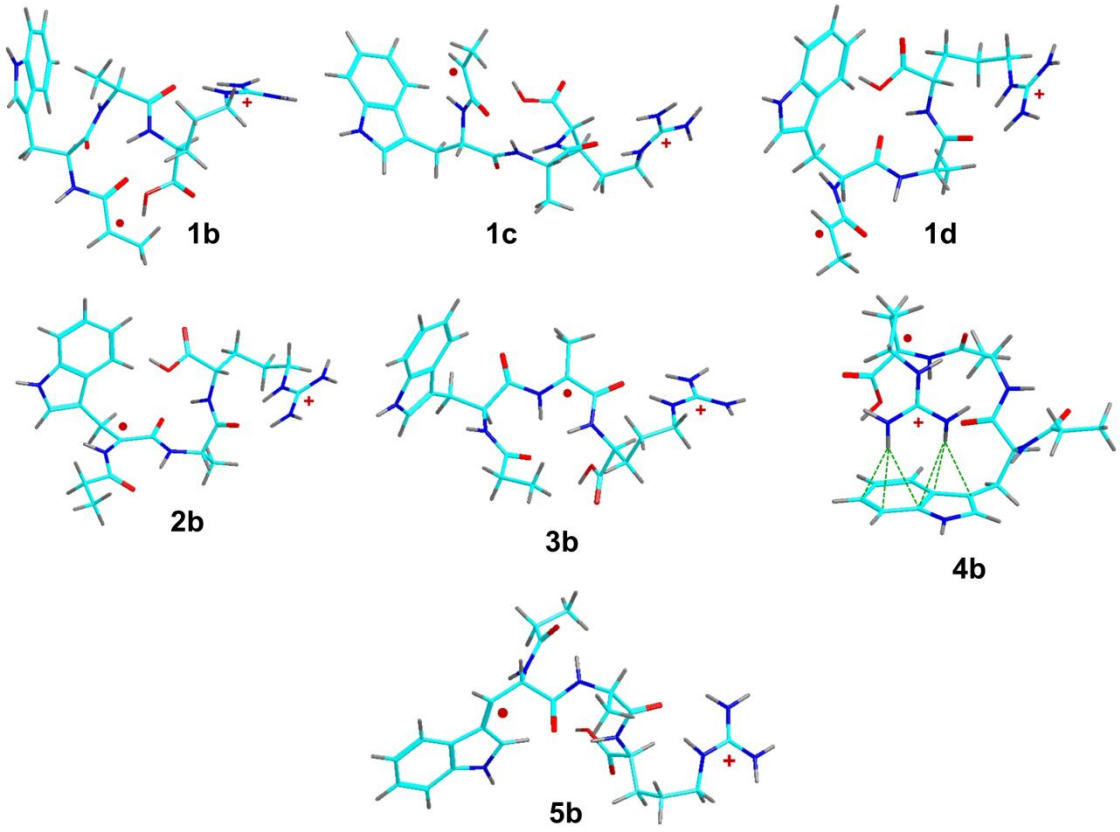

Figure 8. M06-2X/6-31+G(d,p) optimized structures of less-stable conformers of $z_4(^\bullet AWAR^+)$ isomers. See Table S1 for relative energies.

Table 1. Relative Energies of z_4($^{\bullet}$AWAR$^+$) Isomers.

	Relative Energy[a,b]				
Ion	B3LYP[c]	M06-2X[d]	ωB97X-D[c]	LC-BLYP[c]	ROMP2[c]
1a	0.0	0.0	0.0	0.0	0.0
1b	2.9	26	14	15	-
1c	−1.1	34	8.3	11	-
1d	0.1	17	−1.2	5.7	15
2a	−31	3.6	−13	−17	-
2b	−16	−10	−4	−4.8	-
3a	−37	−20	−25	−28	-
3b	−34	−2.3	−12	−19	-
4a	−43	−38	−43	−40	-
4b	−11	−38[x]	4		
5a	−21	8.3	−0.1	−11	4.7
5b	−6	36	20	10	-

[a]In units of kJ mol^{-1}. [b]Including zero point energy corrections. [c]From single-point energy calculations with the 6-311++G(2d,p) basis set on B3LYP/6-31+G(d,p) optimized geometries. . [d]From single-point energy calculations with the 6-311++G(2d,p) basis set on M06-2X/6-31+G(d,p) optimized geometries.

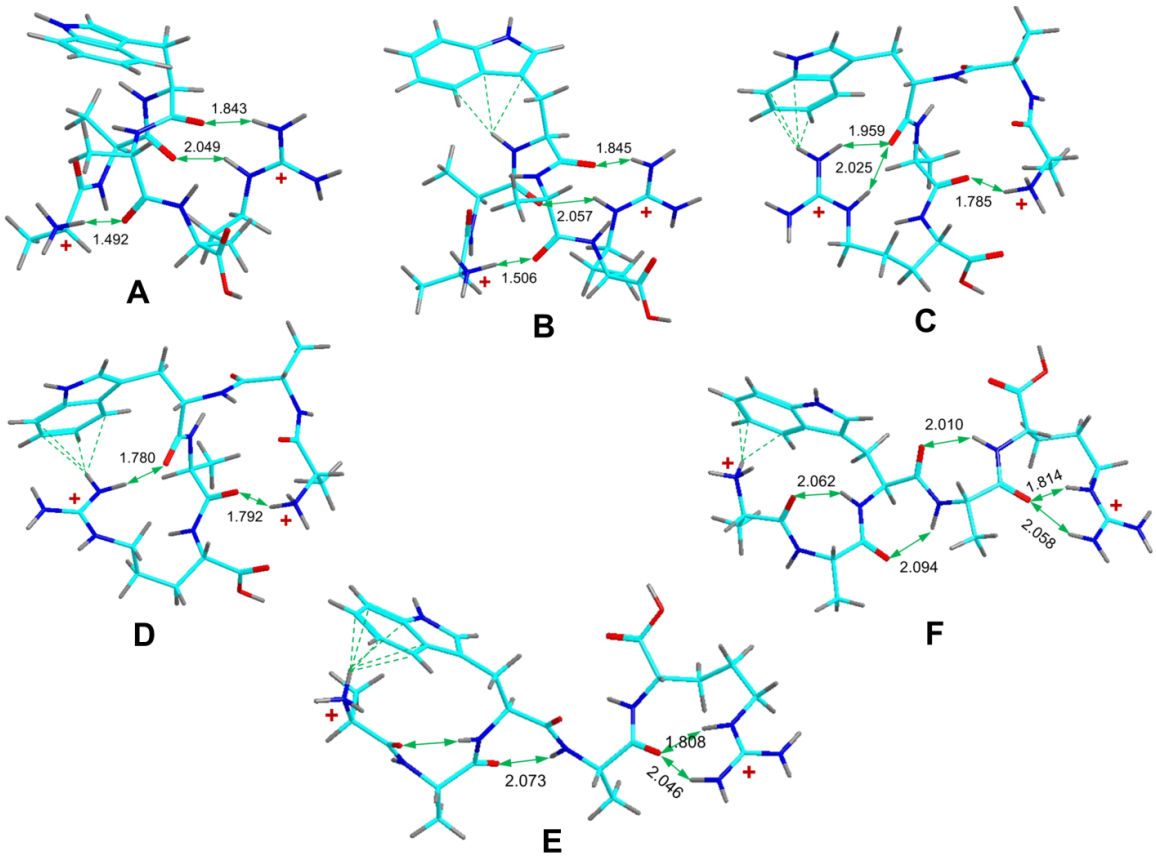

Figure 9. M06-2X/6-31+G(d,p) optimized structures of $[AAWAR + 2H]^{2+}$ conformers. See Table S3 for relative free energies.

Table 2. Relative Energies of $(AAWAR + 2H)^{2+}$ Conformers.

		Relative Energy[a,b]				
Ion	Type	B3LYP[c]	M06-2X[d]	ωB97X-D[c]	LC-BLYP[c]	MP2[c]
A	non-stacked	0.0	0.0	0.0	0.0	0.0
B	non-stacked	1.5	14	2.2	3.8	2.8
C	Arg^+…Trp	16	24	14	11	13
D	Arg^+…Trp	15	22	12	13	12
E	Lys^+…Trp	−14	10	−5.1	−0.8	4.8
F	Lys^+…Trp	−4.0	20	4.3	12	15

[a]Relative free energies in kJ mol^{-1}. [b]Including zero-point corrections and 298 K enthalpies and entropies. [c]Single-point calculations with the 6-311++G(2d,p) basis set on B3LYP/6-31+G(d,p) optimized geometries. [d]Single-point calculations with the 6-311++G(2d,p) basis set on M06-2X/6-31+G(d,p) optimized geometries.

The LC-BLYP and M06-2X calculations of absorption spectra were limited to 20 excited states and provided transitions down to 210-230 nm (Figure 1b-f). The lines for electron transition were artificially broadened by convolution with Lorentzian functions at 12 nm full-width at half maximum. Radical **1a** showed a band at 318-342 nm that matched the 358 nm band in the UV action spectrum of $\boldsymbol{z_4}(^{\bullet}\mathrm{AWAR}^{+})$. The pertinent excited state involves electron promotion from valence π orbitals to the singly-occupied molecular orbital (SOMO) of the π type which is located at the terminal $CH_3CH^{\bullet}CONH$ group (Figure 10). We note that the calculated absorption maxima correspond to energies for vertical electron excitations from the $v = 0$ vibrational state of the cation-radical whereas the experimental action spectra are obtained with thermal ions at 310 K where a number of low wave-number vibrational modes are substantially populated to $v = 1$ and higher vibrational states. The combined vibronic transitions in thermal ions lead to both band broadening and a red shift by ca. 0.2 eV compared to the calculated 0 K transition energies.[37] Interestingly, the calculated absorption spectra of conformers **1a**-**1d** are very similar (Figure 11), indicating that the electron excitations are not much sensitive to the peptide conformation. This differentiates UV action spectroscopy of peptide radicals from infrared-based action spectroscopies of stable gas-phase peptide ions that are strongly sensitive to ion conformation.[38,39] Radicals **2a**-**4a** show no or only very weak bands in the near UV region (Figure 1c-e) and thus can account for the small fraction of $\boldsymbol{z_4}(^{\bullet}\mathrm{AWAR}^{+})$ ions that do not photodissociate at 358 nm. The most stable isomer **4a** showed two transitions at 306 and 309 nm that can account for the 316 nm band in the UV action spectrum. The calculated UV spectra of the Trp C_β radical isomer **5a** showed a substantial variability depending on the TD-DFT method (Figure 1f). According to the LC-BLYP calculations that were benchmarked as most reliable for related benzyl radicals,[33] isomer **5a** is expected to show a weak band at 355 nm and a strong one at 296 nm. This can provide the 316 nm

band in the experimental action spectrum, indicating that **5a** was present as a minor component of the $\boldsymbol{z_4}$ ion population. Note that all isomers showed strong absorption bands at 240-260 nm which are consistent with the pertinent band in the UV action spectrum of $\boldsymbol{z_4}(^{\bullet}\text{AWAR}^{+})$ and explain the complete ion photodepletion in the pulse-dependent measurements at 264 nm. The 220 and 264 nm bands were assigned to the transitions involving the Trp chromophore. This is corroborated by the reference UV action spectrum of $[\text{AAWAR} + 2\text{H}]^{2+}$ which showed major bands at these wavelengths (Figure 12a), as interpreted by TD-DFT calculations of excitation energies and oscillator strengths for several low-energy ion conformers (Figure12b,c).

In summary, the major features of the action spectrum of the $\boldsymbol{z_4}(^{\bullet}\text{AWAR}^{+})$ ion can be assigned to the *N*-terminal radical isomer **1a** or its conformers. The additional bands indicate the presence of other radical isomers produced by electron transfer dissociation.

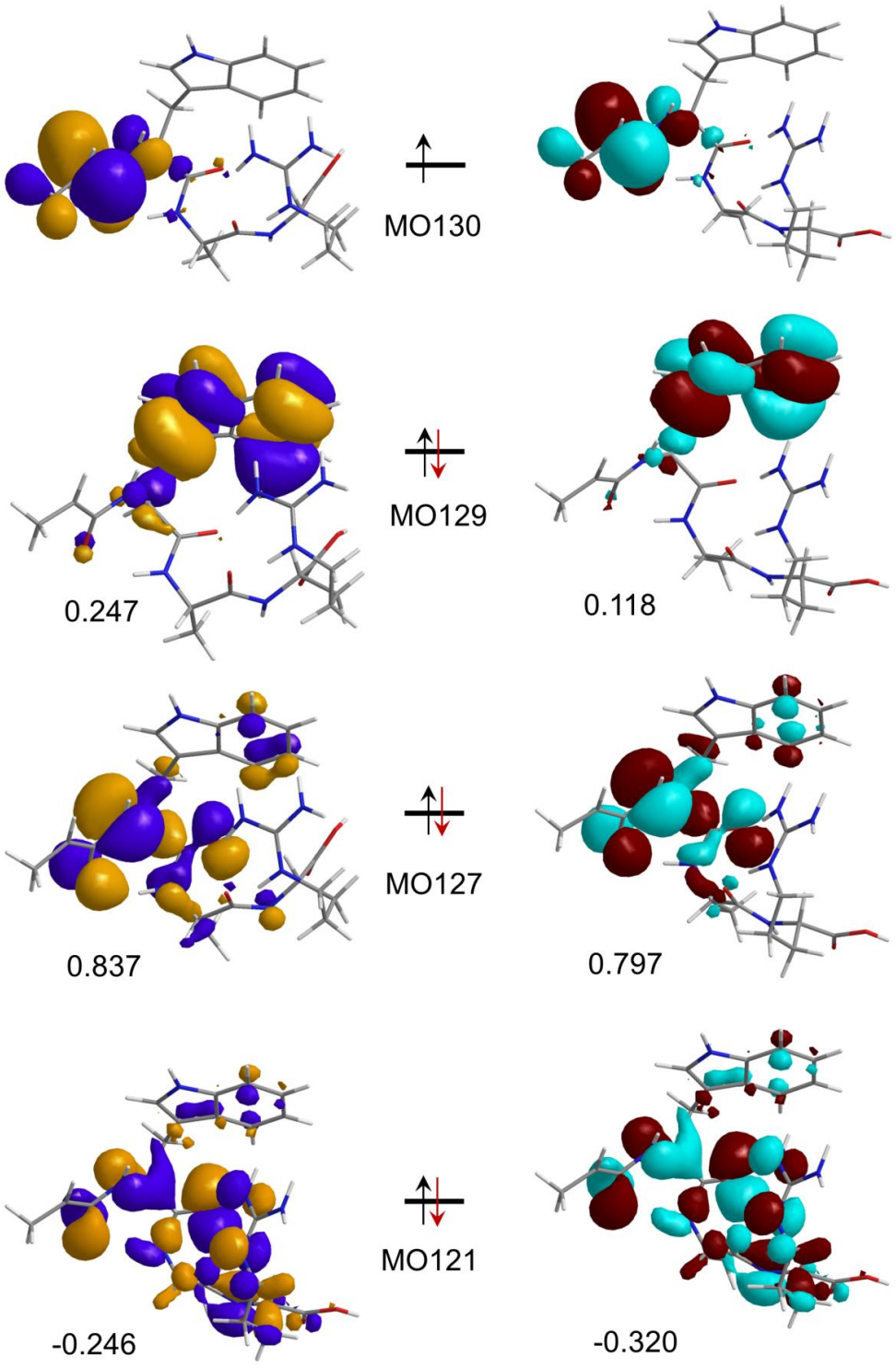

Figure 10. Molecular orbitals for the π → π electron excitation in **1a** from TD-DFT calculations. Left panel: M06-2X/6-311++G(2d,p) orbitals and transition vector amplitudes. Right panel: LC-BLYP/6-311++G(2d,p) orbitals and transition vector amplitudes.

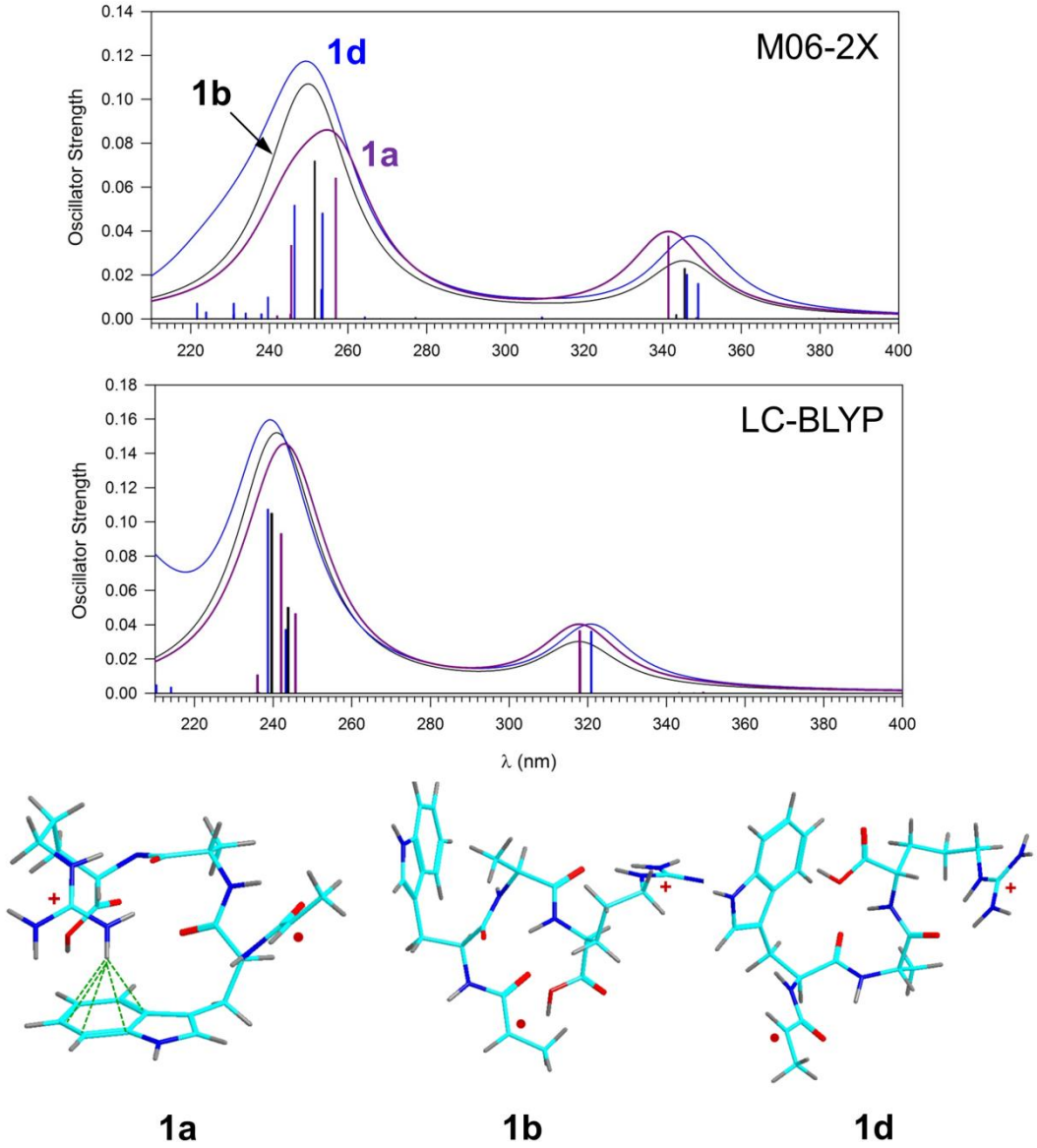

Figure 11. TD-DFT calculated absorption spectra of z_4($^{\bullet}$AWAR^{+}) conformers **1a**, **1b**, and **1d**.

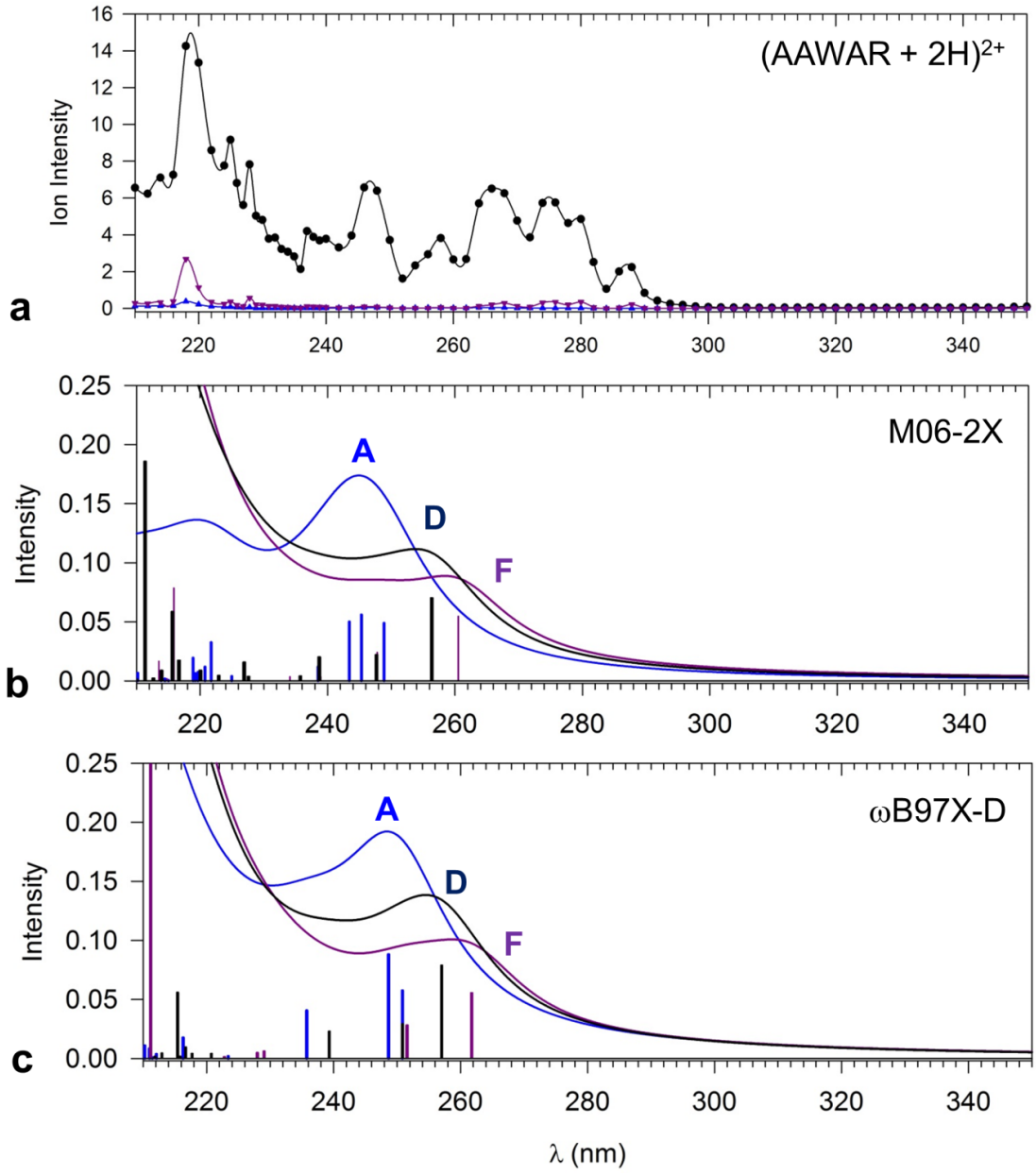

Figure 12. (a) UV Action spectrum of the $[AAWAR + 2H]^{2+}$ ion showing wavelength-dependent intensity profiles of the $\boldsymbol{y}_3^+$ (*m/z* 432, black), $\boldsymbol{a}_3^+$ (*m/z* 301, magenta), and $\boldsymbol{b}_3^+$ (*m/z* 329, blue) fragment ions. TD-DFT-calculated absorption spectra of $(AAWAR)^{2+}$ conformers **A**, **D**, and **F** using (b) M06-2X/6-311++G(2d,p) and (c) ωB97X-D/6-311++G(2d,p).

4. 3. 5 TD-DFT Analysis of AFAR Radical Isomers

The $z_4(^{\bullet}AFAR^+)$ ions differ from $z_4(^{\bullet}AWAR^+)$ in two aspects. First, none of the $z_4(^{\bullet}AFAR^+)$ positional isomers develops a hydrogen bond between the charged Arg^+ group and the Phe aromatic ring. Second, the Phe β-radical (**10a**) is unequivocally more stable than the *N*-terminal isomer **6a**, indicating that a reversible hydrogen atom migration between the Ala-1 C_α and Phe C_β positions would favor **10a**. The calculated absorption spectra of *N*-terminal $z_4(^{\bullet}AFAR^+)$ ions showed two major bands at 315-325 and 215-230 nm (Figure 4b) that were insensitive to the peptide radical conformation, as shown for conformers **6a** and **6b** (Figure 13). These conformers can account for the 351 and 240 nm bands in the action spectrum of the $z_4(^{\bullet}AFAR^+)$ ion. (Table 3 for relative energies) However, the other bands at 275 and 316 nm must be due to a different valence-bond isomer. The calculated TD-DFT spectra of the Phe β-radical **10a** (Figure 4f) display an intense band at 240-280 nm that fits the experimental band at 275 nm, and a weaker band at 280-305 nm that, when vibronically red-shifted, matches the 316 nm absorption in the action spectrum. However, the other AFAR C_α radicals **7a**-**9a** also absorb at 240-270 nm, and so the assignment of the minor isomers is ambiguous if based on the action spectrum alone. The weak band at 316 nm in the action spectrum can be assigned to **8a** which shows a strong absorption at 300-310 nm. Of note is the proportion of the positional isomers formed by ETD and generating the action spectrum. The long wavelength band of 6a is ca. 8-fold less intense than the 240-260 nm bands from **8a** and **10a**, yet it is well represented in the action spectrum. This implies that **1a** is a substantial component of the isomer mixture.

On a final note, the UV photodissociation of the z_4 ($^{\bullet}AWAR^+$) and z_4 ($^{\bullet}AFAR^+$) ions produced fragmentation patterns that were strikingly different from those by CID. For example, single-pulse UVPD at 355 nm chiefly formed $[y_n - 2H]^+$ even-electron fragment ions by amide

CO−NH bond cleavage, whereas CID gave rise to prominent $\boldsymbol{z_2}^{+\bullet}$ cation-radicals and their $\boldsymbol{x_2}^{+\bullet}$ precursors by C_α−CO bond cleavage[13] (cf. Figures 14 and 15). Both types of dissociation involve hydrogen atom migrations, Ala α-H and Phe β-H for the $[\boldsymbol{y_2} - 2H]^+$ and $\boldsymbol{z_2}^{+\bullet}$ ion formation, respectively (Scheme 1),[13] so entropy changes for reaching the respective transition states are likely to be similar. The benzylic β-H migration requires a lower transition-state energy than the α-H migration,[13,40] which is consistent with its predominance at threshold resonant excitations under slow-heating CID conditions. At the same time, the internal energy of the ETD-formed $\boldsymbol{z_4}$ ion[41] should be sufficient to initiate H-atom migrations. The threshold energy for the formation of the $\boldsymbol{z_2}^{+\bullet}$ fragment ions (<150 kJ mol^{-1})[13,40] is well within the range of photon energies in the 210-400 nm region. That the β-H migration-initiated reaction is *suppressed* upon UVPD implies that the UV-induced dissociations may not proceed on the vibrationally hot ground electronic state after vibronic conversion of the 3.5 eV energy from photon absorption. Rather, it appears that UVPD largely reflects specific photochemical, excited-state, dissociations occurring on the potential energy surface of electronic excited states of the peptide radicals. The nature of these dissociations and the pertinent reaction mechanisms are yet to be elucidated.

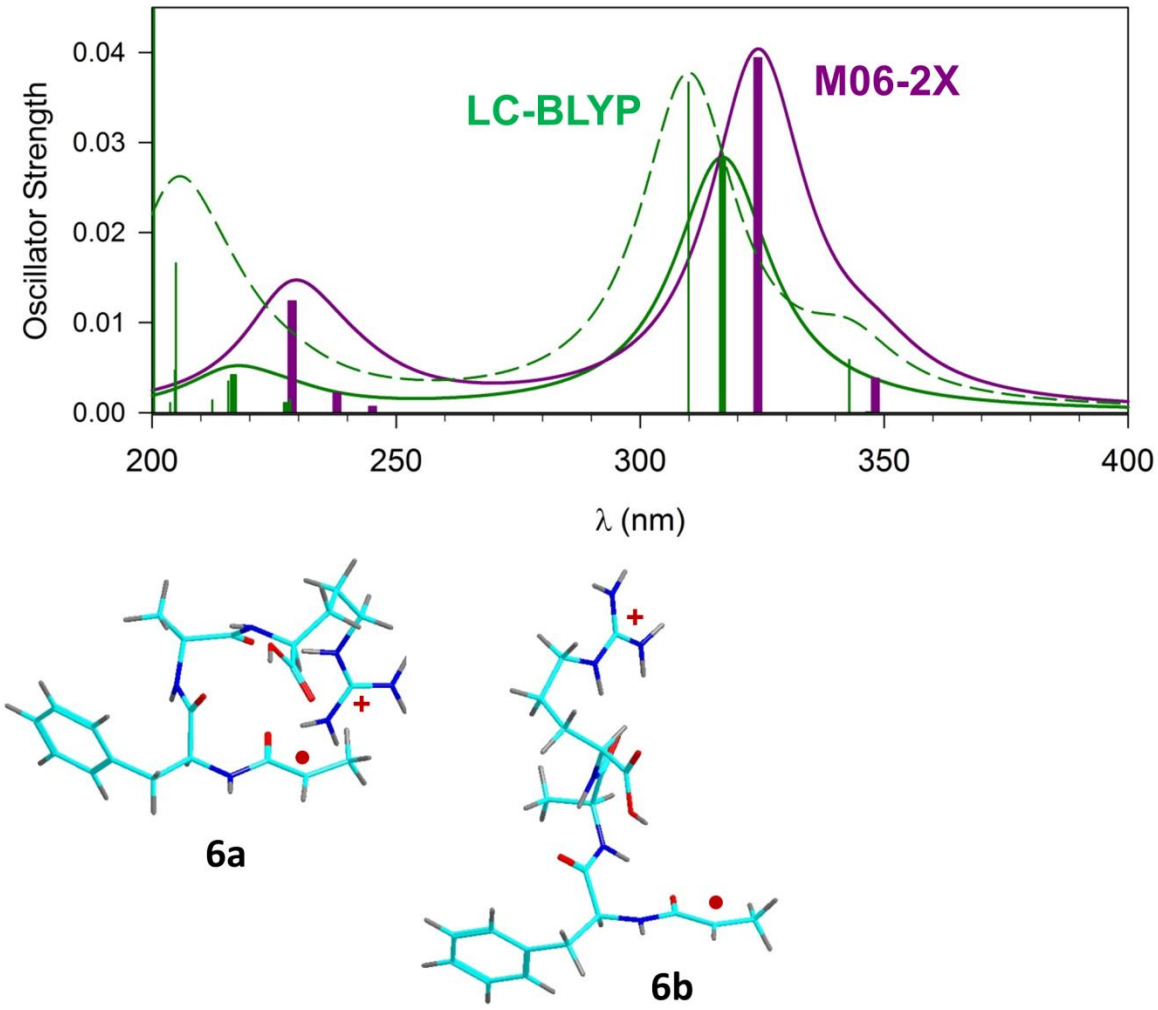

Figure 13. TD-DFT-calculated absorption spectra of z_4($^{\bullet}$AFAR^{+}) conformers **6a** (solid line) and **6b** (dashed line).

Table 2. Relative Energies of z_4($^{\bullet}$AFAR^{+}) Isomers.

	Relative Energy[a,b]				
Ion	B3LYP[c]	M06-2X[d]	ωB97X-D[c]	LC-BLYP[c]	ROMP2[c]
6a	0.0	0.0	0.0	0.0	0.0 (0.0)[e]
6b	5.8	-[x]	5.1	14	19 (19)
7	−8.4	1.1	−2.9	−1.5	−3.9 (−5.2)
8a	−34	−14	−21	−22	−16 (−14)
8b	−0.6	14	10	14	-
9a	−25	−56	−49	−34	−54 (−52)
9b	−32	−55	−44	−37	−46 (−45)
10a	−20	−4.0	−8.5	−16	−6.1 (−4.9)
10b	−12	28	2.8	−3.0	9.8 (11)

[a]In units of kJ mol^{-1}. [b]Including zero point energy corrections and referring to 0 K. [c]From single-point energy calculations with the 6-311++G(2d,p) basis set on B3LYP/6-31+G(d,p) optimized geometries. [d]From single-point energy calculations with the 6-311++G(2d,p) basis set on M06-2X/6-31+G(d,p) optimized geometries. [e]Spin-projected PMP2/6-311++G(2d,p) energies. [x]M06-2X/6-31+G(d,p) geometry optimizations converged to a single structure (**6a**).

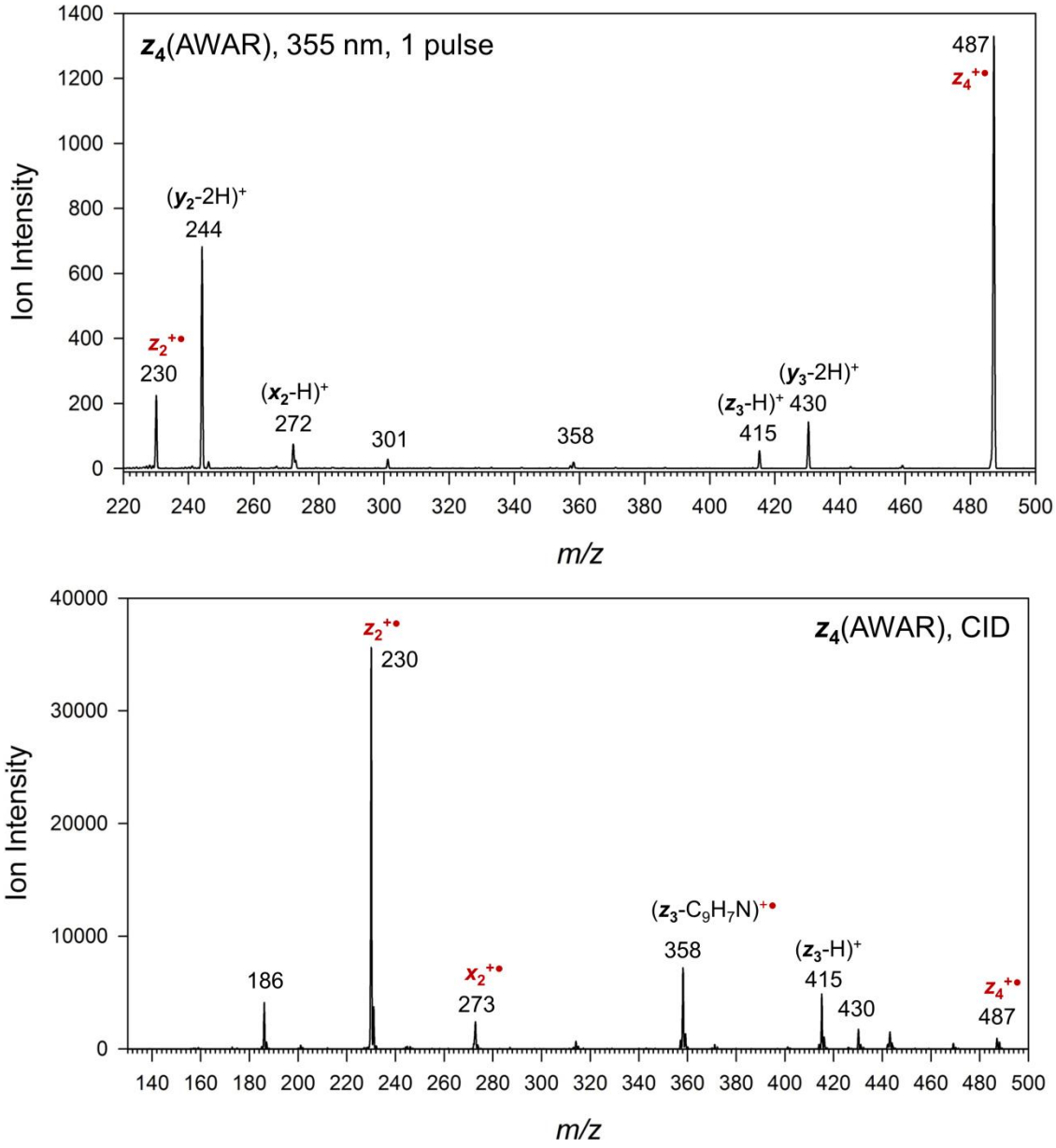

Figure 14. Single-pulse 355 nm UVPD (top) and CID (bottom) spectra of z_4(•AWAR$^+$) ions.

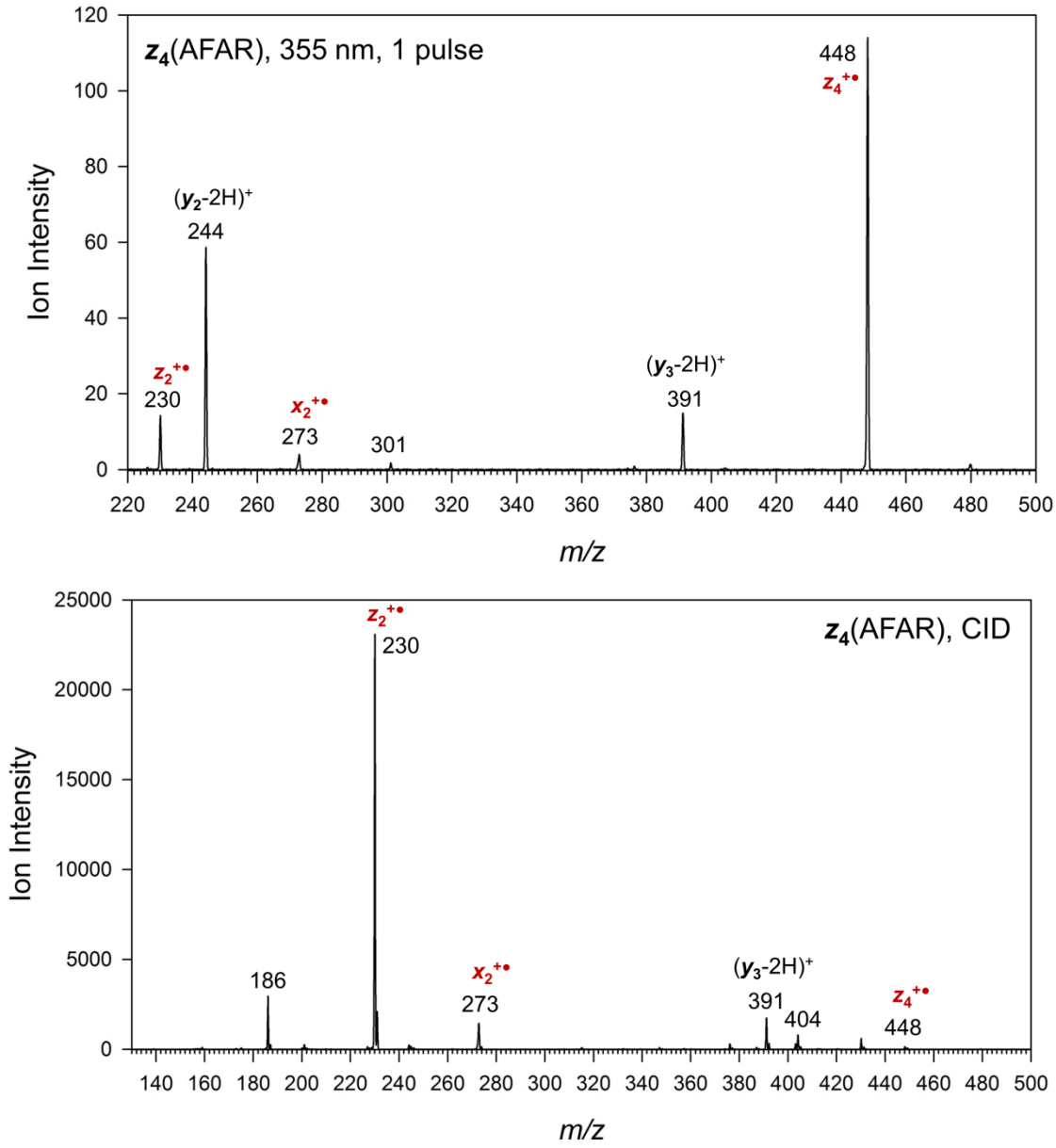

Figure 15. Single-pulse 355 nm UVPD (top) and CID (bottom) spectra of $z_4(^{\bullet}AFAR^{+})$ ions.

4. 4 Conclusions

UV action spectroscopy of peptide cation radicals of the ***z***-type generated by electron transfer dissociation points to the presence of more than one C_{α} radical species formed by spontaneous isomerizations by hydrogen atom migrations. *N*-terminal ***z***-ion radicals are identified as the main components among the produced ions, but the content of isomeric radicals depends on

the aromatic residues, with Phe giving a higher proportion of isomers than Trp. The extent of isomerization is consistent with the relative energies of isomeric radicals of the C_α and C_β type.

4. 5 References

1. Tureček, F.; Julian, R. R. Peptide Radicals and Cation-Radicals in the Gas Phase. *Chem. Rev.* **2013**, *113*, 6691-6733.
2. Stubbe, J.; van der Donk, W. A. Protein Radicals in Enzyme Catalysis. *Chem. Rev.* **1998**, *98*, 705-762.
3. Hawkins, C. L.; Davies, M. J. Generation and propagation of radical reactions on proteins. *Biochim. Biophys. Acta, Bioenerg.* **2001**, *1504*, 196-219.
4. Syka, J. E. P.; Coon, J. J.; Schroeder, M. J.; Shabanowitz, J.; Hunt, D. F. Peptide and Protein Sequence Analysis by Electron Transfer Dissociation Mass Spectrometry. *Proc. Natl. Acad. Sci. U. S. A.* **2004**, *101*, 9528-9533.
5. Ly, T.; Julian, R. R. Ultraviolet Photodissociation: Developments towards Applications for Mass-Spectrometry-Based Proteomics. *Angew. Chemie, Int. Ed.* **2009**, *48*, 7130-7137.
6. Hodyss R.; Cox H. A; Beauchamp J. L. Bioconjugates for tunable peptide fragmentation: free radical initiated peptide sequencing (FRIPS). *J. Am. Chem. Soc.* **2005**, *127*, 12436-7.
7. Oh, H. B.; Moon, B. Radical-driven peptide backbone dissociation tandem mass spectrometry. *Mass Spectrom. Rev.* **2015**, *34*, 116-132.
8. Chu, I. K.; Rodriquez, C. F.; Lau, T.-C.; Hopkinson, A. C.; Siu, K. W. M. Molecular Radical Cations of Oligopeptides. *J. Phys. Chem. B* **2000**, *104*, 3393-3397.
9. Barlow, C. K.; Wright, A.; Easton, C. J.; O'Hair, R. A. J. Gas-phase ion-molecule reactions using regioselectively generated radical cations to model oxidative damage and probe radical sites in peptides. *Org. Biomol. Chem.* **2011**, 9, 3733-3745.

10. Radom, L.; Bouma, W. J.; Nobes, R. H.; Yates, B. F. A Theoretical Approach to Gas-Phase Ion Chemistry. *Pure Appl. Chem.* **1984**, *56*, 1831-1842.
11. Hammerum, S. Distonic Radical cations in Gaseous and Condensed Phase. *Mass Spectrom. Rev.* **1988**, *7*, 123-202.
12. Zubarev, R. A.; Horn, D. M.; Fridriksson, E. K.; Kelleher, N. L.; Kruger, N. A.; Lewis, M. A.; Carpenter, B. K.; McLafferty, F. W. Electron Capture Dissociation for Structural Characterization of Multiply Charged Protein Cations. *Anal. Chem.* **2000**, *72*, 563-573.
13. Ledvina, A. R.; Chung, T. W.; Hui, R.; Coon, J. J.; Tureček, F. Cascade Dissociations of Peptide Cation-Radicals. Part 2. Infrared Multiphoton Dissociation and Mechanistic Studies of z-Ions from Pentapeptides. *J. Am. Soc. Mass Spectrom.* **2012**, *23*, 1351-1363.
14. Chu, I. K.; Zhao, J.; Xu, M.; Siu, S. O.; Hopkinson, A. C.; Siu, K. W. M. Are the Radical Centers in Peptide Radical Cations Mobile? The Generation, Tautomerism, and Dissociation of Isomeric α-Carbon-Centered Triglycine Tadical Cations in the Gas Phase. *J. Am. Chem. Soc.* **2008**, *130*, 7862-7872.
15. Shaffer, C. J.; Marek, A.; Pepin, R.; Slováková, K.; Tureček, F. Combining UV Photodissociation with Electron Transfer for Peptide Structure Analysis. *J. Mass. Spectrom.* **2015**, *50*, 470-475.
16. Brodbelt, J. S. Photodissociation Mass Spectrometry: New Tools for Characterization of Biological Molecules. *Chem. Soc. Rev.* **2014**, *43*, 2757-2783.
17. Reilly, J. P. Ultraviolet Photofragmentation of Biomolecular Ions. *Mass Spectrom. Rev.* **2009**, *28*, 425-447.

18. Byskov, C. S.; Jensen, F.; Joergensen, T. J. D.; Nielsen, S. B. On the Photostability of Peptides after Selective Photoexcitation of the Backbone: Prompt versus Slow Dissociation. *Phys. Chem. Chem. Phys.* **2014**, *16*, 15831-15838.
19. J. M. Janz, Y. Ren, R. Looby, M. A. Kazmi, P. Sachdev, A. Grunbeck, L. Haggis, D. Chinnapen, A. Y. Lin, C. Seibert, T. McMurry, K. E. Carlson, T. W. Muir, S. Hunt, T. P. Sakmar, *J. Am. Chem. Soc.* **2011**, *133*, 15878-15881.
20. J. Coste, D. LeNguyen, B. Castro, *Tetrahedron Lett.* **1990**, *31*, 205-208.
21. Nguyen, H. T. H.; Shaffer, C. J.; Tureček, F. *J. Phys. Chem. B* **2015**, *119*, 3948-3961.
22. C. J. Shaffer, A. Marek, R. Pepin, K. Slováková, F. Tureček, *J. Mass Spectrom.* **2015**, *50*, 470-475.
23. M. J. Frisch, G. W. Trucks, H. B. Schlegel, G. E. Scuseria, M. A. Robb, J. R. Cheeseman, G. Scalmani, V. Barone, B. Mennucci, G. A. Petersson, et al. Gaussian 09, Revision A.02; Gaussian, Inc.: Wallingford, CT, 2009.
24. A. D. Becke, *J. Chem. Phys.* **1993**, *98*, 1372−1377.
25. Y. Zhao, D. G. Truhlar, *Theor. Chem. Acc.* **2008**, *120*, 215−241.
26. F. Furche, A. Ahlrichs, *J. Chem. Phys.* **2002**, *117*, 7433-7447.
27. H. Iikura, T. Tsuneda, T. Yanai, K. Hirao, *J. Chem. Phys.* **2001**, *115*, 3540-3544.
28. J. D. Chai, M. Head-Gordon, *Phys. Chem. Chem. Phys.* **2008**, *10*, 6615-6620.
29. Møller, C.; Plesset, M. S. *Phys. Rev.* **1934**, *46*, 618-622.

30. Zhao, Y.; Truhlar, D. G. The M06 Suite of Density Functionals for Main Group Thermochemistry, Thermochemical Kinetics, Noncovalent Interactions, Excited States, and Transition Elements: Two New Functionals and Systematic Testing of Four M06-Class Functionals and 12 Other Functionals. *Theor. Chem. Acc.* **2008**, *120*, 215−241.
31. Iikura, H.; Tsuneda, T.; Yanai, T.; Hirao, K.: A Long-Range Correction Scheme for Generalized-Gradient-Approximation Exchange Functionals. *J. Chem. Phys.* **2001**, *115*, 3540-3544.
32. Chai, J. D.; Head-Gordon, M. Long-Range Corrected Hybrid Density Functionals with Damped Atom-Atom Dispersion Corrections. *Phys. Chem. Chem. Phys.* **2008**, *10*, 6615-6620.
33. Turecek, F. Benchmarking Electronic Excitation Energies and Transitions in Peptide Radicals. *J. Phys. Chem. A* **2015**, 10101-10111.
34. Mitchell, J. B. O.; Nandi, C. L.; McDonald, I. K.; Thornton, J. M. Amino/Aromatic Interactions in Proteins: Is the Evidence Stacked Against Hydrogen Bonding? *J. Mol. Biol.* **1994**, *239*, 315-331.
35. Steiner, T.; Koellner, G. Hydrogen Bonds with □-Acceptors in Proteins: Frequencies and Role in Stabilizing Local 3D Structures. *J. Mol. Biol.* **2001**, *305*, 535-557.
36. Chakrabarti, P.; Bhattacharya, R. Geometry of Nonbonded Interactions Involving Planar Groups in Proteins. *Prog. Biophys. Mol. Biol.* **2007**, *95*, 830-137.
37. Barbatti, M.; Aquino, A. J, A.; Lischka, H. The UV Absorption of Nucleobases: Semi-Classical an Initio Spectra Simulations. *Phys. Chem. Chem. Phys.* **2010**, *12*, 4959-4967.
38. Polfer, N. C. Infrared Multiple Photon Dissociation Spectroscopy of Trapped Ions. *Chem. Soc. Rev.* **2011**, *40*, 2211-2221.

39. Polfer, N. C.; Dugourd, P., Eds. *Laser Photodissociation and Spectroscopy of Mass-Separated Biomolecules*. Lecture Notes in Chemistry 83, Chapter 4, pp 78-81; Springer: Heidelberg, 2013.

40. Ledvina, A. R.; Coon, J. J.; Tureček, F. Competitive Hydrogen Atom Migrations Accompanying Cascade Dissociations of Peptide Cation-Radicals of the $\boldsymbol{z}^{+\bullet}$ Type. *Int. J. Mass Spectrom.* **2015**, *377*, 44-53.

41. Pepin, R.; Turecek, F. Kinetic Ion Thermometers for Electron Transfer Dissociation. *J. Phys. Chem. B*, **2015**, *119*, 2818-2826.

Chapter 5:

Radical Reactions Affecting Polar Groups in Threonine Peptide Ions

Reproduced with permission from Nguyen, H. T., Andrikopoulos, P. C., Bim, D., Rulisek, L., Dang, A., & Turecek, F. (2017). Radical reactions affecting polar groups in threonine peptide ions. *The Journal of Physical Chemistry B, 121*(27), 6557-6569.

Abstract: Peptide cation-radicals containing the threonine residue undergo radical-induced dissociations upon collisional activation and photon absorption in the 210-400 nm range. Peptide cation-radicals containing a radical defect at the *N*-terminal residue, $[^{\bullet}$Ala-Thr-Ala-Arg+H$]^+$, were generated by electron transfer dissociation (ETD) of peptide dications and characterized by UV-VIS photodissociation action spectroscopy combined with time-dependent density functional theory (TD-DFT) calculations of absorption spectra, including thermal vibronic band broadening. The action spectrum of $[^{\bullet}$Ala-Thr-Ala-Arg+H$]^+$ ions was indicative of the canonical structure of an *N*-terminally deaminated radical whereas isomeric structures differing in the position of the radical defect and amide bond geometry were excluded. This indicated that exothermic electron transfer to threonine peptide ions did not induce radical isomerizations in the fragment cation-radicals. Several isomeric structures, ion-molecule complexes, and transition states for isomerizations and dissociations were generated and analyzed by DFT and Møller-Plesset perturbational ab initio calculations to aid interpretation of the major dissociations by loss of water, hydroxyl radical, $C_3H_6NO^{\bullet}$, C_3H_7NO, and backbone cleavages. Born-Oppenheimer molecular dynamics (BOMD) in combination with DFT gradient geometry optimizations and intrinsic reaction coordinate analysis were used to search for low-energy cation-radical conformers and transition states. BOMD was also employed to analyze the reaction trajectory for loss of water from ion-molecule complexes.

5.1 Introduction

Whereas most peptide and protein chemical reactions involve polar groups with closed electronic shells, there is a growing cohort of biological reactions that are known to proceed via radical intermediates. For example, radical intermediates play a role in several redox enzyme reactions,[1-8] and most recently, a glycyl radical enzyme has been found to metabolize hydroxyproline in human gut microbiome.[9] Peptide and protein radicals can be formed by hydrogen abstraction or oxidative processes involving reactive radical species or transition metals that affect, respectively, the C_α-H bonds of the backbone or oxidation-prone side chains, such as those in cysteine, tyrosine and tryptophan.[10] Peptide-related radicals have received considerable attention regarding their thermodynamic stability and its relationship to the backbone conformation.[11-15] Recently, methods have been developed to generate peptide radicals as isolated species in the gas phase using electron transfer reactions and mass spectrometric product analysis. One of these methods, introduced by Siu and coworkers,[16] uses oxidative intramolecular electron transfer in ternary transition metal-peptide ion complexes[17,18] in the gas phase to produce peptide cation-radicals that are stochiometrically equivalent to neutral peptide molecules and do not contain additional charging protons.[19] These so-called hydrogen-deficient peptide cation radicals are isolated by mass and studied by methods of gas-phase ion chemistry. For example, structures of hydrogen-deficient peptide cation radicals have been studied by multiphoton infrared photodissociation action spectroscopy (IRMPD)[20] and UV-VIS photodissociation action spectroscopy.[21,22] A different type of peptide cation radicals are produced by one-electron reduction of multiply protonated peptide ions.[19] Such peptide radicals are called hydrogen-rich[23] and often occur as short-lived reaction intermediates that dissociate by backbone and side-chain cleavages. Peptide cation-radical dissociations have been extensively utilized for protein sequence

analysis by electron capture[24] and electron transfer dissociation[25] methods of tandem mass spectrometry, and determining the structure and electronic properties of peptide cation-radicals and their dissociation products has been of considerable interest.[19]

Cleavage of backbone bonds between the amide nitrogen and the adjacent alpha carbon of the same residue (N−C_α bond cleavage) is a common radical-triggered dissociation in hydrogen-rich protein and peptide cation radicals.[19] These cleavages produce cation-radicals corresponding to deaminated and truncated C-terminal peptide fragments which are called $[z_n+H]^{+\bullet}$ ions (Scheme 1).[26] These ions typify unusual structures called distonic ions,[27,28] in which the radical and ion sites reside on different and distant atoms. In addition to being of theoretical interest because of their unusual structures, ions of the $[z_n+H]^{+\bullet}$ type have also attracted considerable attention because they retain information on the peptide fragment's amino acid sequence that can be further mined by tandem mass spectrometry via consecutive radical backbone dissociations.[29-33] A particularly important question in this respect is whether the $[z_n+H]^{+\bullet}$ ions retain their canonical structure related to the original peptide ion or undergo radical-driven molecular rearrangements.

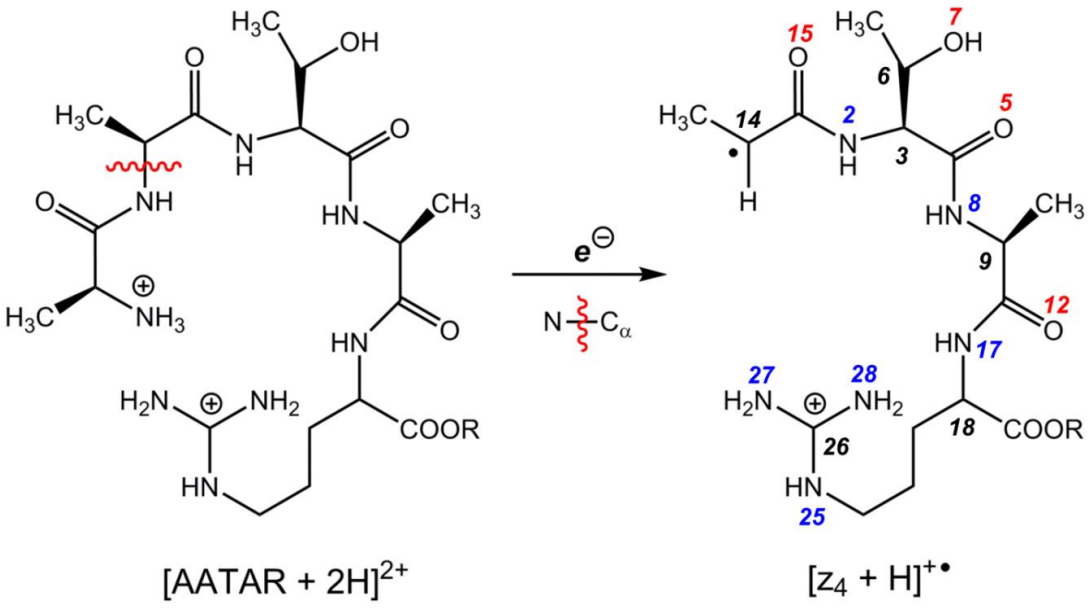

Scheme 1. Formation of $[z_4+H]^{+\bullet}$ ions from $[AATAR+2H]^{2+}$.

To address these questions, structures of hydrogen-rich peptide cation radicals in the gas phase have been recently studied by UV-VIS action spectroscopy,[34] and several $[z_n+H]^{+\bullet}$ ions have been studied by UVPD[21] and IRMPD.[20] Action spectroscopy is a photodissociative method in which resonant absorption of one or multiple photons by a gas-phase ion triggers dissociation ("action") that is detected by mass spectrometry.[35,36] These studies, that so far have been limited to Asp, Phe, Trp, and His, have revealed that the propensity for spontaneous isomerization of $[z_n+H]^{+\bullet}$ ions depended on the amino acid residues in the ion.[20,21] In addition to recent spectroscopic studies, $[z_n+H]^{+\bullet}$ ions have been the subject of investigations that focused on elucidating the collision-induced dissociation mechanisms, kinetics, and characterizing dissociation products. Both survey[37,38] and mechanistic studies[39,40] have been reported that addressed the competition between backbone and side-chain dissociations in peptide cation-radicals, depending on the nature and sequence of amino acid residues. In particular, the complex chemistry of serine-containing peptide cation radicals has been addressed by studies that pointed out competitive dissociations involving the backbone and side chain groups.[41,42]

Previous mechanistic studies of peptide cation-radical chemistry have been aided by ab initio and density functional theory calculations of ion structures, transition states, and UV-VIS absorption spectra. Theoretical calculations of gas-phase peptide ion structures are notoriously difficult because of the multitude of tautomers and conformers that have to be considered to adequately describe the potential energy surface.[43] This is further emphasized in computational studies of transition states for peptide ion dissociations where small changes of energy can have large effects on the calculated unimolecular rate constants and branching ratios.[42] It is therefore important to anchor the calculations to experimental data obtained by spectroscopy or ion mobility measurements.[43] Here, we combine experimental action spectroscopy and computational methods

to elucidate the structure, reaction mechanisms, and dynamics of dissociations of $[z_4+H]^{+\bullet}$ ions containing the polar threonine residue. As models we chose *N*-terminally deaminated tryptic cation radicals $(^{\bullet}$Ala-Thr-Ala-Arg+H$)^+$ and $(^{\bullet}$Ala-Thr-Ala-Arg-OCH_3+H$)^+$ in which the charging proton is sequestered at the arginine residue, thus removing the ambiguity of locating the charge site. The C-terminal methyl ester was used to distinguish the threonine side-chain and terminal carboxyl hydroxyl groups.

The chapter is organized as follows. First we present and analyze unimolecular dissociations of $[z_4+H]^{+\bullet}$ ions containing Thr. Next, we present spectroscopic evidence of the $[z_4+H]^{+\bullet}$ ion structure. Finally, we use density functional theory (DFT) and Born-Oppenheimer molecular dynamics (BOMD) calculations to analyze the energetics and dynamics of isomerizations and dissociations triggered by collisional activation. We wish to show that the threonine residue does not promote spontaneous isomerizations in the $[z_4+H]^{+\bullet}$ ions formed by electron transfer dissociation. Upon collisional activation and photodissociation, the side chain substantially participates in radical reactions that characterize the threonine residue for peptide sequencing by mass spectrometry.

5. 2 Experimental Section

5. 2. 1 Materials

The Ala-Ala-Thr-Ala-Arg (AATAR) peptide was custom-synthesized at >90% purity by GenScript (Piscataway, NJ, USA), and the received sample was checked by electrospray ionization mass spectrometry. The amino acid sequence was checked by an electron-transfer dissociation (ETD) mass spectrum that showed the expected sequence fragment ions of the $[z_n+H]^{+\bullet}$ type

(Figure 1a). The AATAR methyl ester was prepared by esterification of AATAR in anhydrous methanol, as described previously,[44] and characterized by its ETD mass spectrum (Figure 1b).

5. 2. 2 Methods

ETD mass spectra and photodissociation action (UVPD) spectra were measured on a ThermoElectron Fisher (San Jose, CA, USA) LTQ-XL-ETD linear ion trap mass spectrometer equipped with an external EKSPLA NL301G (Altos Photonics, Bozeman, MT) Nd-YAG laser source operating at a frequency of 20 Hz with a 3–6 ns pulse width, as described previously.[21] The pump laser was interfaced to the LTQ via LabView software (National Instruments, Austin, TX). Briefly, photons from the pump were directed into a PG142C unit (Altos Photonics) consisting of a third harmonic generator and optical parametric oscillator coupled with an optional second harmonic generator, that provided wavelength tuning between 210–700 nm at 0.52–12.69 mJ per pulse. The power of the PG142C output beam was measured at each wavelength using an EnergyMax-USB J-10MB energy sensor (Coherent Inc., Santa Clara, CA). The PG142C output beam was focused into the ion trap. The typical experimental setup consisted of electrospraying the peptide solution into the mass spectrometer, isolating the doubly charged ion in the ion trap, and performing ETD at 100-200 ms ion-ion reaction time to produce the desired cation-radical. The fragment cation radical was isolated by mass and subjected to photoactivation from 210–400 nm. The intensities of the resulting UVPD MS^3 photo-fragments were monitored as a function of wavelength, and their final intensities were normalized to the laser output power to plot the action spectra. The number of laser pulses used during each isolation depended on the photo-dissociation yield at each given wavelength, and ranged from 1 to 19 pulses, corresponding to 100–1000 ms activation time, respectively, with each successive pulse spaced by 50 ms.

5. 2. 3 Calculations

Standard ab initio and density functional theory (DFT) calculations were performed with the Gaussian 09 suite of programs.[45] Ion geometries were optimized using the hybrid B3LYP[46,47] functional and the 6-31+G(d,p) basis set in a spin-unrestricted formalism (UB3LYP). Local energy minima and first-order saddle points (transition states) were characterized by harmonic frequency analysis as having the appropriate number of imaginary frequencies (0 and 1, respectively). The structures were used for UB3LYP and Moller-Plesset[48] [UMP2(frozen core)] single-point energy calculations with the 6-311++G(2d,p) basis set. The MP2 energies were corrected by annihilation of higher spin states[49,50] to provide spin-projected (PMP2) energies. In other sets of calculations, B3LYP geometries were used as initial guesses for gradient optimizations with the hybrid ωB97X-D[51,52] and M06-2X[53] methods using the 6-31+G(d,p) basis set, and the obtained optimized geometries were used for single-point energy calculations with the 6-311++G(2d,p) basis set. The calculated energies are given in Table 1. DFT calculations of peptide ion relative energies using different hybrid functionals have been reported to show a divergent trend.[43] Moreover, hybrid functionals including dispersion interactions are necessary for calculations of ion-molecule complexes. To treat a range of peptide cation-radical structures, transition states, and dissociation products, it is desirable to use a variety of computational methods to obtain consensus and identify outliers.

Potential energy surface mapping was performed by Born-Oppenheimer Molecular Dynamics (BOMD) calculations using the semiempirical PM6 method[54] supplemented with dispersion corrections[55], PM6-D3H4. These calculations were run by MOPAC[56] under the Cuby4 platform which acts as the high-level interface.[57] The typical MD run involved a total of 100 ps with a 1 fs time step with the thermostat set at 520 K to sample the conformational space of each

ion. This corresponded to approximately 180 kJ mol^{-1} internal (ro-vibrational) energy which was considered sufficient for breaking and reforming hydrogen bonding interactions in the cation radicals. Two thousand five hundred snapshots were obtained and subsequently optimized with PM6-D3H4, and 11-20 best representative structures were treated with DFT as described above. Excited-state calculations were performed using time-dependent DFT[58] with M06-2X, ωB97X-D, and LC-BLYP[59] functionals and the 6-31+G(d,p) basis set. Previous benchmarking of peptide radical excitation energies[60] identified TD-DFT with the ωB97X-D functional as giving the closest match to high-level equation-of-motion CCSD calculations,[61,62] and therefore ωB97X-D was used throughout this work to interpret the experimental data. TD-DFT calculations with the 6-31+G(d,p) and 6-311++G(2d,p) basis sets showed closely similar excitation energies and absorption wavelengths, as illustrated by the root-mean-square deviation for the *trans*-amide $[^{\bullet}ATAR+H]^{+}$ ion *trans*-**1**, giving rmsd = 2.2 nm for lines in the 200-400 nm region. Therefore, the smaller 6-31+G(d,p) basis set was used throughout for TD-DFT excited-state calculations. Vibronically broadened spectra were generated with Newton-Xspace (version 1.4, www.newtonx.org),[63,64] program. Optimized Cartesian atomic coordinates and harmonic frequencies obtained with B3LYP/6–31+G(d,p) were used to generate random configurations that were weighted according to their Boltzmann factors at 300 K. A total of 12 excited electronic states produced by TD-DFT with ωB97X-D/6-31+G(d,p) and 500 configurations were used to produce the spectrum.

Rice-Ramsperger-Kassel-Marcus (RRKM) calculations[65] were performed using the QCPE program of Zhu and Hase[66] that was recompiled for Windows.[67] Unimolecular rate constants were obtained by direct count of quantum states. Rotational states were treated adiabatically and the RRKM microcanonical rate constants were Boltzmann-averaged for the experimental temperature.

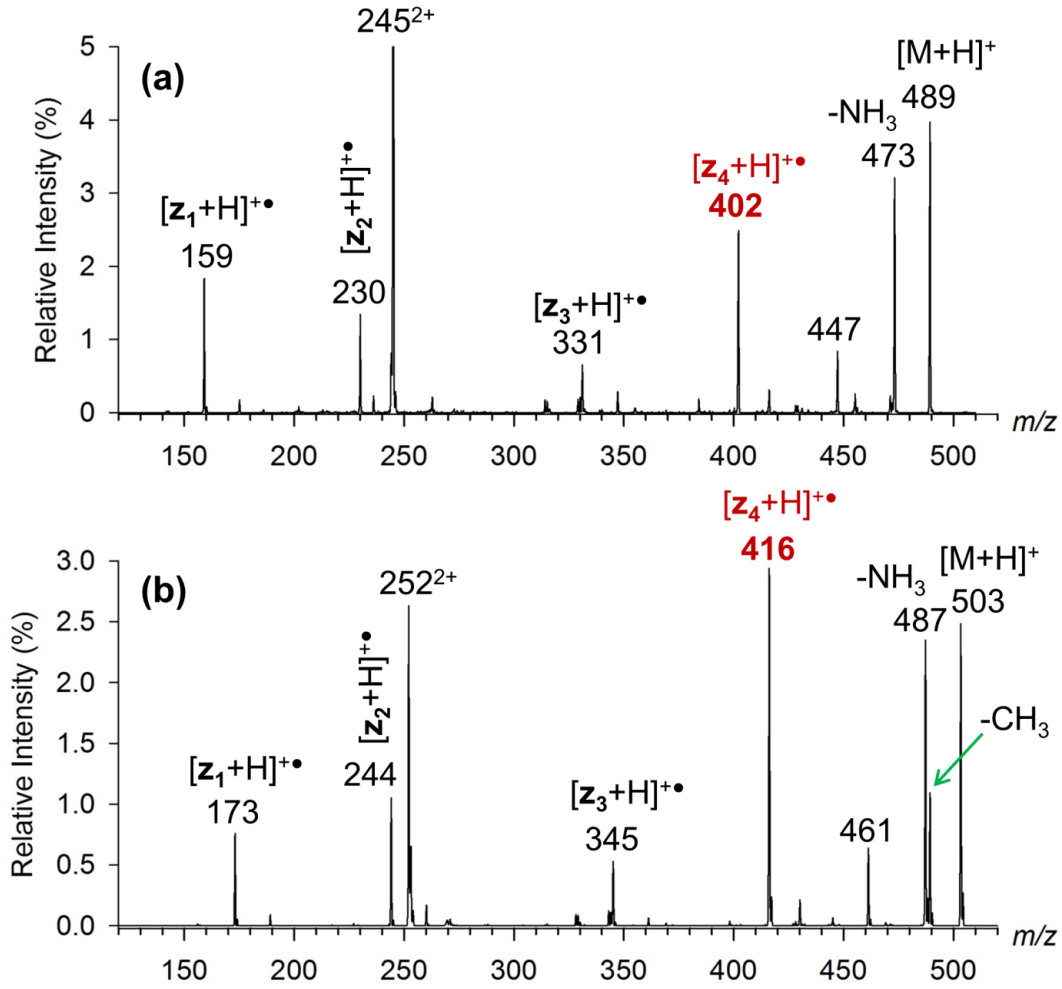

Figure 1. Electron-transfer-dissociation (ETD) mass spectra of (a) $[AATAR+2H]^{2+}$ and (b) $[AATAR\text{-}OCH_3+2H]^{2+}$ions. Both spectra were obtained on an LTQ-XL-ETD linear ion trap mass spectrometer by 200 ms ion-ion reaction with fluoranthene anion-radical.

Table 1. Total and Zero-Point Energies of [•ATAR+H]$^+$ Ions.

	Energy (hartree)							
Ion	B3LYP[a] 6-31+G(d,p)	ZPVE[a] (kJ mol^{-1})	B3LYP[b] 6-311++G(2d,p)	UMP2/PMP2[b] 6-311++G(2d,p)	M06-2X[c] 6-31+G(d,p)	M06-2X[d] 6-311++G(2d,p)	ωB97X-D[e] 6-31+G(d,p)	ωB97X-D[f] 6-311++G(2d,p)
trans-**1**	-1407.602831	1287	-1407.953793	-1404.364888 -1404.367625	-1407.007841	-1407.387254	-1407.197066	-1407.530772
cis-**1**	-1407.597958	1288.6	-1407.948647	-1404.357693 -1404.36061	-1407.001775	-1407.381025	-1407.192323	-1407.525897
trans-**2**	-1407.603659	1289.2	-1407.954461	-1404.361701 -1404.365452	-1407.006976	-1407.386000	-1407.197172	-1407.530672
cis-**2**	-1407.594669	1290.4	-1407.945712	-1404.352299 -1404.355496	-1406.999549	-1407.379214	-1407.191655	-1407.525871
trans-**3**	-1407.597153	1287.7	-1407.948468	-1404.360649 -1404.363716	-1407.005576	-1407.384977	-1407.194593	-1407.528476
trans-**4**	-1407.608037	1289.9	-1407.958919	-1404.368429 -1404.373712	-1407.013219	-1407.39256	-1407.202168	-1407.535699
trans-**5**	-1407.601191	1287.2	-1407.952633	-1404.362995 -1404.365083	-1407.004602	-1407.384389	-1407.195517	-1407.529514
cis-**5**	-1407.58245	1286.45	-1407.934042	-1404.346267 -1404.348487	-1406.991283	-1407.371605	-1407.183355	-1407.517969
6	-1407.565907	1285.5	-1407.916557	-1404.329039 -1404.331841	-1406.971795	-1407.351054	-1407.160811	-1407.494378
7	-1407.572845	1271.8	-1407.926538	-1404.313858 -1404.316792	-1406.961505	-1407.344053	-1407.153527	-1407.489643
8	-1407.613000	1274.3	-1407.965941	-1404.354219 -1404.356797	-1407.002347	-1407.383536	-1407.193909	-1407.528874
9	-1407.626741	1281.5	-1407.978893	-1404.3626 -1404.373512	-1407.016625	-1407.396878	-1407.210286	-1407.545245
10a	-1407.589816	1279.4	-1407.943433	-1404.333128 -1404.335233	-1406.974699	-1407.356611	-1407.164118	-1407.500386
10b	-1407.602504	1278.4	-1407.955376	-1404.347624 -1404.349726	-1406.987495	-1407.368951	-1407.180598	-1407.515895
11a	-1407.558326	1278.4	-1407.905188	-1404.307944 -1404.309705	-1406.957351	-1407.337750	-1407.146652	-1407.481970
11g	-1407.618468	1282.5	-1407.97098,	-[g]	-1407.015854	-1407.396447	-1407.20725	-1407.542094
12	-1407.556748	1273.7	-1407.910081	-1404.313386 -1404.315398	-1406.955394	-1407.337205	-1407.136348	-1407.472877
TS1	-1407.569353	1283.5	-1407.919873	-1404.31907 -1404.329065	-1406.971505	-1407.351981	-[h]	
TS2	-1407.544379	1275.1	-1407.89474	-1404.306701 -1404.312918	-1406.947799	-1407.326954	-1407.141712	-1407.475315
TS3	-1407.568282	1285.4	-1407.919644	-1404.326119 -1404.32931	-1406.96902	-1407.349152	-[h]	
TS4	-1407.553858	1275.5	-1407.904779	-1404.316523 -1404.322633	-1406.960813	-1407.34007	-1407.154525	-1407.488447
TS5	-1407.562318	1281.6	-1407.914863	-1404.320555 -1404.322695	-1406.960098	-1407.34178	-[h]	
TS6	-1407.563001	1278.4	-1407.916072	-1404.298165 -1404.312764	-1406.954349	-1407.336093	-1407.147854	-1407.48384
TS7	-1407.566084	1279.6	-1407.919021	-1404.308247 -1404.323791	-1406.962852	-1407.344006	-1407.151267	-1407.4868
TS8	-1407.551255	1280.1	-1407.903523	-1404.287437 -1404.301166	-1406.946855	-1407.327153	-1407.138372	-1407.473760
TS9	-1407.548047	1275.0	-1407.900731	-1404.289377 -1404.302824	-1406.947107	-1407.328115	-1407.135429	-1407.471027

[a]UB3LYP/6-31+G(d,p) optimized structures. [b]Single-point energies on UB3LYP/6-31+G(d,p) optimized structures. [c]UM06-2X/6-31+G(d,p) optimized structures. [d]Single-point energies on UM06-2X/6-31+G(d,p) optimized structures. [e]UωB97X-D/6-31+G(d,p) optimized structures. [f]Single-point energies on UωB97X-D/6-31+G(d,p) optimized structures. [g]The UMP2 calculations failed to converge. [h]UωB97X-D/6-31+G(d,p) optimizations of TS for the amide rotations were not run.

5. 3 Results and Discussion

5. 3. 1 Cation-Radical Formation and Dissociations

The $[z_4+H]^{+\bullet}$ ions corresponding to $[^{\bullet}ATAR+H]^+$ and $[^{\bullet}ATAR\text{-}OCH_3+H]^+$ amino acid sequences (Scheme 1, R= H, CH_3) were generated by the following standard procedure. Doubly-protonated peptides, $(AATAR+2H)^{2+}$ and $(AATAR\text{-}OCH_3+2H)^{2+}$, respectively, were produced by electrospray ionization from aqueous-methanol solutions, the ions were mass-selected and stored in the linear quadrupole ion trap. An ion-ion reaction with fluoranthene anions of the trapped peptide dications resulted in electron transfer dissociation forming a series of $[z_n+H]^{+\bullet}$ ions shown in Figure 1a,b. The $[z_4+H]^{+\bullet}$ ions, *m/z* 402 and *m/z* 416 for $[^{\bullet}ATAR+H]^+$ and $[^{\bullet}ATAR\text{-}OCH_3+H]^+$, respectively, were isolated by mass and further probed by collisional activation and photodissociation. Collision-induced dissociation (CID) of trapped ions proceeds by incremental vibrational excitation which is essentially a thermal process similar to slow heating. Under these slow-heating conditions, $[^{\bullet}ATAR+H]^+$ and $[^{\bullet}ATAR\text{-}OCH_3+H]^+$ cation-radicals underwent competitive dissociations resulting in loss of water (*m/z* 384), $C_3H_6NO^{\bullet}$ (*m/z* 330, $[z_3]^+$), C_3H_7NO (*m/z* 329, $[z_3 - H]^{+\bullet}$), and N−C_α bond cleavage forming the $[z_2+H]^{+\bullet}$ ions (*m/z* 230) (Figure 2a). These appeared with similar relative intensities at *m/z* 398, 344, 343, and 244 for the respective homologous ions from the peptide methyl ester (Figure 2b) and corroborated the fragment ion assignment. The dissociations leading to $[z_2+H]^{+\bullet}$ ions may proceed in two steps, as reported for other $[z_4+H]^{+\bullet}$ ions.[40] For peptide fragment ion nomenclature see ref 26.

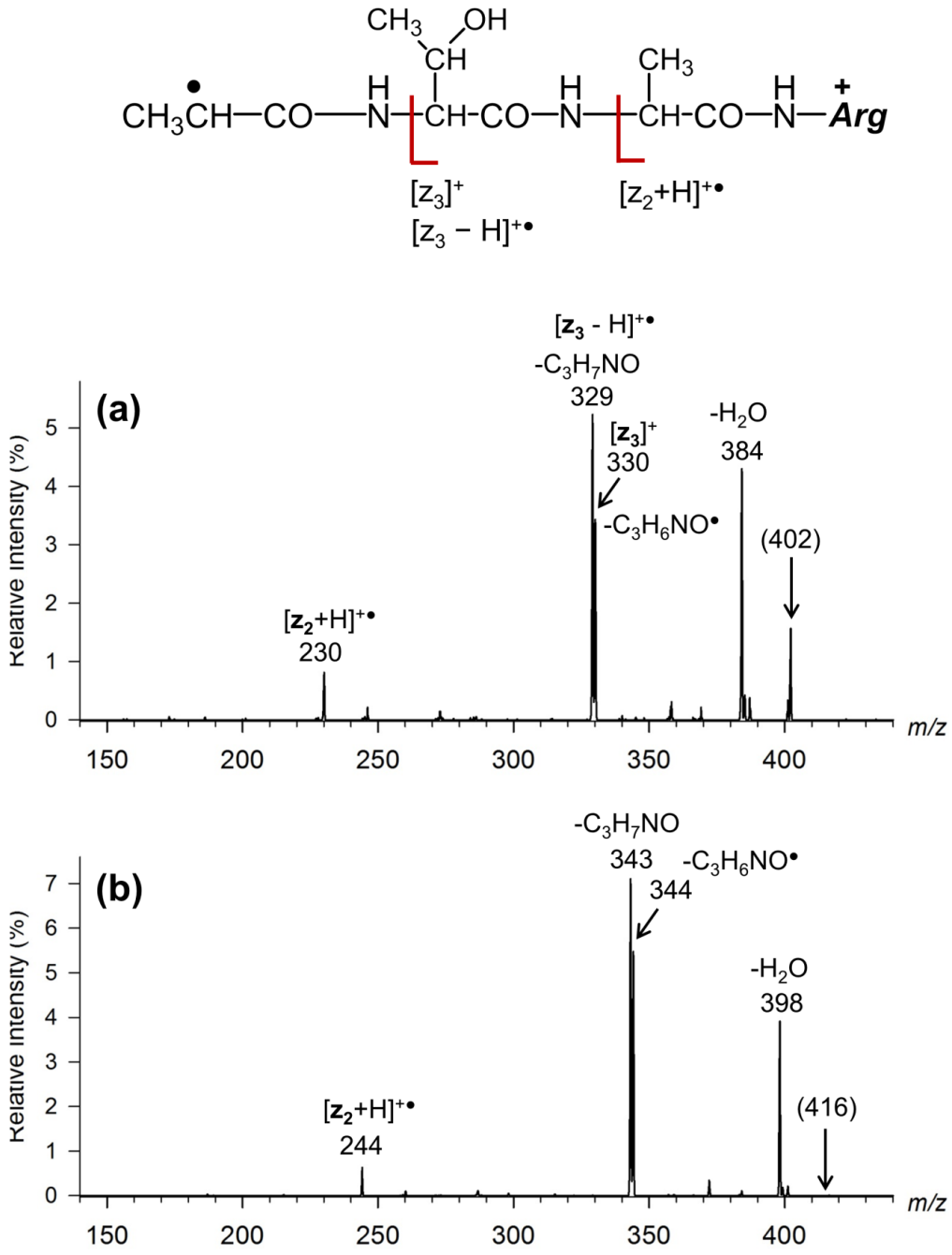

Figure 2. CID of $[z_4+H]^{+\bullet}$ ions generated by ETD of (a) $[AATAR+2H]^{2+}$ and (b) $[AATAR-OCH_3+2H]^{2+}$.

Photodissociation (UVPD) of the $[z_4+H]^{+\bullet}$ ions was initially performed at 355 nm which specifically targets the second (B) excited electronic state of the C_α-CO radical chromophore.[42] UVPD resulted in loss of water, $C_3H_6NO^\bullet$, and C_3H_7NO neutral fragments that were analogous to those in the CID spectrum. In addition, UVPD induced several dissociations that were absent on CID, namely, loss of OH and backbone cleavages resulting in the formation of C-terminal fragment ions with closed electron shells, $[y_3]^+$, $[y_3 - C_2H_4O]^+$, $[y_2+H]^+$, and $[y_2]^+$ at *m/z* 345, 301, 246, and 244, respectively (Figure 3a), that showed the expected 14 Da homologous mass shifts for the $[z_4+H]^{+\bullet}$ methyl ester ion (Figure 3b). All these fragment ions contain the C-terminal arginine residue. The relevant bond dissociations forming these ions and their sketched structures are shown as insets in Figure 2.

The nature of the major CID fragment ions $[z_3]^+$and $[z_3 - H]^{+\bullet}$, was further investigated by selecting them by mass followed by collisional activation and photodissociation at 355 nm (Figure 4). CID of both ions resulted in the elimination of a 84 Da neutral ($C_4H_4O_2$) from the Thr residue, forming the $[y_2+H]^{+\bullet}$ (*m/z* 245) and $[y_2+2H]^+$ (*m/z* 246) ions, respectively (Figure 4a,b). Only the cation-radicals, *m/z* 329 and *m/z* 343 from $[^\bullet ATAR+H]^+$ and $[^\bullet ATAR\text{-}OCH_3+H]^+$, respectively, showed photodissociation, resulting in backbone cleavage between the Thr and Ala residues and formation of $[y_2]^+$ ions at *m/z* 244 and 258 (Figure 4c). The *m/z* 330 and 344 even-electron ions did not photodissociate at 355 nm (Figure 4d).

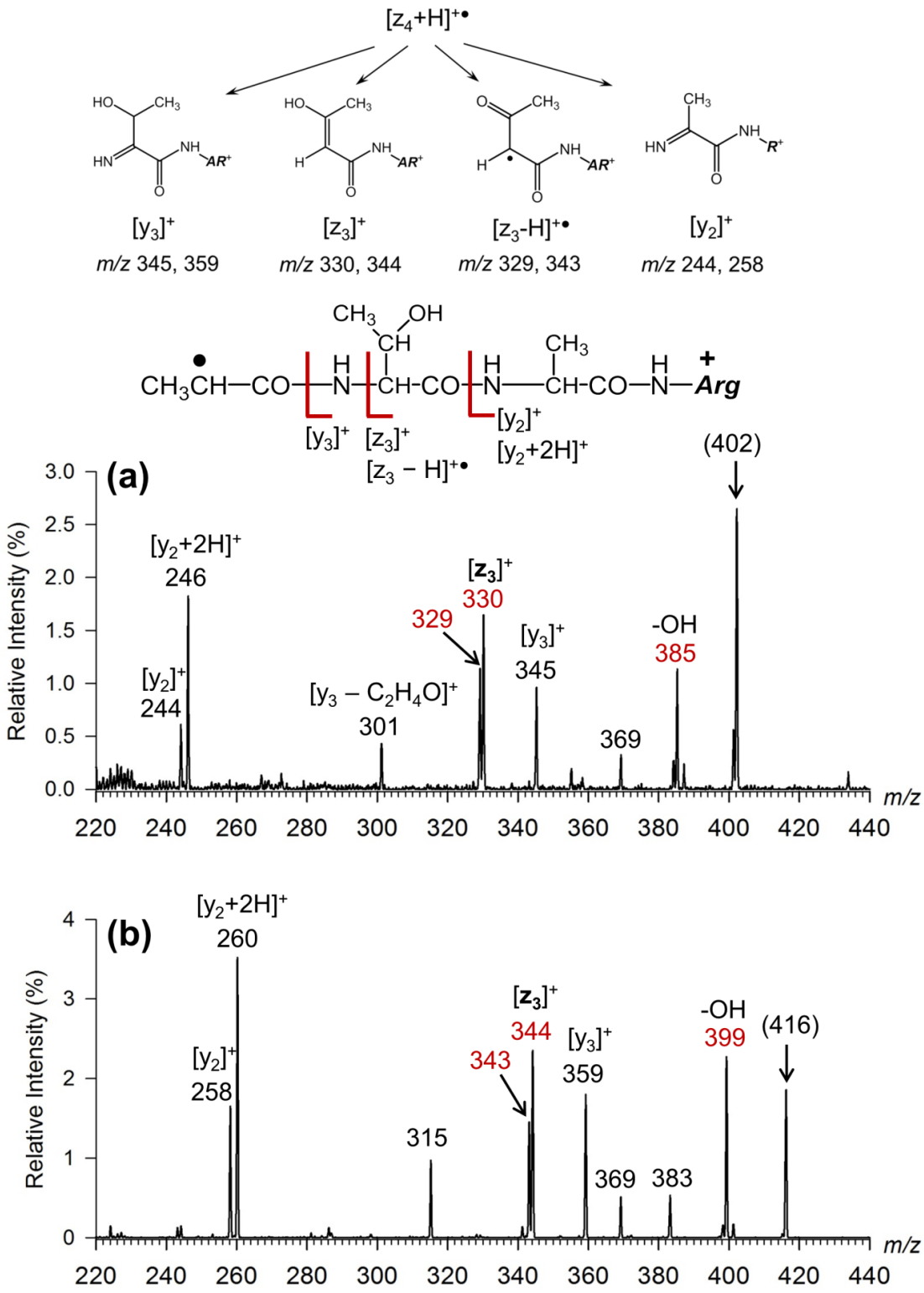

Figure 3. Photodissociation (355 nm, 3 laser pulses) of $[z_4+H]^{+\bullet}$ ions generated by ETD of (a) $[AATAR+2H]^{2+}$ and (b) $[AATAR\text{-}OCH_3+2H]^{2+}$.

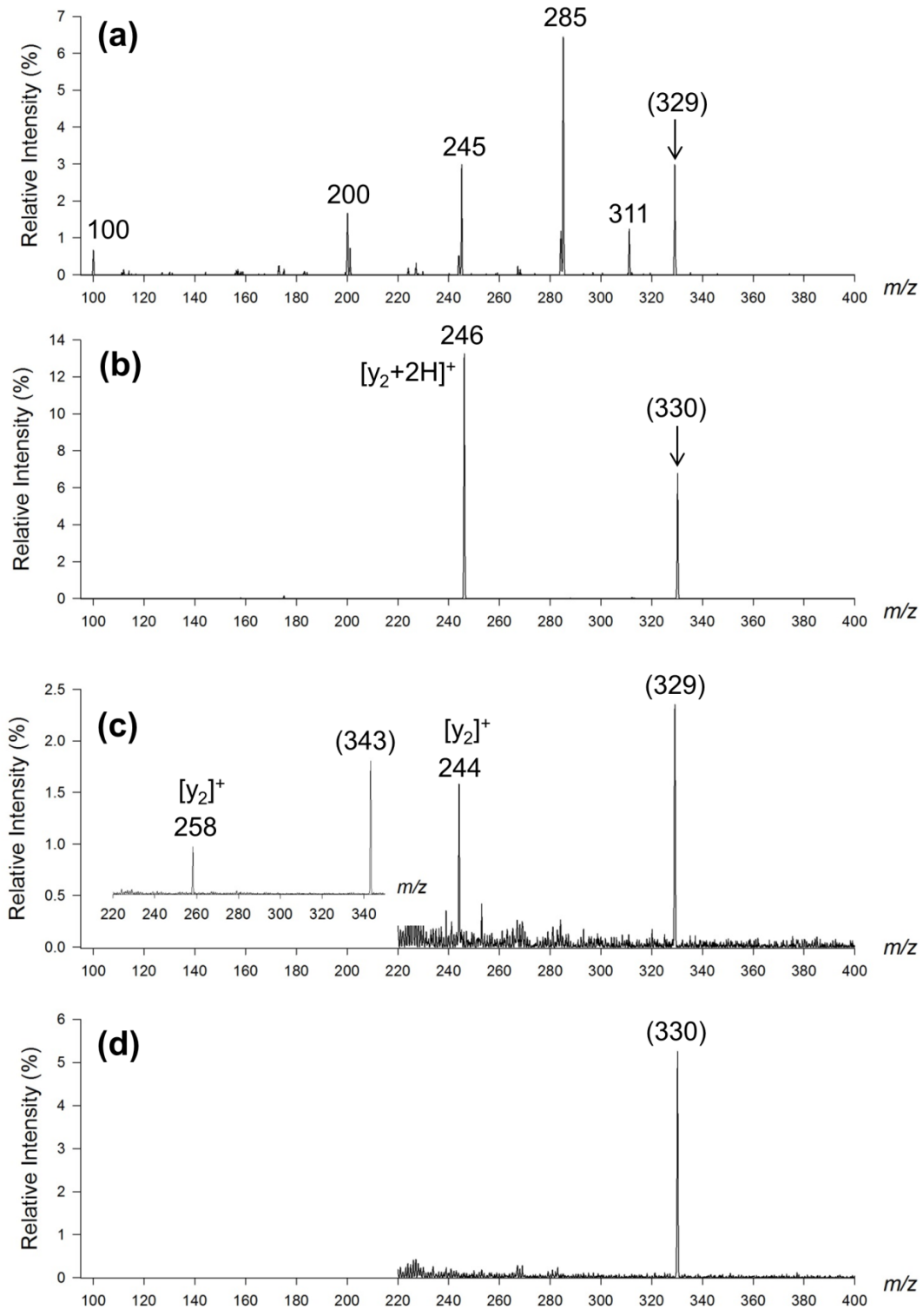

Figure 4. Collision-induced dissociation (CID) mass spectra of (a) $[z_3 - H]^{+\bullet}$ and (b) $[z_3]^+$ ions from $[ATAR+H]^{+\bullet}$. Photodissociation (355 nm) mass spectra (UVPD) of (c) $[z_3 - H]^{+\bullet}$ and (d) $[z_3]^+$ ions from $[ATAR+H]^{+\bullet}$. Inset in (c) shows the UVPD spectrum of the $[z_3 - H]^{+\bullet}$ ion from $[ATAR\text{-}OCH_3+H]^{+\bullet}$.

5. 3. 2 Photodissociation and Action Spectrum of $[z_4+H]^{+\bullet}$ Ions

Before analyzing and discussing the dissociations of the $[z_4+H]^{+\bullet}$ ions, it is desirable to establish their structure. Peptide cation-radicals are known to undergo radical-induced rearrangements by hydrogen migrations[68-78] that can be triggered by internal excitation provided by exothermic electron transfer.[79] To characterize the $[z_4+H]^{+\bullet}$ ions, we first monitored photodissociation of the $[^{\bullet}ATAR+H]^+$ ion at 355 nm as a function of the number of laser pulses. This provided an exponential curve, $I(n) = I_0e^{-0.53n}$, (correlation coefficient: $r^2 = 0.996$, root mean square deviation: rmsd = 2.9%) shown in Figure 5a, where I_0 and $I(n)$ are, respectively, the normalized initial and residual $[z_4+H]^{+\bullet}$ ion intensity after n pulses. The asymptotic decrease to zero of $I(n)$ indicated that all $[z_4+H]^{+\bullet}$ species in the ion population produced by ETD and stored in the ion trap absorbed light at 355 nm and underwent photodissociation upon absorption of the 3.4925 eV (337 kJ mol^{-1}) photon. The homologous $[^{\bullet}ATAR\text{-}OCH_3+H]^+$ ion also showed a single-exponential decay upon irradiation at 355 nm, $I(n) = I_0e^{-0.66n}$, (correlation coefficient: $r^2 = 0.992$, root mean square deviation: rmsd = 2.6%), indicating a close similarity between the $[z_4+H]^{+\bullet}$ ions generated from the peptide and its methyl ester (Figure 5a). The photofragment ion relative intensities increased asymptotically for all even-electron species, as illustrated for ions from $[^{\bullet}ATAR\text{-}OCH_3+H]^+$ (Figure 5b). In contrast, the $[z_4+H - H_2O]^{+\bullet}$ and $[z_3 - H]^{+\bullet}$ cation-radical fragment ions reached a maximum and then were depleted upon further laser pulses, indicating that these species photodissociated at 355 nm.

More detailed absorption characteristics of the $[z_4+H]^{+\bullet}$ ions were obtained from the UVPD action spectrum (Figure 5a,b). The mass-resolved fragment ion channels (Figure 5a) showed two prominent broad absorption maxima at 360 and 225 nm that are visualized by the overall action spectrum, constructed as a sum of normalized photofragment ion intensities at 210-

400 nm from all monitored channels (Figure 5b). The major dissociation channels showed different absorption characteristics along the wavelength axis. In particular, the *m/z* 384 fragment ion by loss of H_2O peaked at 360 nm but relatively decreased at 230 nm. This could be due to consecutive dissociations of this radical fragment ion following absorption of a high energy photon. In contrast, the *m/z* 385 closed-shell fragment ion by loss of OH dominated at 230 nm, possibly because of its stability. The $[z_3]^+$ (*m/z* 330) and $[y_3]^+$ (*m/z* 345) channels showed maxima in both the 340-360 and 220-230 nm regions. The low-mass channels of the $[y_2]^+$ and $[y_2+2H]^+$ fragment ions could not be monitored across the entire wavelength region because of interference from background ions from photodesorbed fluoranthene.[21] The interpretation of the action spectrum (Figure 6c) and structure assignment for the $[z_4+H]^{+\bullet}$ ions required extensive calculations that are described in the next section.

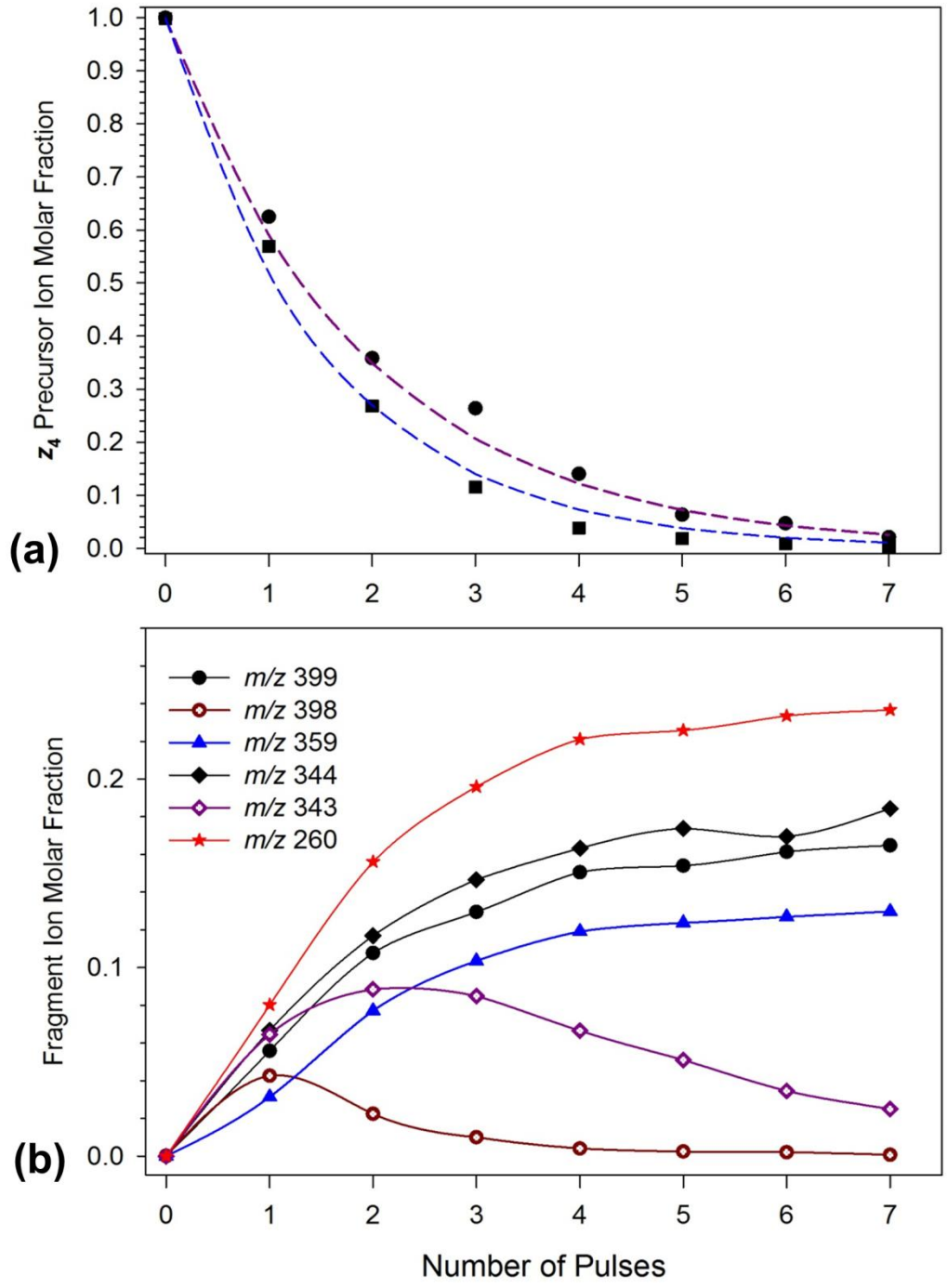

Figure 5. (a) Laser pulse dependence at 355 nm of $[z_4+H]^{+\bullet}$ ions molar fractions for $[^{\bullet}ATAR+H]^+$ (circles) and $[^{\bullet}ATAR\text{-}OCH_3+H]^+$ (squares). (b) Laser pulse dependence at 355 nm of molar fractions for photofragment ions from $[^{\bullet}ATAR\text{-}OCH_3+H]^+$. Loss of OH = *m/z* 399, loss of water = *m/z* 398, $[y_3]^+$ = *m/z* 359, $[z_3]^+$ = *m/z* 344, $[z_3 - H]^{+\bullet}$ = *m/z* 343, $[y_2]^+$ = *m/z* 260.

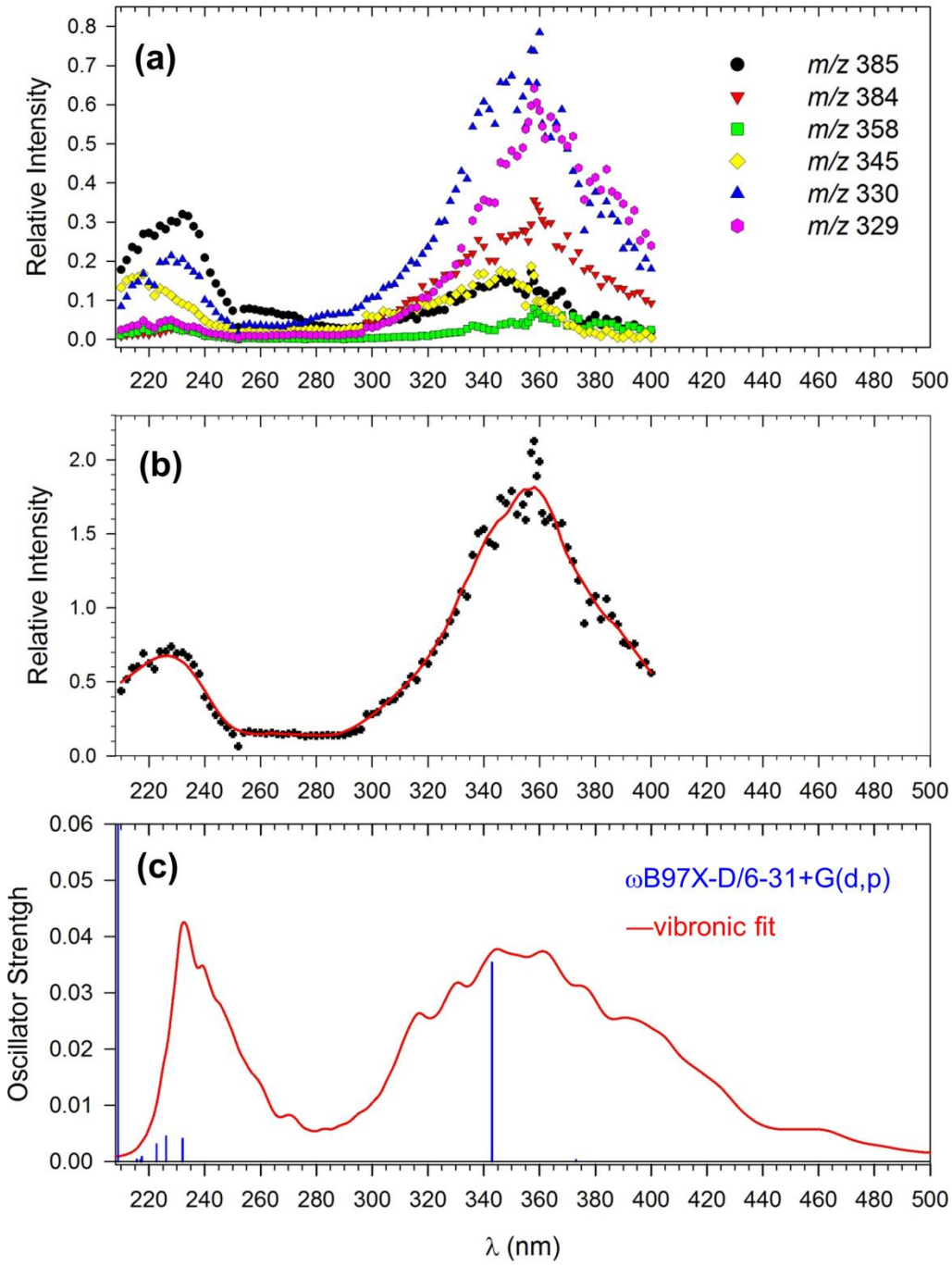

Figure 6. Photodissociation action spectrum of $[^{\bullet}ATAR+H]^{+}$ ion. (a) Mass-channel resolved spectra: the *m/z* 385, 384, 358, 345, 330, and 329 channels correspond to losses of OH, H_2O, C_2H_4O, C_3H_5O, C_3H_6NO, and C_3H_7NO, respectively. (b) Overall action spectrum from the sum of photofragment ion relative intensities. (c) Calculated vibronic absorption spectrum at 300 K of *trans*-**1**. For ion structure see Figure 7.

5. 3. 3 Ion Structures

Investigations of peptide cation-radical structures involve three major features: (1) charge location, (2) radical site location, and (3) peptide conformation. With $[^{\bullet}ATAR+H]^{+}$, the charge is firmly sequestered by protonation of the basic Arg residue (Scheme 1). The radical site can migrate from the former *N*-terminal C_{α} (C-14) to backbone C_{α} positions at Thr (C-3), Ala (C-9), or Arg (C-18), or to the C_{β} position in the Thr residue (C-6, for atom numbering see Scheme 1). All these radicals (*trans*-**2**-**5**, Figure 7) are expected to be low-energy isomers of the initial *N*-terminal C_{α} structure *trans*-**1**.[21] An isomer with the radical site in the Arg side chain (**6**, Figure 7) was found to be substantially destabilized against *trans*-**1**-**5** and is not likely to be formed by ETD. Analysis of the radical position and ion conformation in $[^{\bullet}ATAR+H]^{+}$ followed a multistep procedure aimed at capturing both the local energy minima and the connecting transition states as first-order saddle points. The initial $[^{\bullet}ATAR+H]^{+}$ structure was built from the homologous serine-containing $[z_4+H]^{+\bullet}$ ion, $[^{\bullet}ASAR+H]^{+}$,[42] and optimized with B3LYP. The optimized structure was subjected to BOMD/PM6-D3H4 for 100 ps at 520 K, 2500 snapshots were extracted and optimized by PM6-D3H4. From these, 20 low-energy structures within a 20 kJ mol^{-1} energy range were obtained and fully reoptimized with DFT. The lowest-energy ion (*trans*-**1**) is shown in Figure 7. B3LYP, ωB97X-D/6-31+G(d,p), and M06-2X geometry optimizations yielded very similar lowest-energy ion structures that are represented by *trans*-**1**.

Ion structures in which the radical site migrated to another position were obtained according to the following procedure. Starting with *trans*-**1**, the *N*-terminal amide bond was rotated through **TS1** from the trans to a cis configuration and the resulting *cis*-isomer (*cis*-**1**) was used to search for the transition state (**TS2**) for the Thr alpha H atom migration from C-3 to the *N*-terminal radical site (C-14) using B3LYP. Note that the amide rotation is necessary to make the

alpha and beta hydrogen atoms sterically accessible for transfer through respective five- and six-membered membered cyclic transition states. The critical parameters of the **TS2** geometry, which are the lengths of the forming C-14−H and breaking C-3−H bonds, were constrained while the other atoms were fully dynamic in the subsequent BOMD/PM6-D3H4 trajectory calculations that were run for 100 ps at 520 K. Eleven lowest-energy structures were extracted and fully optimized to the first-order saddle points with B3LYP, ωB97X-D, and M06-2X to obtain new TS geometries. The lowest-energy TS was selected for intrinsic reaction coordinate (IRC)[80] search to find the structure of the *cis*-**1** reactant and the H-migration product, which was a *cis*-amide (*cis*-**2**). Both ions were fully optimized by DFT to give the final structures (Figure 8). This procedure preserves the structural continuity for the *cis*-**1** → **TS2** → *cis*-**2** reaction while providing an electronically and conformationally optimized TS structure for the further analysis of the potential energy surface (*vide infra*). Amide rotation in *cis*-**2** through **TS3** then produced the more stable trans-amide isomer that was subjected to BOMD/PM6-D3H4 run, and 12 lowest-energy structures were fully optimized with DFT to yield *trans*-**2** (Figure 7). The calculations indicated that the hydrogen bonding pattern in *trans*-**1** and *trans*-**2** was conserved, showing internal solvation of the Arg guanidinium ion by the O-15 and O-12 amide carbonyls (Figure 7). Based on this finding, the Ala (C-9) and Arg (C-18) radicals were built from *trans*-**2** and fully optimized by DFT without the BOMD conformational run, yielding radicals *trans*-**3** and *trans*-**4** (Figure 7). In contrast, the hydrogen bonding pattern of the Thr hydroxyl depended on the amide *cis*-*trans* geometry and, therefore, the C-6 beta radical (*trans*-**5,** Figure 7) was generated by a procedure analogous to that employed for *trans*-**2**. Briefly, a TS for the beta H transfer in *cis*-**1** was found by combined DFT/BOMD/DFT (**TS4**) and the *cis*-**5** isomer was obtained by IRC from **TS4** followed by BOMD/DFT optimization (Figure 8). The trans isomer (*trans*-**5**) was obtained after amide rotation

through **TS5**, followed by BOMD/DFT optimization. The *trans*-amide radicals **1**-**5** showed very similar 0 K energies relative to *trans*-**1** that was used as a reference (E_{rel} = 0.0 kJ mol^{-1}, Table 1).

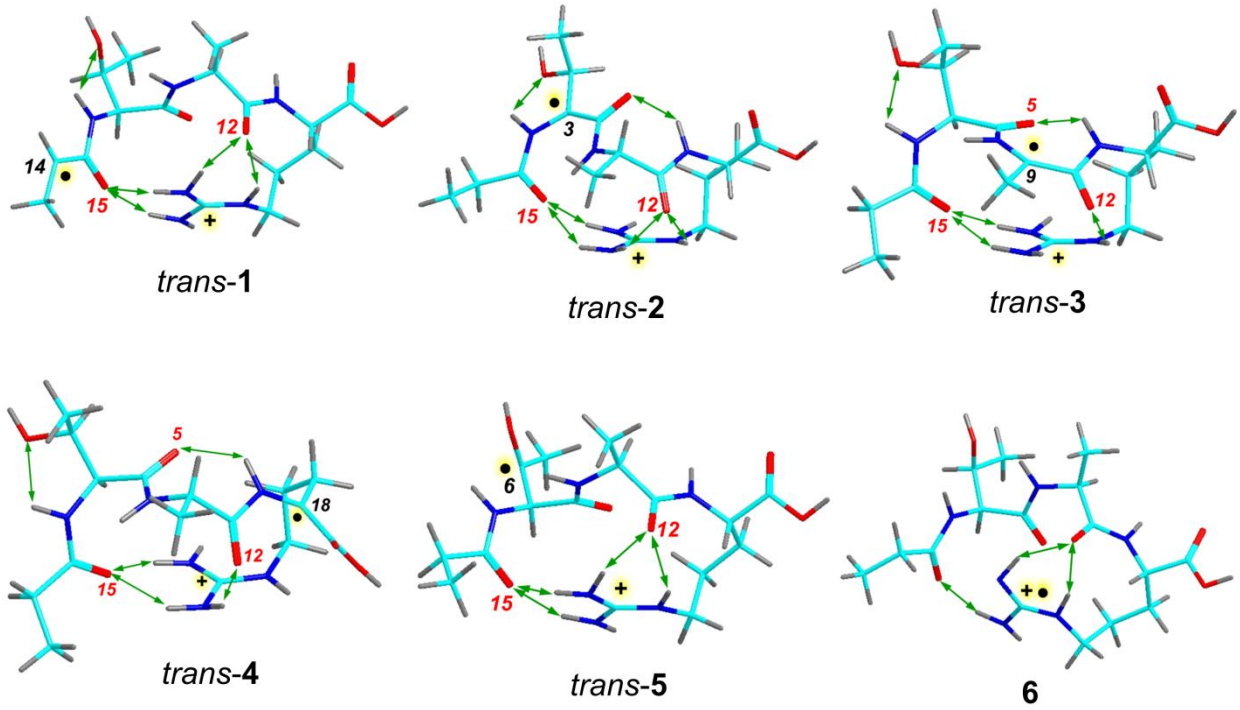

Figure 7. ωB97X-D/6-31+G(d,p) optimized structures of *trans*-**1**-**6**. Green arrows indicate major hydrogen bonds of *d*(X—H) < 2.2 Å. For ion relative energies see Table 1.

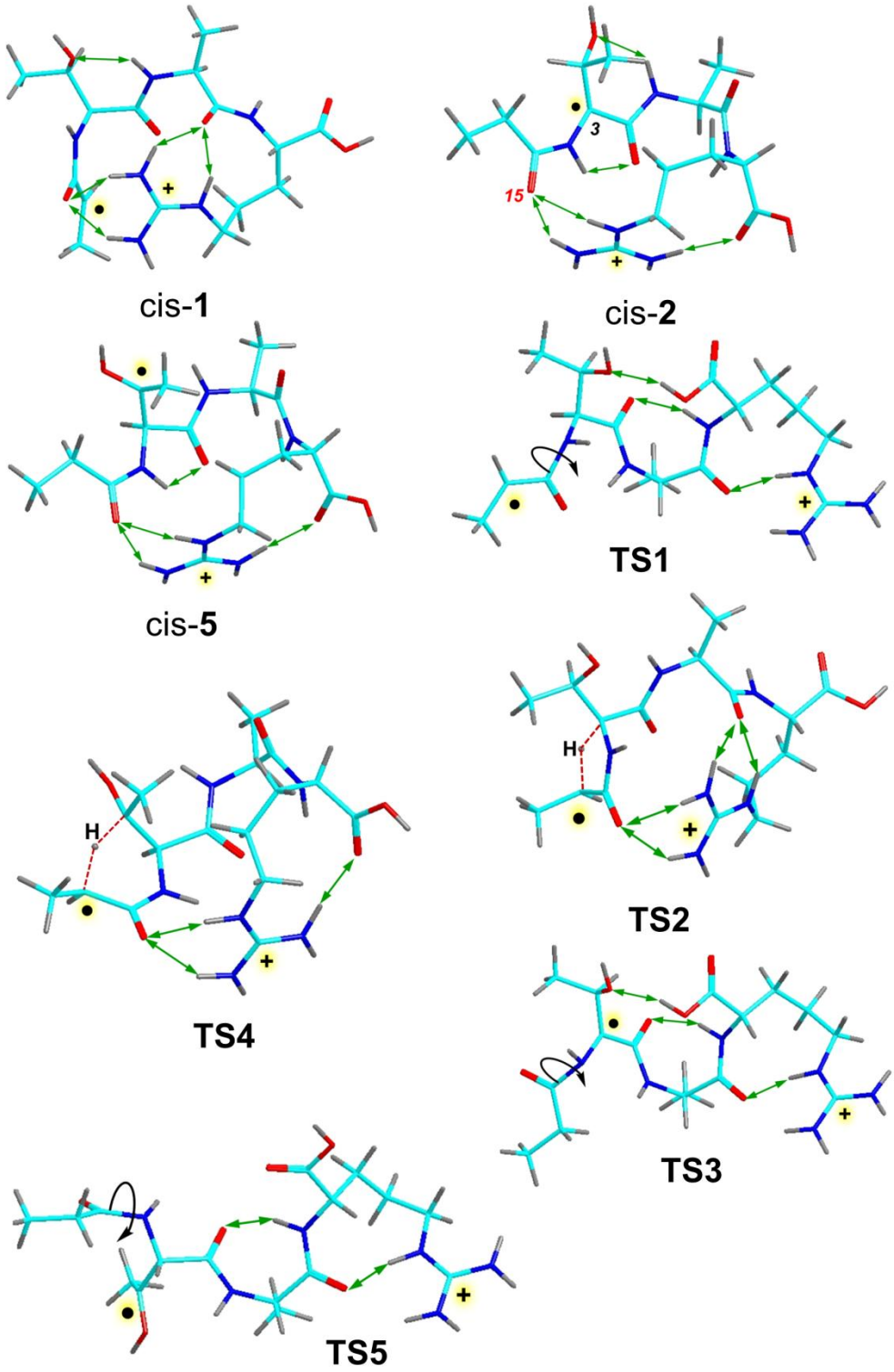

Figure 8. ωB97X-D/6-31+G(d,p) optimized structures of cis-amide reaction intermediates and transition states for amide bond rotation and hydrogen transfers.

5. 3. 4 Action Spectrum Assignment

To interpret and assign the bands in the UVPD action spectrum of the $[z_4+H]^{+\bullet}$ ion, we performed TD-DFT calculations of excitation energies and oscillator strengths of *trans*-isomers **1**-**5**, and also the pertinent *cis*-amide isomers. Ion *trans*-**1** showed major transitions at 343 nm and 209 nm, several minor ones between 220-240 nm, and a very weak band at 374 nm, all based on ωB97X-D TD-DFT calculations (Figure 9). Calculations with the other DFT functionals (M06-2X and LC-BLYP) gave similar absorption patterns for *trans*-**1**, showing wavelength shifts of the calculated lines, as summarized in Table 2. In particular, the LC-BLYP excitation energies were blue shifted relative to those from ωB97X-D and M06-2X, consistent with the results of a previous benchmarking study.[60] The electron transitions leading to the five lowest excited states in *trans*-**1** are listed in Table 3. The prominent band at 343 nm includes excitations from lower β molecular orbitals to the lowest unoccupied MO108β of a π_z type, which is delocalized over the CH_3-$CH^{\bullet}$-CO-NH moiety (Table 3).

Radicals *trans*-**2**-**5** showed distinctly different absorption spectra (Figure 9b,c). The calculated spectrum of *trans*-**2** showed weak bands at 358 and 377 nm whereas the major bands appeared at 302, 260, 245, and 244 nm (Figure 9b). The Ala-C_α radical *trans*-**3** displayed a weak absorption band at 341 nm and stronger ones at 313, 250, and 233 nm (Figure 9c). The Arg-C_α radical *trans*-**4** had a weak band at 316 nm and strong ones at 276 and 232 nm with further moderately strong bands at 228, 222, and 218 nm (Figure 9c). The Thr-C_β radical *trans*-**5** showed the longest wavelength absorption at 287 nm and several moderately strong bands at 250, 243, and 211 nm (Figure 9b). For a complete list of transitions cf. Table 2.

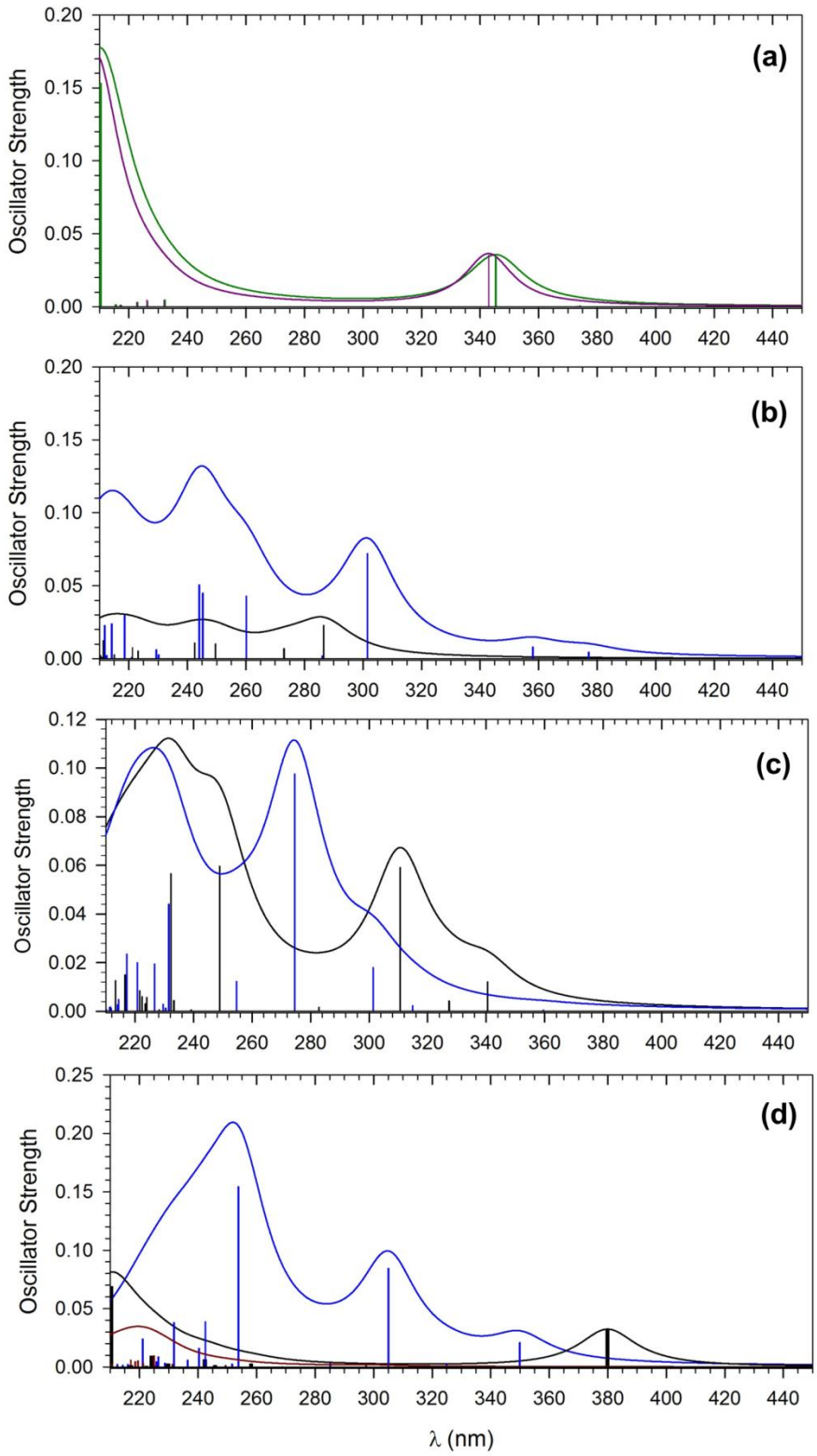

Figure 9. TD-DFT ωB97X-D absorption spectra of (a) *trans*-**1** (purple: calculations with the 6-31+G(d,p) basis set; green: calculations with the 6-311++G(2d,p) basis set; (b) blue: *trans*-**2**, black: *trans*-**5**; (c) black: *trans*-**3**; blue: *trans*-**4**; (d) blue: *cis*-**2**; black: *cis*-**1**; purple: *cis*-**5**.

Table 2. Excitation Wavelengths and Oscillator Strengths of $[ATAR+H]^{+\bullet}$ Cation Radicals.

	Transition Wavelength (nm)		
Ion	ωB97X-D[a,b]	M06-2X[a,b]	LC-BLYP[a,b]
trans-**1**	374 (0.0004)	359 (0.0004)	348 (0.0001)
	345 (0.0342)	333 (0.0351)	317 (0.0274)
	232 (0.0047)	236 (0.0035)	219 (0.0015)
	226 (0.0037)	228 (0.0016)	214 (0.0038)
	223 (0.0029)	223 (0.0015)	208 (0.0006)
	217 (0.001)	217 (0.0011)	207 (0.0073)
	210 (0.153)	212 (0.1452)	202 (0.0627)
trans-**2**	377 (0.0045)	362 (0.0021)	325 (0.0017)
	358 (0.0079)	346 (0.0099)	315 (0.0105)
	302 (0.072)	300 (0.0002)	274 (0.0006)
	286 (0.0018)	277 (0.0128)	256 (0.0189)
	260 (0.0428)	262 (0.1762)	238 (0.2053)
	245 (0.0449)	249 (0.0243)	224 (0.0039)
	244 (0.0505)	246 (0.0042)	216 (0.001)
	230 (0.0027)	244 (0.0172)	214 (0.0034)
	229 (0.0061)	235 (0.0030)	213 (0.0512)
	221 (0.0008)	233 (0.026)	208 (0.0015)
	219 (0.0294)	231 (0.004)	204 (0.0009)
	214 (0.0239)	227 (0.0035)	
	212 (0.0227)	225 (0.0003)	
	206 (0.0295)		
trans-**3**	341 (0.0118)	342 (0.0139)	297 (0.0135)
	328 (0.0042)	327 (0.0032)	286 (0.0577)
	313 (0.0599)	309 (0.0477)	283 (0.0054)
	284 (0.0017)	285 (0.0026)	266 (0.0013)
	250 (0.0601)	260 (0.001)	244 (0.0441)
	241 (0.0007)	256 (0.069)	223 (0.028)
	235 (0.0046)	242 (0.0209)	217 (0.0019)
	233 (0.0571)	238 (0.0259)	214 (0.087)
	229 (0.0008)	234 (0.0031)	213 (0.0039)
	224.5 (0.0027)	230 (0.0128)	211 (0.0011)
	224.0 (0.0039)	229 (0.0031)	193 (0.0021)
	223.5 (0.0104)	227 (0.0047)	189 (0.0218)
	222 (0.0061)	223 (0.0144)	188 (0.0218)
	217 (0.0133)	221 (0.0082)	186 (0.0084)
	214 (0.0119)	219 (0.0021)	
	212 (0.0017)	217 (0.0035)	
	209 (0.0062)	214 (0.0066)	

/continued on next page

Table 2 (continued). Excited states of ATAR Cation Radicals

	Transition Wavelength (nm)		
Ion	ωB97X-D[a,b]	M06-2X[a,b]	LC-BLYP[a,b]
trans-**4**	362 (0.0005)	367 (0.0002)	326 (0.0002)
	316 (0.0023)	309 (0.0038)	285 (0.0018)
	303 (0.0186	304 (0.0135)	277 (0.008)
	276 (0.0959)	276 (0.1005)	254 (0.1144)
	256 (0.0135)	255 (0.0097)	244 (0.016)
	232 (0.0437)	241 (0.0037)	225 (0.0069)
	231 (0.001)	239 (0.0105)	211.9 (0.029)
	230 (0.0027)	233 (0.001)	211.6 (0.039)
	228 (0.0187)	232 (0.0009)	210 (0.0004)
	222 (0.021)	230 (0.0553)	199 (0.0055)
	218 (0.0199)	223.4 (0.0036)	195 (0.0042)
	215.4 (0.0037)	222.6 (0.0066)	192 (0.0227)
	214.7 (0.0044)	220 (0.0170)	186 (0.024)
	213.5 (0.0051)	218 (0.0173)	184 (0.0383)
	212 (0.0001)	217 (0.0007)	
	211 (0.0006)	216 (0.0006)	
		213 (0.0013)	
trans-**5**	287 (0.0228)	294 (0.008)	255 (0.0028)
	273 (0.0069)	281 (0.0185)	241 (0.0007)
	250 (0.0101)	254 (0.0129)	239 (0.0026)
	243 (0.0108)	244 (0.0002)	230 (0.0045)
	223 (0.0052)	242 (0.0055)	224 (0.0073)
	221 (0.0074)	237 (0.0041)	221 (0.0074)
	215 (0.0027)	235 (0.0013)	214 (0.0023)
	211 (0.0124)	231 (0.0011)	213 (0.0011)
	210.4 (0.002)	229 (0.0019)	210 (0.0147)
	209.8 (0.0014)	226 (0.0014)	203 (0.0013)
		219 (0.001)	
		218.8 (0.0046)	
		218 (0.0009)	
		216 (0.0018)	
		215 (0.0002)	
		214.6 (0.0039)	
		211 (0.0078)	

[a]All calculations with the 6-311++G(2d,p) basis set on DFT/6-31+G(d,p) optimized geometries.
[b]Oscillator strength in parentheses.

Table 3. Electronic Transitions in [•ATAR+H]$^+$ Ion *trans*-**1**.

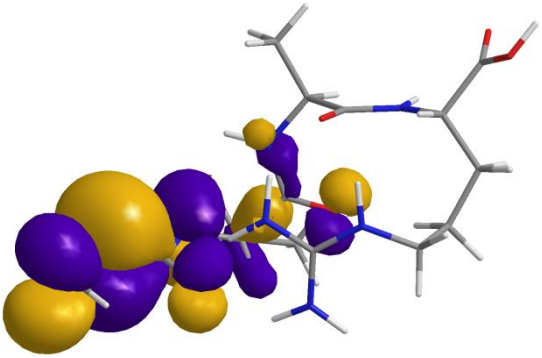

SOMO 108

State	ΔE_{exc} (eV)	Transition (amplitude)
A	3.323	100β → 108β (0.205), 102β → 108β (0.679), 103β → 108β (0.566), 104β → 108β (0.275), 106β → 108β (0.218)
B	3.615	98β → 108β (0.269), 99β → 108β (-0.184), 101β → 108β (0.330), 102β → 108β (-0.127), 103β → 108β (0.122), 104β → 108β (0.195), 105β → 108β (-0.284), 106β → 108β (-0.183), 107β → 108β (0.736)
C	5.344	107α → 109α (-0.124), 98β → 108β (-0.218), 99β → 108β (0.300), 100β → 108β (-0.115), 101β → 108β (-0.315), 102β → 108β (0.117), 103β → 108β (-0.189), 104β → 108β (-0.317), 106β → 108β (0.283), 107β → 108β (0.559)
D	5.482	104α → 109α (-0.107), 106α → 109α (0.158), 106α → 111α (-0.131), 107α → 109α (0.148), 107α → 110α (0.122), 107α → 111α (-0.114), 108α → 109α (-0.127), 101β → 108β (0.375), 104β → 108β (-0.145), 106β → 108β (0.600), 107β → 109β (0.212), 107β → 110β (0.122), 107β → 111β (-0.164), 107β → 112β (0.136)

The calculated absorption spectra of *trans*-**1**-**5** were compared with the photodissociation action spectrum of the $[z_4+H]^{+\bullet}$ ion. The latter did not display absorption bands in the 250-300 nm region that would be expected if isomers *trans*-**2**-**5** were present. In contrast, the action spectrum was consistent with the calculated absorption spectrum of *trans*-**1**. This similarity was further corroborated by comparing the action spectrum with the vibronically broadened absorption spectrum of *trans*-**1** that showed a close match of the band shapes and λ_{max}. The calculated absorption spectra of the *cis*-amide isomers, *cis*-**1**, **2**, and **5** showed patterns that were similar to those for the corresponding *trans*-amide isomers, but displayed red shifts for the long wavelength bands (Figure 9d). In summary, the photodissociation action spectrum of the $[z_4+H]^{+\bullet}$ ion generated by ETD very well matches the calculated absorption spectrum of *trans*-**1** (Figure 6c). This is the expected structure to be formed by dissociation of the N−C_α bond between the Ala and Thr residues in the $(AATAR+2H)^{+\bullet}$ cation-radical. Conversely, the assigned structure provides evidence that, under the ETD conditions, the $[z_4+H]^{+\bullet}$ ions did not undergo isomerization by hydrogen migrations.

The kinetic stability of $[^{\bullet}ATAR+H]^+$ contrasts the behavior of the related cation radicals $[^{\bullet}AFAR+H]^+$, $[^{\bullet}AWAR+H]^+$ (ref[21]), $[^{\bullet}FAR+H]^+$, and $[^{\bullet}DAR+H]^+$, that have been found to isomerize by hydrogen migrations when formed by ETD.[38] The related $[^{\bullet}AHAR+H]^+$ ion has been reported to retain the canonical structure on the basis of an IRMPD action spectrum.[20] We note that analysis of UVPD spectra of $[^{\bullet}AHAR+H]^+$ revealed ca. 6% isomers other than the canonical structure.[38] The structural integrity of $[^{\bullet}ATAR+H]^+$ is not obviously related to the isomerization thermodynamics. The isomeric radicals *trans*-**2** and *trans*-**5** have energies very similar to that of *trans*-**1**, whereas *trans*-**3** and *trans*-**4** are even more stable. The reason for the stability of $[^{\bullet}ATAR+H]^+$ and different behavior of peptide cation radicals carrying different amino acid

residues may be found in the isomerization kinetics and relative stabilities of the intermediates.[21] Isomerization and dissociation mechanisms of $[^{\bullet}ATAR+H]^{+}$ are addressed in the next section.

5. 3. 5 Isomerization and Dissociation Pathways

In this section we present and discuss the energetics of $[z_4+H]^{+\bullet}$ ion isomerizations and dissociations. The $[z_4+H]^{+\bullet}$ ions showed four major dissociations upon collisional activation in the slow-heating regime: loss of H_2O, $C_3H_6NO^{\bullet}$, C_3H_7NO, and formation of the $[z_2+H]^{+\bullet}$ ions. All these dissociations require hydrogen atom migrations to produce intermediates from which the neutral fragments are formed. Since action spectroscopy pointed to *trans*-**1** as the dominant $[z_4+H]^{+\bullet}$ ion species formed by ETD, our investigations of the potential energy surface for isomerizations and dissociations started with this structure. The relative energies from ωB97X-D/6-311++G(2d,p) calculations that include zero-point energy corrections are plotted in a comprehensive potential energy diagram (Figure 10). Relative energies were also obtained by MP2, and M06-2X single-point calculations, as compiled in Table 4. The ωB97X-D, MP2, and M06-2X data largely agree in ranking the ion relative energies across the entire set. The B3LYP calculations overestimate the stabilities of several ion-molecule complexes relative to the bound structures and dissociation products.

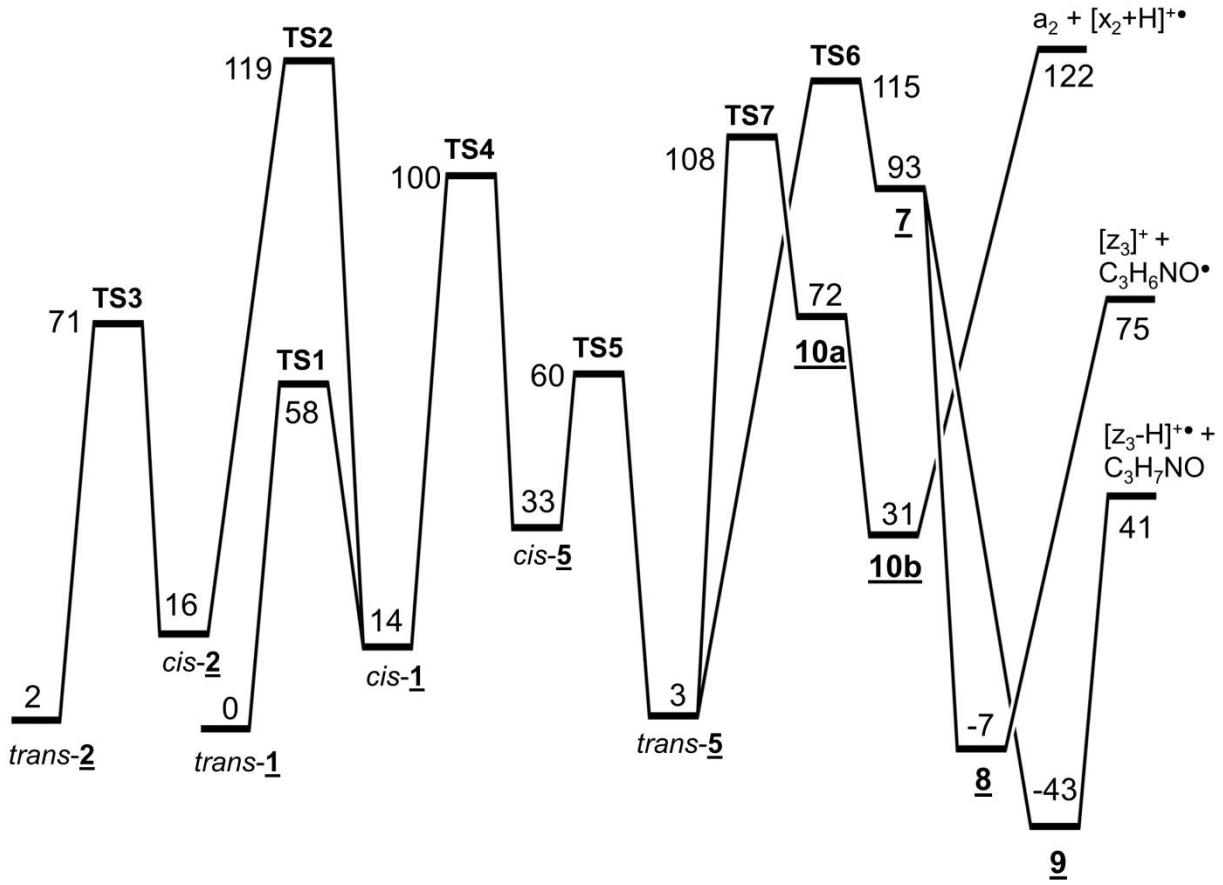

Figure 10. Potential energy diagram of ωB97X-D/6-311++G(2d,p) relative energies (kJ mol^{-1}) including zero-point corrections. **TS1**: amide rotation; **TS2**: Thr-H_α transfer; **TS3**: amide rotation; **TS4**: Thr-H_β transfer; **TS5**: amide rotation; **TS6**: N—C_α bond dissociation; **TS7**: C_α—CO bond dissociation.

Table 4. Relative Energies of $[^{\bullet}ATAR+H]^+$ Cation Radicals.

	Relative Energy[a,b]			
Ion	B3LYP[c]	ωB97X-D[c]	M06-2X[c]	PMP2[c,d]
trans-**1**	0	0	0	0
trans-**2**	0.4	2.4	5.5	7.9
trans-**3**	15	6.7	6.7	11
trans-**4**	−11	−10	−11	−13
trans-**5**	3.2	3.5	7.7	6.9
6	96	94	94	93
cis-**1**	15	14	18	20
cis-**2**	24	16	24	35
cis-**5**	51	33	41	50
TS1	55	58	45	61
TS2	125	119	130	112
TS3	66	71	71	75
TS4	117	100	113	107
TS5	58	60	57	62
TS6	91	115	126	136
TS7	84	108	106	108
TS8	125	143	151	168
TS9	128	145	144	158
7	57	93	99	119
8	−44	−7	−3	16
9	−71	−43	−31	−21
10a	20	72	73	78
10b	−13	31	40	39
11a	119	120	122	144
11g	−49	−34	−31	-[e]
12	102	139	118	122
$[z_3]^+ + C_3H_6NO^{\bullet}$	21	75	79	81
$[z_3 - H]^{+\bullet} + C_3H_7NO$	−5	41	53	63
$[x_2+H]^{+\bullet} + a_2$	65	122	129	127
$[z_4+H - OH]^+ + OH^{\bullet}$	138	159	166	160
$[z_4+H - H_2O]^{+\bullet} + H_2O$	−1	27	36	5
$[y_3]^+ + CH_3CH_2CO^{\bullet}$	129	164	163	165

[a]In kJ mol^{-1}. [b]Including B3LYP/6-31+G(d,p) zero-point energy corrections with frequencies scaled by 0.975 and referring to 0 K. [c]From single-point energy calculations with the 6-311++G(2d,p) basis set. [d]Spin-corrected values. [e]MP2 calculations failed.

The $C_3H_6NO^{\bullet}$ and C_3H_7NO neutral fragments logically originate from the deaminated *N*-terminal Ala residue by cleavage of the N−C_α bond at Thr. By stoichiometry, the neutral fragments must pick up one or two hydrogen atoms, respectively, in the course of dissociation. The N−C_α bond dissociation indicates activation by an adjacent radical. These features led to the proposed reaction sequence (Scheme 2) which starts with *trans*-*cis* amide rotation in *trans*-**1** through a low-energy **TS1**, forming *cis*-**1.** Migration of the beta hydrogen from the Thr side chain in *cis*-**1** through **TS4** forms intermediate *cis*-**5** which can stabilize by amide rotation through **TS5** to form *trans*-**5**. N−C_α bond cleavage in *trans*-**5** via **TS6** forms a complex (**7**) of the incipient $C_3H_6NO^{\bullet}$ radical and the $[z_3]^+$ product ion (Figure 11). Complex 7 can undergo stabilizing isomerizations before the products separate. Thus, prototropic isomerization of the $C_3H_6NO^{\bullet}$ moiety to a more stable C_α-radical can form the lower-energy complex **8**. Further isomerization by hydrogen transfer can form a low-energy complex of the $[z_3 - H]^{+\bullet}$ ion with propionamide (**9**). The dissociation thresholds for loss of $C_3H_6NO^{\bullet}$ from **8** (82 kJ mol^{-1}) and loss of C_3H_7NO from **9** (84 kJ mol^{-1}) are well below the **TS6** energy (122 and 158 kJ mol^{-1} relative to **8** and **9**, respectively), indicating that the dissociations proceeding through **TS6** are not reversible.

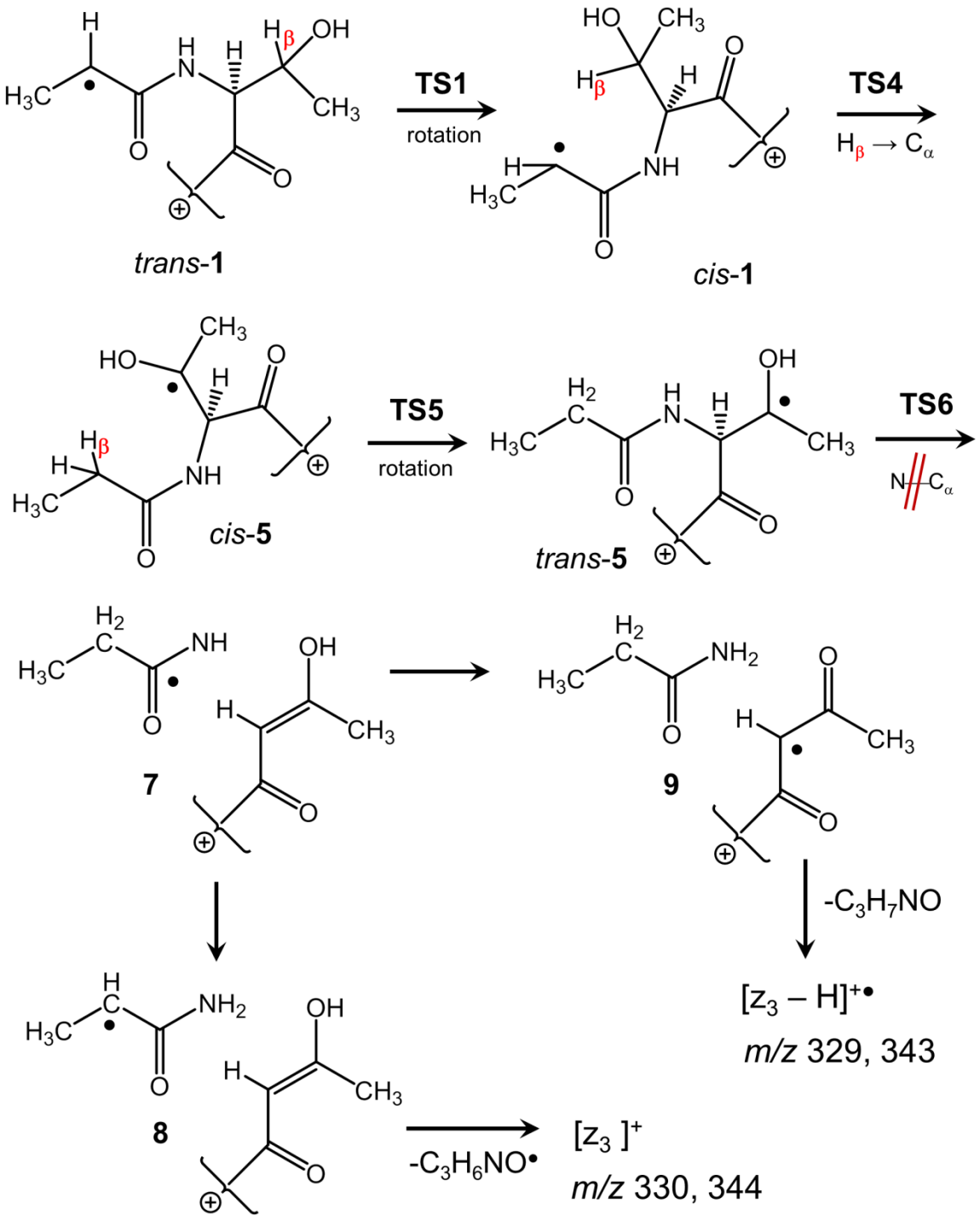

Scheme 2. Proposed reaction sequence leading to the formation of $[z_3]^+$ and $[z_3 - H]^{+\bullet}$ ions. For fully optimized structures see Figure 11.

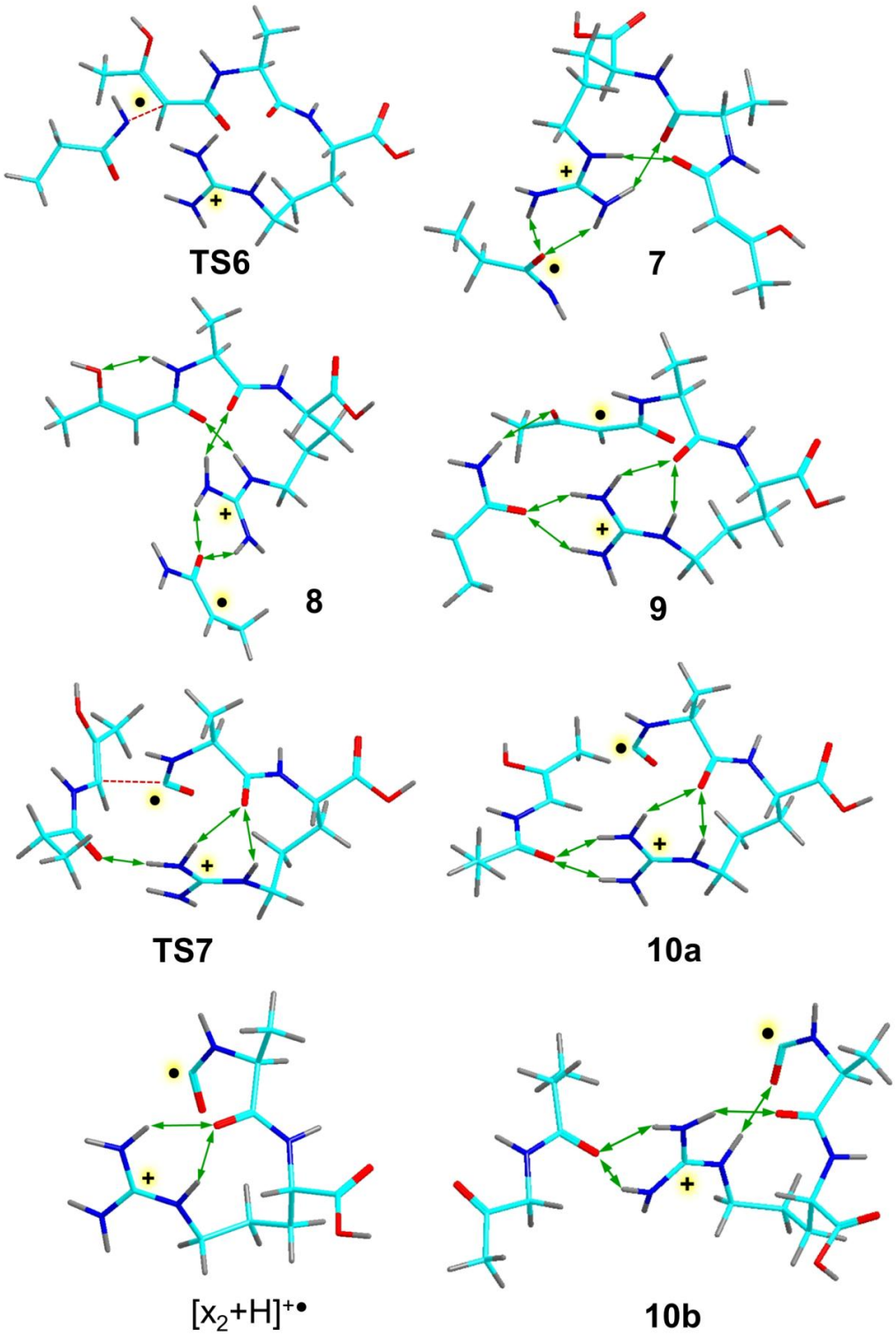

Figure 11. ωB97X-D/6-31+G(d,p) optimized structures of reaction intermediates and transition states for backbone dissociations via **TS6** and **TS7**.

The assumption of a common rate-determining step (**TS6**) and intermediate (**7**) for the loss of $C_3H_6NO^{\bullet}$ and C_3H_7NO is consistent with the relatively weak dependence on ion internal energy of the branching ratio for these dissociations, expressed as the product ion intensity ratio [*m/z* 330]/[*m/z* 329]. Vibrational excitation by collisional activation gave [*m/z* 330]/[*m/z* 329] = 0.67 from [$^{\bullet}$ATAR+H^+] and [*m/z* 344]/[*m/z* 343] = 0.78 for the homologous [$^{\bullet}$ATAR-OCH_3+H^+]. Upon higher-energy photoexcitation these ratios shift to 0.95 and 1.02, respectively, equally favoring the C_3H_7NO and $C_3H_6NO^{\bullet}$ loss. This can be explained by energy-dependent competition between fragment separations in **7.** This can proceed through a loose transition state for loss of $C_3H_6NO^{\bullet}$ which is preferred at higher internal energies, or a hydrogen migration (tight transition state) forming $CH_3CH_2CONH_2$ in the very stable complex **9**, which is expected to be competitive at internal energies closer to **TS6**. It should be noted, however, that the dissociation kinetics are expected to be affected by substantial kinetic shifts,[81,82] requiring excess energy for the reaction to proceed on the experimental time scale. RRKM calculations of rate constants (Figure 12) indicate a 110 kJ mol^{-1} kinetic shift for 50% conversion of *trans*-**1** via **TS6** at 30 ms which is comparable to the experimental time scale for the dissociations. The mean energy in photoexcited *trans*-**1** is composed of the ion 310 K ro-vibrational enthalpy (80 kJ mol^{-1}) and the 355 nm photon energy to give E = 80 + 337 = 417 kJ mol^{-1} which substantially exceeds the energy needed to proceed through **TS6** even considering the kinetic shift.

The Thr beta radical *trans*-**5** can also represent an intermediate for the formation of the $[z_2+H]^{+\bullet}$ fragment ion observed in the CID spectrum. In the proposed reaction sequence (Scheme 3), radical-promoted cleavage of the adjacent C_α–CO bond can proceed via **TS7,** forming a complex of the incipient a_2 and $[x_2+H]^{+\bullet}$ fragments (**10a**). The a_2 molecule can undergo a stabilizing prototropic rearrangement (**10b**) that lowers the dissociation threshold for the formation

of the $[x_2+H]^{+\bullet}$ ion. This ion spontaneously dissociates by loss of HNCO[40] to form the $[z_2+H]^{+\bullet}$ ion.

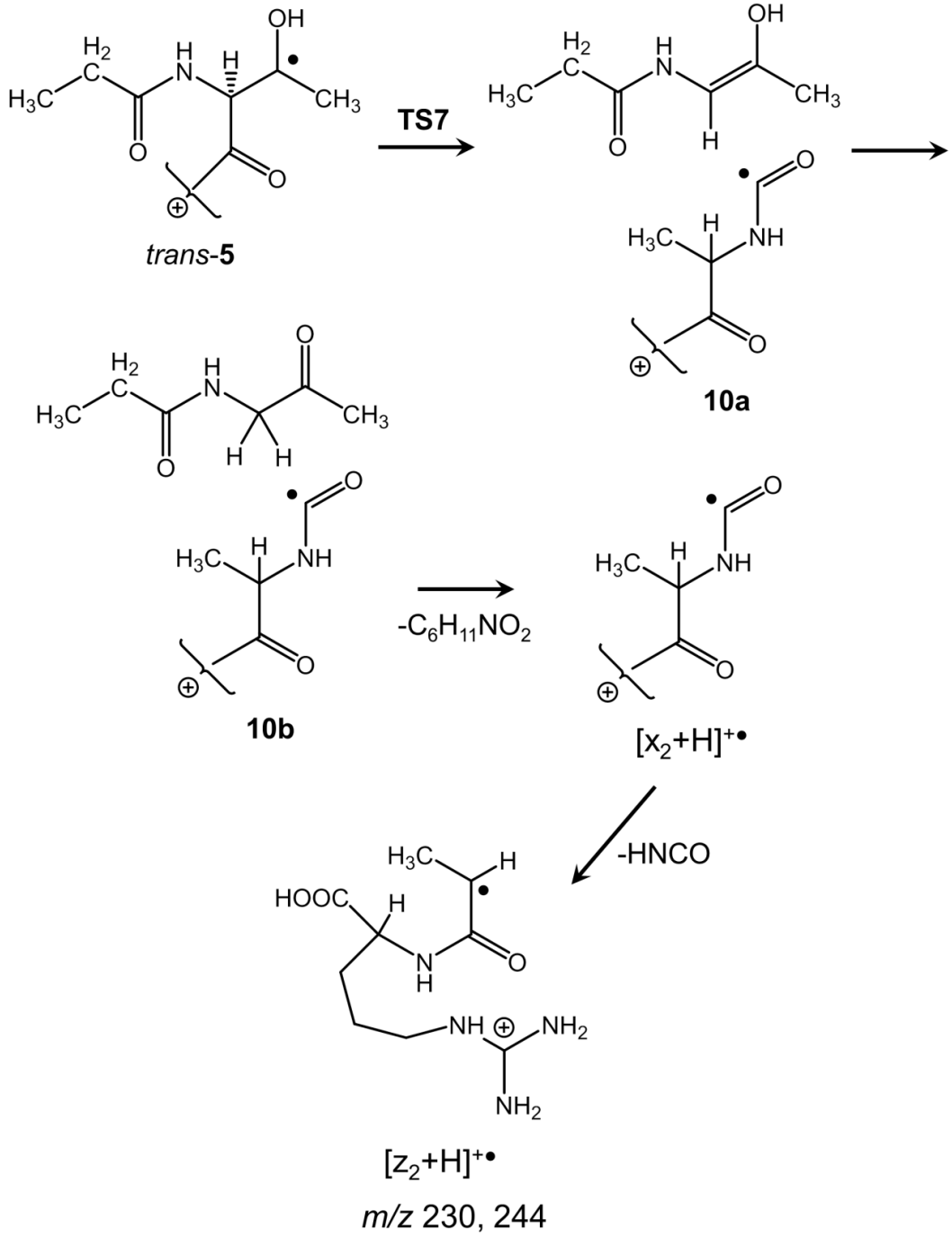

Scheme 3. Proposed reaction scheme leading to the formation of $[z_2+H]^{+\bullet}$ ions

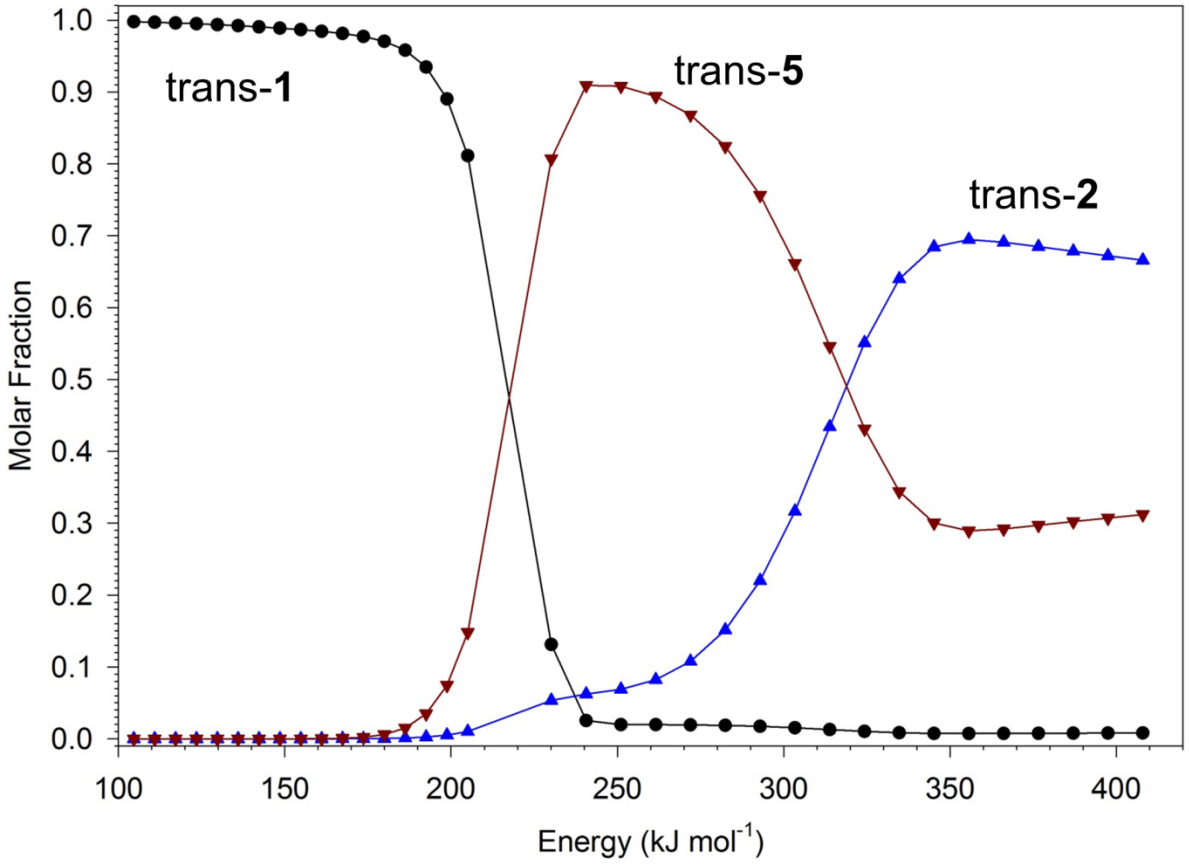

Figure 12. Internal energy dependent molar fractions of *trans*-**1**, *trans*-**2**, and *trans*-**5** calculated from isomerization kinetics on a 30 ms time scale. *trans*-**2** is formed by the reaction sequence trans-**1** ⇔ **TS1** ⇔ cis-**1** ⇔ **TS2** ⇔ cis-**2** ⇔ **TS3** ⇔ *trans*-**2**. *trans*-**5** is formed by the reaction sequence *trans*-**1** ⇔ **TS1** ⇔ *cis*-**1** ⇔ **TS4** ⇔ *cis*-**5** ⇔ **TS5** ⇔ *trans*-**5**. Refer to Figure 6 of the main text for the TS energies.

5. 3. 6 Born-Oppenheimer Molecular Dynamics of Water Complexes

The role of ion-molecule complexes is further emphasized by the analysis of the dissociation pathways for the elimination of water from the Thr side chain, which is one of the major CID processes of $[^{\bullet}\text{ATAR+H}]^{+}$ and $[^{\bullet}\text{ATAR-OCH3+H}]^{+}$ ions, accounting respectively for 23 and 22% of the total fragment ion intensity. We note that the side-chain hydroxyl, such as in Ser and Thr, substantially promotes loss of water from $[z_4\text{+H}]^{+\bullet}$ ions; in the absence of a side-chain OH the loss of water accounts for only 0.1-4.7% for various amino acid residues.[37]

Upon UVPD, the loss of water from $[^{\bullet}ATAR+H]^+$ competes with the loss of the side-chain OH radical, which indicates a common transition state for these dissociations involving cleavage of the threonine C−OH bond. We considered that dissociation of the C−OH bond can be promoted in the C_α radical *trans*-**2** which is accessible from *trans*-**1** via **TS2** and **TS3** (Figure 10). In the TS for the OH loss (**TS8**) the C_β−OH bond is almost interrupted at 2.444 Å, and the OH radical is hydrogen bonded to the Arg guanidinium cation. The further development along the reaction pathway depends on the ion internal energy. At high energies accessed by photon absorption, the OH radical departs forming the $[z_4 + H - OH]^+$ fragment ions. At lower excitations accessed by collisional activation, the OH radical abstracts a hydrogen atom from the $[z_4 + H - OH]^+$ ion and departs as a water molecule.

The search for a transition state for water elimination is difficult because of multiple hydrogen-bonding interactions between the polar counterparts that can lead to many possible transition states. We therefore resorted to a BOMD analysis that was performed with nine reaction trajectories starting with a complex (**11a**) accessed from **TS8**. The general feature of these trajectories was an early abstraction of a guanidinium hydrogen (H-52, Scheme 4) by the OH radical, (O-7−H-54, Scheme 4), forming a water complex with the $[z_4+H - H_2O]^+$ ion. The further development of the water complex differed among the trajectories, but several included a transfer a hydrogen atom from the Thr methyl group. To illustrate a possible reaction sequence leading to loss of water, we plot one trajectory showing the development of interactions of the hydroxyl O-7 and H-54 atoms with several atoms in the $[z_4+ H - OH]^+$ counterpart. In the course of 200 fs, the OH radical captures the H-bonding Arg hydrogen atom (H-52) forming a water complex with a guanidine cation radical (**11b**, Scheme 4). This is shown in Figure 13 as a crossing of the O-7−H-52 (red) and N-28−H-52 (green) trajectories at 200 fs.

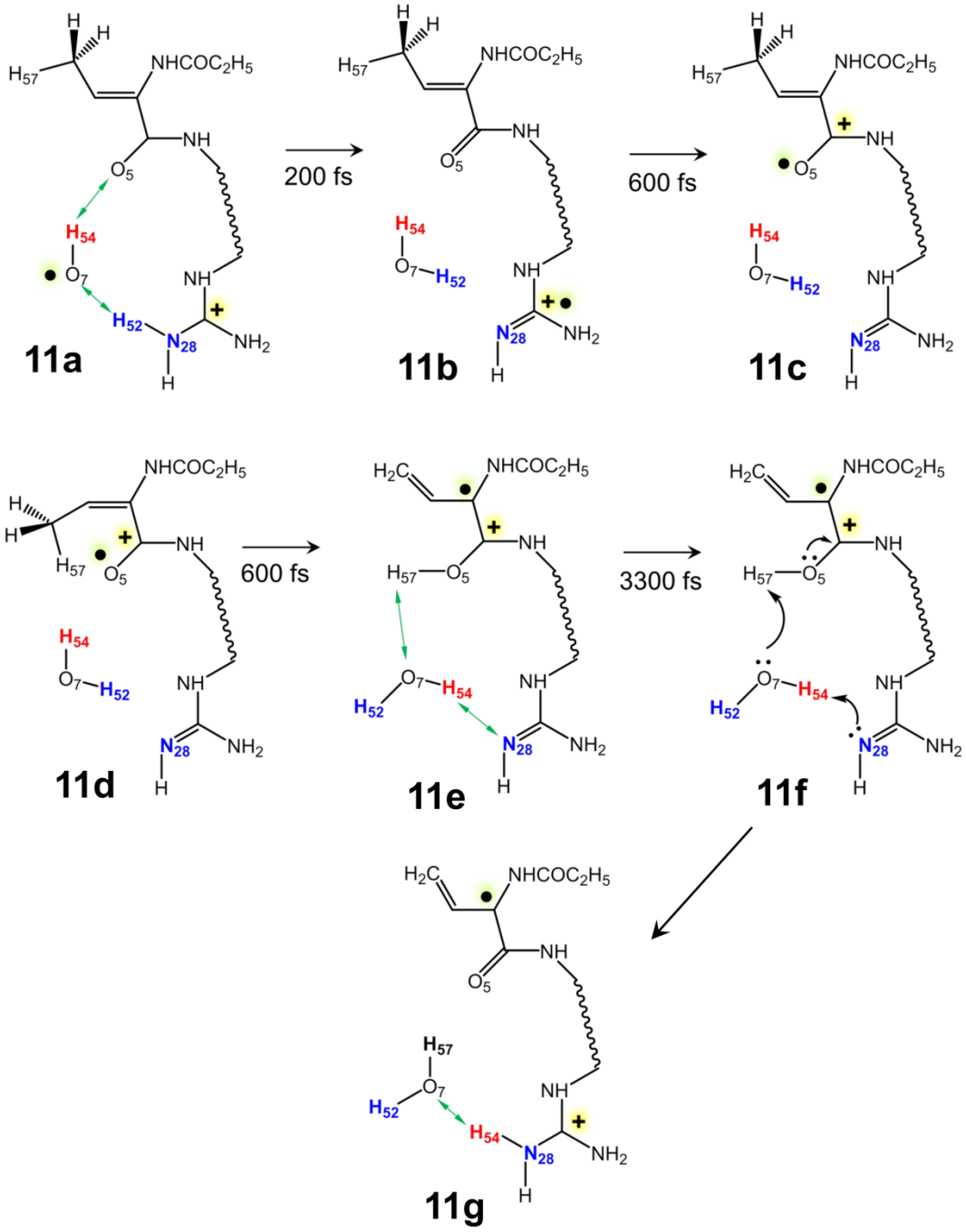

Scheme 4. Snapshot structures of critical points along a selected BOMD trajectory for loss of water.

At 600 fs, complex **11b** undergoes electron transfer to the guanidine group, ionizing the Thr ene-amide group (**11c**). Intramolecular electron transfer was indicated by ωB97X-D/6-31+G(d,p) population analysis of several snapshots on the trajectory at 575-590 fs that showed ~95% spin density accumulation in the Thr residue, chiefly at the C_α and C_β atoms. This intramolecular red-ox reaction is only slightly endothermic, as deduced from the calculated ionization energies of ethylguanidines (7.75-8.09 eV) and the ene-amide fragment (8.27 eV, Table S30, Supporting Information) and can be promoted by the thermal energy of the complex. The electron transfer is followed by rotation about the enamide double bond (**11d**) and transfer of H-57 from the Thr methyl to the amide O-5 (**11e**). This is shown in Figure 13 by the collapse of the O-5−H-57 (purple) trajectory to within 1 Å at 600 fs. In the subsequent development, the water molecule reorients itself, forming complex **11f** developing H-bonds to H-54 and the guanidine N-28. This is shown in Figure 13 by the N-28−H-54 bond distance (turquoise trajectory) oscillating between 1.6 and 3.4 Å. This configuration lasts until about 3.2 ps when a very fast tandem proton transfer occurs moving H-57 to O-7 (blue curve) and H-54 to N-28 (crossing of the black and turquoise curves) and forming another complex (**11g**). Thus, in the course of 3 ps, the O-7 atom in the water molecule interacts with several protons, including the initially exchangeable (H-52, H-54) and non-exchangeable (H-57) hydrogen atoms, and resulting in isomerizations in the remote parts of the complex. The intricate trajectory in complexes **11a-g** is a result of a stepwise exothermic isomerization which is counterbalanced by the substantial water binding energy (61 kJ mol^{-1} in **11b-g**) that delays immediate dissociation.

The C_α radical *trans*-**2** can be considered as an intermediate for another dissociation pathway leading to the $[y_3]^+$ fragment ion which is realized upon UVPD but not CID. Scheme 5 shows cleavage of the CO—NH bond in *trans*-**2** proceeding through **TS9** and forming intermediate

complex **12** at 139 kJ mol^{-1} relative to *trans*-**1**. Fragment separation in **12** is asymptotically endothermic, leading to the loss of $CH_3CH_2CO^{\bullet}$ and formation of the $[y_3]^+$ ion with a threshold energy of 164 kJ mol^{-1} relative to *trans*-**1** (Table 4). The relatively high dissociation threshold for the formation of $[y_3]^+$ may explain why the dissociation is not competitive under CID conditions. However, it can also be argued that the photodissociative loss of $CH_3CH_2CO^{\bullet}$ proceeds on the potential energy surface of the excited electronic state where the formation of *trans*-**2** can be avoided.[38]

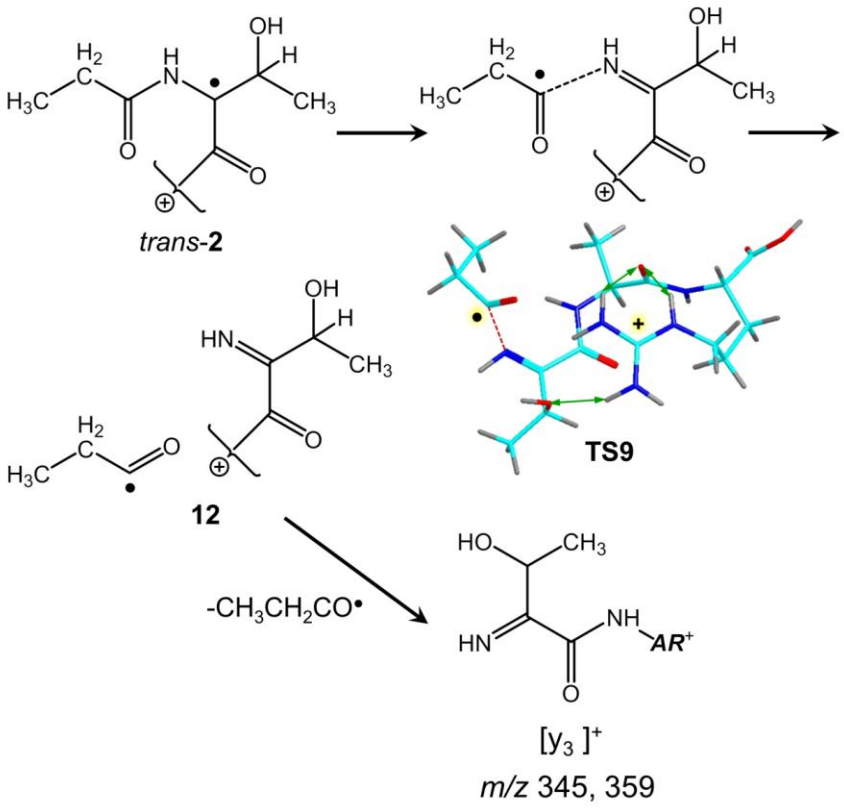

Scheme 5. Proposed reaction scheme leading to the formation of $[y_3]^+$ ions.

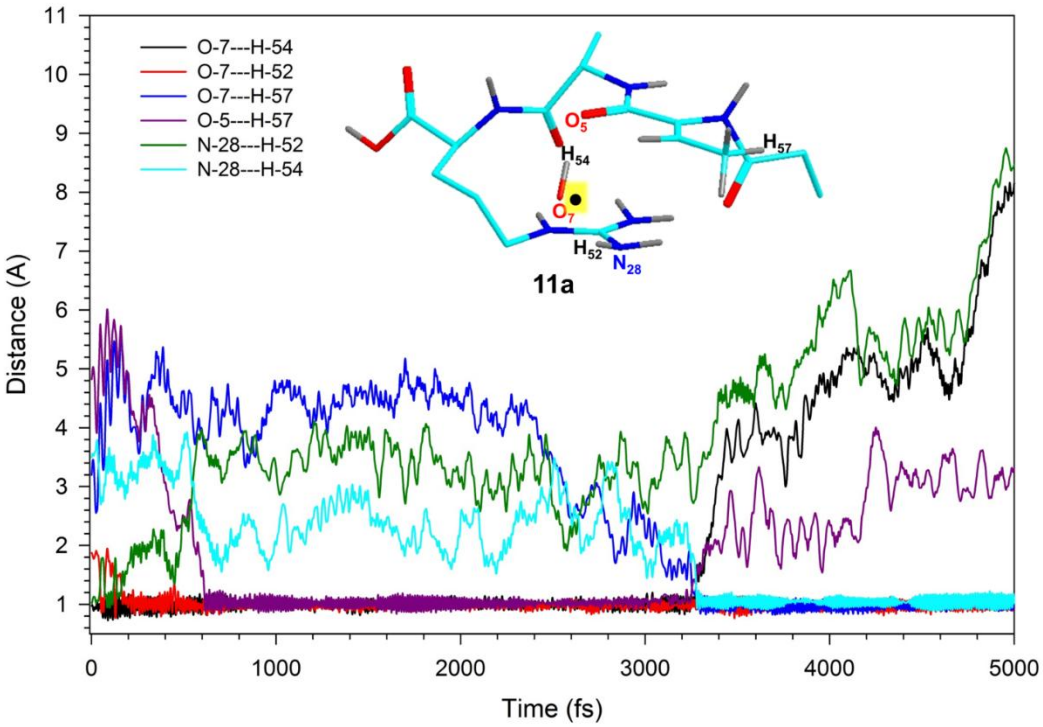

Figure 13. PM6-D3H4 BOMD trajectory analysis of N−H and O−H atomic distances in complexes **11a-g**.

5. 4 Conclusions

UV-VIS photodissociation action spectroscopy provides unequivocal evidence that the $[^{\bullet}$Ala-Thr-Ala-Arg+H$]^+$ ion formed by electron transfer dissociation retains its canonical structure in which the radical defect is at the deaminated Ala N-terminus. This finding contributes to our understanding of $[z_n+H]^{+\bullet}$ ions structure and stability when formed by exothermic electron transfer dissociation. Extensive TD-DFT calculations of $[z_4+H]^{+\bullet}$ ion isomers indicated that the radical position in the peptide ion affects the absorption spectra to allow one to identify the radical isomers. This conclusion is further corroborated by TD-DFT calculations that include vibronic band broadening, leading to improved fit with experimental action spectra. The combination of Born-Oppenheimer molecular dynamics, DFT gradient optimization, and intrinsic reaction

coordinate search has been applied for the first time to analyze the potential energy surface of an open-shell peptide ion. This approach holds a tremendous potential in providing potential energy surfaces of improved quality that can be used for calculations of absolute rate constants for peptide radical reactions.

5. 5 References

(1) Voicescu, M.; El Khoury, Y.; Martel, D.; Heinrich, M.; Hellwig, P. Spectroscopic Analysis of Tyrosine Derivatives: On the Role of the Tyrosinehistidine Covalent Linkage in Cytochrome c Oxidase. *J. Phys. Chem. B* **2009**, *113*, 13429–13436.

(2) Sjoberg, B.M.; Reichard, P.; Graslund, A.; Ehrenberg, A. Nature of the Free Radical in Ribonucleotide Reductase from Escherichia coli. *J. Biol. Chem.* **1977**, *252*, 536–541.

(3) Knappe, J.; Sawers, G. A Radical-Chemical Route to Acetyl-CoA: The Anaerobically Induced Pyruvate Formate-Lyase System of Escherichia coli. *FEMS Microbiol. Rev*. **1990**, *6*, 383–398.

(4) Sawers, G.; Watson, G. A Glycyl Radical Solution: Oxygen-Dependent Interconversion of Pyruvate Formate-Lyase. *Mol. Microbiol.* **1998**, *29*, 945–954.

(5) Whittaker, M. M.; DeVito, V. L.; Asher, S. A.; Whittaker, J. W. Resonance Raman Evidence for Tyrosine Involvement in the Radical Site of Galactose Oxidase. *J. Biol. Chem.* **1989**, *264*, 7104–7106.

(6) Ulas, G.; Lemmin, T.; Wu, Y.; Gassner, G. T.; DeGrado, W. F. Designed Metalloprotein Stabilizes a Semiquinone radical. *Nature Chem*. **2016**, *8*, 354–359.

(7) Moore, G. F.; Hambourger, M.; Gervaldo, M.; Poluektov, O. G.; Rajh, T.; Gust, D.; Moore, T. A.; Moore, A. L. A Bioinspired Construct That Mimics the Proton Coupled Electron Transfer

Between P680•+ and the TyrZ-His190 Pair of Photosystem II. *J. Am. Chem. Soc.* **2008**, *130*, 10466–10467.

(8) Stubbe, J.; van der Donk, W. A. Protein Radicals in Enzyme Catalysis. *Chem. Rev.* **1998**, *98*, 705–762.

(9) Levin, B. J.; Huang, Y. Y.; Peck, S. C.; Wei, Y.; Martinez-del Campo, A,; Marks, J. A.; Franzosa, E. A.; Huttenhower, C.; Balskus, E. P. A Prominent Glycyl Radical Enzyme in Human Gut Microbiomes Metabolizes *trans*-4-Hydroxy-L-proline. *Science* **2017**, 355, eaai8386 (doi:10.1126/science.aai.8386).

(10) Hawkins, C. L.; Davies, M. J. Generation and Propagation of Radical Reactions on Proteins. *Biochim. Biophys. Acta* **2001**, 1*504*, 196-219.

(11) Yu, D.; Rauk, A.; Armstrong, D. A. Radicals and Ions of Glycine: An Ab initio Study of the Structures and Gas-Phase Thermochemistry. *J. Am. Chem. Soc.* **1995**, *117*, 1789-1796.

(12) Rauk, A.; Yu, D.; Armstrong, D. A. Toward Site Specificity of Oxidative Damage in Proteins: C-H and C-C Bond Dissociation Energies and Reduction Potentials of the Radicals of Alanine, Serine, and Threonine Residues-An Ab initio Study. *J. Am. Chem. Soc.* **1997**, *119*, 208-217.

(13) Block, D. A.; Yu. D.; Armstrong, D. A.; Rauk. A. On the Influence of Secondary Structure on the α-C-H Bond Dissociation Energy of Proline Residues in Proteins: A Theoretical Study. *Can. J. Chem.* **1998**, *76*, 1042-1048.

(14) Rauk, A.; Yu, D.; Taylor, J.; Shustov, G. V.; Block, D. A.; Armstrong, D. A. Effects of Structure on RC-H Bond Enthalpies of Amino Acid Residues: Relevance to H Transfers in Enzyme Mechanisms and in Protein Oxidation. *Biochemistry* **1999,** *38,* 9089-9096.

(15) Green, M. C.; Dubnicka, L. J.; Davis, A. C.; Rypkema, H. A.; Francisco, J. S.; Slipchenko, L. V. Thermodynamics and Kinetics for the Free Radical Oxygen Protein Oxidation Pathway in a

Model for β-Structured Peptides. *J. Phys. Chem. A* **2016**, *120*, 2493–2503.

(16) Chu, I. K.; Rodriquez, C. F.; Lau, T. C.; Hopkinson, A. C.; Siu, K. W. M. Molecular Radical Cations of Oligopeptides. *J. Phys. Chem. B* **2000**, *104*, 3393– 3397.

(17) Gatlin, C. L.; Tureček, F.; Vaisar, T. Copper(II) Amino Acid Complexes in the Gas Phase. *J. Am. Chem. Soc.* **1995**, *117*, 3637-3638.

(18) Tureček, F. Copper-Biomolecule Complexes in the Gas Phase. The Ternary Way. *Mass Spectrom. Rev.* **2007**, *26*, 563-582.

(19) Tureček, F.; Julian, R. R. Peptide Radicals and Cation-Radicals in the Gas Phase. *Chem. Rev.* **2013**, *113*, 6691-6733.

(20) Martens, J.; Grzetic, J.; Berden, G.; Oomens, J. Structural Identification of Electron Transfer Dissociation Products in Mass Spectrometry Using Infrared Ion Spectroscopy. *Nature Commun.* **2016**, *7*, 11754.

(21) Nguyen, H. T. H.; Shaffer, C. J.; Pepin, R.; Tureček, F. UV Action Spectroscopy of Gas-Phase Peptide Radicals. *J. Phys. Chem. Lett.* **2015**, *6*, 4722-4727.

(22) Viglino. E.; Shaffer, C. J.; Tureček, F.: UV-VIS Action Spectroscopy and Structures of Tyrosine Peptide Cation Radicals in the Gas Phase. *Angew. Chem. Int. Ed.* **2016**, *55*,7469-7473.

(23) Zubarev, R. A. Reactions of Polypeptide Ions with Electrons in the Gas Phase. *Mass Spectrom. Rev.* **2003**, *22*, 57-77.

(24) Zubarev, R. A.; Kelleher, N. L.; McLafferty, F. W. Electron Capture Dissociation of Multiply Charged Protein Cations. A Nonergodic Process. *J. Am. Chem. Soc.* **1998**, *120*, 3265–3266.

(25) Syka, J. E. P.; Coon, J. J.; Schroeder, M. J.; Shabanowitz, J.; Hunt, D. F. Peptide and Protein Sequence Analysis by Electron Transfer Dissociation Mass Spectrometry. *Proc. Natl. Acad. Sci. U.S.A.* **2004**, *101*, 9528–9533.

(26) Chu, I. K.; Siu, C.-K.; Lau, J. K.-C.; Tang, W. K.; Mu, X.; Lai, C. K.; Guo, X.; Wang, X.; Li, N.; Yao, Z. et al: Proposed Nomenclature for Peptide Ion Fragmentation. *Int. J. Mass Spectrom.* **2015**, *390*, 24-27.

(27) Yates, B. F.; Bouma, W. J.; Radom, L. Distonic Radical Cations. Guidelines for the Assessment of Their Stability. *Tetrahedron* **1986**, *42*, 6225-6234.

(28) Hammerum, S. Distonic Radical Cations in Gaseous and Condensed Phase. *Mass Spectrom. Rev.* **1988**, *7*, 123-202.

(29) Swaney, D. L.; McAlister, G. C.; Wirtala, M.; Schwartz, J. C.; Syka, J. E. P.; Coon, J. J. Supplemental Activation Method for Highly Efficient Electron Transfer Dissociation of Doubly Protonated Peptide Precursors. *Anal. Chem.* **2007**, *79*, 477–485.

(30) Xia, Y.; Han, H.; McLuckey, S. A. Activation of Intact Electron-Transfer Products of Polypeptides and Proteins in Cation Transmission Mode Ion/Ion Reactions. *Anal. Chem.* **2008**, *80*, 1111–1117.

(31) Brodbelt, J. S. Photodissociation Mass Spectrometry: New Tools for Characterization of Biological Molecules. *Chem. Soc. Rev.* **2014**, *43*, 2757–2783.

(32) Ledvina, A. R.; McAlister, G. C.; Gardner, M. W.; Smith, S. I.; Madsen, J. A.; Schwartz, J. C.; Stafford Jr., G. C.; Syka, J. E. P.; Brodbelt, J. S.; Coon, J. J. Infrared Photoactivation Reduces Peptide Folding and Hydrogen-Atom Migration Following ETD Tandem Mass Spectrometry. *Angew. Chem. Int. Ed.* **2009**, *48*, 8526–8528.

(33) Ledvina, A. R.; Beauchene, N. A.; McAlister, G. C.; Syka, J. E. P.; Schwartz, J. C.; Griep-Raming, J.; Westphall, M. S.; Coon, J. J. Activated Ion Electron Transfer Dissociation Improves the Ability of Electron Transfer Dissociation to Identify Peptides in a Complex Mixture. *Anal. Chem.* **2010**, *82*, 10068–10074.

(34) Pepin, R.; Layton, E. D.; Liu, Y.; Afonso, C.; Tureček, F. Where Does the Electron Go? Stable and Metastable Peptide Cation Radicals Formed by Electron Transfer. *J. Am. Soc. Mass Spectrom.* **2017**, *28*, 164-181.

(35) Antoine, R.; Dugourd, P. Visible and Ultraviolet Spectroscopy of Gas Phase Protein Ions. *Phys. Chem. Chem. Phys.* **2011**, *13*, 16494–16509.

(36) Antoine, R.; Dugourd, P. UV-Visible Activation of Biomolecular Ions. (Laser Photodissociation and Spectroscopy of Mass-Separated Biomolecular Ions) *Lect. Notes Chem.* **2013**, *83*, 93–116.

(37) Chung, T. W.; Hui, R.; Ledvina, A. R.; Coon, J. J.; Tureček, F. Cascade Dissociations of Peptide Cation-Radicals. Part 1. Scope and Effects of Amino Acid Residues in Penta-, Nona- and Decapeptides. *J. Am. Soc. Mass Spectrom.* **2012**, *23*, 1336-1350.

(38) Nguyen, H. T. H.; Tureček, F. Near-UV Photodissociation of Tryptic Peptide Cation Radicals. Scope and Effects of Amino Acid Residues and Radical Sites. *J. Am. Soc. Mass Spectrom.* **2017**, *29*, DOI: 10.1007/s13361-016-1586-7.

(39) Chung, T. W.; Tureček, F. Backbone and Side-Chain Specific Dissociations of ***z*** Ions from Non-Tryptic Peptides. *J. Am. Soc. Mass Spectrom.* **2010**, *21*, 1279-1295.

(40) Ledvina, A. R.; Chung, T. W.; Hui, R.; Coon, J. J.; Tureček, F. Cascade Dissociations of Peptide Cation-Radicals. Part 2. Infrared Multiphoton Dissociation and Mechanistic Studies of z-Ions from Pentapeptides. *J. Am. Soc. Mass Spectrom.* **2012**, *23*, 1351-1363.

(41) Thomas, D. A.; Sohn, C. H.; Gao, J.; Beauchamp, J. L. Hydrogen Bonding Constrains Free Radical Reaction Dynamics at Serine and Threonine Residues in Peptides. *J. Phys. Chem. A* **2014**, *118*, 8380-8392.

(42) Nguyen, H. T. H.; Shaffer, C. J.; Ledvina, A.; Coon, J. J.; Tureček, F. Serine Effects on

Collision-Induced Dissociation and Photodissociation of Peptide Cation Radicals of the $z^{+\bullet}$ Type. *Int. J. Mass Spectrom.* **2015**, *378*, 20-30.

(43) Moss, C. L.; Chamot-Rooke, J.; Brown, J.; Campuzano, I.; Richardson, K.; Williams, J.; Bush, M.; Bythell, B.; Paizs, B.; Tureček, F. Assigning Structures to Gas-Phase Peptide Cations and Cation-Radicals. An Infrared Multiphoton Dissociation, Ion Mobility, Electron Transfer and Computational Study of a Histidine Peptide Ion. *J. Phys Chem. B.* **2012**, *116*, 3445-3456.

(44) Pepin, R.; Laszlo, K. J.; Marek, A.; Peng, B.; Bush. M. F.; Lavanant, H.; Afonso, C.; Turecek, F. Toward a Rational Design of Highly Folded Peptide Cation Conformations. 3D Gas-Phase Ion Structures and Ion Mobility Characterization. *J. Am. Soc. Mass Spectrom.* **2016,** *27*, 1647-1660.

(45) Frisch, M. J.; Trucks, G. W.; Schlegel, H. B.; Scuseria, G. E.; Robb, M. A.; Cheeseman, J. R.; Scalmani, G.; Barone, V.; Mennucci, B.; Petersson, G. A., et al.: Gaussian 09, Revision A.02. Gaussian Inc.: Wallingford CT (2009).

(46) Becke, A.D.: New Mixing of Hartree-Fock and Local Density-Functional Theories. *J. Chem. Phys.* **1993**, *98*, 1372–1377.

(47) Becke, A.D. Density Functional Thermochemistry. III. The Role of Exact Exchange. *J. Chem. Phys.* **1993**, *98*, 5648–5652.

(48) Møller, C.; Plesset, M. S. A Note on an Approximation Treatment for Many-Electron Systems. *Phys. Rev.* **1934**, *46*, 618–622.

(49) Schlegel, H. B. Potential Energy Curves Using Unrestricted Moller-Plesset Perturbation Theory with Spin Annihilation. *J. Chem. Phys.* **1986**, *84*, 4530.

(50) Mayer, I. Spin-projected UHF method. IV. Comparison of Potential Curves Given by Different One-Electron Methods. *Adv. Quantum Chem.* **1980**, *12*, 189–262.

(51) Chai, J. D.; Head-Gordon, M. Systematic Optimization of Long-Range Corrected Hybrid Density Functionals. *J. Chem. Phys.* **2008**, *28*, 084106/1–084106/15.

(52) Chai, J. D.; Head-Gordon, M. Long-Range Corrected Hybrid Density Functionals with Damped Atom-Atom Dispersion Corrections. *Phys. Chem. Chem. Phys.* **2008**, 10, 6615–6620.

(53) Zhao, Y.; Truhlar, D. G. The M06 Suite of Density Functionals for Main Group Thermochemistry, Thermochemical Kinetics, Noncovalent Interactions, Excited States, and Transition Elements: Two New Functionals and Systematic Testing of Four M06-Class Functionals and 12 Other Functionals. *Theor. Chem. Acc.* **2008**, *120*, 215–241.

(54) Stewart, J. J. P. Optimization of Parameters for Semi-Empirical Methods. V. Modification of NDDO Approximations and Application to 70 Elements. *J. Mol. Model.* **2007**, *12*, 1173–1213.

(55) Řezáč, J.; Fanfrlík, J. Salahub, D. Hobza, P. Semi-Empirical Quantum Chemical PM6 Method Augmented by Dispersion and H-Bonding Correction Terms Reliably Describes Various Types of Noncovalent Complexes. *J. Chem. Theory Comput.* **2009**, *5*, 1749–1760.

(56) MOPAC 16, Stewart, J. J. P. Stewart Computational Chemistry: Colorado Springs, CO, USA.

(57) Rezac, J. Cuby: An Integrative Framework for Computational Chemistry *J. Comput. Chem.* **2016**, *37*, 1230-1237. Available at: http://cuby4.molecular.cz.

(58) Furche, F.; Ahlrichs, A. Adiabatic Time-Dependent Density Functional Methods for Excited State Properties. *J. Chem. Phys.* **2002**, *117*, 7433−7447.

(59) Iikura, H.; Tsuneda, T.; Yanai, T.; Hirao, K. A Long-Range Correction Scheme for Generalized-Gradient-Approximation Exchange Functionals. *J. Chem. Phys.* **2001**, *115*, 3540−3544.

(60) Turecek, F. Benchmarking Electronic Excitation Energies and Transitions in Peptide Radicals. *J. Phys. Chem. A* **2015**, *119*, 10101-10111.

(61) Sekino, H.; Bartlett, R. J. A Linear Response, Coupled-Cluster Theory for Excitation Energy. *Int. J. Quantum Chem.* **1984**, *26*, 255−265.

(62) Comeau, D. C.; Bartlett, R. J. The Equation-of-Motion Coupled-Cluster Method. Applications to Open- and Closed-Shell Reference States. *Chem. Phys. Lett.* **1993**, *207*, 414−423.

(63) Barbatti, M.; Aquino, A. J.; Lischka, H. The UV Absorption of Nucleobases: Semi-classical Ab initio Spectra Simulations. *Phys. Chem. Chem. Phys.* **2010**, *12*, 4959 –4967.

(64) Barbatti, M.; Ruckenbauer, M.; Plasser, F.; Pittner, J.; Granucci, G.; Persico, M.; Lischka, H. Newton-X: A Surface-Hopping Program for Nonadiabatic Molecular Dynamics. *Wiley Interdisciplinary Reviews: Comput. Mol. Sci.* **2014**, *4*, 26–33.

(65) Gilbert, R. G.; Smith, S. C. *Theory of Unimolecular and Recombination Reactions*, Blackwell Scientific Publications, Oxford: 1990, pp. 52–132.

(66) Zhu, L.; Hase, W.L.: Quantum Chemistry Program Exchange. Indiana University: Bloomington; Program No. QCPE 644 (1994).

(67) Frank, A. J.; Sadílek, M.; Ferrier, J. G.; Tureček, F. Sulfur Oxoacids and Radicals in the Gas Phase. A Variable-Time Neutralization-Photoexcitation- Reionization Mass Spectrometric and Ab initio/RRKM Study. *J. Am. Chem. Soc.* **1997**, *119*, 12343-12353.

(68) Osburn, S.; Berden, G.; Oomens, J.; O'Hair, R. A. J.; Ryzhov, V. Structure and Reactivity of the N-Acetyl-Cysteine Radical Cation and Anion: Does Radical Migration Occur? *J. Am. Soc. Mass Spectrom.* **2011**, *22*, 1794–1803.

(69) Hao, Q.; Song, T.; Ng, D. C. M.; Quan, Q.; Siu, C. K.; Chu, I. K. Arginine Facilitated Isomerization: Radical-Induced Dissociation of Aliphatic Radical Cationic Glycylarginyl(iso)leucine Tripeptides. *J. Phys. Chem. B* **2012**, *116*, 7627–7634.

(70) Zhao, J.; Song, T.; Xu, M.; Quan, Q.; Siu, K. W. M.; Hopkinson, A. C.; Chu, I. K.

Intramolecular Hydrogen Atom Migration along the Backbone of Cationic and Neutral Radical Tripeptides and Subsequent Radical-Induced Dissociations. *Phys. Chem. Chem. Phys.* **2012**, *14*, 8723–8731.

(71) Osburn, S.; Berden, G.; Oomens, J., O'Hair, R. A. J.; Ryzhov, V. S-to-αC Radical Migration in the Radical Cations of Gly-Cys and Cys-Gly. *J. Am. Soc. Mass Spectrom.* **2012**, *23*, 1019–1023.

(72) Laskin, J.; Kong, R. P. W.: Song, T.; Chu, I. K. Effect of the Basic Residue on the Energetics and Dynamics of Dissociation of Phosphopeptides. *Int. J. Mass Spectrom.* **2012**, *330–332*, 295–301.

(73) Zhang, X.; Julian, R.R. Exploring Radical Migration Pathways in Peptides with Positional Isomers, Deuterium Labeling, and Molecular Dynamics Simulations. *J. Am. Soc. Mass Spectrom.* **2013**, *24*, 524– 533.

(74) Osburn, S.; Berden, G.; Oomens, J.; Gulyuz, K.; Polfer, N. C.; O'Hair, R. A. J.; Ryzhov, V. Structure and Reactivity of the Glutathione Radical Cation: Radical Rearrangement from the Cysteine Sulfur to the Glutamic Acid α-Carbon Atom. *ChemPlusChem.* **2013**, *78*, 970–978.

(75) Lai, C.-K.; Mu, X.; Hao, Q.; Hopkinson, A. C.; Chu, I. K. Formation, Isomerization, and Dissociation of ε- and α-Carbon-Centered Tyrosyl Glycyl Glycine Radical Cations. *Phys. Chem. Chem. Phys.* **2014**, *16*, 24235–24243.

(76) Xu, M.; Tang, W.-K.; Mu, X.; Ling, Y.; Siu, C.-K.; Chu, I. K. α-Radical Induced CO2 Loss from the Aspartic Acid Side Chain of the Collisionally Induced Tripeptide Aspartylglycylarginine Radical Cation. *Int. J. Mass Spectrom.* **2015**, *390*, 56–62.

(77) Lesslie, M.; Osburn, S.; van Stipdonk, M. J.; Ryzhov, V. Gas-Phase Tyrosine-to-Cysteine Radical Migration in Model Systems. *Eur. J. Mass Spectrom.* **2015**, *21*, 589–597.

(78) Osburn, S.; Chan, B.; Ryzhov, V.; Radom, L.; O'Hair, R. A. J. Role of Hydrogen Bonding on

the Reactivity of Thiyl Radicals: A Mass Spectrometric and Computational Study Using the Distonic Radical Ion Approach. *J. Phys. Chem. A* **2016**, *120*, 8184–8189.

(79) Pepin, R., Tureček, F.: Kinetic Ion Thermometers for Electron Transfer Dissociation. *J. Phys. Chem. B* **2015**, *119*, 2818–2826.

(80) Gonzalez, C.; Schlegel, H. B. An Improved Algorithm for Reaction Path Following. *J. Chem. Phys.* **1989**, *90*, 2154-2161.

(81) Lifshitz, C. Time-Resolved Appearance Energies, Breakdown Graphs, and Mass Spectra: The Elusive Kinetic Shift. *Mass Spectrom. Rev.* **1982**, *1*, 309-340.

(82) Laskin, J.; Futrell, J. H.; Chu, I. K. Is Dissociation of Peptide Cation-Radicals an Ergodic Process? *J. Am. Chem. Soc.* **2007**, *129*, 9598-9599.

Chapter 6: Photodissociative Crosslinking of Noncovalent Peptide-Peptide Ion Complexes in the Gas Phase

Reproduced with permission from Nguyen, H. T., Andrikopoulos, P. C., Rulíšek, L., Shaffer, C. J. & Tureček, F. (2018). *Manuscript in Progress*

***Abstract*:** We report a gas-phase UV photodissociation study investigating non-covalent interactions between neutral hydrophobic pentapeptides and peptide ions incorporating a diazirine-tagged photoleucine residue. Phenylalanine (Phe) and proline (Pro) were chosen as the conformation-affecting residues that were incorporated into a small library of neutral pentapeptides. Gas-phase ion-molecule complexes of these peptides with photolabeled pentapeptides were subjected to photodissociation. Selective photocleavage of the diazirine ring at 355 nm formed short-lived carbene intermediates that underwent crosslinking by insertion into H-X covalent bonds of the target peptide. The crosslink positions were established from collision-induced dissociation tandem mass spectra (CID-MS^3) providing sequence information on the covalent adducts. Effects of the amino acid residue (Pro or Phe) and its position in the target peptide sequence were evaluated. For proline-containing peptides, interactions in these complexes resulting in covalent crosslinks became more prominent as proline was moved towards the C-terminus of the target peptide sequence. The photocrosslinking yields of phenylalanine-containing peptides were strongly dependent on the position of both phenylalanine and photoleucine. Born-Oppenheimer molecular dynamics (BOMD) calculations were used for conformational analysis of close contacts in the peptide ion complexes, and the computational results are discussed vis-a-vis the experimental data.

6.1 Introduction

Chemical crosslinking relies on the formation of covalent bonds between components of a non-covalent complex or different sites in a single large molecule [1,2]. With the introduction and development of photoactivated [2] and photodissociative [3-5] crosslinking reagents it became possible to generate highly reactive and short lived intermediates to map contacts between the transient reactive group and sites in the target molecule. The diazirine ring, in particular, has been utilized as a photocleavable group that undergoes specific elimination of nitrogen at 355-370 nm [6]. Diazirine photolysis forms a transient reactive carbene that can undergo insertion into proximate X-H bonds, forming covalent cross links (Scheme 1).

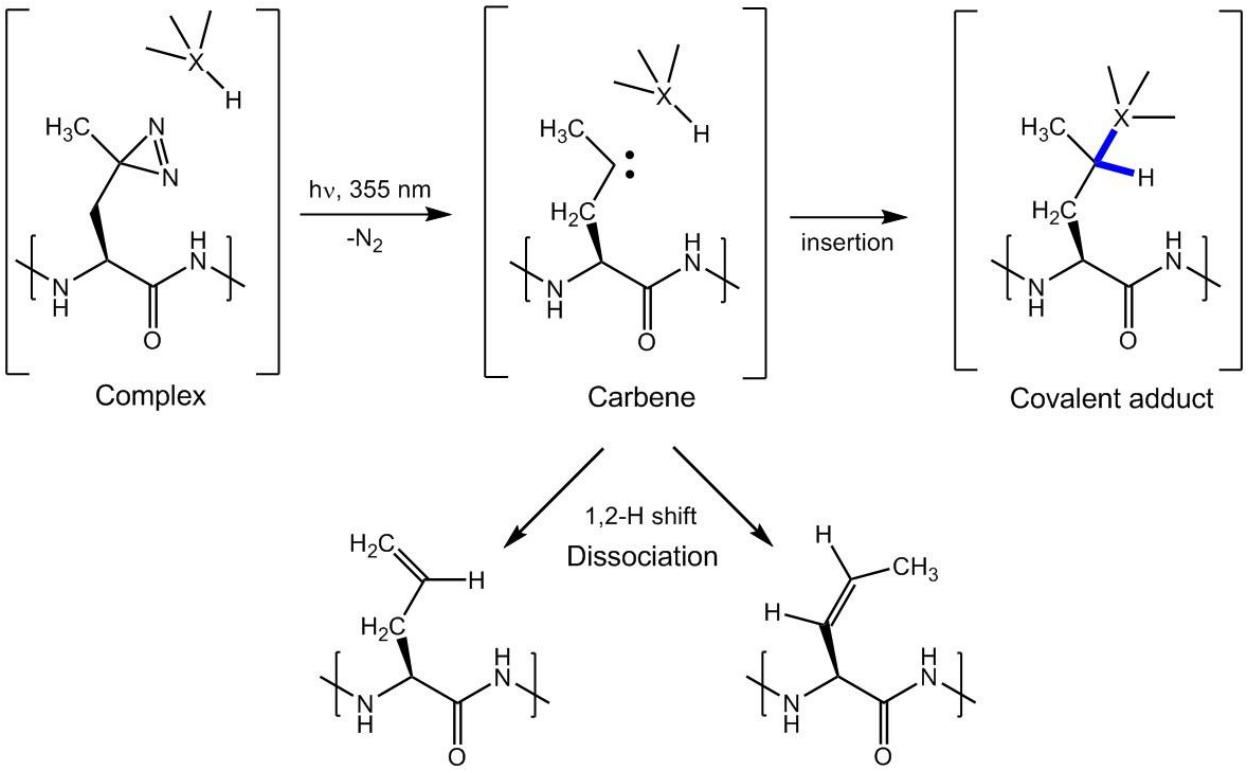

Scheme 1. Diazirine photodissociation and carbene reactions.

The diazirine ring can be introduced into the protein or peptide of interest by using photolabile amino acid residues such as photoleucine (L-2-amino-4,4-azi-pentanoic acid, L*), photomethionine (L-2-amino-5,5-azi-hexanoic acid, M*) [7], or the recently reported photolysine (L-2,6-diamino-4,4-azi-hexanoic acid)[8]. Photoleucine has been shown to be a useful surrogate for the corresponding natural amino acid, and can be used for photochemical footprinting in expressed proteins [7].

Recently, photochemical cross-linking using diazirine tags has been applied to gas-phase peptide-peptide ion complexes [9]. In this approach, we used electrospray ionization to produce non-covalent ion-molecule complexes of a photo-tagged peptide with target peptides that were selected by mass, and stored in an ion trap mass spectrometer. Irradiation with a 355-nm laser beam of the mass-selected complex resulted in N_2 elimination that was associated with covalent bond formation in cross-links. Crosslinking in gas-phase peptide-peptide ion complexes has been shown to achieve efficiencies [9,10] that exceed those observed in solution crosslinking using diazirine-tagged peptides [11]. Recently, we have expanded the portfolio of diazirine-tagged amino acid residues for gas-phase peptide cross linking by position-tunable tags placed at the ε-amino group in lysine residues and *N*-terminal amino groups [10]. Photodisociation at 157 nm of peptide complexes [12] and cation-anion reactions [13] have also been used to form covalent bonds in the gas-phase ions.

Scheme 1 indicates that photolytically produced carbene intermediates can be quenched by competitive 1,2-hydrogen shifts from the neighboring methylene or methyl group, forming unreactive olefins. While these side reactions, as well as reactions with solvent, are detrimental in solution studies [14], the nanosecond kinetics of the 1,2-H shift [15] provides an internal clock for crosslinking in gas-phase complexes where insertions in the X-H bonds occur only if they proceed

on a comparable time scale. We utilize this feature for determining the time scale for molecular dynamics calculations of trajectories describing the thermal motion in gas-phase complexes with the goal of identifying close contacts between the incipient carbene atom of the photo-tagged peptide and X-H bonds in the target peptide. Herein, we exploit our gas-phase crosslinking technique to study conformations of gas-phase ion-molecule complexes generated from the combination of photoactive peptides GL*LLK, GLL*LK, and GLLL*K with two small libraries of neutral hydrophobic pentapeptides. One library includes proline-containing pentapeptides PGLMG, GPLMG, GLPMG, GLMPG, and GLMGP. In the other library, Pro residues were replaced by Phe as in GFLMG, GLFMG, and GLMFG. Proline is known to affect the chain conformation in proteins [16-20] where it forms β turns, reversing the direction of the polypeptide chain. [20] Proline has a distinctive cyclic structure and tertiary amide nitrogen, giving it an exceptional conformational rigidity compared with other residues. [18] We hypothesized that the conformational rigidity of proline could potentially play a role in affecting the conformation of a small neutral peptide in the gas phase, and thus enhance the specificity of its interaction with photopentapeptides. Polyproline peptide ions have been shown by ion mobility to exhibit interesting conformational properties in the gas phase [21]. In addition to proline, we also considered phenylalanine as another residue for modulating non-covalent interactions of the neutral pentapeptide with its photopeptide counterpart. In contrast to proline, phenylalanine does not have a strong effect on the backbone conformation of the peptide sequence. However, the aromatic side chain could restrict the motion of the neutral Phe-containing peptides in the direction perpendicular to the ring plane, which is aligned with the peptide ion backbone. Pro- and Phe-containing peptides with the sequences used in this study appear as sequence motifs in a number of biologically important proteins. For example, the motif PGLMG was found in over 1000

proteins present in the Boreoeutheria class. [22] The PGLMG motif appears mostly in type I through IV collagen proteins, which are the major structural components of the basement membrane. Hence, the insight gained from the gas-phase study could enhance our understanding of non-covalent binding in large biomolecules.

The size of the neutral target peptides was limited to five residues to allow us to conduct a computational analysis of conformational trajectories using Born Oppenheimer molecular dynamics (BOMD) and compare the results to experimental data. All BOMD calculations were run at the PM6-D3H4 augmented semi-empirical level of quantum theory that accounts for hydrogen bonding and London dispersion interactions [23]. Both these interactions must be considered in addressing the stability and dynamics of the gas-phase complexes [23]. We wish to demonstrate the effect that proline and phenylalanine have in modulating non-covalent interactions of dimer complexes formed in the gas phase. Our other goal was to illustrate the utility of diazirine photochemistry in conjunction with BOMD computational analysis for probing the structure and dynamics of peptide-peptide ion interactions in the gas phase.

6.2 Experimental Section

6. 2. 1 Materials: Photo-labeled peptides: GL*LLK, GLL*LK, and GLLL*K were synthesized using standard solid phase peptide Fmoc techniques on Wang resin (Bachem Americas, Torrance, CA, USA) [24, 25]. Photoleucine (L*, L-2-amino-4,4-azi-pentanoic acid) and its and Fmoc protected derivative were purchased from Life Technologies, Rockford, IL, U.S.A.)). All neutral peptides, PGLMG, GPLMG, GLPMG, GMLPG, GLMGP, GFLMG, GLFMG, GMLFG were synthesized on a CEM Liberty Blue synthesizer (CEM, Matthews, N.C., U.S.A) using standard Fmoc techniques.

6. 2. 2 Methods: The peptide-peptide complexes were formed by electrospray of peptide mixture solutions. Typically, 50 μL of the neutral peptide solution (5−10 μM in 50:50:1 methanol/water/acetic acid) was mixed with 100 μL of the photopeptide solution (5−10 μM in 50:50:1 methanol/water/acetic acid). The mixed solution was electrosprayed at 2.2-2.3 kV from a pulled fused silica with a syringe pump capillary. The singly-charged complex ions were mass-selected, stored in a modified LTQ-XL ETD linear ion trap (LIT) mass spectrometer (ThermoElectron Fisher, San Jose, CA, USA), and then photodissociated at 355 nm [26]. Photodissociative loss of N_2 formed product ions that were subjected to CID-MS^3 for sequencing.

Briefly, the UV photodissociation-tandem mass spectrometry (UVPD-MS^2) experiments were conducted by first isolating the singly-charged complex ions of interest in the LIT for a period of time, and then irradiating them with the laser beam, which is produced by an EKSPLA NL 301 HT (Altos Photonics, Bozeman, MT, USA) Nd-YAG laser operating at 20 Hz frequency with a 3-6 ns pulse width. Due to the maximum frequency at which the laser is fired (20 Hz), each laser pulse requires a 50-ms ion storage time. The number of laser pulses could be varied to accomplish a pulse-dependent study by changing the storage time of the trapped ions in the LIT. A third harmonic frequency generator was also included in the path to produce a single 355 nm wavelength at a maximum 120 mJ/pulse peak power. However, a typical photodissociation experiment only uses 18 mJ/pulse light intensity. Both the laser system and the LTQ-XL are set on an optical table for optimum alignment. The laser was interfaced to the LTQ by LabView software (National Instruments, Austin, TX, USA) that receives a signal from a TTL pulse on pin14 of the J1 connector on the LTQ console. Laser pulses are triggered internally by the EKSPLA system, but the power is controlled for each pulse by commands from the LabView software.

6. 2. 3 Born Oppenheimer Molecular Dynamics (BOMD) calculations. All molecular dynamics calculations used the all-electron semiempirical PM6-D3H4 [23] method with the Berendsen thermostat algorithm [27] at a constant temperature of 310 K. Twenty-five initial structures were generated with different orientations of the photoactivable diazirine, and the charging proton was placed on the ε-amine of the lysine residue of the photopentapeptide. For each initial structure, a preliminary MD was conducted with a duration of 20 ps to obtain 200 snapshots. The total of 25 × 200 = 5000 snapshot structures were then subjected to full optimization with PM6-D3H4 that was run by MOPAC coupled with the Cuby4 framework that provided a high-level platform [28,29]. The 5000 fully optimized PM6-D3H4 snapshot structures were sorted out by energy, and 650 low-energy structures were re-optimized by density functional theory (DFT) calculations with BLYP [30,31]/def-SV(P) [32] including dispersion corrections. These calculations were run with TurboMole [33]. Twelve complexes with the lowest DFT energies, and having conformations with different orientations of the L* and target peptide subunits, were then selected and submitted as initial structures to a full BOMD run for 100 ps. The trajectories were run at 310 K, which was the ion trap temperature used in the measurements (310 K).

Thermochemical calculations were performed using the Gaussian 09 (Revision A.02.)[34]and Gaussian 16 (Revision A.03) [35] suites of programs. Twelve lowest-energy structures from the BLYP/def-SV(P) calculations were re-optimized with B3LYP/6-31G(d,p) to provide harmonic frequencies that were used to evaluate enthalpies, entropies, and thermal free-energy corrections at 310 K. In separate runs, these 12 initial structures were re-optimized with ωB97X-D [36,37] and the 6-31+G(d,p) basis set. These calculations included dispersion interactions in the complexes, and the obtained energies were used to evaluate the electronic terms of the free energies. The calculated relative free energies including electronic, vibrational, and

rotational terms (Table 5) were used to calculate equilibrium molar fractions of the gas-phase complexes at 310 K (Table 6).

Note on the Complex Ion Nomenclature: To describe the fragment ions originating from the complexes, we utilize the nomenclature system previously described by Shaffer *et.al* [9]. Briefly, all the target peptides are referred to with a small letter (m) while the photopeptides are labeled with a capital letter (M), such as $(mM - N_2 + H)^+$ for complexes produced by loss of N_2. Fragment ions resulting from backbone dissociation in the target peptide are denoted as b_n (retaining *N*-terminal residues) and y_n (retaining C-terminal residues). Similarly, fragment ions resulting from backbone cleavage in the photopeptides are denoted as B_m and Y_m. The combination of fragments from both neutral and photo-peptides are labeled adequately [b_nB_m, y_nY_m, etc), according to the observed *m/z*. A simple representation for this ion nomenclature system is illustrated in Figure 1 for the dimer complex $(GLPMG + GLL^*LK + H)^+$.

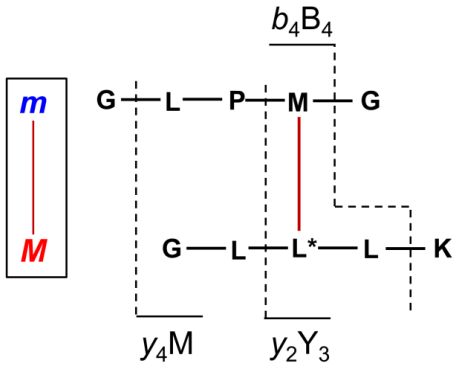

Figure 1. Fragment-ion nomenclature in peptide-peptide crosslinks.

6. 3 Results and Discussion

6. 3. 1 Photocrosslinking of Pro-Containing Target Peptides:

Electrospray ionization (ESI) of peptide-peptide complexes yielded singly charged ions of the non-covalent complexes in 1.9-14.4% yields relative to the singly charged peptide ions that were the main species in the ESI mass spectra (Table 1). This is illustrated for the complex of GPLMG with GL*LLK at *m/z* 1028 (Figure 2a). The $(GPLMG + GL^*LLK + H)^+$ complex was selected by mass and subjected to collision-induced dissociation (CID) and photodissociation at 355 nm (UVPD). CID-MS^2 of $(GPLMG + GL^*LLK + H)^+$ resulted in complex dissociation, forming $(GL^*LLK + H)^+$ (*m/z* 555) as the major charged fragment along with its dissociation product, $(GL^*LLK - N_2 + H)^+$ (*m/z* 527, Figure 2b). CID-MS^2 of the other complexes gave very similar results. These results indicated that the non-covalent interactions of the peptide moieties in the complexes were readily disrupted by CID without substantially affecting the photoactive diazirine group [9,10]. In contrast, UVPD-MS^2 resulted in a major loss of N_2 while preserving the complex as an $(mM - N_2 + H)^+$ ion. This is illustrated by the UVPD-MS^2 spectrum of $(GPLMG + GL^*LLK + H)^+$ displaying the $(mM - N_2 + H)^+$ ions at *m/z* 1000 (Figure 2c). To achieve high (>50%) conversion of the precursor ions, 36 laser pulses were uniformly used for UVPD-MS^2. Note that the photodissociation products are transparent at 355 nm and do not undergo further depletion by photodissociation. In addition to loss of N_2, UVPD-MS^2 also resulted in the breakdown of the complex forming $(M - N_2 + H)^+$ ions, as shown for GL*LLK (Figure 2c). The formation of $(M - N_2 + H)^+$ monomers upon UVPD was indicative of the fraction of complexes in which the photopeptide lost N_2 forming an olefin without crosslinking to the target peptide. This is consistent with the energetics of N_2 elimination from L* followed by carbene isomerization to

an olefin. The diazirine to olefin conversion in L* has been calculated to be ca. 200 kJ mol^{-1} exothermic [38], thus providing internal energy to drive dissociation of the non-covalent complex.

Table 1. Yields of gas-phase peptide-peptide ion complexes by electrospray ionization.

	Yield (%)[a,b]		
Target peptide	GL*LLK	GLL*LK	GLLL*K
PGLMG	6.8	4.8	4.2
G**P**LMG	3.1	1.9	5.5
GL**P**MG	14.4	9.0	14.0
GML**P**G	8.7	4.2	12.0
GMLG**P**	5.6	9.4	12.0
G**F**LMG	5.3	2.2	4.8
GL**F**MG	10.3	10.5	11.9
GML**F**G	5.2	4.0	11.3

[a]Relative to the combined intensities of target $(m + H)^+$ and photopeptide $(M + H)^+$ ions. [b]Average of three measurements made on different days.

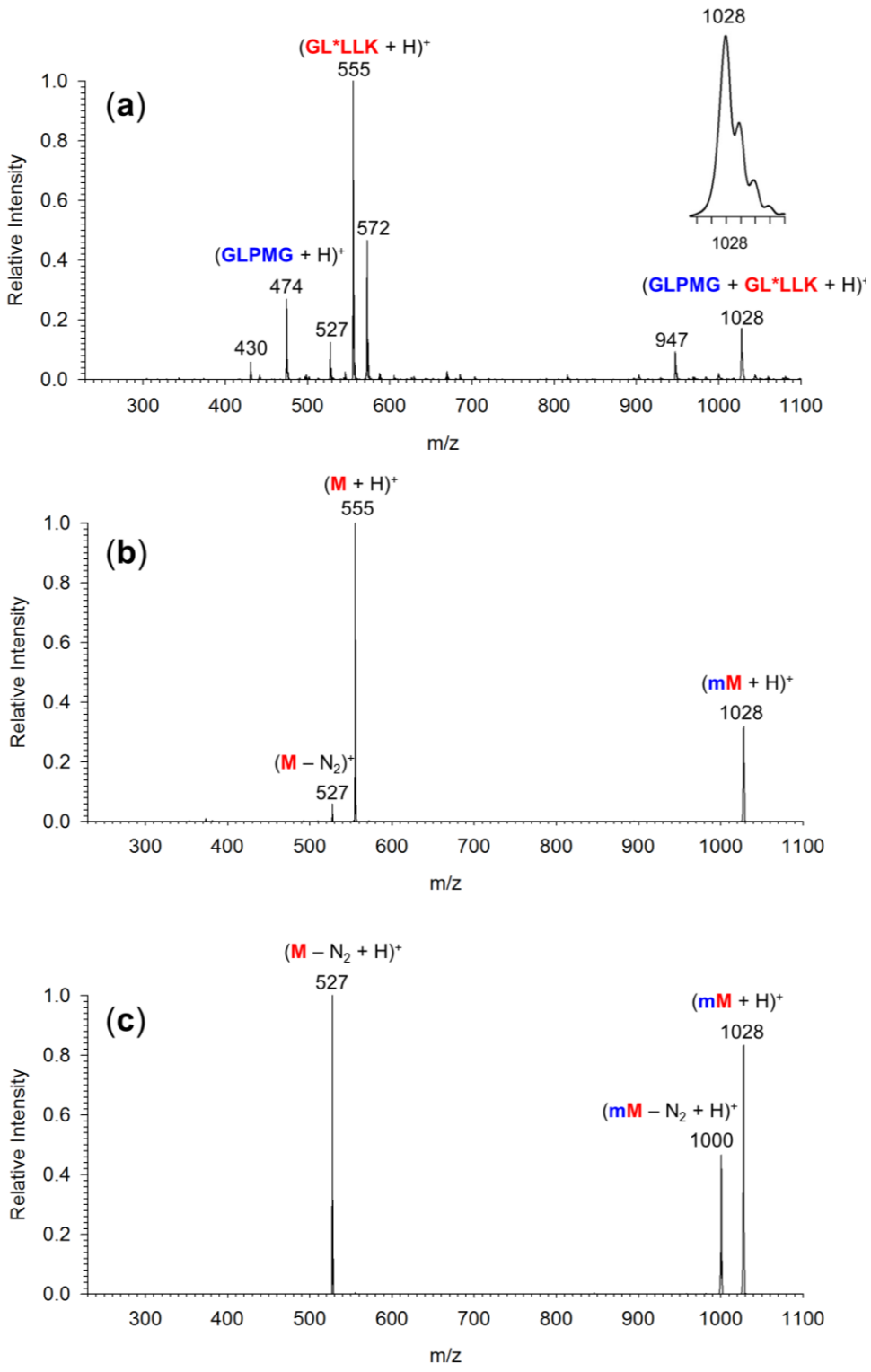

Figure 2. (a) Electrospray mass spectrum of a 1:1 mixture of GLPMG and GL*LLK. Inset shows the *m/z* 1028 peak of the $(GLPMG + GL^*LLK + H)^+$ complex ion denoted $(mM + H)^+$. (b) CID-MS^2 spectrum of the $(mM + H)^+$ ion. (c) UVPD-MS^2 spectrum (355 nm, 36 laser pulses, 18 mJ/pulse) of the $(mM + H)^+$ ion.

The formation of the new covalent bond upon carbene insertion was detected by subjecting the $[mM - N_2 + H]^+$ ions to CID for structural analysis by gas-phase sequencing. CID of $[mM - N_2 + H]^+$ ions revealed that the majority of fragment ions originated from covalent adducts, as indicated by the *m/z* values that were between that of $(mM - N_2 + H)^+$ and $(M - N_2 + H)^+$. This is exemplified by the CID-MS^3 spectrum of $(GPLMG + GL^*LLK - N_2 + H)^+$ (Figure 3). The fragment ions were assigned on the basis of the known sequence of the photoactive and target peptides.

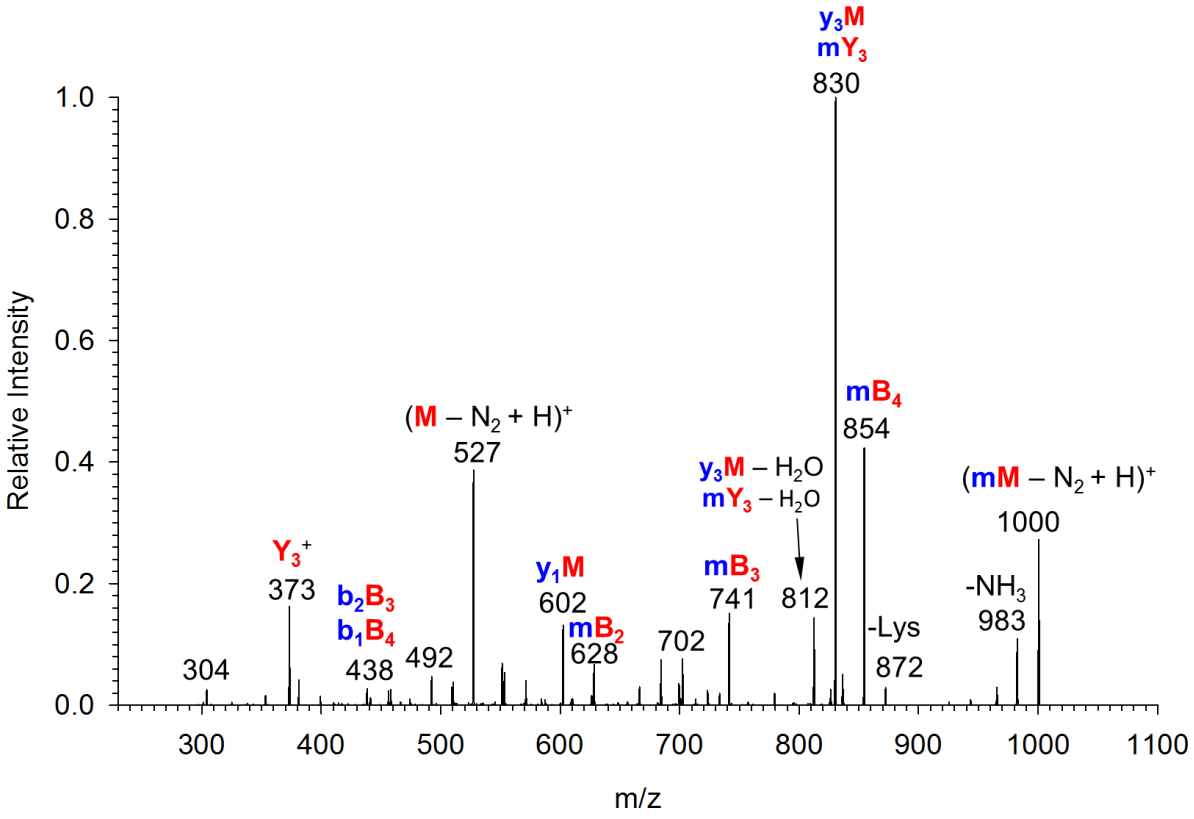

Figure 3. CID-MS^3 spectrum of the $(GLPMG + GL^*LLK - N_2 + H)^+$ ion at *m/z* 1000.

The photodissociative conversion of peptide-peptide ion complexes was quantified in two ways [9, 10]. First, the relative intensities of the total covalent and non-covalent $(mM - N_2 + H)^+$ ion fraction in the UVPD-MS^2 spectra were expressed as per cent ratios $R(MS^2)$ (eq 1):

$$R(MS^2) = 100 \times [mM - N_2 + H]^+ / \{[mM - N_2 + H]^+ + [M - N_2 + H]^+\} \quad (1)$$

The $R(MS^2)$ values for all studied combinations of proline target peptides and photopeptides exceeded 30% (Table 2). The sequence positions of the Pro and L* residues had only a moderate effect on $R(MS^2)$. As a general trend, moving the Pro residue from the *N*-terminus to the C-terminus resulted in a slightly increased $R(MS^2)$ for complexes with all three L*-tagged photopeptides (Table 2). The highest $R(MS^2)$ was observed for the $(GMLPG + GLL^*LK + H)^+$ complex (44%, Table 2).

Table 2. UVPD-MS^2 yields of $(mM - N_2 + H)^+$ complex ions.

	Yield (%)[a]					
Target peptide	GL*LLK		GLL*LK		GLLL*K	
	$R(MS^2)$	R(total)	$R(MS^2)$	R(total)	$R(MS^2)$	R(total)
PGLMG	30	21	30	19	32	24
G**P**LMG	30	23	38	27	32	26
GL**P**MG	31	26	39	29	34	19
GML**P**G	34	26	44	35	38	30
GLMG**P**	41	28	40	28	39	32
G**F**LMG	33	23	36	25	34	37
GL**F**MG	35	23	33	22	36	28
GLM**F**G	31	21	38	25	38	30

[a]See text for yield definitions.

Second, the fractions of crosslinked complexes were determined from CID-MS^3 spectra as a percent ratio of the sum of backbone fragment ion intensities (F_i) relative to all fragment ions including the $(M - N_2 + H)^+$ monomer (eq 2):

$$R(MS^3) = 100 \times \sum F_i / \{\sum F_i + [M - N_2 + H]^+\} \quad (2)$$

The $R(MS^3)$ values ranged between 64-85% and displayed different trends depending on the Pro and L*positions (Table 3), as discussed below. We note that the reported $R(MS^3)$ yields should be viewed as lower bounds of the actual crosslinked complexes for two reasons. First, including in $R(MS^3)$ the intensities of fragment ions formed by loss of ammonia and water from $(mM - N_2 + H)^+$ ions further increased the $R(MS^3)$ by as much as 20% to reach the high of 90% covalent cross linking in the $(GLPMG + GL*LLK + H)^+$ complex (Table 3). The fragment ion intensities due to the loss of ammonia depended on the target peptide sequence (Table 3). We did not attempt to interpret these effects because the origin of the ammonia molecule, i.e., from the photopeptide or target peptide, was unknown. Second, covalent bonds susceptible to dissociation, such as those in esters and amides formed by carbene insertion to carboxyl O–H and amide N–H bonds, respectively, may undergo CID cleavage, forming $(M - N_2 + H)^+$ fragment ions that would be counted as originating from non-covalent $(mM - N_2 + H)^+$ complexes. Carbene cross-linking to target peptide carboxyl group forming an ester linkage was discussed previously and found likely in some structures [9]. The combined yields, $R(MS^2) \times R(MS^3)$, were between 19-35% for the combinations of Pro target and L* tagged peptides (Table 2).

Table 2. UVPD-MS^2 yields of $(mM - N_2 + H)^+$ complex ions.

	Yield (%)[a]					
Target peptide	GL*LLK		GLL*LK		GLLL*K	
	R(MS^2)	R(total)	*R*(MS^2)	R(total)	*R*(MS^2)	*R*(total)
PGLMG	30	21	30	19	32	24
G**P**LMG	30	23	38	27	32	26
GL**P**MG	31	26	39	29	34	19
GML**P**G	34	26	44	35	38	30
GLMG**P**	41	28	40	28	39	32
G**F**LMG	33	23	36	25	34	37
GL**F**MG	35	23	33	22	36	28
GLM**F**G	31	21	38	25	38	30

[a]See text for yield definitions.

Table 3. Covalent and non-covalent fractions from photodissociation of $(mM + H)^+$ complexes of proline target peptides.

	Ion Relative Intensity (%)[a]			
Complex	$(M - N_2 + H)^+$	$\sum F_{seq}$[b]	$(mM - N_2 - NH_3 + H)^+$	Total covalent
PGLMG + GL*LLK	23 ± 3[c]	71 ± 5	6 ± 1	77 ± 4
PGLMG + GLL*LK	30 ± 2	*67* ± 2	3 ± 0.1	*70* ± 2
PGLMG + GLLL*K	14 ± 1	81 ± 1	5 ± 0.2	86 ± 1
G**P**LMG + GL*LLK	17 ± 1	64 ± 6	19 ± 5	83 ± 1
G**P**LMG + GLL*LK	26 ± 1	*60* ± 5	14 ± 4	*74* ± 1
G**P**LMG + GLLL*K	14 ± 2	66 ± 7	20 ± 5	86 ± 2
GL**P**MG + GL*LLK	10 ± 7	85 ± 10	5 ± 3	90 ± 7
GL**P**MG + GLL*LK	22 ± 0.4	*73* ± 2	4 ± 1	*78* ± 1
GL**P**MG + GLLL*K	15 ± 1	75 ± 3	10 ± 2	85 ± 1
GML**P**G + GL*LLK	14 ± 0.5	82 ± 1	4 ± 1	86 ± 1
GML**P**G + GLL*LK	16 ± 11	*81* ± 11	3 ± 1	*84* ± 11
GML**P**G + GLLL*K	11 ± 0.2	85 ± 1	4 ± 1	89 ± 1
GLMG**P** + GL*LLK	23 ± 3	58 ± 1	19 ± 3	77 ± 3
GLMG**P** + GLL*LK	33 ± 1	*54* ± 4	13 ± 3	*67* ± 1
GLMG**P** + GLLL*K	16 ± 1	70 ± 2	14 ± 2	84 ± 1

[a]Averages of three measurements made on different days. [b]Sum of sequence fragment ions relative intensities. [c]Standard deviations.

6. 3. 2 Photocrosslinking of Phe-Containing Target Peptides

Electrospray ionization of solution mixtures composed of Phe-containing target peptides and photo-labelled peptides formed singly charged non-covalent dimer complexes at *m/z* 1078. The ESI yield of the formation of Phe-containing complexes was 2.2-12% relative to the singly charged monomers, as shown for $(GFLMG + GL*LLK + H)^+$ (Figure 4a). The non-covalent dimer complexes (*m/z* 1078) were selected by mass and subjected to CID-MS^2 and UVPD-MS^2 in a

similar fashion as for the Pro-containing dimer complexes. CID-$MS^{2\ of}$ Phe-containing dimers showed two main product ions, which were the $(M - N_2 + H)^+$ (*m/z* 527) and $(M + H)^+$ (*m/z* 555) (Figure 4b). UVPD-MS^2 at 355 nm of the complexes resulted in the formation of $(M - N_2 + H)^+$ (*m/z* 527) and a major loss of N_2, to form $(mM - N_2 + H)^+$ (*m/z* 1050) ions, as illustrated for the $(GFLMG + GL^*LLK + H)^+$ complex (Figure 4c). The dissociations of the complexes observed upon CID-MS^2 indicated that the non-covalent interactions between the peptide components were broken under CID conditions and were not residue-specific. The formation of $(mM - N_2 + H)^+$ (*m/z* 1050) under UVPD conditions suggested the formation of a new covalent bond between the two monomers, and this was further probed by subjecting the $(mM - N_2 + H)^+$ ions to CID-MS^3, as illustrated for $(GFLMG + GL^*LLK - N_2 + H)^+$ (*m/z* 1050) (Figure 5).

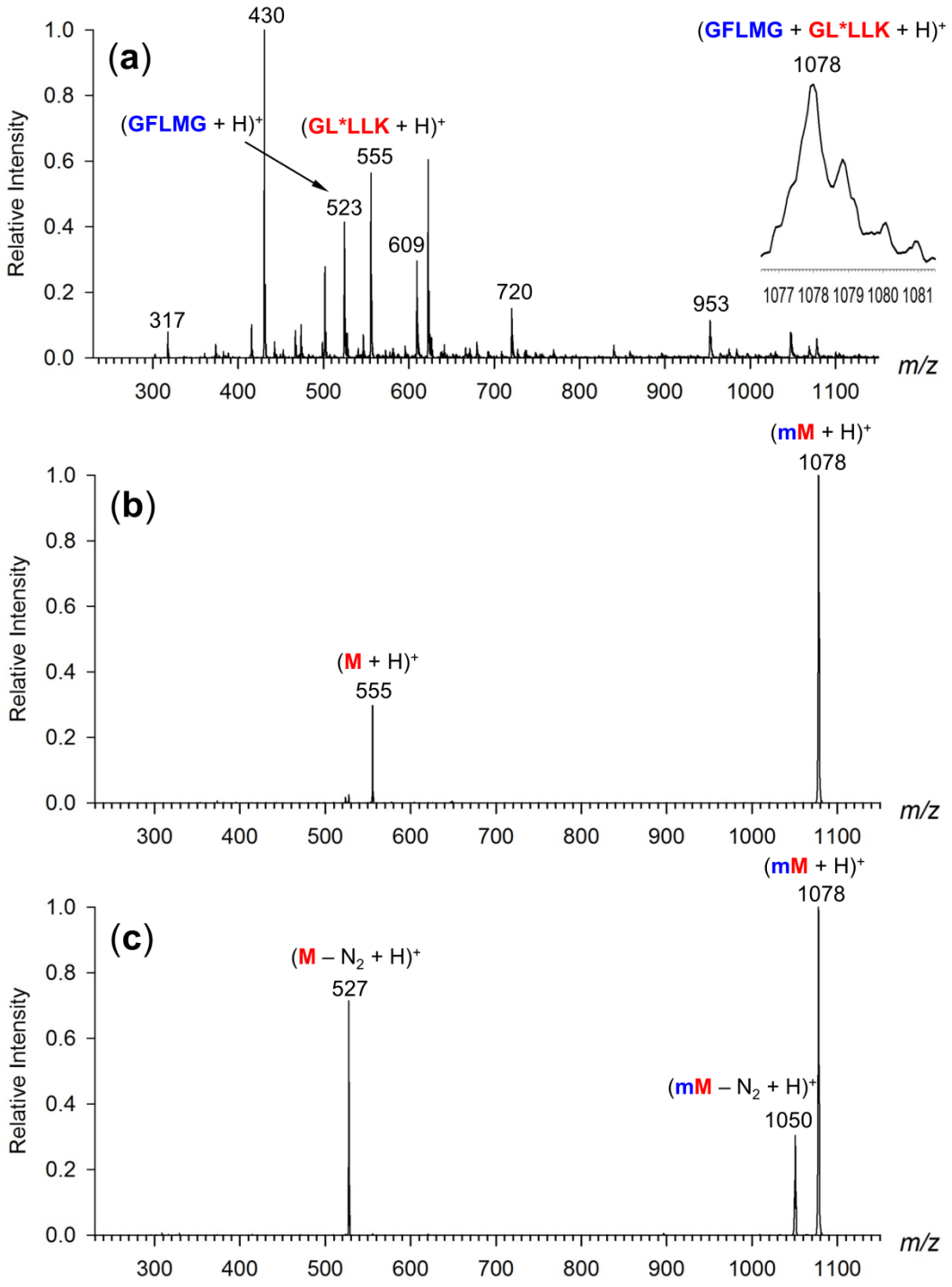

Figure 4. (a) Electrospray mass spectrum of a 1:1 mixture of GFLMG and GL*LLK. Inset shows the *m/z* 1078 peak of the (GLMPG + GL*LLK + H)$^+$ complex ion denoted (mM + H)$^+$. (b) CID-MS^2 spectrum of the (mM + H)$^+$ ion. (c) UVPD-MS^2 spectrum (355 nm, 36 laser pulses) of the (mM + H)$^+$ ion.

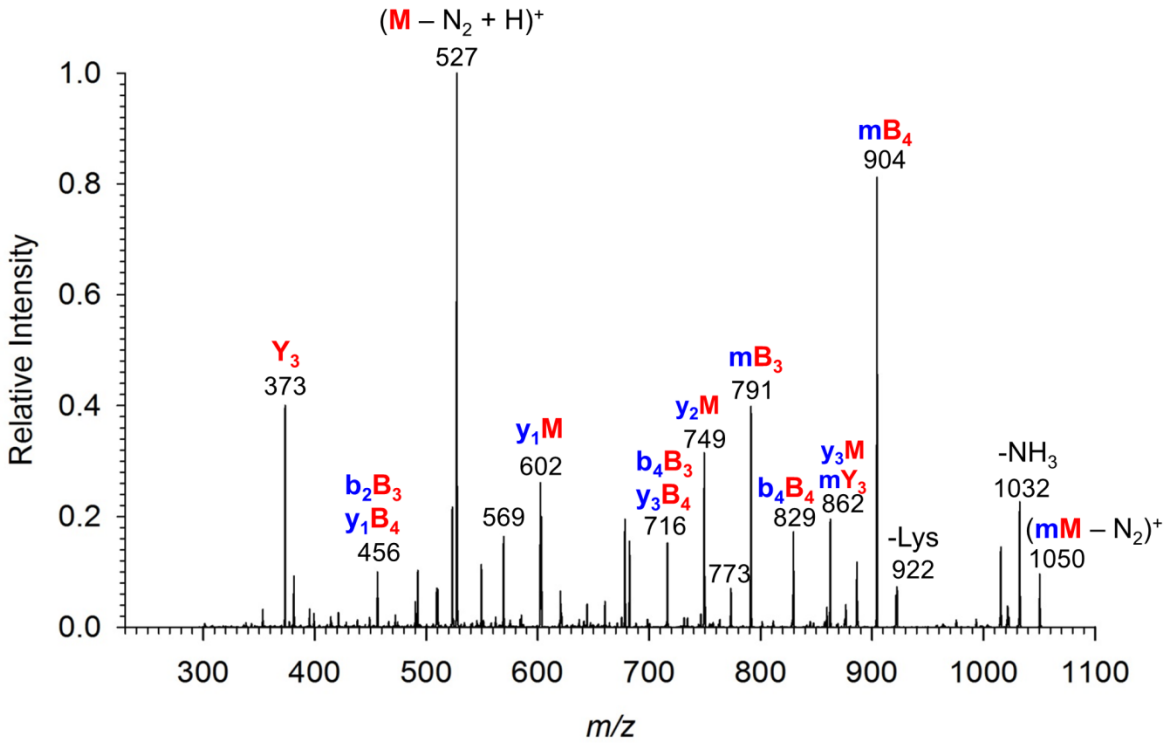

Figure 5. CID-MS^3 spectrum of the (GFLMG + GL*LLK – N_2 + H)$^+$ ion at *m/z* 1050.

The *R*(MS^2) values of all Phe-containing complexes were in the 31-38% range (Table 2), whereby the highest *R*(MS^2) value was obtained when both the Phe and the L* residues were near the C-terminus. This indicated that there may exist an interaction between the π system of the aromatic ring of the Phe residue and the charge located on the ε-amine of the C-terminal lysine residue. This type of interaction could potentially help enhance the photocrosslinking efficiency between the peptide units. The *R*(MS^3) values of the Phe-containing complexes ranged within 65-80%, and were not much affected by including minor (mM – N_2 – NH_3 + H)$^+$ ion intensities (Table 4) The highest *R*(MS^3) among all the combinations of target and photoactive peptides were obtained when L* was near the C-terminus. The combined yields, which were calculated by *R*(total) = *R*(MS^2) × *R*(MS^3) were in the range of 21-30% (Table 2).

Table 4. Covalent and non-covalent fractions from photodissociation of $(mM + H)^+$ complexes of phenylalanine target peptides.

	Ion Relative Intensity (%)[a]			
Complex	$(M - N_2 + H)^+$	$\sum F_{seq}$[b]	$(mM - N_2 - NH_3 + H)^+$	Total covalent
G**F**LMG + GL*LLK	19	76	4	81
G**F**LMG + GLL*LK	29	*68*	3	*71*
G**F**LMG + GLLL*K	16	80	4	84
GL**F**MG + GL*LLK	19	77	4	81
GL**F**MG + GLL*LK	26	*71*	3	*74*
GL**F**MG + GLLL*K	15	81	5	86
GML**F**G + GL*LLK	20	76	5	80
GML**F**G + GLL*LK	26	*71*	3	*74*
GML**F**G + GLLL*K	16	80	4	84

[a]Averages of three measurements made on different days. [b]Sum of sequence fragment ions relative intensities.

6. 3. 3 Sequence Analysis of Proline-Containing Crosslinks:

The CID-MS^3 spectra showed a number of sequence fragment ions originating from dissociations within the target (m) and de-nitrogenated photopeptide (M) chains. These were used for assigning the crosslink sites in the target peptides, following the previously reported procedure [9,10]. Briefly, several criteria and features were used in the analysis. First, only the diazirine-bearing L* residue can be involved in photocrosslinking, and thus all logical backbone fragments must contain it. For example, fragment ions that would indicate $(m,b,y)Y_1$, $(m,b,y)Y_2$ and $(m,b,y)Y_3$ crosslinks would be illogical for GL*LLK photo peptides and therefore would have been excluded from the analysis. Second, only fragment ions resulting from backbone cleavage in the target peptide can be used for cross-link assignment. The total relative intensities of sequence-specific fragment ions

of the y_mM, b_nM, and $(y_m,b_n)(Y_p,B_q)$ type varied for the different combinations of the target and photo-labeled peptides. It should be noted that when the target peptide contained proline, backbone cleavages upon CID were not likely to occur uniformly at all amide bonds because of the well-known proline effect, enhancing dissociation of the CO-N(Pro) amide bond [39-42]. It is also difficult to assess how a crosslink at a given residue affects backbone dissociations of the target peptide. However, the charging proton position in the complexes was firmly established in the photopeptide and its denitrogenated photoproduct, as revealed by the CID and UVPD mass spectra (Figure 2b,c). It is also of note that there were a few isobaric combinations of the Pro and (L* – N_2) (both 97 Da) and Leu residues that were then assigned to both possible chain combinations. These factors may result in over counting sequential C-terminal and *N*-terminal crosslinks when based on y_nM^* and b_nM^* fragment ions, respectively. With all these caveats considered, the results of sequence analysis of all fifteen Pro-containing complexes are displayed in Figure 6a-e. The fractions of crosslinks were normalized to the overall crosslinking yield for each photopeptide-target- pair.

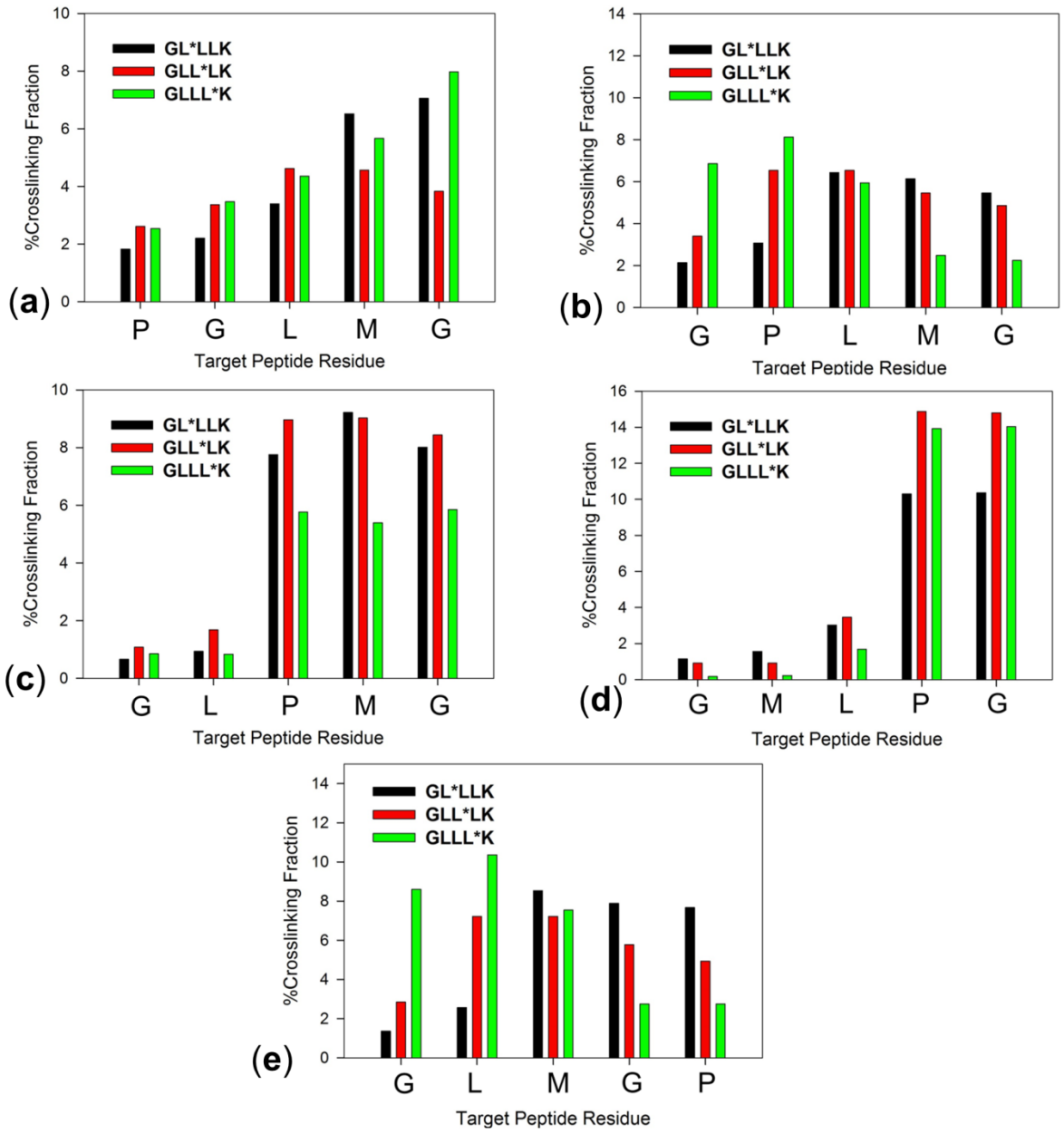

Figure 6. Crosslink distributions in proline target peptides. (a) **P**GLMG, (b) G**P**LMG, (c) GL**P**MG, (d) GML**P**G, (e) GLMG**P**. The fractions were normalized to the *R*(total) efficiencies for each photopeptide-target peptide pair (cf. Table 2).

The data demonstrate that the Pro position in the target peptide had a substantial effect on the specificity of the carbene insertion and crosslink formation (Figure 6a-e). Differences were also observed for crosslinking of the same target peptide with photopeptides having the L* residue in different positions. Starting with PGLMG, the CID-MS^3 data indicated a tendency for crosslinks with GL*LLK and GLLL*K to increasingly occur at residues close to the C-terminus of this target peptide (Figure 6a). In contrast, crosslinks to GLL*LK were more evenly distributed among the target peptide residues, with largest fractions appearing at Leu and Met. Analysis of the CID-MS^2 spectrum of the target peptide ion alone, $(PGLMG + H)^+$ indicated enhanced cleavage of the Met4-Gly5 and Leu3-Met4 amide bonds. This indicated that crosslinks at Met4 and Gly5 could be somewhat overestimated in the sequence analysis of the complexes. A relatively non-selective distribution of crosslinks among the amino acid residues was obtained for photodissociation of GPLMG with all three photopeptides (Figure 6b). The target peptide ion, $(GPLMG + H)^+$, was found to favor cleavage of the Met4-Gly5 and Leu3-Met4 amide bonds, indicating again that crosslinks at Met4 and Gly5 in the complexes could be somewhat overestimated by the sequence analysis.

The CID-MS^3 data for GLPMG indicated highly preferential crosslinking at the Pro3, Met4 and C-terminal Gly5 residues (Figure 6c). The fragment ion intensities are affected by the facile backbone cleavage at the Pro3 residue, leading to the dominant y_3M ion at *m/z* 830 (Figure 3). Note, however, that the sequence-complementary b_2(M,Y,B) fragment ions were much less intense than the y_3M ion, indicating less efficient cross linking within the *N*-terminal Gly1-Leu2 sequence segment. The distinction of cross links at Pro3, Met4 and C-terminal Gly5 was more difficult to achieve. The reference CID-MS^2 spectrum of the target peptide ion, $(GLPMG + H)^+$, showed a dominant dissociation of the Leu2-Pro3 amide bond, and thus crosslinks at Pro3, Met4, and Gly5

were expected to give rise to y_3M ions regardless of the specific crosslink position within the PMG segment. However, specific crosslinking at C-terminal Gly5 and Met4 was indicated by the respective y_1M (*m/z* 602) and y_2M (*m/z* 733) fragment ions (Figure 3). An interesting feature of the CID-MS^3 data for GLPMG was the very similar crosslink distributions originating from GL*LLK, GLL*LK, and GLLL*K, and indicating preferential interactions with the target peptide C-terminal residues for all three photopeptides.

The proline effect on backbone dissociations also played a role in affecting the CID-MS^3 data for GMLPG (Figure 6d). The reference CID-MS^2 spectrum of $(GMLPG + H)^+$ exhibited a prominent y_2 fragment ion by Leu3-Pro4 amide bond cleavage which could hamper distinction of crosslinks at Pro4 and Gly5 in the complexes. However, regardless of the L* residue position in the photopeptide, the data indicated preferential interactions and crosslinking at the C-terminal Pro4 and Gly5 residues. Crosslinks at Pro4 and C-terminal Gly5 were indicated by the respective y_2M and y_1M fragment ions in the CID-MS^3 spectrum. Again, the sequence-complementary b_3(M,Y,B) fragment ions were much less intense than the y_2M ion, indicating less efficient crosslinking at the *N*-terminal Gly1, Met2 and Leu3 residues of the target peptide.

Crosslinking of the Pro-C-terminal target peptide GLMGP displayed dependence on the position of the L* residue (Figure 6e). With GL*LLK and GLL*LK, a broad distribution of crosslinks was formed that peaked around the middle Met3 residue. In contrast, with GLLL*K the majority of crosslinks were formed at the Leu2, Met3, and *N*-terminal Gly1 residues. These results indicated different interactions with the target peptide of the carbene intermediates when generated at different positions of the photopeptide. We note that the reference CID-MS^2 spectrum of the target peptide ion $(GLMGP + H)^+$ indicated preferred dissociation at Gly4-Pro5, and hence the

assignment of crosslinks at the *N*-terminal residues in the complex would not be seriously affected by a similar dissociation bias.

6. 3. 4 Phenylalanine-containing peptides:

In contrast to the Pro-containing peptides, the preferred position for photocrosslinking in Phe-containing peptides was strongly dependent on the positions of both phenylalanine and photoleucine residues within their respective sequences. In particular, as shown in Figure 7, the neutral peptide GFLMG did not prefer a particular photocrosslinking position with any photopeptide counterparts. However, as the Phe and L* residues moved towards the C-termini of their respective sequences, the crosslinking yield increased. In the case of GMLFG, the most efficient crosslinking was at the C-terminal Gly5 in a complex with GLLL*K. Similarly, GLFMG showed prominent crosslinking at Gly5 when interacting with GLLL*K. The increase in the yield of photocrosslinking among Phe-containing peptides may be accounted for by the interaction between the π-system of the Phe ring and the charge at the Lys ε-amine in the photopeptide. This π-system interaction would favor close positioning of the L* and Phe residues, subsequently increasing the probability of crosslinking at positions nearby phenylalanine.

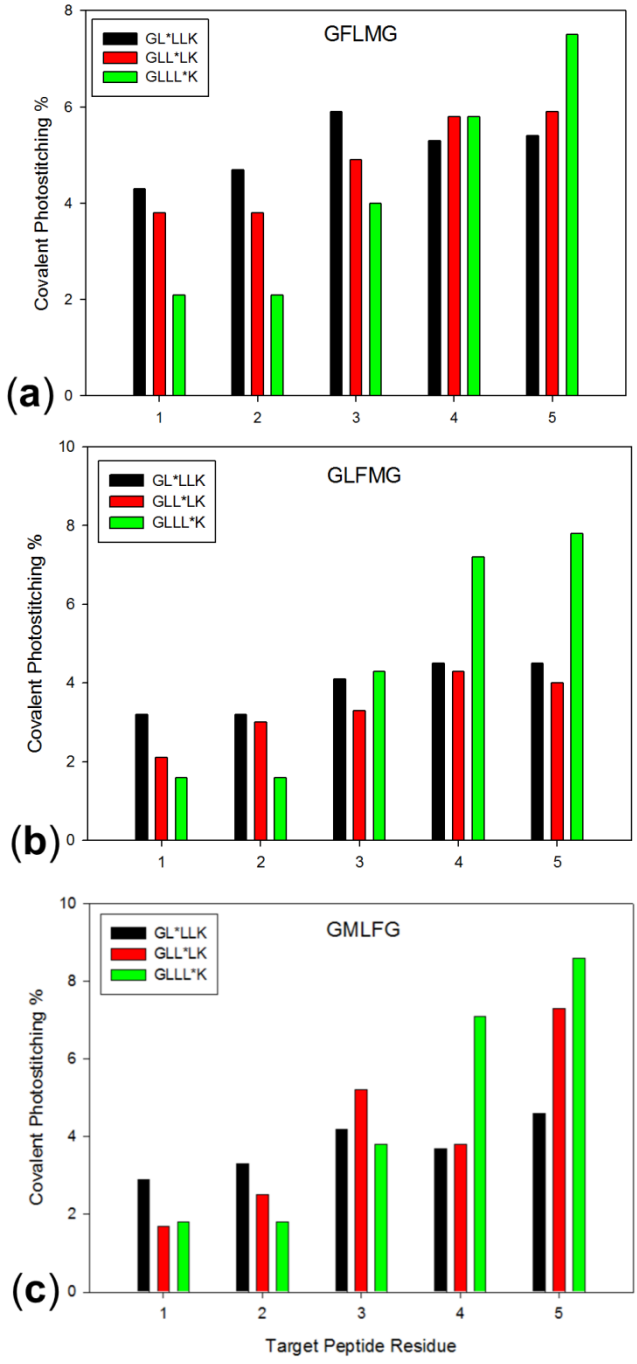

Figure 7. Crosslink distributions in phenylalanine target peptides.
(a) G**F**LMG, (b) GL**F**MG, (c) GML**F**G.

***6. 3. 5 Complex Ion Structures and Born-Oppenheimer Molecular Dynamic Analysis*:**

In order to further elucidate the non-covalent interactions of Pro-containing complexes, we selected the (GLPMG + GLL*LK + H)$^+$ complex as our model system for BOMD trajectory calculations. One of the reasons for selecting this peptide pair over the others was the middle position of the proline residue within the target peptide sequence. BOMD analysis could potentially resolve the ambiguity in determining the position of cross links within the Pro-Met-Gly sequence (*vide supra*) and provide structures of the complexes. BOMD trajectories starting from different (GLPMG + GLL*LK + H)$^+$ conformers were analyzed for 12 complexes that were selected from lowest-energy DFT structures. Simulations were run for 100 ps at 310 K. The choice of temperature was based on our experimental setting. The 100 ps timeframe is compatible with the half-life of a carbene intermediate, which is typically within the range of 0.1-5 ns [15]. The trajectories were analyzed for close contacts between the diazirine carbon (C35) on L* and X–H bonds in the target peptide. Close contacts were identified for all C35---X distances within 4.5 Å, corresponding to a projection of a sum of van der Waals radii of atoms constituting the diazirine ring and X-H bonds [9]. The numbering system for the close contact analysis is depicted in Table 7. The conformer populations of the systems under study were presumed to be heterogeneous whereby each conformer had a different statistical weight for contributing to the overall crosslinking efficiency. These statistical weights were determined by the isomer molar fractions, which were obtained by thermodynamic analysis (Tables 5 and 6).

In order to evaluate the molar fraction representation of gas-phase (GLPMG + GLL*LK + H)$^+$ isomers, we first determined their relative free energies (ΔG_{310}, Table 5). These were based on ωB97X-D energies for fully optimized structures, whereas enthalpies and entropies were taken from B3LYP frequency calculations. The free energies were then used to calculate pair-wise

equilibrium constants K_{in} and molar fractions x_{in}, $K_{in} = \exp(-\Delta G_{in}/RT)$, $x_i = K_{in}/\sum K_{in}$ where n refers to the reference complex and i = 1,..,12. (Table 6). The calculations identified five isomers (**1**-**5**) that had ΔG_{310} within 25 kJ mol^{-1} of the lowest energy complex **2**. Out of these, complexes **2**-**5** were canonical structures with a protonated Lys side chain in GLL*LK and a neutral target peptide (Figure 8). This is compatible with the CID-MS^2 experiments that showed prevalent proton retention in the photopeptides (Figure 2b). Structure **1** of a slightly higher ΔG_{310} than **2** was a complex of a GLL*LK zwitterion with GLPMG protonated at the *N*-terminus (Figure 8). Complexes **6**-**12** had higher ΔG_{310} excluding them from being substantially populated in an equilibrium mixture (Table 6). Complexes **7**, **8**, **9**, **11**, and **12** were canonical structures whereas and **6** and **10** were zwitterions (Figure 9). The non-covalent bonding in all these isomers was mediated by hydrogen bonds of the charged NH_3 and neutral COOH groups to amide electron donors in the peptide counterpart. For example, complex **1** displayed four strong intermolecular hydrogen bonds that were between the Lys-5 carboxylate and Gly5 carboxyl, and Leu4-Gly5, Leu4-Pro3, and Leu2-Leu2 amides (Figure 8). In the lowest free-energy complex **2**, there were strong intermolecular H-bonds between Gly1-Gly5, Lys5-NH_3^+-Pro3, and Lys5-Leu2. The third most stable complex **5** displayed H-bonding between Lys5-NH_3^+, Leu4 and the Gly5 carboxyl group.

Table 5. Relative Energies of (GLPMG + GLL*LK + H)$^+$ Dimer Complexes.

Ion	Relative Energy (kJ mol^{-1})^a					
	ΔH_0		ΔH_{310} ^{b}		ΔG_{310} ^{b}	
	B3LYP	ωB97X-D^c	B3LYP	ωB97X-D^c	B3LYP	ωB97X-D^c
1	4.3	0.0	4.2	0.0	5.5	0.0
2	14	12	19	17	–1.0	–3.7
3	0.0	17	0.0	17	0.0	16
4	9.3	27	12	29	3.9	20
5	8.0	28	13	33	–10	8.2
6	30	28	31	29	26	22
7	39	32	41	33	34	25
8	33	35	34	36	32	33
9	45	48	46	49	33	35
10	59	55	58	54	61	56
11	26	57	28	59	23	53
12	75	59	77	61	73	55

^{a}Including B3LYP/6-31G(d,p) zero-point energies. ^{b}Including vibrational, rotational, and translational terms based on B3LYP/6-31G(d,p) optimized structures, energies, and harmonic frequencies. ^{c}ωB97X-D/6-31+G(d,p) optimized structures.

Table 6. Equilibrium Molar Fractions of $(GLPMG + GLL^*LK + H)^+$ Dimer Complexes.

	Molar Fraction[a]	
Ion	B3LYP	ωB97X-D
1	0.0019	0.19
2	0.023	0.80
3	0.016	0.0004
4	0.0036	8.4×10^{-5}
5	0.955	0.008
6	7.6×10^{-7}	3.2×10^{-5}
7	2.8×10^{-8}	1.0×10^{-5}
8	8.0×10^{-8}	5.1×10^{-7}
9	4.3×10^{-8}	2.7×10^{-7}
10	8.8×10^{-13}	8.2×10^{-11}
11	1.8×10^{-6}	2.2×10^{-10}
12	1.0×10^{-14}	1.0×10^{-10}

[a]From the calculated ΔG_{310}.

Table 7. Close contacts in (GLPMG + GLL*LK +H)$^+$ complexes

Close Contacts with Target Peptide Residues and Atoms

	Gly-1		Leu-2					Pro-3			Met-4				Gly-5			
Conformer	N87	C90	N95	C100	C103	C105	C109	C117	C123	C120	N128	C132	C135	C139	N145	C147	O152	Total
1	0	0	0	4	0	0	1	0	0	0	0	0	0	0	0	0	0	6
2	0	0	0	0	0	0	0	0	0	1	85	3	15	27	1	0	21	153
3	0	0	0	0	0	0	0	0	0	0	0	0	0	2	0	0	21	23
4	0	0	0	0	0	0	0	0	0	0	0	0	0	0	0	0	0	0
5	0	0	0	0	0	0	0	0	0	0	0	0	0	11	0	4	0	15
6	0	0	0	0	0	0	0	0	0	0	0	0	0	0	0	0	0	0
7	0	0	0	0	0	0	0	0	0	0	0	0	0	0	0	0	56	56
8	80	20	0	0	0	0	0	0	0	0	0	0	0	0	0	0	0	100
9	6	0	0	0	0	0	0	0	0	0	0	0	0	0	0	0	0	6
10	0	0	90	0	0	0	0	3	1	1	0	0	0	0	0	0	0	95
11	54	57	0	0	6	3	7	0	0	0	0	0	0	0	0	0	0	132
12	0	0	0	0	0	0	0	0	0	0	0	0	0	0	0	0	0	0

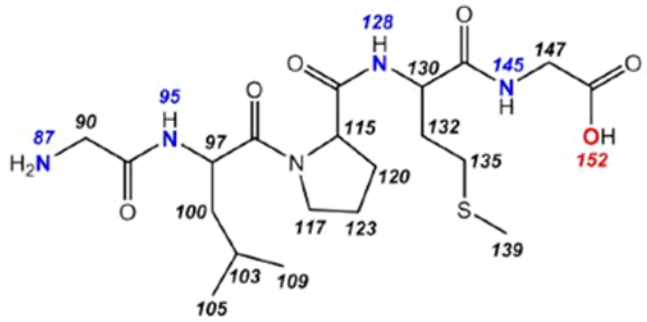

The hydrogen bonding pattern had a significant effect on the target peptide secondary structure. This is shown in the right hand panel of Figure 8 depicting the target GLPMG peptide moieties in conformations with which they appear in the complexes. The structures reveal that the target peptides in **1**, **3**, **4**, and **5** folded to form β-turns at Pro. The hairpin conformations were cooperatively favored by intramolecular H-bonding of the Pro-flanking residues in the target peptides, and intermolecular H-bonding to the photopeptide. The lowest free-energy complex **2** was exceptional in that the target peptide unit was extended by intermolecular H bonding (*vide supra*) and did not form a β-turn at Pro.

The BOMD analysis provided insights regarding the intermolecular and intramolecular interactions between the peptide components under thermal motion. This is illustrated by the close contact data in Table 7, which shows the percentage of time during the 100 ps BOMD run, consisting of 100000 steps, when the carbon atom (C35) of the diazirine ring was within 4.5 Å of the hydrogen carrying atoms of the target peptide. For example, in complex **1**, C35 was within the contact distance with the C100 methylene of the Leu2 residue in the target peptide for 4.4% of the time, corresponding to 4429 contacts, while not getting into contact with the X-H atoms on the other residues of the target peptide. Among the low-energy structures, complex **2** showed multiple (153353) C35 contacts that were chiefly with atoms at the Met4 and Gly5 residues of the target peptide.

The contact data for thermal motion in the complexes (Table 7) are further compared to the geometries of the local energy minima of **1-5** (Figure 8), corresponding to 0 K structures.

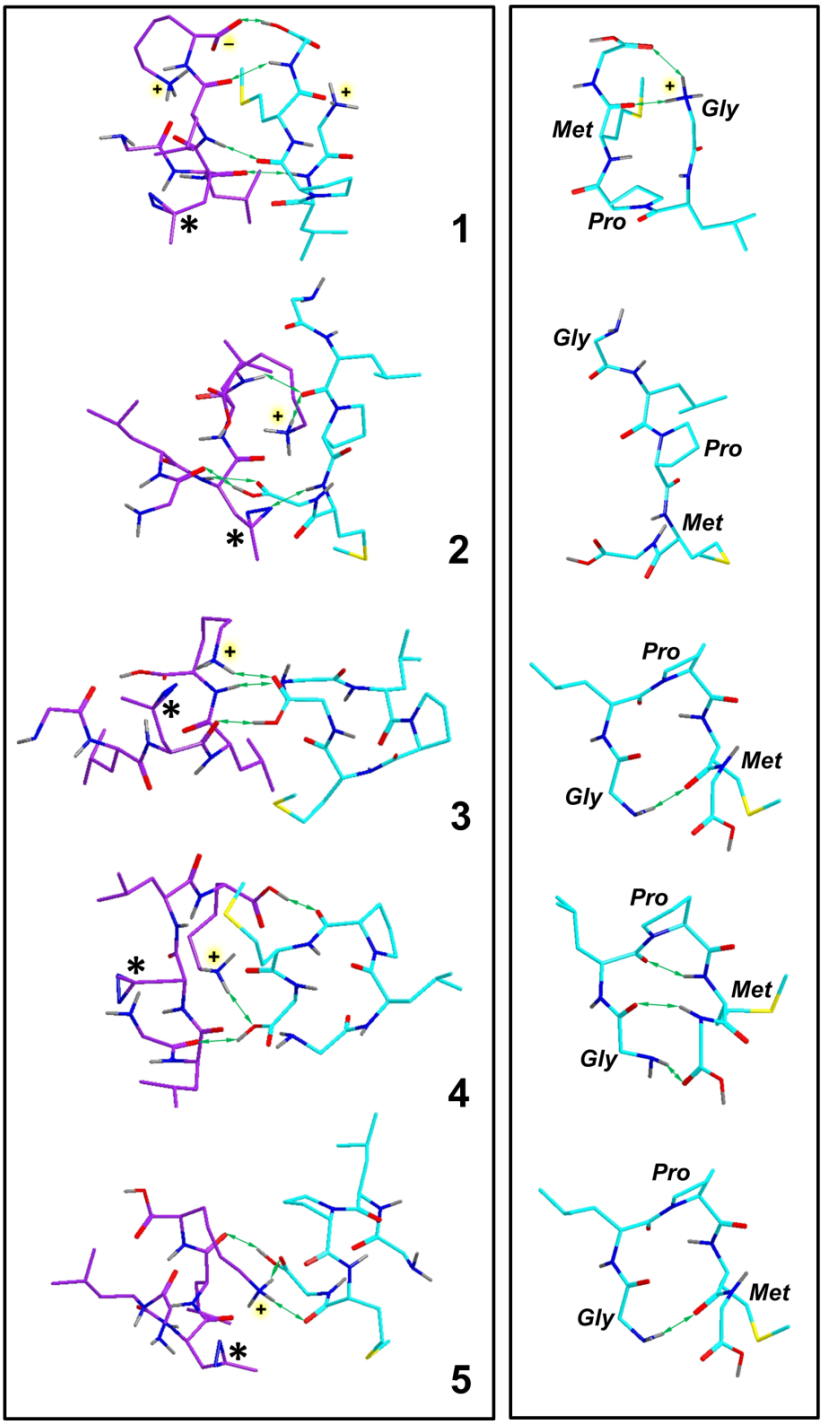

Figure 8. Left panel: ωB97X-D/6-31+G(d,p) optimized structures of low free-energy (GLPMG + GLL*LK + H)$^+$ complexes **1**-**5**. Green arrows indicate major hydrogen bonds between the photopeptide and target peptide. Asterisks indicate the diazirine rings. Right panel: Target peptide geometries in the complexes. Green arrows indicate major hydrogen bonds in the target peptide. Atom color coding: Cyan or magenta = C, gray = H, blue = N, red = O, yellow = S. Only exchangeable (N-H, O-H) hydrogen atoms are shown.

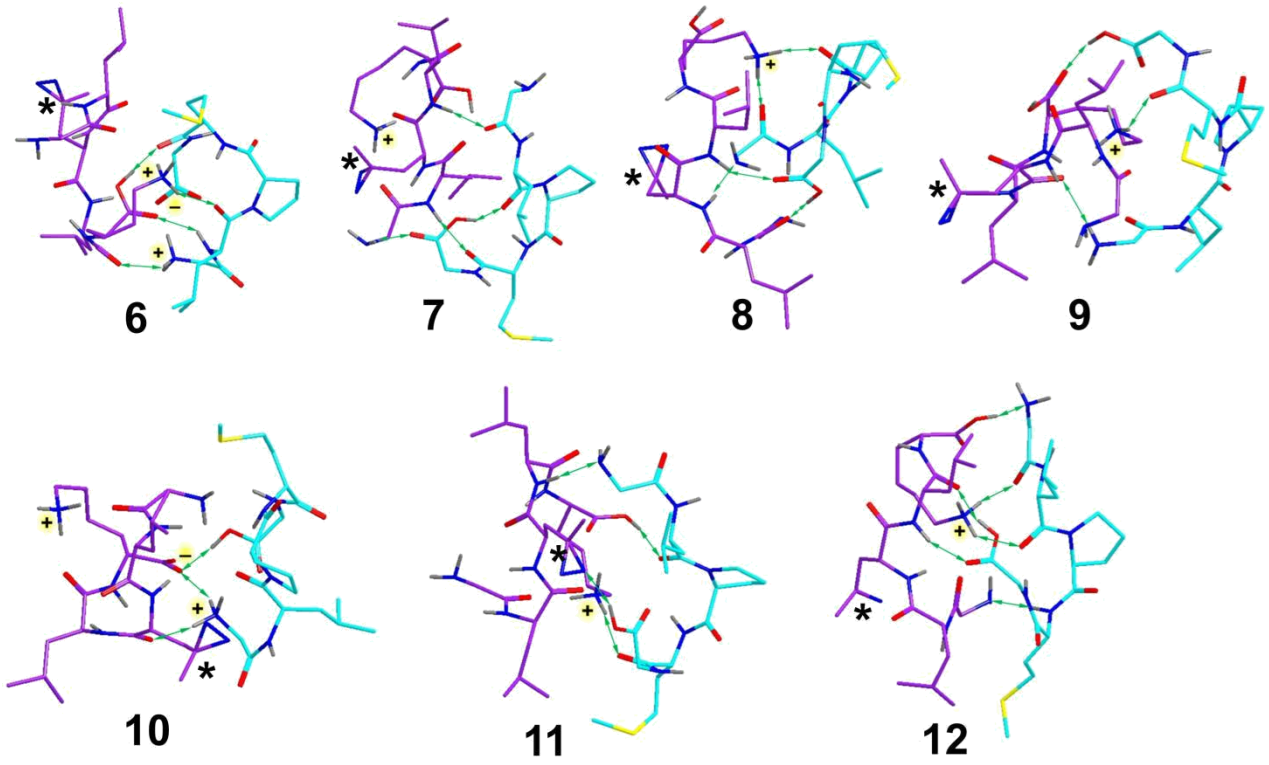

Figure 9. ωB97X-D/6-31+G(d,p) optimized structures of (GLPMG + GLL*LK + H)$^+$ complexes **6-12**. Green arrows indicate major hydrogen bonds between the photopeptide and target peptide. Asterisks indicate the diazirine rings. Atom color coding: Cyan or magenta = C, gray = H, blue = N, red = O, yellow = S. Only exchangeable (N-H, O-H) hydrogen atoms are shown.

Complex **1** showed no close contacts between C35 and the target peptide residues in the 0 K structure. The X-H atom in the target peptide which was closest to C35 was C115 of the Pro residue at 6.14 Å. However, thermal motion in the complex did not result in a close contact with Pro X-H atoms. Rather, C35 developed close contacts with the flexible Leu2 side chain as a result of thermal motion. Similar conclusions followed from analysis of 0 K structures and thermally induced close contacts in all the other complexes. The majority of close contacts occurred in regions that were close to C35 in 0 K structures or could be approached via rotations of the Leu2 and Met4 side chains or the *N*-terminal Gly. These results strongly indicate that the hydrogen bonding framework of the complexes was not disrupted by thermal motion at 310 K. Our previous analysis of conformational changes in monomeric peptide ions indicated that hydrogen bond

rearrangements occurred via a slipping motion whereby the energy needed to disrupt one hydrogen bond was compensated by cooperative formation of another hydrogen bond [43-45]. The present results for peptide-peptide ion complexes indicate no such slippage, as the main hydrogen bonds connecting the peptide moieties were not rearranged by thermal motion. This can be attributed to a stable core framework of polar groups and hydrogen bonds that resist substantial rearrangement in thermal complexes.

The BOMD analysis of close contacts in $(GLPMG + GLL^*LK + H)^+$ (Table 7) was combined with the calculated populations of conformational isomers **1**-**12** (Table 6) to estimate the overall crosslinking sites in a thermal equilibrium mixture of the complexes. When based on molar fractions obtained from the ωB97X-D free energies, the population-averaged crosslink distribution was 0.0, 0.9, 0.9, 84, and 14% at G, L, P, M, and G, respectively. An evaluation using B3LYP free energies and molar fractions gave a similar population-averaged breakdown of 0, 0.1, 0.2, 75, and 25% for crosslinks at G, L, P, M, and G, respectively. This result is consistent with the experimental distribution of crosslinks obtained from gas-phase sequencing (Figure 6). The majority (>90%) of the observed crosslinks were assigned to the Pro3-Met4-Gly5 segment. However, distinction within this segment was difficult because of the proline effect favoring CID at the *N*-terminal side of Pro. Thus upon CID, complexes crosslinked at Pro3, Met4, and Gly5 can be expected to to undergo abundant backbone cleavage at Pro3 to give the dominant y_3M fragment ions without distinguishing the crosslink position within the Pro3, Met4, and Gly5 residues. In contrast, the proline effect did not affect the identification of crosslinks at Gly1 and Leu2 because the complementary b_2M fragment ions should be readily formed by backbone cleavage at Pro3. The BOMD contact analysis indicated that Pro3 was not likely (1%) to be involved in crosslinking. We conclude that, in accord with experiment, the majority of crosslinks in the (GLPMG +

GLL*LK + H)$^+$ complex were formed in the Met4 side chain and a significant fraction involved the Gly5 carboxyl.

6. 4 Conclusions

The combination of diazirine photo-crosslinking, ion activation, tandem mass spectrometry (UVPD/CID), and all-electron molecular dynamics allowed us to gain insight regarding the non-covalent interactions of neutral proline- and phenylalanine-containing peptides in gas-phase complexes. The structures of the gas-phase complexes are maintained by a stable core framework of polar groups and hydrogen bonds that do not substantially rearrange by thermal motion. Polar non-covalent bonding in the complexes has a substantial effect on the secondary structure of the target peptide. Close contacts in the complexes leading to crosslinks in carbene intermediates predominantly occur in residues that are suitably positioned already in the 0 K structures. The experimental data indicate that diazirine photodissociation results in 19-37% fractions of covalent cross links. Gas-phase crosslinking using diazirine-tagged peptides represents a high-yield method that provides experimental background for structural information by all-electron molecular dynamics calculations. Applications of this combined approach to elucidations of non-covalent peptide-peptide interactions are in progress in this laboratory.

6.5 References

(1) Fancy, D.A., Kodadek, T.: Chemistry for the analysis of protein–protein interactions: Rapid and efficient cross-linking triggered by long wavelength light. *Proc. Natl. Acad. Sci. U.S.A.* **96**, 6020–6024 (1999).

(2) Das, J.: Aliphatic diazirines as photoaffinity probes for proteins: recent developments. *Chem. Rev.* **111**, 4405–4417 (2011)

(3) Singh, A., Thornton, E.R., Westheimer, F.H.: Photolysis of diazoacetylchymotrypsin. *J. Biol. Chem.* **237**, PC3006–PC3008 (1962)

(4) Fleet, G.W.J., Porter, R.R., Knowles, J.R.: Affinity labeling of antibodies with aryl nitrene as reactive group. *Nature (London)* **224**, 511–512 (1969)

(5) Knowles, J.R.: Photogenerated reagents for biological receptor-site labeling. *Acc. Chem. Res.* **5**, 155–160 (1972)

(6) Liu, M.T.H.: *Chemistry of Diazirines*, Vols. I and II. CRC Press, Boca Raton, FL (1987)

(7) Suchanek, M., Radzikowska, A., and Thiele, C. Photo-leucine and photo-methionine allow identification of protein-protein interactions in living cells. *Nat. Methods*. **2005**, *2*, 261-268

(8) T. Yang, X.-M. Li, X. Bao, Y. M. E. Fung, D. Li. Photolysine captures proteins that bind lysine post-traslation modifications. *Nat. Chem. Biol.* **12**, 70 (2016).

(9) Shaffer, C. J., Andrikopoulos, P. C., Řezáč, J., Rulíšek, L., and Tureček, F. Efficient Covalent Bond Formation in Gas-Phase Peptide–Peptide Ion Complexes with the Photoleucine Stapler. *J. Am. Soc. Mass Spectrom*. **27**, 633-645 (2016)

(10) Pepin, R., Shaffer, C. J.; Turecek, F. Position-tunable diazirine tags for peptide-peptide ion cross-linking in the gas phase. *J. Mass Spectrom.* 2017, 52, 557-560.

(11) A. Sinz, C. Arlt, D. Chorev, M. Sharon. Chemical cross-linking and native mass spectrometry: A fruitful combination for structural biology. *Protein Sci.* 2015, 24, 1193.

(12) Lee, S., Valentine, S.J., Reilly, J.P., Clemmer, D.E.: Controlled formation of peptide bonds in the gas phase. *J. Am. Chem. Soc.* 133, 15834–15837 (2011)

(13) McGee, W.M., McLuckey, S.A.: Efficient and directed peptide bond formation in the gas phase via ion/ion reactions. *Proc. Natl. Acad. Sci. U. S. A.* 111, 1288–1292 (2014)

(14) K. Koelbel, S.Warnke, J. Seo, G. von Helden, R.Moretti, J.Meiler, K. Pagel, A. Sinz. Conformational shift of a β-hairpin peptide upon complex formation with an oligo-proline peptide studied by mass spectrometry. *Chem. Select* 2016, 1, 3651.

(15) J. P. Pezacki, P. Couture, J. A. Dunn, J. Warkentin, P. D. Wood, J. Lusztyk, F. Ford, M. S. Platz. Rate constants for 1,2-hydrogen migration in cyclohexylidene and in substituted cyclohexylidenes. *J. Org. Chem.* 1999, 64, 4456.

(16) Schimmel, P. R., and Flory, P. J. Conformational energies and configurational statistics of copolypeptides containing L-proline. *J Mol. Biol*. **1968**, 34, 105-120.

(17) Lewis, P. N.; Momany, F. A.; Scheraga, H. A. Folding of polypeptide chains in Proteins: A proposed mechanism for folsing. *Proc Nat. Acad. Sci. U.S.A.* 1971, 68, 2293-2297.

(18) Kuntz, I. D. Protein folding. *J. Am. Chem. Soc.* 1972, 94, 4009-4012.

(19) Crawford, J. L.; Lipscomb, W. N.; Schellman, C. G. The reverse turn as a polypeptide conformation in globular proteins. *Proc Natl. Acad. Sci. U.S.A.* 1973, 70, 538-542.

(20) MacArthur, M. W., and Thornton, J. M. Influence of proline residues on protein conformation. *J Mol. Biol*. **1991**, *218*, 397-412.

(21) Shi, L., Holliday, A.E.; Bohrer, B. C., Kim, D., Servage, K. A., Russell, D. H., Clemmer, D. E. Wet versus Dry Folding of Polyproline. *J. Am. Soc. Mass Spectrom.* 2016, 27, 1037-1047.

(22) Basic Local Alignment Search Tool (BLAST) Available at: http://blast.ncbi.nlm.gov. Accessed 10 June 2015.

(23) Řezáč, J., Fanfrlík, J., Salahub, D., and Hobza, P. Semiempirical quantum chemical PM6 method augmented by dispersion and H-bonding correction terms reliably describes various types of noncovalent complexes. *J. Chem. Th. Comput*. **2009**, *5*, 1749-1760.

(24) Janz, J.M., Ren, Y., Looby, R., Kazmi, M.A., Sachdev, P., Grunbeck, A., Haggis, L., Chinnapen, D., Lin, A.Y., Seibert, C., McMurry, T., Carlson, K.E., Muir, T.W., Hunt, S., Sakmar, T.P.: Direct interaction between an allosteric agonist pepducin and the chemokine receptor CXCR4. *J. Am. Chem. Soc.* 133, 15878–15881 (2011)

(25) Coste, J., LeNguyen, D., Castro, B.: PyBOP: a new peptide coupling reagent devoid of toxic by-product. *Tetrahedron Lett.* 31, 205–208 (1990)

(26) Shaffer, C. J.; Marek, A.; Nguyen, H. T. H.; Tureček, F. Combining Near-UV Photodissociation with Electron Transfer. Reduction of the Diazirine Ring in a Photomethionine-Labeled Peptide Ion. *J. Am. Soc. Mass Spectrom.* **2015**, *26*, 1367-1381.

(27) Berendsen, H. J., Postma, J. V., van Gunsteren, W. F., DiNola, A. R. H. J., & Haak, J. R. Molecular dynamics with coupling to an external bath. *J. Chem. Phys.* **1984** *81*, 3684-3690.

(28) J. Řezáč, Cuby – ruby framework for computational chemistry, version 4, http://cuby4.molecular.cz

(29) Řezáč J. Cuby: an integrative framework for computational chemistry. *J. Comput. Chem.* 2016;37:1230-1237.

(30) Becke, A.D.: Density-functional exchange-energy approximation with correct asymptotic behavior. *Phys. Rev. A* 38, 3098–3100 (1988)

(31) Lee, C., Yang, W., Parr, R.G.: Development of the Colle-Salvetti correlation-energy formula into a functional of the electron density. *Phys. Rev.* B37, 785–789 (1988)

(32) Schäfer, A., Horn, H., Ahlrichs, R.: Fully optimized contracted Gaussian basis sets for atoms lithium to krypton. *J. Chem. Phys.* 97, 2571–2577 (1992)

(33) TURBOMOLE V6.6 2014, a development of University of Karlsruhe and Forschungszentrum Karlsruhe GmbH, 1989-2014, TURBOMOLE GmbH, since 2007; available at: http://www.turbomole.com. Accessed 7 June 2017

(34) M. J. Frisch, G. W. Trucks, H. B. Schlegel, G. E. Scuseria, M. A. Robb, J. R. Cheeseman, G. Scalmani, V. Barone, B. Mennucci, G. A. Petersson, H. Nakatsuji, M. Caricato, X. Li, H. P. Hratchian, A. F. Izmaylov,

J. Bloino, G. Zheng, J. L. Sonnenberg, M. Hada, M. Ehara, K. Toyota, R. Fukuda, J. Hasegawa, M. Ishida, T. Nakajima, Y. Honda, O. Kitao, H. Nakai, T. Vreven, J. A. Montgomery, Jr., J. E. Peralta, F. Ogliaro, M. Bearpark, J. J. Heyd, E. Brothers, K. N. Kudin, V. N. Staroverov, R. Kobayashi, J. Normand, K. Raghavachari, A. Rendell, J. C. Burant, S. S. Iyengar, J. Tomasi, M. Cossi, N. Rega, J. M. Millam, M. Klene, J. E. Knox, J. B. Cross, V. Bakken, C. Adamo, J. Jaramillo, R. Gomperts, R. E. Stratmann, O. Yazyev, A. J. Austin, R. Cammi, C. Pomelli, J. W. Ochterski, R. L. Martin, K. Morokuma, V. G. Zakrzewski, G. A. Voth, P. Salvador, J. J. Dannenberg, S. Dapprich, A. D. Daniels, O. Farkas, J. B. Foresman, J. V. Ortiz, J. Cioslowski, D. J. Fox, Gaussian, Inc., Wallingford CT, 2009.

(35) M. J. Frisch, G. W. Trucks, H. B. Schlegel, G. E. Scuseria, M. A. Robb, J. R. Cheeseman, G. Scalmani, V. Barone, G. A. Petersson, H. Nakatsuji, X. Li, M. Caricato, A. V. Marenich, J. Bloino, B. G. Janesko, R. Gomperts, B. Mennucci, H. P. Hratchian, J. V. Ortiz, A. F. Izmaylov, J. L. Sonnenberg, D. Williams-Young, F. Ding, F. Lipparini, F. Egidi, J. Goings, B. Peng, A. Petrone, T. Henderson, D. Ranasinghe, V. G. Zakrzewski, J. Gao, N. Rega, G. Zheng, W. Liang, M. Hada, M. Ehara, K. Toyota, R. Fukuda, J. Hasegawa, M. Ishida, T. Nakajima, Y. Honda, O. Kitao, H. Nakai, T. Vreven, K. Throssell, J. A. Montgomery, Jr., J. E. Peralta, F. Ogliaro, M. J. Bearpark, J. J. Heyd, E. N. Brothers, K. N. Kudin, V. N. Staroverov, T. A. Keith, R. Kobayashi, J. Normand, K. Raghavachari, A. P. Rendell, J. C. Burant, S. S. Iyengar, J. Tomasi, M. Cossi, J. M. Millam, M. Klene, C. Adamo, R. Cammi, J. W. Ochterski, R. L. Martin, K. Morokuma, O. Farkas, J. B. Foresman, D. J. Fox, Gaussian, Inc., Wallingford CT, 2016.

(36) Chai, J.D., Head-Gordon, M.: Systematic optimization of long-rangecorrected hybrid density functionals. J. Chem. Phys. 128, 084106/1–084106/15 (2008)

(37) Chai, J.D., Head-Gordon, M.: Long-range corrected hybrid density functionals with damped atom-atom dispersion corrections. Phys. Chem. Chem.Phys. 10, 6615–6620 (2008)

(38) Marek, A.; Tureček, F. Collision-Induced Dissociation of Diazirine-Labeled Peptide Ions. Evidence for Brønsted-Acid Assisted Elimination of Nitrogen. *J. Am. Soc. Mass Spectrom.* **2014**, *25*, 778-789.

(39) Schwartz, B. L., and Bursey, M. M. Some Proline Substituent Effects in the Tandem Mass Spectrum of Protonated Penta-Alanine. *Biol. Mass Spectrom*. **1992**, 21, 92–96.

(40) Vaisar, T., and Urban, J. Probing the Proline Effects in CID of Protonated Peptides. *J. Mass Spectrom.* **1996**, 31, 1185–1187.

(41) Loo, J. A., Edmonds, C. G., and Smith, R. D. Tandem mass spectrometry of very large molecules. 2. Dissociation of multiply charged proline-containing proteins from electrospray ionization. *Anal. Chem.* **1993**, *65*, 425-438.

(42) M. M. Savitski, F. Kjeldsen, M. L. Nielsen, R. A. Zubarev. Complementary sequence preferences of electron-capture dissociation and vibrational excitation in fragmentation of polypeptide polycations. *Angew. Chem. Int. Ed.* 2006, 45, 5301.

(43) Pepin, R.; Laszlo, K. J.; Peng, B.; Marek, A.; Bush, M. F.; Tureček, F.; Comprehensive Analysis of Gly-Leu-Gly-Gly-Lys Peptide Dication Structures and Cation-Radical Dissociations Following Electron Transfer: From Electron Attachment to Backbone Cleavage, Ion-Molecule Complexes and Fragment Separation. *J. Phys. Chem. A* **2014**, *118*, 308-324.
(44) Tureček, F.; Chen, X.; Hao, C. Where Does the Electron Go? Electron Distribution and Reactivity of Peptide Cation-Radicals Formed by Electron Transfer in the Gas Phase. *J. Am. Chem. Soc.* **2008**, *130*, 8818-8833.
(45) Nguyen, H. T. H.; Andrikopoulos, P. C.; Bím, D.; Rulíšek, L.; Dang, A.; Tureček, F.: Radical Reactions Affecting Polar Groups in Threonine Peptide Ions. *J. Phys. Chem. B*, **2017**, *121*, 6557-6569.